

Isolation of Reactive Main Group Fragments by Frustrated Lewis Pairs

by

Alvaro A. Omaña Moreno

A thesis submitted in partial fulfillment of the requirements for the degree of

Doctor of Philosophy

Department of Chemistry

University of Alberta

© Alvaro A. Omaña Moreno, 2022

Abstract

The work in this Thesis describes significant progress made in the field of frustrated Lewis pairs (FLPs) at the intersection between modern main group chemistry and materials chemistry. Mainly, this work focuses on the use of an intramolecular phosphine-borane FLP (namely, *o*-ⁱPr₂P(C₆H₄)BCy₂ or **PB**) for the isolation of “bottleable” single-source molecular precursors to valuable materials.

Initially, new Group 14 element-based dihydrides (E = SiH₂, GeH₂) were prepared *via* E(II) dihalide capture by **PB** to form [PB{SiCl₂}] and [PB{GeCl₂}], and subsequent X/H group exchange gives their respective [PB{EH₂}] (E = Si or Ge) adducts in high yields. Upon gentle heating of [PB{EH₂}] (> 100 °C) in solution, the formation of H₂ gas and free **PB** ligand were confirmed by multinuclear (¹H, ³¹P, ¹¹B) NMR spectroscopy, along with observed Si or Ge deposition. The deposited Si or Ge materials were studied by SEM/EDX, XPS and Raman spectroscopy to confirm that: (1) elemental Si(0) and Ge(0) could be deposited; and (2) broad amorphous Si–Si and Ge–Ge stretching could be observed using Raman spectroscopy at 485 cm⁻¹ and 480 cm⁻¹, respectively. Consistently, **PB** could be re-collected after Group 14 element deposition with ~70 % recovery and re-used, allowing for a closed loop process. Isolation and thermolysis of a polymer precursor, [PB{SiMe₂}], was studied, showing that well-defined polydimethylsilane, [SiMe₂]_n, could be formed at < 110 °C.

Next, the development of FLP-chelated boron nitride precursors was explored by targeting the BN complex, [PB{BN}]. First, a [PB{H₂BNH₂}] adduct was accessed in high yield by dehydrogenation of ammonia-borane (H₃B•NH₃) and binding of

{H₂BNH₂} using **PB**. Unlike free amine-boranes, [PB{H₂BNH₂}] (and new related FLP-aminoborane complexes) did not undergo catalytic dehydrogenation with transition metal complexes, likely due to low polarity of the B^{δ+}-H^{δ-} linkages that would otherwise serve as initiation sites for catalysis. Instead, a step-wise halogenation/dehalogenation route was used to afford [PB{HBNH}], an FLP-chelate of the parent iminoborane HBNH. Unfortunately, due to low reactivity of the B-H and N-H linkages, [PB{HBNH}] did not undergo catalytic dehydrogenation to form [PB{BN}]. Upon addition of strong chlorinating agents to [PB{HBNH}], towards the useful intermediate [PB{ClBNH}], B-Cy bond activation in the ligand was observed.

Finally, a closer look at the reactivity of [PB{SiX₂}] (X = Cl, Br) adducts was performed in the hopes that subsequent reduction would yield [PB{E=E}PB] species; however, only free **PB** was formed according to NMR spectroscopy. To see if the related [PB{C=C}PB] dimer could be accessed, [PB{CH₂}] was isolated; however, deprotonation attempts resulted in P-C bond cleavage in the ligand. New phosphine-borane FLP chelates were synthesized, although these ligands were met with limited success in the binding of Group 14 element centers (Si, Ge). The work in this Thesis demonstrates that FLPs can be used to access valuable main group element motifs, as well as molecular precursors for the low temperature deposition of industrially relevant materials from the nano-scale to the bulk.

Preface

A portion of the work presented in this Thesis has been done in collaboration with other researchers and support staff within the Department of Chemistry at the University of Alberta.

Most X-ray crystallographic studies for the compounds in this Thesis (mainly Chapters 2 and 3) were performed by either Dr. M. J. Ferguson or Dr. Y. Zhou, including crystal mounting, data collection, and structure refinement to produce a full crystallographic report. Elemental analyses and thermal gravimetric analyses were performed by Dr. Wayne Moffat and Jennifer Jones at the Analytical Instrument Lab (University of Alberta). Computational studies were performed with the essential help of the Shared Hierarchical Academic Computing Network (SHARCNET: www.computeCanada.ca), WestGrid (www.westgrid.ca), and Compute/Calcul Canada (www.computeCanada.ca). The work in this Thesis was supported by the Canada Foundation for Innovation, the Faculty of Science at the University of Alberta, the Natural Sciences and Engineering Research Council of Canada, the Alberta Graduate Excellence Scholarship, and the University of Alberta Doctoral Recruitment Scholarship programs.

In Chapter 1, all writing was completed by Alvaro A. Omaña, with feedback from Prof. Eric Rivard between Thesis drafts; sections 1.1.2.1. and 1.1.2.2. were adapted and modified from a previously published *Chem. Rev.* article (see below). In Chapters 2 and 4, $^{29}\text{Si}\{^1\text{H}\}$ and ^1H -coupled ^{29}Si NMR spectra were successfully collected based on valuable insight received from Mark Miskolzie from the NMR Spectrometry Laboratory at the Department of Chemistry, University of Alberta.

Raman studies were performed by Taylor Lynk (M.Sc. student, McDermott Lab) at the University of Alberta. Scanning electron microscopy (SEM) and Energy-dispersive X-ray spectroscopy (EDX) were performed by Dr. Yingjie He (Veinot Group), while X-ray photoelectron spectroscopy (XPS) samples were submitted to NanoFab by Dr. Sarah Milliken (Veinot Group) at the University of Alberta. Full nanomaterial characterization was performed with great insight and feedback from Prof. Jonathan G. C. Veinot (University of Alberta). The attempted use of PB^{Mes} as a dihalotetrelene-stabilizing ligand was explored by a previous Rivard Lab undergraduate student Rachel K. Green. The first attempted isolations of $[\text{PB}\{\text{SiBr}_2\}]$ were performed by a visiting Ph.D. student Ryo Kobayashi (Iwamoto Lab, Tohoku University). Initial computational studies for Chapter 2 were performed by former undergraduate Evan R. Antoniuk in the group of Prof. Alex Brown (University of Alberta). After obtaining high quality X-ray crystallography data, the associated computations were re-optimized using solid-state structures as starting points, using valuable insight from Dr. Emanuel Hupf (University of Alberta/Universität Bremen). Rivard Lab Ph.D. alumnus, Dr. Matthew M. D. Roy, is thanked for his advice for synthesizing $[\text{PB}\{\text{SiCl}_2\}]$ more efficiently. In Chapter 3, the synthesis and characterization of $[\text{PB}\{\text{NBH}_2\}]$ was performed by Brandon L. Frenette, a current Rivard Lab Ph.D. candidate. The isolation of $[\text{PB}\{\text{H}_2\text{BN}(\text{Me})\text{H}\}]$ was performed by a previous Rivard Lab member Ryan Watt (University of Alberta). In Chapter 4, the characterization of $[\text{PB}\{\text{CCl}_2\}]$ was performed by Brandon L. Frenette, and initial reactions between $[\text{PB}\{\text{SiCl}_2\}]$ and Cp^*Li were performed by Dr. Eike Dornsiepen (University of Alberta).

According to the Thesis policy within our research group, each Chapter of this Thesis is essentially self-contained, and prepared in the form of a paper that is intended for publication in peer-reviewed journals.

A portion of this Thesis has been previously published and the publications are listed below:

Chapter 1:

M. M. D. Roy, A. A. Omaña, A. S. S. Wilson, M. S. Hill, S. Aldridge, E. Rivard, *Chem. Rev.* **2021**, *121*, 12784–12965.

Chapter 2:

A. A. Omaña, R. K. Green, R. Kobayashi, Y. He, E. R. Antoniuk, M. J. Ferguson, Y. Zhou, J. G. C. Veinot, T. Iwamoto, A. Brown, E. Rivard, *Angew. Chem. Int. Ed.* **2021**, *60*, 228–231.

Chapter 3:

(a) B. L. Frenette, A. A. Omaña, M. J. Ferguson, Y. Zhou, E. Rivard, *Chem. Commun.* **2021**, *57*, 10895–10898; (b) A. A. Omaña, R. Watt, Y. Zhou, M. J. Ferguson, E. Rivard, accepted to *Inorg. Chem.* (August 30th 2022).

In addition to the work described in this Thesis, contributions were also made in the following paper, published in a peer-reviewed journal:

Z. R. Najafabadi, A. A. Omaña, E. Rivard, J. B. P. Soares, *Macromol. Chem. Phys.* **2021**, *222*, 2100189.

Dedicated to my parents, Humberto Adolfo Omaña Contreras and Durvis Zulay

Moreno Cepeda, for their sacrifices and eternal support

Acknowledgements

Above all, I thank my family. My parents, Humberto and Durvis, sacrificed so much to give my siblings and I a life full of opportunities, and I am forever grateful. Los quiero mucho, viejitos. I thank my sister Vanessa for watching over me; I thank my brother Humberto for the big laughs he provides us with; I thank my in-laws Ed and Emily for always helping me out; and I thank Iggy, Vinny, and Lulu for the joy they bring to our lives. To my partner-in-crime, Dr. Chrissy Braun: you have given me so much support, so many ridiculous laughs, so much needed Chaotic Good in my life (including Jazzy). My happiest moments here have been because of you, and I thank you for all you've done for me.

To my supervisor, Prof. Eric Rivard: thank you for taking a chance on me and giving me guidance throughout this process. You pushed me to achieve at a level that I could not imagine before. I thank you for your passion and attentive mentorship. In addition, I would like to thank my committee (including non-examining chair and external) for their insightful feedback: Prof. Dennis Hall, Prof. Steven H. Bergens, Prof. Julianne Gibbs, Prof. Arthur Mar, Prof. Joe Takats, and Prof. Caleb D. Martin.

To all Rivardians, hear ye, hear ye! My journey would have been impossible without your ridiculous shenanigans. Shout out to previous members: Dr. Emanuel Hupf, Reverend Dr. MMD Roy, Dr. Sarah Parke, Dr. Bruno "The Brunester" Luppi, Dr. Ian "Bungler" Watson, Dr. Jocelyn "JOC" Sinclair, and Dr. Eike Dornsiepen. Shout out to previous filthy undergrads, namely Linkun Miao, Nicole Martinek, Rachel K. Green, Dominic Laverne, and Evangeline "Heartbreaker/Fav Undergrad" Dugbenu.

I also thank current members: Dr. Tanja Kunz, Samuel “Lab Daddy” R. Baird, Brandon “Rando without BN” L. Frenette, William “Billiam” Medroa del Pino, Abhishek “Abhi” V. Muralidharan, Mamak Bahktiari, and Janelle “JBiebz” Bykowski. You all made The Lab a special place to be; and now, you are all legally dead to me forever. One last note to quell the swirling rumors: I do not dye my hair.

We have great staff at the University of Alberta, all hard-working and friendly people I am lucky to have collided with. Massive shout out to The Machine Shop Dynamic Duo (Dirk Kelm and Paul Crothers), Dr. Jason Cooke, Dr. Yoram Apelblat, Dr. Mike “Magic Mike” Ferguson, Dr. Yuqiao Zhou, Dr. Wayne Moffat, Jennifer Jones, Matthew Kingston, Andrew Yeung, Ryan Lewis, Mike Bartowski, and Mark Miskolzie.

I am also very grateful at the human connections I made during my time here. In no specific order and in an incomplete, chaotic fashion: Dr. Nuri Kohn, Dr. Patrick “Party Pat” Moon, Dr. Hansol Park, Dr. Ben Rehl, Kevin “KDawg” Hooton, Anis Fahandej, Dr. Riley Endean, Kelsey Marilyn, Kevin “KTown” O’Connor, Dr. Jay He, Jasper Woodard, Ellen Buckie, Aaron Kirkey, Alyssa Fu, Emily Cheong, Riley Hooper, Dr. Chris Cooze, Arsh Hazrah, Nicholas Kissoon, Dr. Sarah Milliken, Cheryl and Fleming, and Dellah Cohlmin. Without your friendships, my degree would have been just a monotonous montage of stirring vials, NMRs, disappointment; rinse, repeat.

To my London and Waterloo pseudo-family, I thank you for your ever-lasting friendship and patience despite my patchy communication. In particular: Derek “Duhrek” Stocking, Juan Gomez, Mike Hooymayers, Travis “Iceman” Ko, Jen Ping. Every time I come back to see you; it feels like I never left. Thank you. Onward!

Table of Contents

Chapter 1 – Introduction	1
1.1 Study of Reactive Group 14 Element Species	1
1.1.1 Kinetic and Electronic Stabilization of Low-oxidation State Group 14 Elements within Molecular Species	5
1.1.2 Small Molecule Activation Involving Group 14 Element Hydrides (Si and Ge)	34
1.1.2.1 Stoichiometric Reactivity of Group 14 Element Tetrelenes and Related Hydrides (Si and Ge)	35
1.1.2.2 Catalytic Hydride Transfer (Hydroboration, Hydrosilylation, and Hydrocyanation)	38
1.2 Frustrated Lewis Pairs (FLPs): History and Chemistry	44
1.2.1 Traditional Lewis Base/Lewis Acid Chemistry and Early Studies of FLPs	45
1.2.2 Cooperative Activation of Small Molecules <i>via</i> FLPs	49
1.3 Silicon (Si) and Germanium (Ge) Films	55
1.3.1 Properties and Applications	55
1.3.2 Chemical Vapor Deposition (CVD) for the Growth of Si Films	59
1.3.3 Chemical Vapor Deposition (CVD) for the Growth of Ge Films	64
1.4 BN-Containing Polymers and Precursors to Bulk Boron Nitride	69
1.4.1 BN-Containing Polymers: Properties and Applications	71
1.4.2 Bulk BN: Properties and Applications	81

1.4.3 Known Preparations of Bulk Boron Nitride	82
1.5 Thesis Objectives	87
1.6 References	89
 Chapter 2 – Frustrated Lewis Pair Chelation as a Vehicle for Low Temperature Semi-conductor Element and Polymer Deposition	 105
2.1 Introduction	105
2.2 Results and Discussion	106
2.3 Conclusions	133
2.4 Experimental Details	134
2.4.1 General Considerations	134
2.4.2 Synthetic Procedures	137
2.4.3 X-ray Crystallography	150
2.5 References and Notes	155
 Chapter 3 – Frustrated Lewis Pair Chelation and Reactivity of Complexed Parent Iminoborane and Aminoborane	 160
3.1 Introduction	160
3.2 Results and Discussion	162
3.3 Conclusions	189
3.4 Experimental Details	190

3.4.1 General Considerations	190
3.4.2 Synthetic Procedures	191
3.4.3 X-ray Crystallography	202
3.5 References and Notes	208
Chapter 4 – Frustrated Lewis Pair-ligated Tetrelenes	213
4.1 Introduction	213
4.2 Results and Discussion	216
4.3 Conclusions	238
4.4 Experimental Details	239
4.4.1 General Considerations	239
4.4.2 Synthetic Procedures	241
4.4.3 X-ray Crystallography	255
4.5 References and Notes	260
Chapter 5 – Summary and Future Directions	266
5.1 References	275
Complete Bibliography	277

List of Figures

- Figure 1.1.** Molecular orbital (MO) diagram of planar (D_{2h}) and *trans*-bent (C_{2h}) conformations for ditetrelenes (R_2EER_2). 12
- Figure 1.2.** General molecular orbital (MO) diagram for tetrelenes (EH_2) in C_{2v} symmetry ($E = Si-Pb$). 14
- Figure 1.3.** CGMT model equations and their relevance to the observed geometry of ditetrelenes, by comparison of $H_2C=CH_2$ and Lappert's distannene $\{(Me_3Si)_2CH\}_2Sn=Sn\{CH(SiMe_3)_2\}_2$ (**1**). 15
- Figure 1.4.** Molecular orbital diagram for tetrelenes (EH_2), depicting the frontier molecular orbitals for singlet *vs.* triplet ground states. 15
- Figure 1.5.** FMOs of $[\{(Me_3Si)_2N\}_2Ge]$ (**28**), depicting π -donation and σ -withdrawal by neighboring N ligands. 18
- Figure 1.6.** Diagram showing the σ -donating and π -accepting orbital interactions for *N*-heterocyclic carbenes (NHCs) and cyclic alkyl amino carbenes (CAACs). 19
- Figure 1.7.** Computational (B3LYP/6-311+G** level of theory) potential energy surface with energies in kcal/mol for the oxidative addition of H_2 by Me_2Si and $\{HC=CH\}Si$. 28
- Figure 1.8.** Selected examples of germylenes (R_2Ge) and related low-oxidation state Ge(II) species (**61-70**). 31
- Figure 1.9.** Selected examples of amine-borane dehydrocoupling FLP catalysts (**107-110**), including structures of the amine-borane substrates tested. 53

- Figure 1.10.** Representative schematic for a typical CVD process, depicting: (a) mass transport; (b) gas diffusion; (c) adsorption; (d) gas phase reaction; (e) heterogeneous/surface reaction; (f) desorption and mass transport. 58
- Figure 1.11.** Selected examples of elemental Si film CVD precursors: (a) halosilanes; (b) mixed halo/hydridosilanes; (c) hydridosilanes; (d) organosilanes. 60
- Figure 1.12.** Selected examples of siloxanes used in SiO₂ film CVD. 64
- Figure 1.13.** Selected examples of Ge CVD film precursors: (a) halogermanes; (b) hydridogermanes; (c) organogermanes. 68
- Figure 2.1.** Molecular structure of [ⁱPr₂P(C₆H₄)Li(OEt₂)]₂ (left) and **PB** (right) with thermal ellipsoids at a 30 % probability level. 107
- Figure 2.2.** Molecular structure of **PB^{Mes}** with thermal ellipsoids at a 30 % probability level. 108
- Figure 2.3.** Molecular structure of [PB{GeCl₂}] (**1**) (left) and [PB{GeH₂}] (**2**) (right) with thermal ellipsoids at a 30 % probability level. 110
- Figure 2.4.** Molecular structure of [PB{HCl}] with thermal ellipsoids at a 30 % probability level. 112
- Figure 2.5.** Molecular structure of [PB{SiCl₂}] (**3**) (left) and [PB{SiH₂}] (**4**) (right) with thermal ellipsoids at a 30 % probability level. 113
- Figure 2.6.** TGA profile of [PB{GeH₂}] (**2**), ranging from 25 °C to 600 °C in a N₂ atmosphere at a heating rate of 10 °C/min. 114
- Figure 2.7.** TGA profile of [PB{SiH₂}] (**4**), ranging from 25 °C to 600 °C in a N₂ atmosphere at a heating rate of 10 °C/min. 115

- Figure 2.8.** TGA profile of **PB**, ranging from 25 °C to 600 °C in a N₂ atmosphere at a heating rate of 10 °C/min. 115
- Figure 2.9.** Computed relative Gibbs free energies in kcal/mol for Pathway 1 in the thermolysis of [PB{EH₂}] (E = Si (red lines) and Ge (black lines)) in the gas phase; values in parentheses correspond to those obtained with a toluene polarizable continuum model (PCM). 117
- Figure 2.10.** Computed relative Gibbs free energies in kcal/mol for Pathway 2 in the thermolysis of [PB{EH₂}] (E = Si (red lines) and Ge (black lines)) in the gas phase; values in parentheses correspond to those obtained with a toluene polarizable continuum model (PCM). 118
- Figure 2.11.** Secondary-electron SEM image showing Ge from the thermolysis of **2** on top of an aluminum stub. 119
- Figure 2.12.** An overlaid energy dispersive X-ray (EDX) map showing the distribution of C, O, P and Ge in a sample of deposited Ge. 120
- Figure 2.13.** EDX mapping images that show the spatial distribution of (a) P; (b) C; (c) Ge; (d) O in a deposited sample of Ge. 120
- Figure 2.14.** Angled (54°) secondary-electron SEM image of a Ge film deposited onto a Si wafer *via* thermolysis of **2** in toluene (1.06×10^{-2} M, 20 hrs, 110 °C). 121
- Figure 2.15.** Secondary-electron SEM image showing Si deposited from the thermolysis of **4** onto carbon tape. 122

- Figure 2.16.** An overlaid energy dispersive X-ray (EDX) map showing the distribution of C, O, P and Si in a sample of deposited Si. 122
- Figure 2.17.** EDX mapping images that show the spatial distribution of (a) P; (b) C; (c) Si; (d) O. 123
- Figure 2.18.** Angled (52°) secondary-electron SEM image of a Si film deposited onto a Ge wafer *via* thermolysis of **4** in toluene (3.22×10^{-2} M, 20 hrs, 110°C). 123
- Figure 2.19.** An overlaid EDX map of patterned Si film on a Ge wafer, showing the distribution of C, O, Ge and Si. 124
- Figure 2.20.** EDX mapping images to show the spatial distribution of (a) C; (b) O; (c) Si; (d) Ge. 124
- Figure 2.21.** Survey XPS spectra of deposited Ge. Sample preparation required temporary exposure of Ge to atmosphere prior to XPS analysis, resulting in partial oxidation of Ge. 126
- Figure 2.22.** High-resolution XPS spectra of a sample of bulk Ge with (a) C 1s; (b) O 1s; (c) Ge 2p; (d) Ge 3d regions shown. 127
- Figure 2.23.** Survey XPS spectrum of deposited Si. 127
- Figure 2.24.** High-resolution XPS spectra of bulk Si with (a) C 1s; (b) O 1s; (c) Si 2p regions shown (Si $2p_{3/2}$ and Si $2p_{1/2}$ peaks are separated by 0.68 eV). 128
- Figure 2.25.** Raman spectrum of deposited Ge using a 632.8 nm laser at 100 % power (5 mW) in static mode (10 seconds, 18 accumulations), showing the expected broad amorphous Ge–Ge stretching near 280 cm^{-1} . 129

- Figure 2.26.** Raman spectrum of deposited Si using Ge using a 632.8 nm diode laser at 100 % power (5 mW) in static mode (10 seconds, 15 accumulations), showing the expected broad amorphous Si–Si stretching near 485 cm^{-1} . 129
- Figure 2.27.** Molecular structure of $[\text{PB}\{\text{SiMe}_2\}]$ (**5**) with thermal ellipsoids at a 30 % probability level. 130
- Figure 2.28.** FT-IR spectrum for deposited polydimethylsilane $[\text{SiMe}_2]_n$ after precipitation from cold methanol and dried under high vacuum. 131
- Figure 2.29.** GPC elution profile for deposited polydimethylsilane $[\text{SiMe}_2]_n$. 132
- Figure 2.30.** ^1H - ^{29}Si HMBC 2D NMR spectrum of deposited polydimethylsilane $[\text{SiMe}_2]_n$ in C_6D_6 . 132
- Figure 3.1.** Molecular structure of $[\text{PB}\{\text{H}_2\text{BNH}_2\}]$ (**1**) with thermal ellipsoids at a 30 % probability level. 163
- Figure 3.2.** Molecular structure of $[\text{PB}\{\text{BH}_3\}]$ (**2**) with thermal ellipsoids at a 30 % probability level. 166
- Figure 3.3.** Molecular structure of $[\text{PB}\{\text{H}_2\text{BN}(\text{Me})\text{H}\}]$ (**3**) with thermal ellipsoids at a 30 % probability level. 168
- Figure 3.4.** Molecular structure of $[\text{P9B}\{\text{H}_2\text{BNH}_2\}]$ (**4**) with thermal ellipsoids at a 30 % probability level. 172
- Figure 3.5.** Optimized gas phase geometry of $[\text{P9B}\{\text{H}_2\text{BNH}_2\}]$ (**4**) computed at a M06-2X/cc-pVTZ level of theory with (a) calculated and experimental

- bond lengths [\AA], and (b) Wiberg bond indices (WBI) and natural charges (Q_{NPA}). 173
- Figure 3.6.** Molecular structure of $[\text{PB}\{\text{H}(\text{I})\text{BNH}_2\}]$ (**6**) with thermal ellipsoids at a 30 % probability level. 175
- Figure 3.7.** Molecular structure of $\text{Me}_2\text{S}\cdot\text{BI}_3$ with thermal ellipsoids at a 30 % probability level. 176
- Figure 3.8.** Molecular structure of $[\text{PB}\{\text{HBNH}\}]$ (**7**) with thermal ellipsoids at a 30 % probability level. 177
- Figure 3.9.** Computed (black trace; at a M06-2X/cc-pVTZ level of theory) and measured (red trace) IR spectra (powder, KBr plate) of $[\text{PB}\{\text{HBNH}\}]$ (**7**). 178
- Figure 3.10.** Computed natural bond orbitals (NBOs; at a M06-2X/cc-pVTZ level of theory) of $[\text{PB}\{\text{HBNH}\}]$ (**7**) depicting [with e^- occupancy]: (a) the B–N π orbital [$2.0 e^-$]; (b) the B–N π^* orbital [$0.0 e^-$]; (c and d) B–N σ and σ^* orbitals [2.0 and $0.0 e^-$]; (e and f) B–N and P–B σ -orbital [each $2.0 e^-$] involving the **PB** ligand. 179
- Figure 3.11.** Optimized gas phase geometry of $[\text{PB}\{\text{HBNH}\}]$ (**7**) computed at a M06-2X/cc-pVTZ level of theory with (a) calculated and experimental bond lengths [\AA], and (b) Wiberg bond indices (WBI) and natural charges (Q_{NPA}) for $[\text{PB}\{\text{HBNH}\}]$ (**7**). 180
- Figure 3.12.** TGA profile of $[\text{PB}\{\text{H}_2\text{BNH}_2\}]$ (**1**), ranging from $25\text{ }^\circ\text{C}$ to $500\text{ }^\circ\text{C}$ in a N_2 atmosphere at a heating rate of $10\text{ }^\circ\text{C}/\text{min}$. 182

- Figure 3.13.** TGA profile of [PB{HBNH}] (**7**), ranging from 25 °C to 500 °C in a N₂ atmosphere at a heating rate of 10 °C/min. 183
- Figure 3.14.** Molecular structure of [PB{H(Bn)BNH}{K(THF)₂}] (**8**) with thermal ellipsoids at a 30 % probability level. 185
- Figure 3.15.** Molecular structure of [ⁱPr₂P(C₆H₄)BCy{Cl₂BNH}] (**9**) with thermal ellipsoids at a 30 % probability level. 187
- Figure 3.16.** Computed molecular orbitals for [ⁱPr₂P(C₆H₄)BCy{Cl₂BNH}] (**9**) at a M06-2X/cc-pVTZ level of theory depicting: (a) HOMO with B-N π orbital character; (b) LUMO with B-N π* orbital character. 187
- Figure 4.1.** Selected examples of: (a) C-/N-donor-stabilized tetrelenes and EH₂ complexes (E = Si or Ge); (b) miscellaneous/mixed donor Si and Ge hydride complexes. 214
- Figure 4.2.** Molecular structure of [PB{SiBr₂}] (**5**) with thermal ellipsoids at a 30 % probability level. 218
- Figure 4.3.** Molecular structure of [PB{AgOTf}]₂ (**6**) with thermal ellipsoids at a 30 % probability level. 224
- Figure 4.4.** Molecular structure of [PB{CH₂}] (**8**) with thermal ellipsoids at a 30 % probability level. 227
- Figure 4.5.** Optimized gas phase geometry of [PB{CH₂}] (**8**) computed at a M06-2X/cc-pVTZ level of theory with (a) calculated and experimental bond lengths for molecule A in the crystallographic unit cell of **8** [Å], and (b)

Wiberg bond indices (WBI) and natural charges (Q_{NPA}) for $[\text{PB}\{\text{CH}_2\}]$ (8). 229

Figure 4.6. Lowest unoccupied molecular orbital (LUMO; at a M06-2X/cc-pVTZ level of theory) of $[\text{PB}\{\text{CH}_2\}]$ (8) depicting significant P–C(*i*Pr) σ^* character. 230

Figure 4.7. Molecular structure of $[\{(\text{THF})_3\text{Li}\}^i\text{PrP}(\text{C}_6\text{H}_4)\text{BCy}_2\{\text{CH}_2\}]$ (9) with thermal ellipsoids at a 30 % probability level. 232

Figure 4.8. Molecular structure of $[\text{}^i\text{Pr}_2\text{PCH}_2(\text{C}_6\text{H}_4)\text{Li}(\text{OEt}_2)]_2$ (10) with thermal ellipsoids at a 30 % probability level. 234

Figure 4.9. Molecular structure of $^{\text{CH}_2}\text{PB}$ with thermal ellipsoids at a 30 % probability level. 235

List of Tables

Table 1.1.	Comparison of polypropylene $[\text{H}_2\text{C}-\text{C}(\text{H})\text{Me}]_n$ and poly(<i>N</i> -methylaminoborane) $[\text{H}_2\text{B}-\text{N}(\text{H})\text{Me}]_n$.	79
Table 1.2.	Structural data and properties for boron nitride phases.	81
Table 2.1.	X-ray crystallographic data for compounds $[\text{}^i\text{Pr}_2\text{P}(\text{C}_6\text{H}_4)\text{Li}(\text{OEt}_2)]_2$, PB^{Mes} , and PB .	152
Table 2.2.	X-ray crystallographic data for compounds [PB{HCl}] , 1 , and 2 .	153
Table 2.3.	X-ray crystallographic data for compounds 3-5 .	154
Table 3.1.	X-ray crystallographic data for compounds 1-3 .	204
Table 3.2.	X-ray crystallographic data for compounds 4 , 6 , and $\text{Me}_2\text{S}\cdot\text{BI}_3$.	205
Table 3.3.	X-ray crystallographic data for compounds 7-9 .	206
Table 4.1.	Notable crystallographic features in the partial FLP-dihydridotetrelene series isolated so far.	227
Table 4.2.	X-ray crystallographic data for compounds 5 , 6 , and 8 .	257
Table 4.3.	X-ray crystallographic data for compounds 9 , 10 , and CH²PB .	259

List of Schemes

- Scheme 1.1.** Isolation and reactivity of the first distannene $\{(\text{Me}_3\text{Si})_2\text{CH}\}_2\text{Sn}=\text{Sn}\{\text{CH}(\text{SiMe}_3)_2\}_2$ (**1**) by the Lappert Group. 2
- Scheme 1.2.** The first isolated (a) Si=C; (b) Si=Si and (c) P=P bonded compounds. 3
- Scheme 1.3.** (a) Kipping's attempt to prepare $\text{Ph}_2\text{Si}=\text{SiPh}_2$ (**14**) *via* reduction; (b) laser flash pyrolysis of $[\{(\text{H}_2\text{C})_4(\text{Me}_2\text{Si})_2\}]\text{SiPh}_2$ (**15**) to generate Ph_2Si : (**16**) *in-situ*. 7
- Scheme 1.4.** Activation of H_2 by the digermynes $\text{Ar}^{\text{iPr}_4}\text{GeGeAr}^{\text{iPr}_4}$ (**20**). 9
- Scheme 1.5.** Activation of H_2 by the distannynes $\text{Ar}^{\text{iPr}_4}\text{SnSnAr}^{\text{iPr}_4}$ (**24**) and $\text{Ar}^{\text{iPr}_8}\text{SnSnAr}^{\text{iPr}_8}$ (**25**). 10
- Scheme 1.6.** Isolation of (a) $\text{IPr}\cdot\text{Si}=\text{Si}\cdot\text{IPr}$ (**30**) using KC_8 as a reducing agent, and (b) $\text{IPr}\cdot\text{Ge}=\text{Ge}\cdot\text{IPr}$ (**32**) by using $\{(\text{Mes}\text{Nacnac})\text{Mg}\}_2$ as a reducing agent. 20
- Scheme 1.7.** Synthesis of Si(II) precursors (a) $\text{IPr}\cdot\text{SiCl}_2$ (**35**); (b) $\text{NHC}\cdot\text{SiBr}_2$ [IPr (**37**), MeIPr (**38**)]. 22
- Scheme 1.8.** Lewis base-induced disproportionation of (a) Si_2Cl_6 to form Si(II) and Si(IV) adducts, **29** and **35**; (b) Si_2Br_6 to form Si(II) and Si(IV) adducts, **36-39**. 23
- Scheme 1.9.** Synthesis of $\text{IPr}\cdot\text{SiH}_2\cdot\text{BH}_3$ (**41**) starting from $\text{IPr}\cdot\text{SiCl}_2$ (**35**). 24
- Scheme 1.10.** Synthesis of $\text{IPr}\cdot\text{H}_2\text{SiGeH}_2\cdot\text{W}(\text{CO})_5$ (**44**) and $\text{IPr}\cdot\text{H}_2\text{SiSnH}_2\cdot\text{W}(\text{CO})_5$ (**45**). 25
- Scheme 1.11.** Selected examples of H_2 activation by silylenes. 27

- Scheme 1.12.** Selected examples of (a) N–H bond activation; (b) B–H bond activation or; (c) synergistic H^+/H^- addition by silylenes and related low-oxidation state silicon species. 30
- Scheme 1.13.** Divergent reactivity of $[Ge(O^tBu)_2]$ (**75**) with $Me_2S \cdot BH_3$ or HBpin. 33
- Scheme 1.14.** Synthesis of the amidophosphine-ligated Si(II) complexes (**81** and **82**) and their reactivity with olefins, silanes or phosphines. 36
- Scheme 1.15.** Stoichiometric hydrogermylation of alkenes and alkynes with amido(hydrido)germylenes. 37
- Scheme 1.16.** Hydroboration of aldehydes and ketones with the pre-catalysts **95** and **96**. 39
- Scheme 1.17.** (a) Catalytic hydroboration using the terphenyl-supported pre-catalysts (**98-100**); (b) stoichiometric oxidative addition of HBpin with **98** to form $[Ar^{iPr_6}GeH\{C(H)Ph-PPh_2\}(Bpin)]$ (**101**). 41
- Scheme 1.18.** (a) Si-catalyzed pyridine hydroboration using a Si(II) species (**102**); (b) hydrocyanation of aldehydes by a Si(IV) hydride (**103**). 42
- Scheme 1.19.** Divergent one- or two-electron reactivity pathways using Me_3P or tBu_3P in the presence of $B(C_6F_5)_3$ and Ph_3SnH . 45
- Scheme 1.20.** (a) Deprotonation of pyridine hydrochloride by 2,6-lutidine; (b) displacement of 2,6-lutidine by pyridine in the BF_3 -adduct. 47
- Scheme 1.21.** Cooperative activation of a benzyne by Ph_3P and BPh_3 . 47

- Scheme 1.22.** (a) Initial activation of the R_3Si-H bond by $B(C_6F_5)_3$; (b) nucleophilic attack onto R_3Si by a ketone; (c) final hydride transfer from $[HB(C_6F_5)_3]^-$ to form the hydrosilylated product, $R'(R'')(H)CO-SiR_3$. 48
- Scheme 1.23.** Reversible dihydrogen activation by $Mes_2P(C_6F_4)B(C_6F_5)_2$ (**105**). 49
- Scheme 1.24.** Stoichiometric dehydrocoupling of amine-boranes using $tBu_3P/B(C_6F_5)_3$ mixtures. 50
- Scheme 1.25.** (a) Stoichiometric dehydrocoupling of dimethylamine-borane into a mixture of products; (b) attempted dehydrocoupling of diphenylphosphine-borane by the FLPs R_3EOTf/TMP ($ER_3 = SiMe_3$ or Sn^rBu_3). 51
- Scheme 1.26.** Attempted dehydrocoupling of $Ar^{iPr_6}SnH_3$ (**111**) by a mixture of $tBu_3P/B(C_6F_5)_3$. 54
- Scheme 1.27.** Asymmetric transfer hydrogenation of imines using a borane/sulfinamide FLP system. 55
- Scheme 1.28.** Dehydrogenation and regeneration of a cyclic amine-borane (**128**) in search of regeneratable hydrogen storage materials. 70
- Scheme 1.29.** Ir-catalyzed dehydropolymerization of: (a) ammonia-borane; (b) primary amine-borane adducts. 72
- Scheme 1.30.** (a) Synergistic H^+/H^- exchange between primary amine-boranes and the iminoborane $H_2B=N^iPr_2$; (b) low temperature ($-40\text{ }^\circ\text{C}$) amine-induced dehydropolymerization of primary amine-boranes. 74

- Scheme 1.31.** Catalytic dehydrocoupling mechanisms for: (a) the polymerization of parent ammonia-borane using [(POCOP)IrH₂]; (b) the formation of cyclic dimer [H₂B-NMe₂]₂ from [Cp₂Ti]. 76
- Scheme 1.32.** General route to a variety of amine-boranes by salt metathesis and subsequent dehydropolymerization. 78
- Scheme 1.33.** Selected examples of routes to bulk crystalline BN forms (*h*-BN or *c*-BN) using *a*-BN as a reagent. 85
- Scheme 2.1.** Step-wise syntheses of **PB^{Mes}** and **PB**. 107
- Scheme 2.2.** Step-wise and one-pot syntheses of [PB{GeH₂}] (**2**). 109
- Scheme 2.3.** Syntheses of [PB{SiH₂}] (**4**) using different SiCl₂ sources. 111
- Scheme 3.1.** (a) Large-scale synthesis of boron nitride (BN); (b) first isolated complex of HBNH (**A**); (c) previous work using FLP-chelated EH₂ (Si, Ge) complexes (**B** and **C**) and their use to deposit films of silicon and germanium, respectively. 161
- Scheme 3.2.** Proposed reaction sequence leading to the formation of [PB{H₂BNH₂}] (**1**) and computed energetics (THF polarized continuum model, M06-2X/cc-pVTZ). 165
- Scheme 3.3.** Proposed reaction sequence leading to the formation of [PB{H₂BN(Me)H}] (**3**) and computed energetics (THF polarized continuum model, M06-2X/cc-pVTZ). 169
- Scheme 3.4.** Synthesis of [PB{HBNH}] (**7**) from [PB{H₂BNH₂}] (**1**) *via* B–H/B–I exchange and subsequent dehalogenation with K[N(SiMe₃)₂]. 174

- Scheme 3.5.** Proposed route involved in the chlorination of $[\text{PB}\{\text{HBNH}\}]$ (**7**) by TCCA to yield $[\text{}^i\text{Pr}_2\text{P}(\text{C}_6\text{H}_4)\text{BCy}\{\text{Cl}_2\text{BNH}\}]$ (**9**), and the computed energies associated with the isomerization of intermediate **9**^{INT} into **9** via a 1,3-chloride shift. 188
- Scheme 4.1.** Syntheses of $[\text{PB}\{\text{EH}_2\}]$ [$\text{E} = \text{Si}, \text{Ge}$ (**3** and **4**)] and their use as precursors to bulk Si and Ge, respectively. 215
- Scheme 4.2.** Potassium-mediated reduction of $[\text{PB}\{\text{SiCl}_2\}]$ (**1**) and $[\text{PB}\{\text{GeCl}_2\}]$ (**2**). 217
- Scheme 4.3.** Synthesis of $[\text{PB}\{\text{SiBr}_2\}]$ (**5**) from Khyp (Khyp = $[\text{K}(\text{THF})_2][\text{Si}(\text{SiMe}_3)_3]$) and SiBr_4 and attempted reductions using two equiv. of KC_8 . 217
- Scheme 4.4.** Lewis base-induced disproportionation of higher halosilanes, Si_2Cl_6 or Si_2Br_6 , with IPr in the presence of **PB**, leading to the formation of $[\text{PB}\{\text{SiCl}_2\}]$ (**1**) and $[\text{PB}\{\text{SiBr}_2\}]$ (**5**). 219
- Scheme 4.5.** Synthesis of $[\text{PB}\{\text{AgOTf}\}]_2$ (**6**) from **PB** or $[\text{PB}\{\text{SiCl}_2\}]$ (**1**). 224
- Scheme 4.6.** Preparation of the methylene complex $[\text{PB}\{\text{CCl}_2\}]$ (**7**) and attempted reduction. 226
- Scheme 4.7.** Proposed route to silicon or germanium carbide precursors $[\text{PB}\{\text{C}=\text{E}=\text{C}\}\text{PB}]$ ($\text{E} = \text{Si}$ or Ge). 229
- Scheme 4.8.** Synthetic route to a new methylene-linked FLP, **CH²PB**. 234
- Scheme 4.9.** Synthesis of $[\text{}^i\text{Pr}_2\text{PCH}_2(\text{C}_6\text{H}_4)\text{BMes}_2\{\text{GeCl}_2\}]$ (**11**) and attempted synthesis of $[\text{}^i\text{Pr}_2\text{PCH}_2(\text{C}_6\text{H}_4)\text{BMes}_2\{\text{GeH}_2\}]$ (**12**). 236

Scheme 5.1. Proposed routes to $\text{Si}_x\text{Ge}_{1-x}$ and SiC precursors.	268
Scheme 5.2. Attempted route to the dimeric species $[\text{PB}\{\text{BN}\}_2\text{PB}]$ (dashed arrows) and B–Cy ligand activation of $[\text{PB}\{\text{HBNH}\}]$ from Chapter 3.	270
Scheme 5.3. Proposed route to new sterically protected FLPs.	271
Scheme 5.4. Proposed synthesis of a dimeric FLP-stabilized BN precursor.	271
Scheme 5.5. Syntheses of $^{\text{CH}_2}\text{PB}$, $^{\text{CH}_2}\text{PB}_{\text{Mes}}$ and $[\text{CH}_2\text{PB}_{\text{Mes}}\{\text{GeCl}_2\}]$.	272
Scheme 5.6. (a) Proposed route to dimeric FLP ligands and their target $[\text{FLP}\{\text{E}=\text{E}\}\text{FLP}]$ complexes; (b) reported route to 2-pyridinyl-phosphine ligands.	274

List of Symbols, Nomenclature, and Abbreviations

{ ⁿ X}	Decoupled to ⁿ X nucleus
Å	Ångström
Ad	1-Adamantyl
Ar	Aryl
Ar ^C	4- ⁱ PrC ₆ H ₄
Ar ^F	3,5-(F ₃ C) ₂ C ₆ H ₃
Ar ^{*Me}	2,6,4-Ph ₂ CH ₂ MeC ₆ H ₂
Ar ^{*iPr}	2,6,4-Ph ₂ CH ₂ ⁱ PrC ₆ H ₂
Ar ^{iPr4}	2,6-Dipp ₂ C ₆ H ₃
Ar ^{iPr6}	2,6-Trip ₂ C ₆ H ₃
Ar ^{iPr8}	C ₆ H-2,6-Trip ₂ -3,5- ⁱ Pr ₂
Ar ^{Me6}	2,6-Mes ₂ C ₆ H ₃
atm	Atmospheric (unit of pressure)
avg.	Average
B3LYP	Becke, 3-parameter, Lee–Yang–Parr
BBN	9-Borabicyclo[3.3.1]nonane
B.E.	Binding Energy
Bn	Benzyl (CH ₂ Ph)
br	Broad
°C	Degree centigrade

C_6D_6	Benzene- d_6
<i>ca.</i>	<i>Circa</i> (Latin for approximately)
cat.	Catalyst
CAAC	Cyclic alkyl amino carbene
cc-pVTZ	Correlation-consistent polarized valence-only triple-zeta
$CDCl_3$	Chloroform- d
CGMT	Carter-Goddard-Malrieu-Trinquier
CHS	Cyclohexasilane $[H_2Si]_6$
cm^{-1}	Wavenumber
COD	1,5-Cyclooctadiene
COE	Cyclooctene
COSY	2-D 1H - 1H Correlation spectroscopy
Cp	Cyclopentadienyl $[C_5H_5]^-$
Cp*	Pentamethylcyclopentadienyl $[C_5Me_5]^-$
Cp ^{3M}	$[C_5Me_3H_2]^-$
Cp ^{4M}	$[C_5Me_4H]^-$
Cp ^{4ME}	$[C_5Me_4Et]^-$
Cp ^{TMS}	$[C_5(Me_3Si)H_4]^-$
CPS	Cyclopentasilane $[H_2Si]_5$
CVD	Chemical vapor deposition
Cy	Cyclohexyl
\mathcal{D}	Polydispersity (M_w/M_n ; see PDI below)

d	Doublet
D ₃	Hexamethylcyclotrisiloxane [Me ₂ SiO] ₃
D ₄	Octamethylcyclotetrasiloxane [Me ₂ SiO] ₄
dd	Doublet of doublets
Dsi	CH(SiMe ₃) ₂
dt	Doublet of triplets
δ	Delta (partial charge or chemical shift)
ΔE _{S-T}	Single-triplet energy gap
ΔE [‡]	Activation energy
ΔG [‡]	Activation Gibbs free energy
δ ⁺ /δ ⁻	Partial positive/negative charge
DABCO	1,4-Diazabicyclo[2.2.2]octane
DFT	Density functional theory
diox	Dioxane
Dipp	2,6- <i>i</i> -Pr ₂ C ₆ H ₃
Dipp ⁻ Nacnac	[(HC(MeCNDipp) ₂)] ⁻
Dipp ⁻ /NMe ₂ ⁻ Nacnac	[HC(Me ₂ NCNDipp) ₂] ⁻
DMAP	4-Dimethylaminopyridine
DMSO	Dimethyl sulfoxide
dppp	1,3- <i>Bis</i> (diphenylphosphino)propane
E	Variable main group element
EA	Elemental analysis

ECR-MP	Electron-cyclotron-resonance microwave plasma (ECR-MP)
EDX	Energy dispersive X-ray analysis
Ee	Enantiomeric excess
<i>e.g.</i>	<i>Exempli gratia</i> (Latin for “for the sake of example”)
E _g	Electronic band gap
EPR	Electron paramagnetic resonance
equiv	Molar equivalents
Et	Ethyl (C ₂ H ₅)
η ⁿ	Hapticity (n)
Et ₂ O	Diethyl ether
eV	Electron volt
Fc	Ferrocenyl
FLP	Frustrated Lewis pair
FT-IR	Fourier transform infrared spectroscopy
FMO	Frontier molecular orbital
FWHM	Full-width half max
Fxyl	3,5-(F ₃ C) ₂ C ₆ H ₃
g	Gram
GPC	Gel permeation chromatography
HBcat	Catecholborane
HBpin	Pinacolborane
HF-CVD	Hot filament/wire CVD

HMBC	Heteronuclear multiple bond correlation
HMDSO	Hexamethyldisiloxane
HOMO	Highest occupied molecular orbital
HSQC	Heteronuclear single quantum coherence
HT-HP	High temperature-high pressure
Hz	Hertz
<i>i</i> Bu	<i>iso</i> -Butyl
<i>i.e.</i>	<i>Id est</i> (Latin for “that is”)
ImMe ₂	(HCNMe) ₂ C:
ImMe ₄	(MeCNMe) ₂ C:
<i>in-situ</i>	Latin for “on-site” or “in-position”
IPr	(HCNDipp) ₂ C:
<i>i</i> Pr	Isopropyl (Me ₂ CH)
K	Kelvin
KC ₈	Potassium graphite
Kcal	Kilocalorie
kDa	Kilodaltons (1,000 g/mol)
Khyp	[K(THF) ₂][Si(SiMe ₃) ₃]
LA	Lewis acid
LB	Lewis base
LED	Light-emitting diode
LUMO	Lowest unoccupied molecular orbital

m	Multiplet
M06	Minnesota 06 functional
Me	Methyl
^{Me} IPr	(MeCNDipp) ₂ C:
Mes	Mesityl (2,4,6-Me ₃ C ₆ H ₃)
Mes*	2,4,6- ^t Bu ₃ C ₆ H ₃
^{Mes} Nacnac	[(HC(MeCNMes) ₂] ⁻
mg	Milligram
MHz	Megahertz
mL	Milliliter
mmol	Millimole
M _n	Number average molecular weight
MO	Molecular orbital
mol	Mole
M.p.	Melting point
MS	Mass spectrometry
M _w	Weight average molecular weight
n	Principal quantum number
Nacnac	General β-diketimine ligand
NBO	Natural bonding orbital
ⁿ Bu	<i>normal</i> -Butyl
NHC	<i>N</i> -Heterocyclic carbene

NHO	<i>N</i> -Heterocyclic olefin
${}^nJ_{AB}$	<i>n</i> Bond coupling constant between A and B
NMR	Nuclear magnetic resonance
NPA	Natural population analysis
ν	Nu (wave number)
q	Quartet
OTf	Trifluoromethanesulfonate or triflate
Pa	Pascal
PCE	Power conversion efficiency
PCM	Polarizable continuum model
PCVD	Plasma/photo/laser-assisted CVD (PCVD)
PDI	Polydispersity index; see <i>D</i> above
Ph	Phenyl
POCOP	[1,3-(<i>t</i> Bu ₂ PO) ₂ C ₆ H ₃] ⁻
ppm	Parts per million
pseudo-d	Pseudo-doublet
pseudo-t	Pseudo-triplet
R	Variable functional group
(<i>R</i>)-	<i>Rectus</i> (Latin for “right”)
R ^F	-C(CF ₃) ₃
RI	Refractive index
ρ	Rho (density)

q	Quartet
Q _{NPA}	Natural electron charges (derived from NPA)
s	Singlet
(S)-	<i>Sinister</i> (Latin for “left”)
^s Bu	<i>sec</i> -Butyl
SEM	Scanning electron microscopy
Σ _X	Sum of angles (°) about X
t	Triplet
^t Bu	<i>tert</i> -Butyl
TCCA	Trichloroisocyanuric acid
TEOS	Tetraethylorthosilicate
T _g	Glass transition temperature
TGA	Thermogravimetric analysis
THF	Tetrahydrofuran
TMEDA	<i>N,N,N',N'</i> -Tetramethylethylenediamine
TMP	2,2,6,6-Tetramethylpiperidine
TOF	Turn-over frequency
Torr	Unit of pressure
Trip	2,4,6- ^t Pr ₃ C ₆ H ₂
UV-vis	Ultraviolet/visible spectroscopy
<i>via</i>	Latin for “by way of”
<i>vide infra</i>	Latin for “see below”

<i>vide supra</i>	Latin for “see above”
vs.	<i>Versus</i> (Latin for “facing”)
W	Watt
WAXS	Wide-angle X-ray scattering
WBI	Wiberg-bond index
wt. %	Weight percent
X	Variable halide group
XPS	X-ray photoelectron spectroscopy
Xyl	2,6-Me ₂ C ₆ H ₄
Z	Atomic number

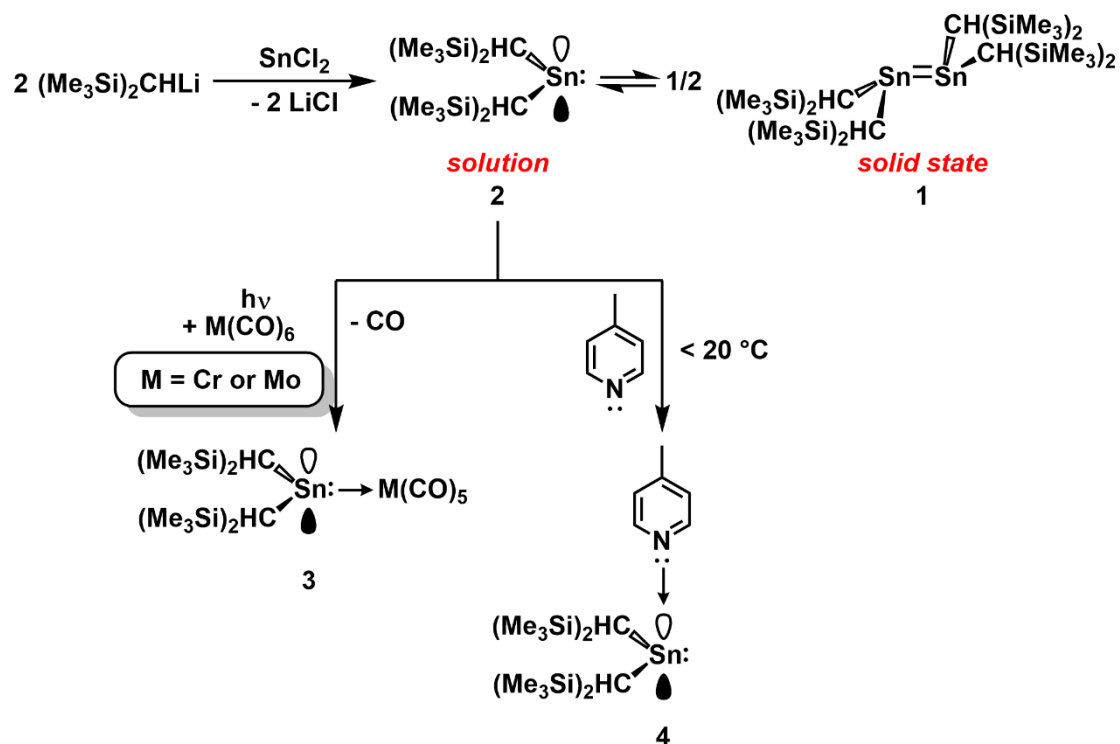
Chapter 1 – Introduction

1.1 Study of Reactive Group 14 Element Species

Until the 1970s, the prevailing view of main group element chemistry was that all observed reactivity was well-understood and general interest had shifted onto organometallic chemistry, a shift that gave rise to major advances in metal-mediated catalysis.^{1,2} Key developments, such as the Fischer-Tropsch process for converting CO into hydrocarbons using heterogeneous transition metals (*e.g.*, Co, Fe, and Ru) or the large-scale synthesis of methanol over a ZnO surface, had likewise spurred the parallel advancement of homogeneous catalysis.^{3,4} This was reflected by the emergence of the [HCo(CO)₄]-catalyzed carbonylation of methanol and other industrial-scale syntheses of valuable chemicals.^{3,4}

The study of main group element chemistry continued with the underlying philosophy that *s*- or *p*-block elements could not mediate chemical transformations in a similar manner as transition metals, largely due to the lack of energetically accessible *d*-orbitals and limitations in frontier orbital symmetries within the resulting compounds.⁵ Another limiting concept prior to the 1980s was the “double-bond rule”, the idea that only the *p*-block elements from B to O (principal quantum number of two) could form stable π -bonds.^{1,2,6} The first example of a “double-bond rule” exception was reported by Lappert in 1973, wherein the distannene $\{(Me_3Si)_2CH\}_2Sn=Sn\{CH(SiMe_3)_2\}_2$ (**1**) was obtained from salt metathesis between two equiv. of $\{(Me_3Si)_2CH\}Li$ and $SnCl_2$ (Scheme 1.1).⁷ In solution, the distannene (**1**) dissociates into the monomeric stannylene units $\{(Me_3Si)_2CH\}_2Sn$: (**2**), as confirmed

by cryoscopy and mass spectrometry (MS).⁷ The ambiphilic nature of the stannylene can be demonstrated by adding metal carbonyls (and light to induce CO loss) to form compound **3** or by adding a neutral *N*-donor to form compound **4** (Scheme 1.1).⁷

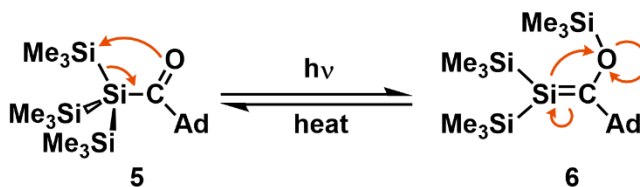


Scheme 1.1. Isolation and reactivity of the first distannene $\{(\text{Me}_3\text{Si})_2\text{CH}\}_2\text{Sn}=\text{Sn}\{\text{CH}(\text{SiMe}_3)_2\}_2$ (**1**) by the Lappert Group.

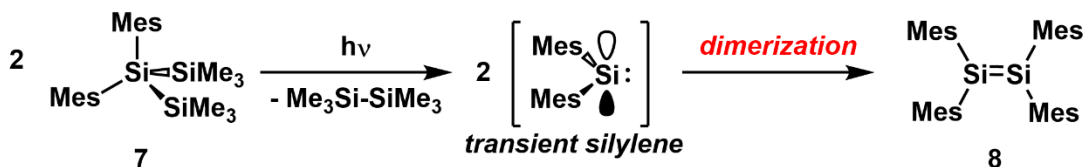
Despite Lappert's advances in breaking the "double-bond rule", there still remained confidence in the validity of this concept.⁶ The "double-bond" rule was further disproved by three major achievements in 1981: the isolation of stable Si=C, Si=Si and P=P bonded species by Brook, West, and Yoshifuji, respectively (Scheme 1.2).⁸⁻¹⁰ Upon photolytic Si-Si bond activation of either Brook's $(\text{Me}_3\text{Si})_3\text{Si-C}(\text{O})\text{Ad}$ (Ad = 1-adamantyl; **5**) or West's $\text{Me}_2\text{Si}(\text{SiMe}_3)_2$ (**7**) precursors, their respective Si=E

(E = C or Si) species $(\text{Me}_3\text{Si})_2\text{Si}=\text{C}(\text{OSiMe}_3)\text{Ad}$ (**6**) or $\text{Mes}_2\text{Si}=\text{SiMes}_2$ (Mes = 2,4,6- $\text{Me}_3\text{C}_6\text{H}_2$) (**8**) could be accessed.^{8,9} Using a milder route, Yoshifuji's Mes^*PCl_2 (**9**; $\text{Mes}^* = 2,4,6\text{-}t\text{Bu}_3\text{C}_6\text{H}_2$) precursor could be reacted with two equiv. of Mg metal at room temperature to afford the diphosphene¹⁰ $\text{Mes}^*\text{P}=\text{PMes}^*$ (**10**); this work has inspired other mild routes to diphosphenes and related species due to its synthetic ease.¹¹

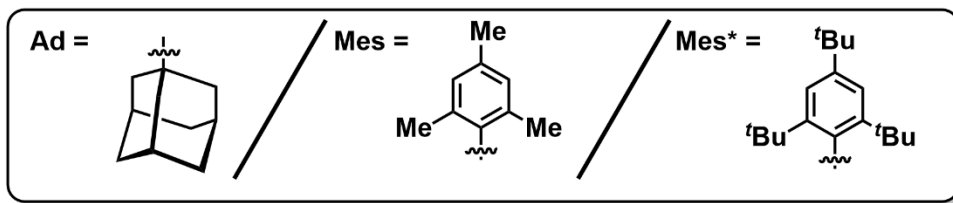
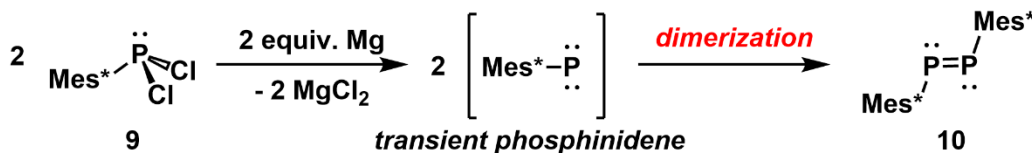
(a) First isolated Si=C bonded compound (Brook)



(b) First isolated Si=Si bonded compound (West)



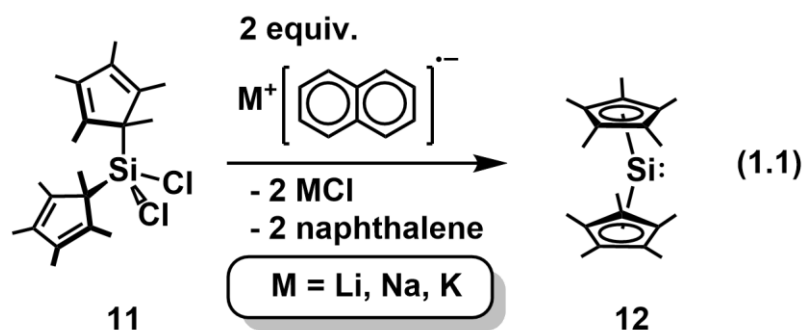
(c) First isolated P=P bonded compound (Yoshifuji)



Scheme 1.2. The first isolated (a) Si=C; (b) Si=Si and (c) P=P bonded compounds.

With the exception of Brook's disilene (which likely occurs through a concerted 1,3-trimethylsilyl shift), the doubly-bonded species introduced above (compounds **6**, **8**, and **10**) are proposed to be the result of dimerization of reactive $\text{R}\ddot{\text{P}}:$ or $\text{R}_2\text{Si}:$ species.^{9,10}

Of note, the R groups present have enough steric bulk to enable the formation of well-defined diphosphene or disilene products (as opposed to oligomeric mixtures). To show that intermediate Si(II) species could be observed under ambient conditions, the isolation of the first Si(II) species by Jutzi, Cp*₂Si (Cp* = [C₅Me₅]⁻) (**12**), is shown in Equation 1.1.¹² By applying alkali metal-mediated reduction of Cp*₂SiCl₂ (**11**), compound **12** can be obtained, which has a slightly distorted “metallocene”-type structure in the solid-state (Equation 1.1).¹² A distinction must be made here between compounds featuring E(II) centers and tetrelenes (R₂E); a compound must be two-coordinate to be classified as a tetrelene (R₂E). Since the Si(II) environment in Jutzi’s Cp*₂Si (**12**) contains two [η⁵-Cp*]⁻ ligands,¹² it cannot be classified as a silylene. Expanding further on these definitions, low-oxidation state Group 14 element (tetrel) compounds are often classified as tetrelynes (REER; R = anionic ligand), ditetrelenes (R₂EER₂; R = anionic ligand), tetrelenes (R₂E; R = anionic ligand), ditetrelones (L_xEEL_x; L = neutral ligand) or tetrelones (L_xE); these different compound classes will be discussed with examples in later sections.



Although the isolation of Cp*₂Si (**12**) demonstrated that molecular complexes of silicon can exist in lower oxidation states under ambient conditions, Lappert’s

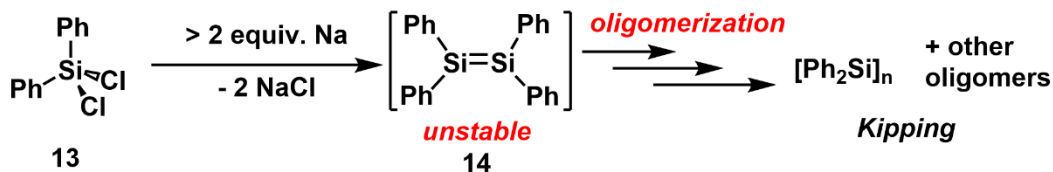
distannene $\{(\text{Me}_3\text{Si})_2\text{CH}\}_2\text{Sn}=\text{Sn}\{\text{CH}(\text{SiMe}_3)_2\}_2$ (**1**) demonstrated dynamic behavior between monomeric and dimeric forms, adding validity to the proposed transient $\text{R}_2\text{Si}:$ silylene in the synthesis of West's disilene $\text{Mes}_2\text{Si}=\text{SiMes}_2$ (**8**).^{7,9,12} As the next sections will demonstrate, there are now many examples of highly reactive main group element species, which challenge the notion that main group elements cannot behave similarly to transition metals. Today, the field of modern main group element chemistry includes fundamentally intriguing and catalytically-active main group element-based complexes that were prepared with kinetic stabilization and/or electronic stabilization; both strategies will be discussed now using selected examples involving Si- and Ge-based compounds.

1.1.1 Kinetic and Electronic Stabilization of Low-oxidation State Group 14 Elements within Molecular Species

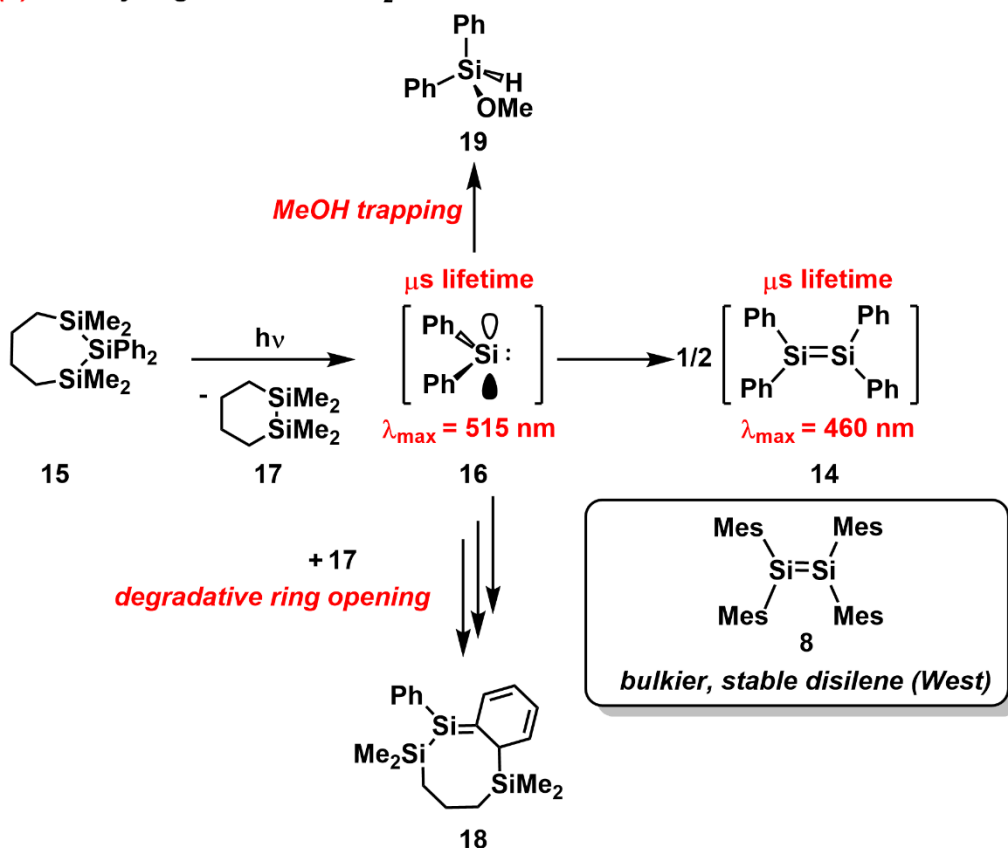
All examples of isolable compounds featuring low-oxidation state Group 14 elements in Section 1.1 used bulky groups to provide chemical stability. This is known as “kinetic stabilization”: the use of sterically hindered, often organic, groups to prevent uncontrolled reactivity (*e.g.*, oligomerization or ligand activation) and/or further redox degradation of the compound.¹³ In some cases studied by the Power Group, kinetic stabilization has been shown to involve cumulative intramolecular London dispersion effects within the C–H bonds, which can help block kinetic pathways that would otherwise result in degradation.¹³ As a specific example of kinetic stabilization, it is possible to compare West's $\text{Mes}_2\text{Si}=\text{SiMes}_2$ (**8**) (Scheme 1.2) with the unstable (not

isolable) species $\text{Ph}_2\text{Si}=\text{SiPh}_2$ (**14**), which was targeted by F. S. Kipping in the early 1900s by sodium reduction of Ph_2SiCl_2 (**13**) (Scheme 1.3a).¹⁴ Whereas West's $\text{Mes}_2\text{Si}=\text{SiMes}_2$ (**8**) is isolable at room temperature, the reactive Si=Si double bond at the core of the disilene $\text{Ph}_2\text{Si}=\text{SiPh}_2$ (**14**) does not have sufficient steric protection and rapidly forms a mixture of oligomers that likely includes some linear polymer $[\text{Ph}_2\text{Si}]_n$.¹⁴ Still, both the free silylene $\text{Ph}_2\text{Si}:$ (**16**; $\lambda_{\text{max}} = 515 \text{ nm}$) and $\text{Ph}_2\text{Si}=\text{SiPh}_2$ (**14**; $\lambda_{\text{max}} = 460 \text{ nm}$) have been observed as transient species by UV-vis spectroscopy from the laser flash pyrolysis of $[\{(\text{H}_2\text{C})_4(\text{Me}_2\text{Si})_2\}]\text{SiPh}_2$ (**15**), albeit with μs -scale lifetimes (Scheme 1.3b).¹⁵ By performing the photolysis of **15** in the absence of trapping agent, a C–H/Si–Si bond activation product (**18**) can be isolated from nucleophilic attack on the extruded disilane $\{(\text{CH}_2)_4(\text{Me}_2\text{Si})_2\}$ (**17**) by-product by Ph_2Si (**15**) (Scheme 1.3). Alternatively, upon addition of MeOH as a trapping agent to compound **16** oxidative addition occurs to give $\text{Ph}_2\text{Si}(\text{H})\text{OMe}$ (**19**) (Scheme 1.3b).

(a) Sodium reduction of Ph_2SiCl_2



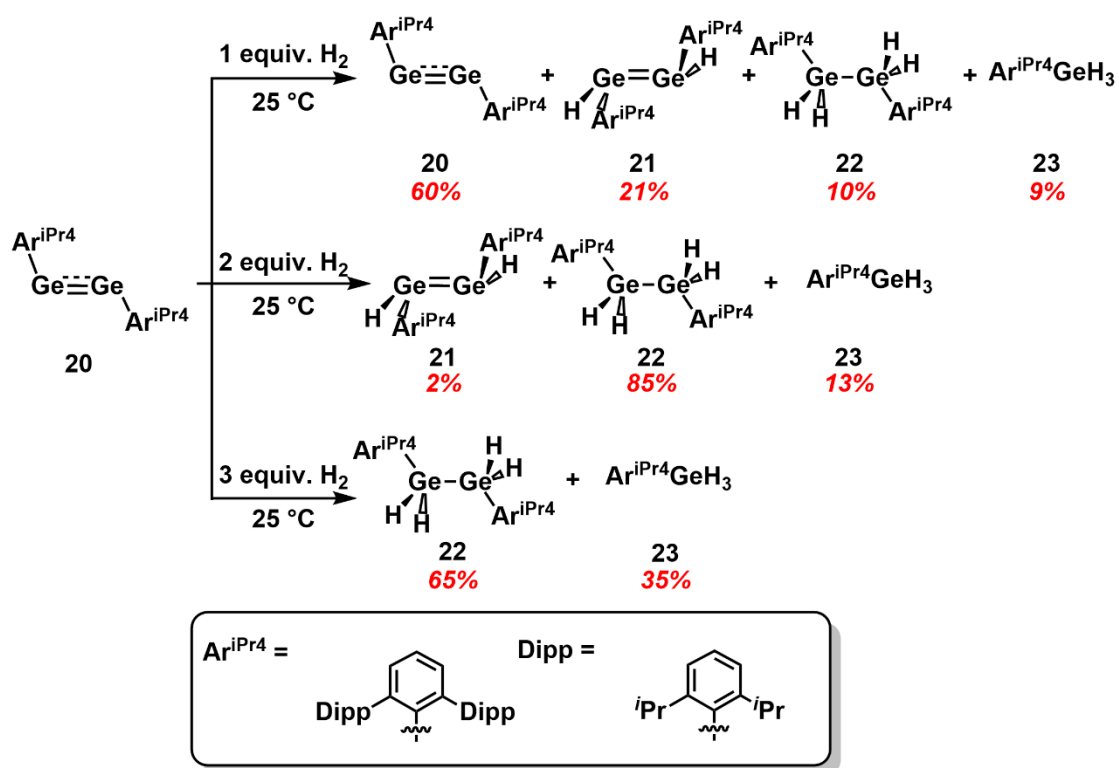
(b) Photolytic generation of Ph_2Si :



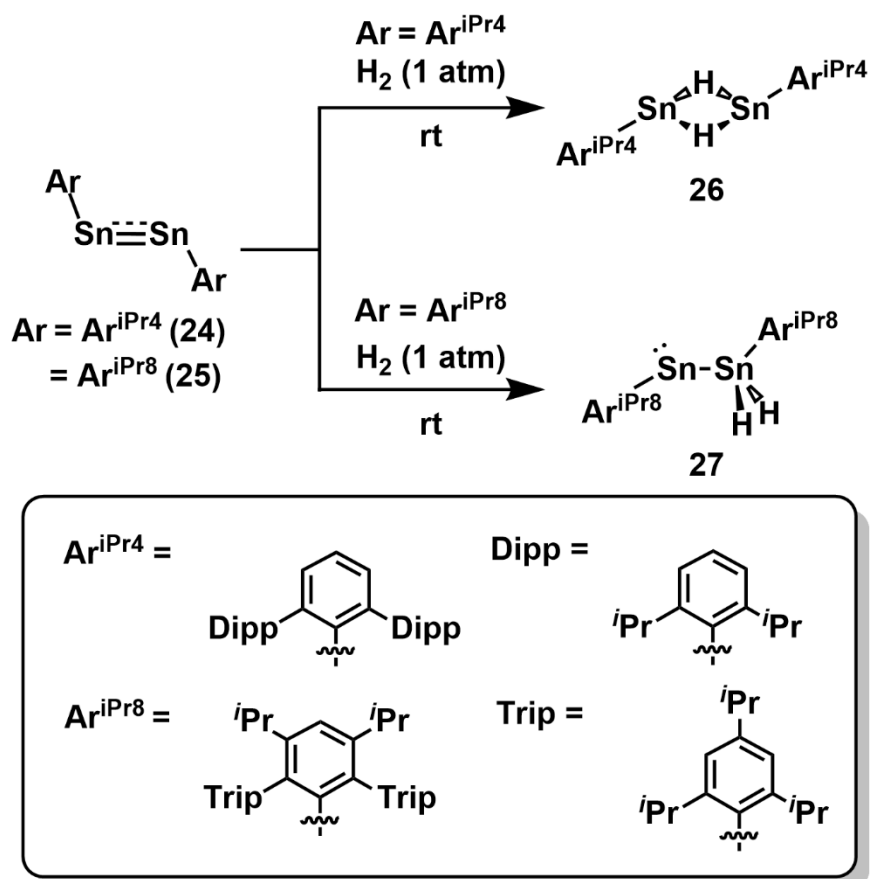
Scheme 1.3. (a) Kipping's attempt to prepare $\text{Ph}_2\text{Si}=\text{SiPh}_2$ (14) *via* reduction; (b) laser flash pyrolysis of $[\{(\text{H}_2\text{C})_4(\text{Me}_2\text{Si})_2\}]\text{SiPh}_2$ (15) to generate Ph_2Si : (16) *in-situ*.

By taking full advantage of steric protection, the Power group has been able to use terphenyl groups (based on *meta*-diphenylbenzene) to isolate a variety of heavy element analogues to alkenes and alkynes, with the general formulas ArEEAr and $\text{Ar}_2\text{E}'=\text{E}'\text{Ar}_2$ ($\text{E}' = \text{Ge}-\text{Pb}$).¹⁶ When bound by highly bulky groups, the tetrel centers in

these species retain their reactivity and can cooperatively activate substrates, such as H₂ gas or olefins.¹⁶ Of relevance to this Thesis, both terphenyl-supported digermynes (ArGeGeAr) and distannynes (ArSnSnAr) are able to activate H₂ at ambient conditions to form a variety of hydrogenated products (Schemes 1.4 and 1.5).¹⁶ Using Ar^{iPr₄}GeGeAr^{iPr₄} (**20**; Ar^{iPr₄} = 2,6-Dipp₂C₆H₃; Dipp = 2,6-ⁱPr₂C₆H₃), monohydrogenated (Ar^{iPr₄}(H)Ge=Ge(H)Ar^{iPr₄}; **21**), dihydrogenated (Ar^{iPr₄}H₂Ge-GeH₂Ar^{iPr₄}; **22**) and triply hydrogenated (Ar^{iPr₄}GeH₃; **23**) species can be formed in varying yields depending on the number of equiv. of H₂ added (Scheme 1.4).¹⁶ Alternatively, upon addition of one equiv. of H₂ the distannynes ArSnSnAr (Ar = Ar^{iPr₄} for **24**; Ar = Ar^{iPr₈} for **25**; Ar^{iPr₈} = C₆H-2,6-Trip₂-3,5-ⁱPr₂; Trip = 2,4,6-ⁱPr₃C₆H₂) can either form the Sn(II) hydride dimer ArSn(μ-H)₂SnAr (**26**; Ar = Ar^{iPr₄}) or the unsymmetric product ArSn-SnH₂Ar (**27**; Ar = Ar^{iPr₈}), depending on the degree of ligand steric bulk (Scheme 1.5).¹⁶ These are some of the earliest reports of H₂ oxidative addition localized at a Group 14 element center under ambient conditions and highlight the promising reactivity that is available among low-oxidation state Group 14 element-based compounds.



Scheme 1.4. Activation of H₂ by the digermine Ar^{iPr₄}GeGeAr^{iPr₄} (**20**).



Scheme 1.5. Activation of H_2 by the distannynes $\text{Ar}^{\text{iPr}4}\text{SnSnAr}^{\text{iPr}4}$ (**24**) and $\text{Ar}^{\text{iPr}8}\text{SnSnAr}^{\text{iPr}8}$ (**25**).

The planar conformation (D_{2h} symmetry) observed in $\text{Ar}_2\text{C}=\text{CAr}_2$ species, and even some $\text{Ar}_2\text{SiSiAr}_2$ complexes (e.g., **8**), is often not found in the heavier element alkene analogues (Ge–Pb). Specifically, a *trans*-bent conformation (C_{2h} symmetry) is found often in the heavier element alkene/alkyne analogues.¹⁷ For example, Lappert's *trans*-bent distannene $\{(\text{Me}_3\text{Si})_2\text{CH}\}_2\text{Sn}=\text{Sn}\{\text{CH}(\text{SiMe}_3)_2\}_2$ (**1**) features an out-of-plane angle ($\text{Sn}-\text{Sn}-\text{CH}$) of 41° whereas West's disilene $\text{Mes}_2\text{Si}=\text{SiMes}_2$ (**8**) exhibits a planar geometry about the central $\text{Si}=\text{Si}$ unit (Schemes 1.1 and 1.2).^{7,9} The propensity

to form *trans*-bent over planar geometries is the result of added orbital mixing in the frontier molecular orbitals (FMOs) of the ditetrelynes (REER) and ditetrelenes (R_2EER_2), known as pseudo second-order Jahn-Teller distortion.¹⁷ Since complexes of tetrelenes (R_2E) and ditetrelenes (R_2EER_2) are the targets of Chapter 4 of this Thesis, discussion of Jahn-Teller distortion will be centered around the MO diagram of ditetrelenes. Accordingly, Figure 1.1 shows the MO diagram for both D_{2h} and C_{2h} symmetric ditetrelenes (R_2EER_2) to demonstrate how this phenomenon ties in with the expected increase in *p*-character within the E–E bond as the Group 14 element (E) becomes heavier.¹⁷ The conformational change from planar (D_{2h}) to *trans*-bent (C_{2h}) for R_2EER_2 complexes allows for the HOMO (initially of E–E π character) to decrease in energy and form a mostly non-bonding b_u -symmetric HOMO in the *trans*-bent form, while raising the energy of the LUMO (initially of E–E π^* character) to give a mostly non-bonding LUMO (a_g) upon bending (Figure 1.1).¹⁷

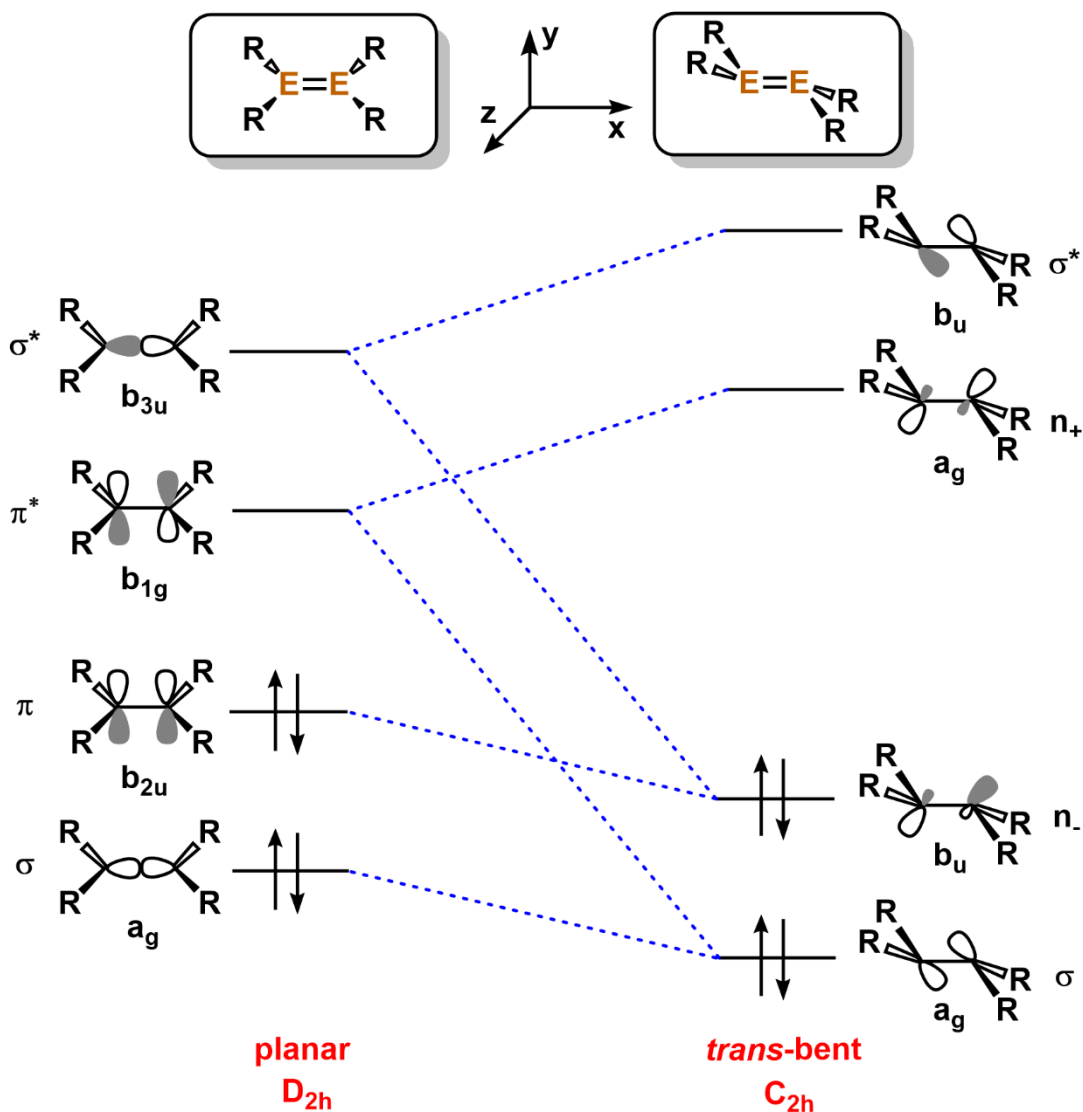


Figure 1.1. Molecular orbital (MO) diagram of planar (D_{2h}) and *trans*-bent (C_{2h}) conformations for ditetrelenes (R_2EER_2). Figure adapted from Figure 5 in ref. 17.

To predict whether a ditetrelene (R_2EER_2) will exhibit a *trans*-bent or planar geometry, the Carter-Goddard-Malrieu-Trinquier (CGMT) model was developed. This model relates the singlet-triplet energy gap (ΔE_{S-T}) of tetrelenes (R_2E) to the combined energies of the adjacent E–E σ bonds and E–E π -bonds [the sum of which is shown as

$E(\sigma+\pi)$] (Figure 1.2).¹⁸ The MO diagram of a generic R_2E compound shows that ΔE_{S-T} can be calculated from the total energy difference between the computed triplet and singlet states (Figures 1.3 and 1.4).¹⁸ Subsequently, both $E(\sigma+\pi)$ and ΔE_{S-T} terms can be calculated and compared, such that if $(2 \times \Delta E_{S-T})$ is greater in magnitude than $E(\sigma+\pi)$, a *trans*-bent geometry can be expected in the ditetrelene complex (R_2EER_2). Alternatively, if $(2 \times \Delta E_{S-T})$ is lesser in magnitude than $E(\sigma+\pi)$, a planar (D_{2h}) geometry can be expected (Figure 1.3).¹⁸ To further illustrate this point, Figure 1.3 compares the planar (D_{2h} symmetry) $H_2C=CH_2$ with the *trans*-bent conformation observed in Lappert's distannene **1**, which exhibits organic groups that fold below/above the Sn-Sn bond axis by 41° in its single-crystal X-ray crystal structure.¹⁸ In addition, if ΔE_{S-T} itself is positive, a singlet ground state is expected; if ΔE_{S-T} is negative, a triplet ground state is expected (Figures 1.3 and 1.4). Similarly to ethylene ($H_2C=CH_2$), tetrafluoroethylene ($F_2C=CF_2$) exhibits a planar conformation; and their monomeric units (CH_2 vs. CF_2) will be compared below.¹⁸

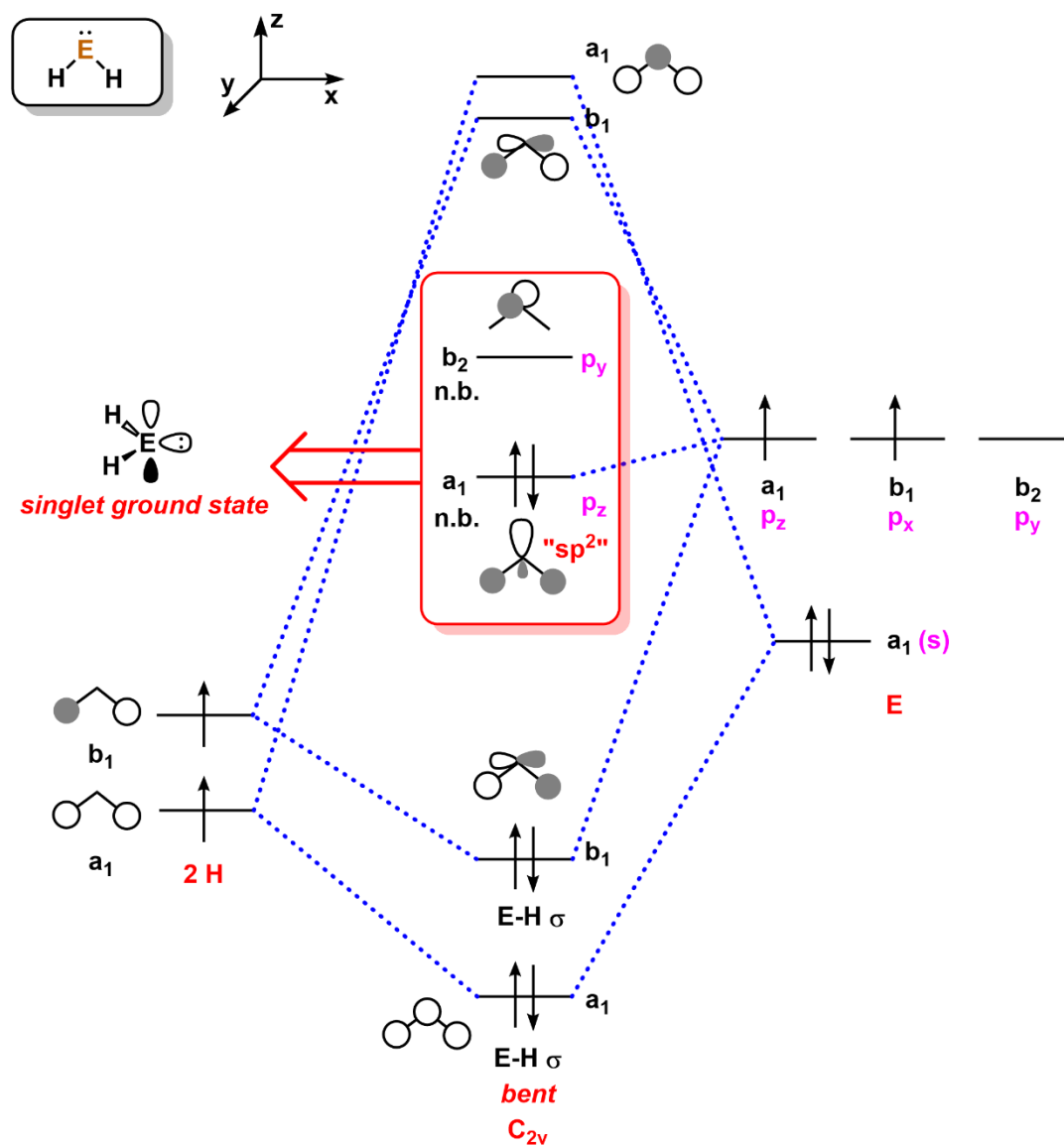


Figure 1.2. General molecular orbital (MO) diagram for tetrelenes (EH_2) in C_{2v} symmetry (E = Si–Pb).

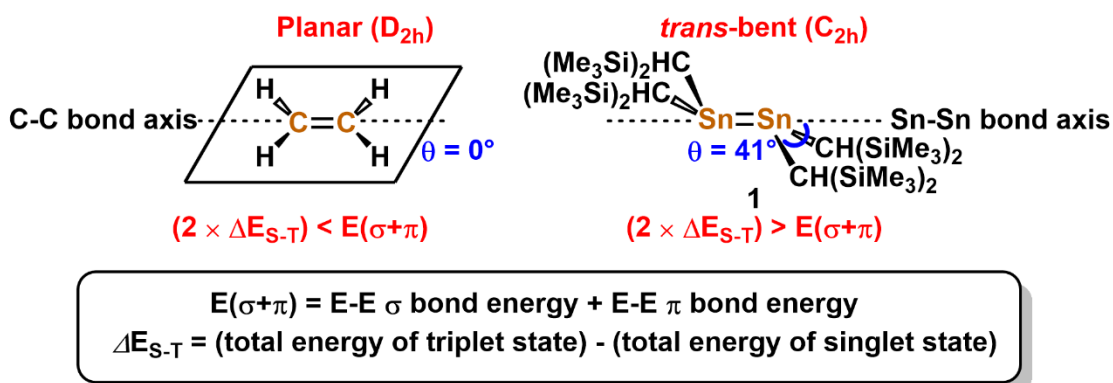


Figure 1.3. CGMT model equations and their relevance to the observed geometry of ditetrelenes, by comparison of $H_2C=CH_2$ and Lappert's distannene $\{(Me_3Si)_2CH\}_2Sn=Sn\{CH(SiMe_3)_2\}_2$ (1).

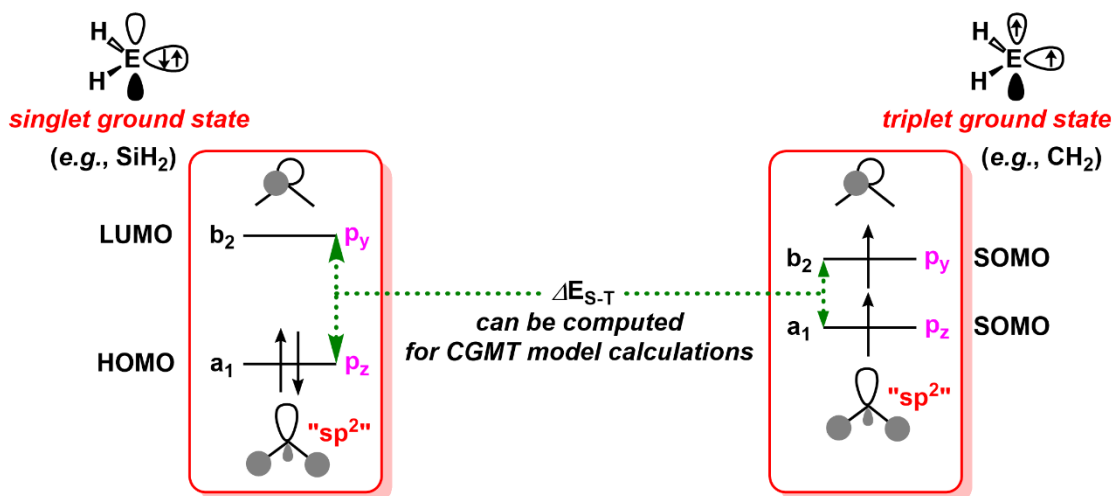


Figure 1.4. Molecular orbital diagram for tetrelenes (EH_2), depicting the frontier molecular orbitals for singlet vs. triplet ground states.

Based on the general MO diagram shown in Figure 1.2 for tetrelenes (EH_2 ; C_{2v} symmetry) in a singlet ground state, the LUMO consists of an empty p -orbital (non-bonding, b_2 symmetry) orthogonal to the filled HOMO (sp^2 -character lone pair, a_1

symmetry).^{18b} By comparison of the FMOs for a tetrelene (EH₂) in the triplet ground state (Figures 1.3 and 1.4), the ΔE_{S-T} can be related to the energy difference between the aforementioned b₂ and a₁ symmetric FMOs (although the energy values are not the same).¹⁸ From this, two general trends can be discerned: (1) electron-donating groups lower the energy of the b₂ symmetric MO (empty *p*-orbital) and (2) substitution of E in R₂E with heavier elements (compared to C) lowers the energy of the a₁ symmetry MO (non-bonding “*sp*²” lone pair) as a result of lower energy *s*-character and *p*-character orbitals.¹⁸ Practically, this means electron-donating groups in R₂E decrease the triplet-singlet energy gap (ΔE_{S-T}), whereas electron-withdrawing groups increase ΔE_{S-T} .¹⁸ Heavy element substitution (descending the Periodic Table) in R₂E increases the triplet-singlet energy gap (ΔE_{S-T}).¹⁸ This is consistent with the observation that CH₂ has a triplet ground state, while both CF₂ and the parent silylene, SiH₂, have a singlet ground state.¹⁸ As will be discussed in the next section, the CGMT model can be applied to explain the reactivity of acyclic silylenes (R₂Si), specifically in relation to the oxidative addition of H₂ to these species.¹⁹

The study of parent tetrelenes (EH₂) is fundamentally intriguing and of great value in understanding the growth of Si and Ge thin films in industry, particularly in computer chips, where transient EH₂ species are thought to be formed *en route* to bulk Si and Ge *via* the pyrolysis of SiH₄ and GeH₄, respectively. Towards understanding the underlying mechanism behind controlled decomposition of EH₄ gases, laser-ablation of Si and Ge in the presence of H₂ have led to the identification of SiH₂ and GeH₂ as intermediates (after their isolation in cryogenic matrices).²¹ In particular, work by the

Andrews Group²¹ has been essential in the observation of $\text{EH}_{1,2,3}$ species, dimetallynes E_2H_2 and ditetrelenes E_2H_4 ($\text{E} = \text{Si}$ and Ge); ligand-stabilized low-oxidation state Group 14 element hydrides will be discussed in the next sections.

Expanding from the terphenyl-stabilized ditetrylenes (ArEEAr) and ditetrelenes (Ar_2EEAr_2) examined thus far, alternative ligand systems may be used to coordinate reactive Group 14 element motifs *via* a combination of kinetic and electronic stabilization. As an overview, electronic stabilization involves the use of σ - and/or π -donating or withdrawing groups to protect reactive sites on a molecule; the most reactive sites being empty p -orbitals and lone pairs in tetrelenes (ER_2), since they can readily accept or donate electron pairs.²² Since the concept of electronic stabilization can be complicated (depending on the exact MO diagram of the species), a simplified example using the *bis*-amide [$\{(\text{Me}_3\text{Si})_2\text{N}\}_2\text{Ge}$] (**28**) complex from Lappert and co-workers is presented here (Figure 1.5).²³ Based on the FMOs in compound **28** (Figures 1.2 and 1.4), the energy of the LUMO (non-bonding empty p -orbital on Ge, formally b_2 symmetry) on the Ge center is raised by π -donation from an adjacent π -symmetry nitrogen lone pair. The energy of the HOMO (non-bonding Ge lone pair, formally a_1 symmetry) is lowered as a result of the σ -withdrawing character of the more electronegative nitrogen centers (Figure 1.5).^{22,23} Carbenes, which are dicoordinate R_2C : electron-pair donors, often feature flanking N -aryl groups to provide steric protection while the empty orthogonal p -orbital on the carbon center allows for π -donation from the bound motif (Figure 1.6).²⁴

The most popular carbon-based ligands used in the area of main group element coordination are NHCs (*N*-heterocyclic carbenes) and CAACs (cyclic alkyl amino carbenes) (Figure 1.6).²⁴ Partly, this is because precursors to NHCs and CAACs (imidazolium and iminium salts, respectively) are easy to synthesize on a gram scale *via* condensation routes.²⁴ NHCs, which are of particular relevance to this Thesis, have flanking aryl groups that can be changed to tune the σ -donating and/or π -accepting ability of the NHC center, although IPr or IMes [$\text{IMes} = (\text{HCNMe})_2\text{C}:$] are typically sufficient for most stabilization protocols in the main group (*vide infra*).²⁴

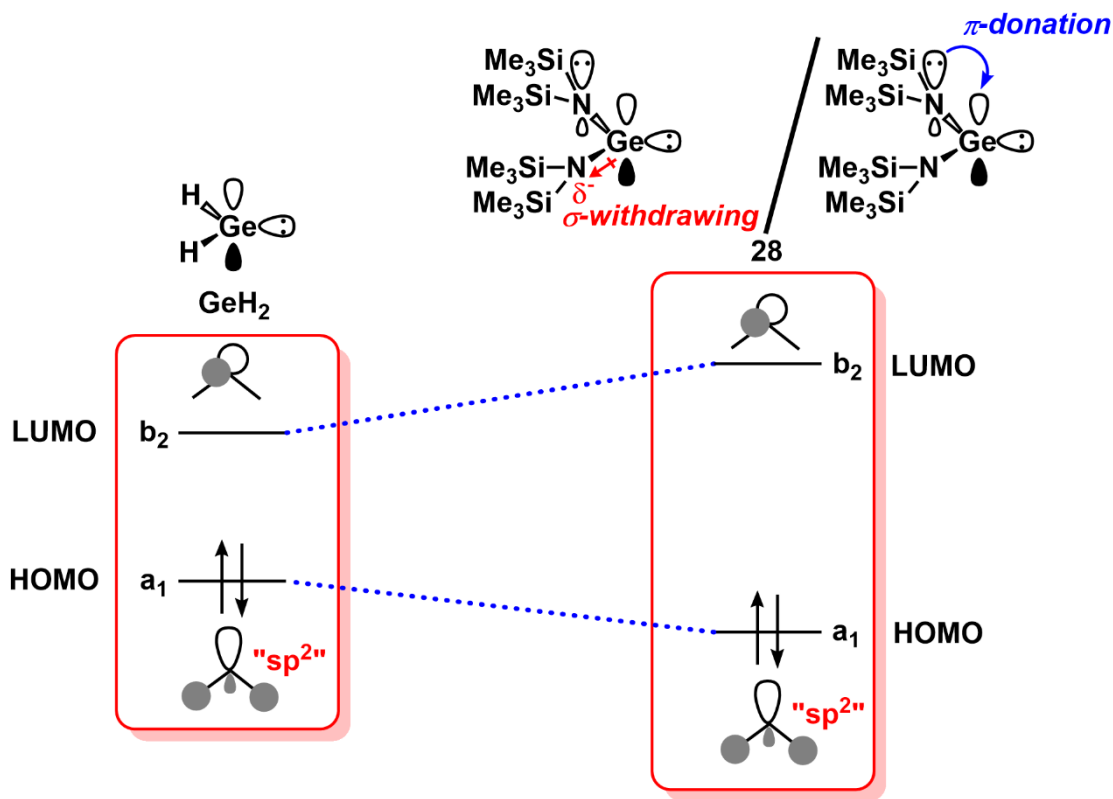


Figure 1.5. FMOs of $[(\text{Me}_3\text{Si})_2\text{N}]_2\text{Ge}$ (**28**), depicting π -donation and σ -withdrawal by neighboring N ligands.

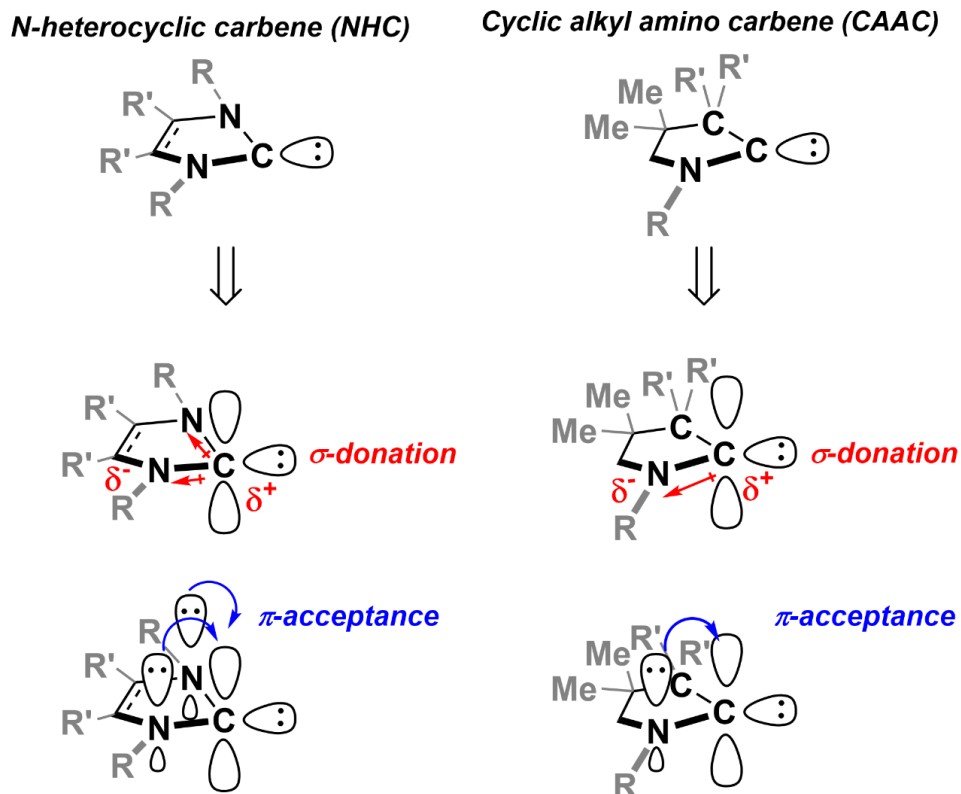
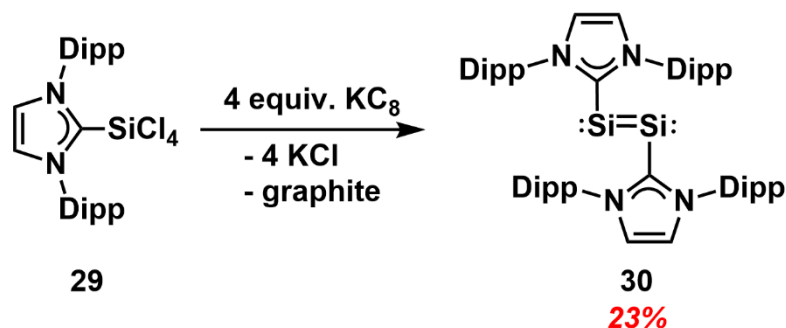


Figure 1.6. Diagram showing the σ -donating and π -accepting orbital interactions for *N*-heterocyclic carbenes (NHCs) and cyclic alkyl amino carbenes (CAACs). Figure adapted from Figure 1 in ref. 24.

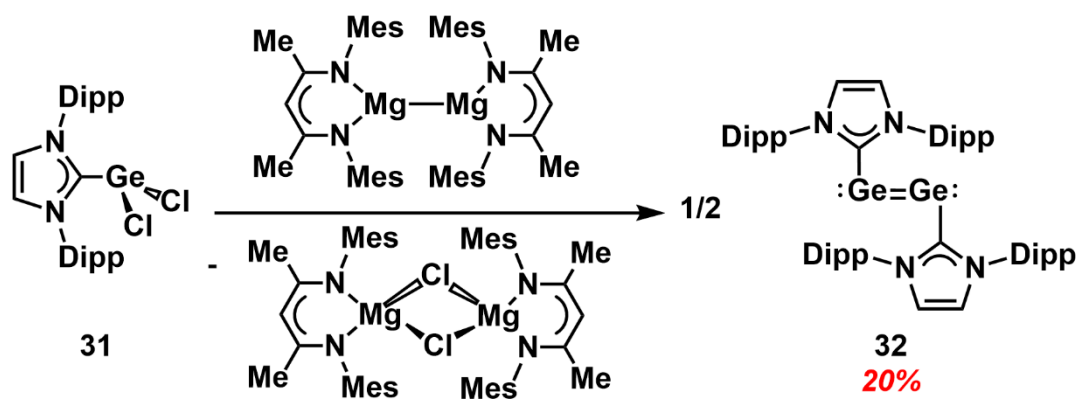
Selected examples of NHC-bound ditetrelones (L_xEEL_x ; E = Si or Ge; L = neutral ligand) are shown in Scheme 1.6, which demonstrate the effectiveness in using both kinetic and electronic stabilization strategies.²⁵ Upon reduction of $I\text{Pr}\cdot\text{SiCl}_4$ (**29**) with four equiv. of KC_8 , the intended $I\text{Pr}\cdot\text{Si}=\text{Si}\cdot I\text{Pr}$ (**30**) product was obtained by Robinson and co-workers in a 23 % isolated yield (Scheme 1.6a).^{25a} Alternatively, the addition of the Mg(I) dimer reducing agent, $\{(\text{MesNacnac})\text{Mg}\}_2$,²⁶ ($\text{MesNacnac} = [(\text{HC}(\text{MeCNMe})_2)^-]$) to $I\text{Pr}\cdot\text{GeCl}_2$ (**31**) afforded access to Jones' adduct $I\text{Pr}\cdot\text{Ge}=\text{Ge}\cdot I\text{Pr}$ (**32**) in a 20 % isolated yield (Scheme 1.6b).^{25b} These are the first molecular examples

of LSi(0)=Si(0)L and LGe(0)=Ge(0)L complexes, which has since sparked greater interest in monomeric tetrelones with higher coordination numbers (*e.g.*, L_2E ; L = neutral ligand).²⁷ Although dative σ -donation from IPr to each E center helps to stabilize the central E=E unit, the π -accepting ability of IPr is also crucial to the isolation of the $\text{IPr}\cdot\text{E=E}\cdot\text{IPr}$ complexes under ambient conditions. The following section will expand on the use of both kinetic and electronic stabilization to intercept reactive silylenes, germylenes and related hydrides (*e.g.*, SiH_2 and GeH_2).

(a) Isolation of $\text{IPr}\cdot\text{Si=Si}\cdot\text{IPr}$



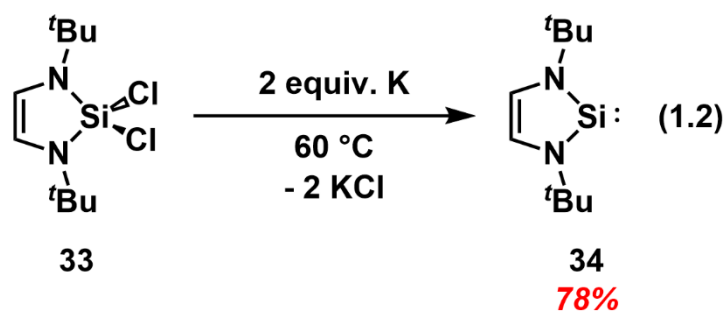
(b) Isolation of $\text{IPr}\cdot\text{Ge=Ge}\cdot\text{IPr}$



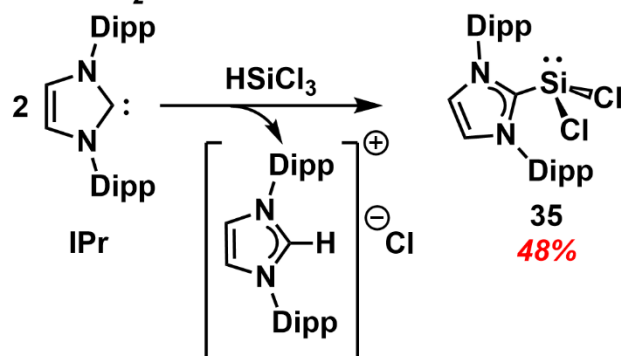
Scheme 1.6. Isolation of (a) $\text{IPr}\cdot\text{Si=Si}\cdot\text{IPr}$ (**30**) using KC_8 as a reducing agent, and (b) $\text{IPr}\cdot\text{Ge=Ge}\cdot\text{IPr}$ (**32**) by using $\{(\text{MesNacnac})\text{Mg}\}_2$ as a reducing agent.

1.1.1.1 Synthesis of Silylenes and Related Hydrides

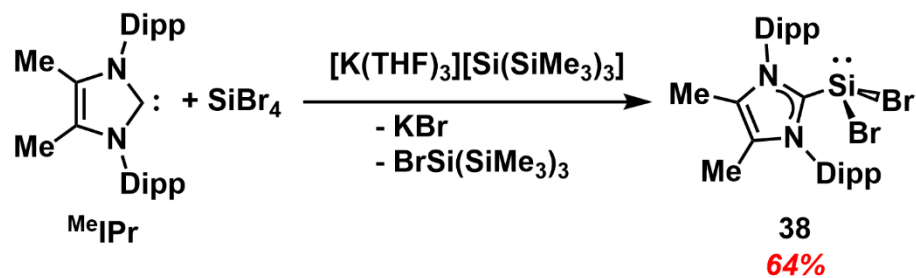
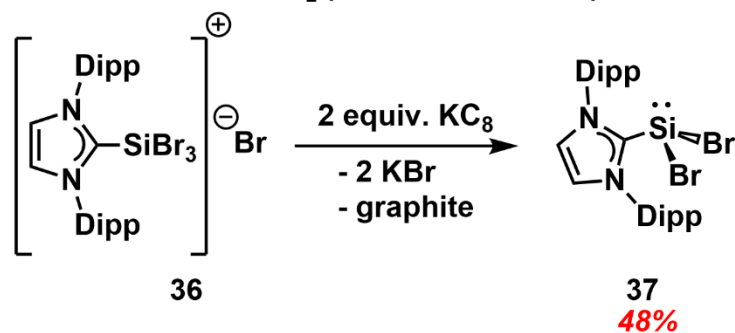
The aforementioned ditetrelenes (R_2EER_2) and ditetrelynes ($REER$) were accessed *via* alkali metal-mediated reduction of element halide precursors, which remains the most common route to low-oxidation state Group 14 compounds to date.² In contrast with Ge(II) sources, such as $Cl_2Ge \cdot dioxane$ and GeI_2 , there are no commercially available Si(II) compounds, since silicon exhibits a distinct preference for +4 oxidation states. Thus, $LB \cdot SiX_4$ and/or R_2SiX_2 ($LB =$ Lewis base; $X = Cl, Br, I$) species are often isolated first, followed by reduction to break the Si–X bonds and form the desired low-oxidation state species.² For example, in 1994 the West Group used potassium reduction of a $(HCN^tBu)_2SiCl_2$ precursor (**33**) to afford the first stable molecular silylene $(HCN^tBu)_2Si:$ (**34**) which contains a rigorously two-coordinate Si(II) center (Equation 1.2).²⁸ Of added note, a common source of Si(II) is $IPr \cdot SiCl_2$ (**35**), the synthesis of which is depicted in Scheme 1.7.^{29a} The synthesis of $IPr \cdot SiCl_2$ requires the use of two equiv. IPr , since the deprotonation of $HSiCl_3$ by IPr results in loss of one equiv. as the imidazolium salt $[IPrH]Cl$;^{29a} Alternatively, Filippou and co-workers were able to reduce $IPr \cdot SiBr_4$ (**36**) with two equiv. of KC_8 to access $IPr \cdot SiBr_2$ (**37**) in a 48 % isolated yield.^{29b} The backbone-protected $MeIPr \cdot SiBr_2$ [**38**; $MeIPr = (MeCNDipp)_2C:$] was recently reported by the Rivard group and was prepared from a mixture of free $MeIPr$, $SiBr_4$ and $[K(THF)_2][Si(SiMe_3)_3]$ as a reducing agent.^{29c} Of relevance to Chapter 4 in this Thesis, the use of higher halosilanes, such as Si_2Cl_6 and Si_2Br_6 , as SiX_2 synthons in the presence of IPr or $MeIPr$ has also been explored by the Holthausen and Ghadwal groups (to give **29** and **35** from Si_2Cl_6 ; and **36-39** from Si_2Br_6 ; Scheme 1.8).³⁰



(a) Synthesis of $\text{IPr}\cdot\text{SiCl}_2$

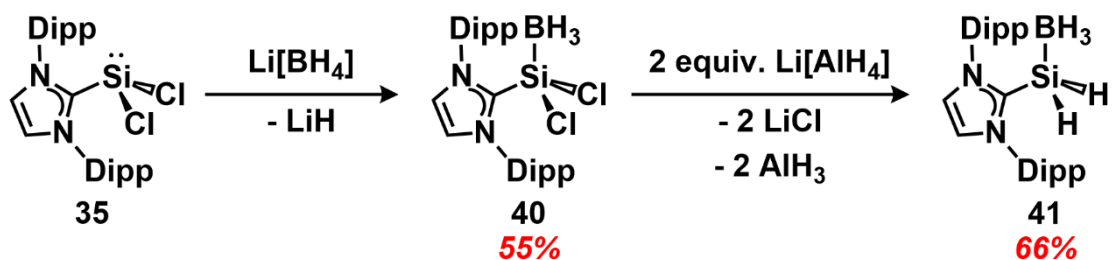


(b) Syntheses of $\text{NHC}\cdot\text{SiBr}_2$ ($\text{NHC} = \text{IPr}$ or $^{\text{Me}}\text{IPr}$)

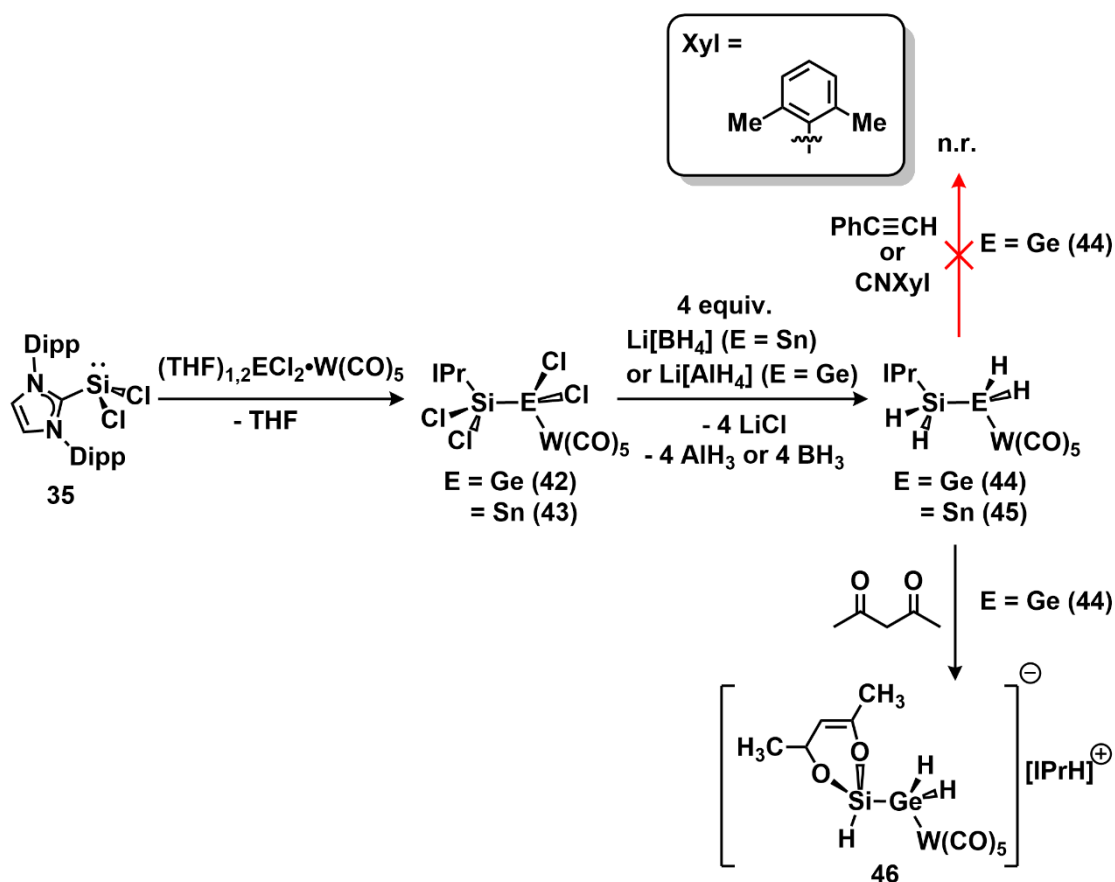


Scheme 1.7. Synthesis of Si(II) precursors (a) $\text{IPr}\cdot\text{SiCl}_2$ (**35**); (b) $\text{NHC}\cdot\text{SiBr}_2$ [IPr (**37**), $^{\text{Me}}\text{IPr}$ (**38**)]. Yields are listed in red.

Sn, **43**) (Scheme 1.10).³³ While $\text{IPr}\cdot\text{H}_2\text{SiGeH}_2\cdot\text{W}(\text{CO})_5$ (**44**) did not undergo hydride transfer chemistry with phenylacetylene ($\text{HC}\equiv\text{CPh}$) or CNXyl ($\text{Xyl} = 2,6\text{-Me}_2\text{C}_6\text{H}_4$), it was able to undergo hydrosilylation with acetylacetone to yield the salt $[\text{IPrH}][\{\text{MeC}(\text{O})\text{H}-\text{CH}=\text{C}(\text{Me})\text{O}\}\text{SiH}-\text{GeH}_2\cdot\text{W}(\text{CO})_5]$ (**46**), which features a rare anionic $\{\text{H}(\text{OR})_2\text{Si}-\text{GeH}_2\}$ unit (Scheme 1.10).³³



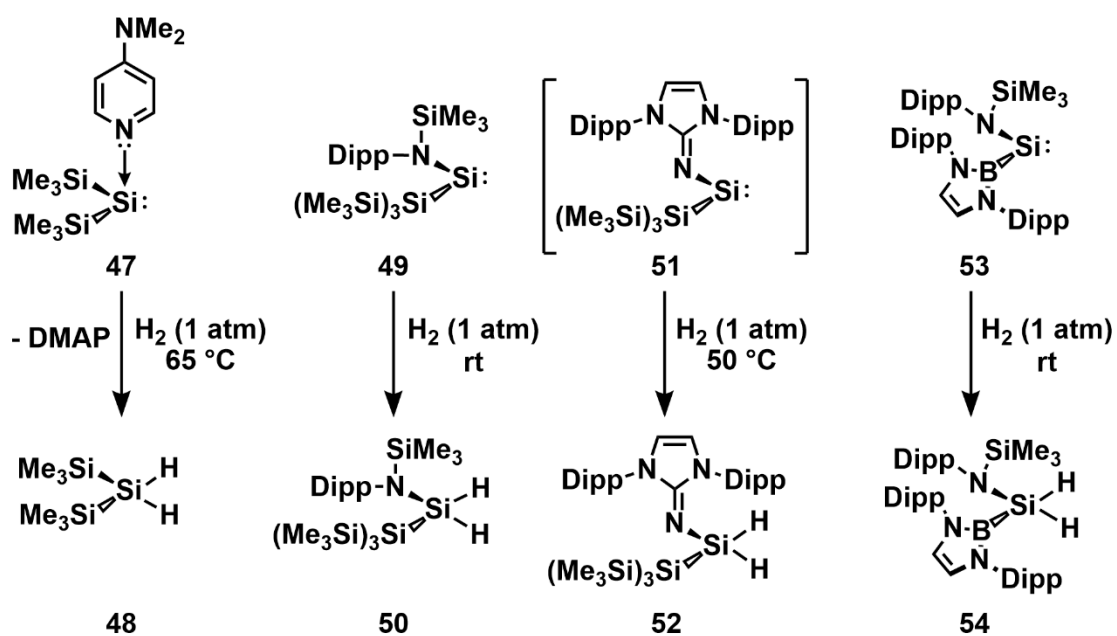
Scheme 1.9. Synthesis of $\text{IPr}\cdot\text{SiH}_2\cdot\text{BH}_3$ (**41**) starting from $\text{IPr}\cdot\text{SiCl}_2$ (**35**).



Scheme 1.10. Synthesis of $\text{IPr} \cdot \text{H}_2\text{SiGeH}_2 \cdot \text{W}(\text{CO})_5$ (**44**) and $\text{IPr} \cdot \text{H}_2\text{SiSnH}_2 \cdot \text{W}(\text{CO})_5$ (**45**).

Notably, reactive disilynes (RSiSiR), disilyenes (R_2SiSiR_2) and silylenes (R_2Si) can be used to prepare new Si hydrides by oxidative addition of H–H bonds, as shown by the selected examples in Scheme 1.11.^{2,31,34} As highlighted in this section, R_2Si species can be quite reactive, further emphasized by the observed activation of H_2 gas at temperatures < 100 °C (Scheme 1.11).^{2,31,34} Using CGMT as a model (Figures 1.2-1.4),¹⁸ the substitution of hydride with electron-donating substituents (such as $-\text{SiR}_3$, $-\text{BR}_2$, $-\text{NR}_2$) lowers the $\Delta E_{\text{S-T}}$ for silylenes (SiR_2) by lowering the energy of the b_2

symmetry MO (Scheme 1.11).^{2,19,31,34} Thus, H₂ oxidative addition occurs readily under ambient (or near-ambient) conditions for silylenes with a low (computationally derived) ΔE_{S-T} .^{2,19,31,34} As shown in Scheme 1.11, most reports of H₂ oxidative additions at a silicon center involve acyclic silylenes.^{2,19,31,34} Computations have uncovered that the three-membered SiH₂ transition state involved in H₂ addition is much lower in energy (ΔE^\ddagger) for acyclic (*e.g.*, 13.3 kcal/mol for Me₂Si) compared to cyclic silylenes (*e.g.*, 53.1 kcal/mol for {HC=CH}Si) (Figure 1.7).¹⁹ It should be noted that {HC=CH}Si is used for comparison with Me₂Si since cyclic silylenes often exhibit resonance in the cyclic ligand backbone (*e.g.*, with aryl groups). For acyclic silylenes, the H–H σ MO can directly donate into the empty p_z (b₂ symmetry LUMO) orbital directly above the Si center, while the Si lone pair (a₁ symmetry HOMO) can donate into the H–H σ^* MO to mediate oxidative addition (Figure 1.7).^{18,19} In the case for cyclic silylenes, the three-membered SiH₂ transition state is greatly strained, as the flanking organic groups do not easily fold back below the plane of the forming Si–H bond axes.¹⁹



Scheme 1.11. Selected examples of H₂ activation by silylenes.

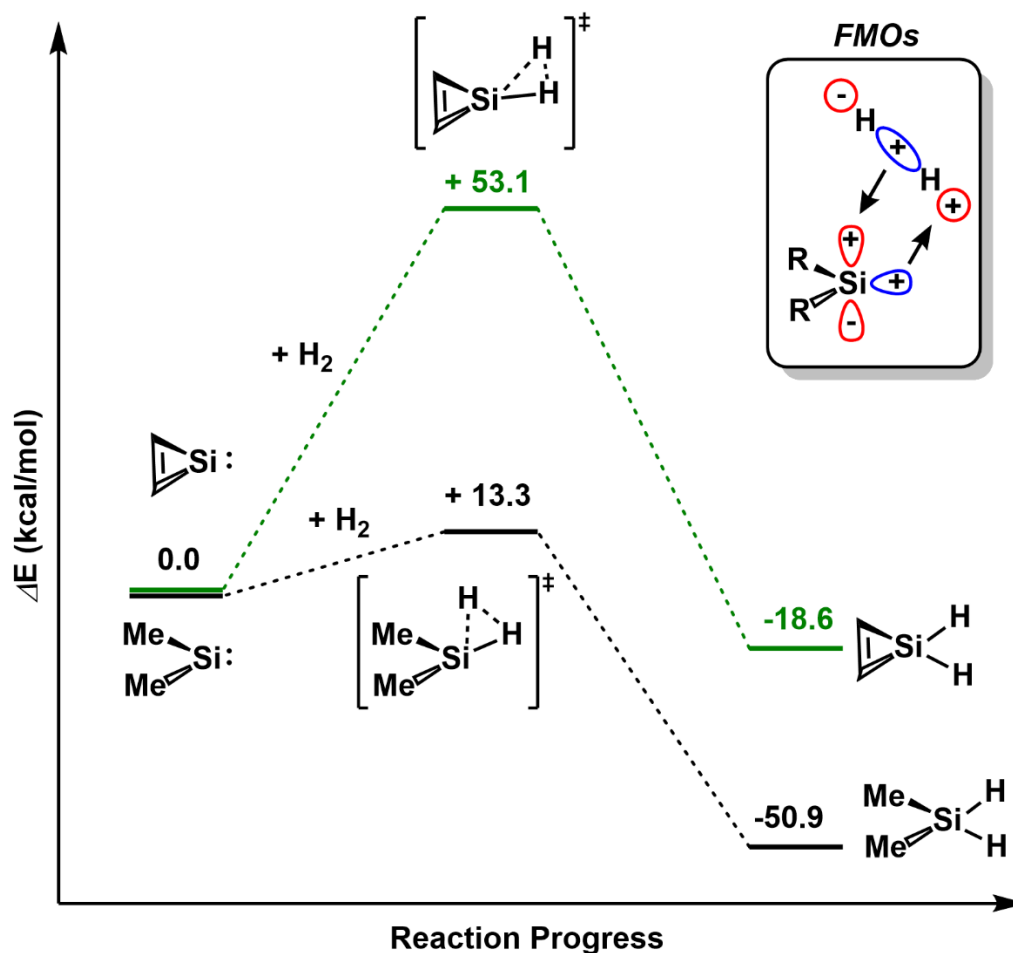
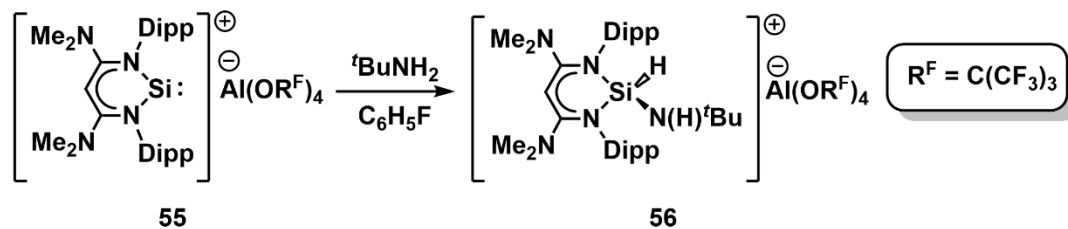


Figure 1.7. Computational (B3LYP/6-311+G** level of theory) potential energy surface with energies in kcal/mol for the oxidative addition of H₂ by Me₂Si and {HC=CH}Si. Figure adapted from Figure 2 in ref. 19 and Figure 1 in ref. 2.

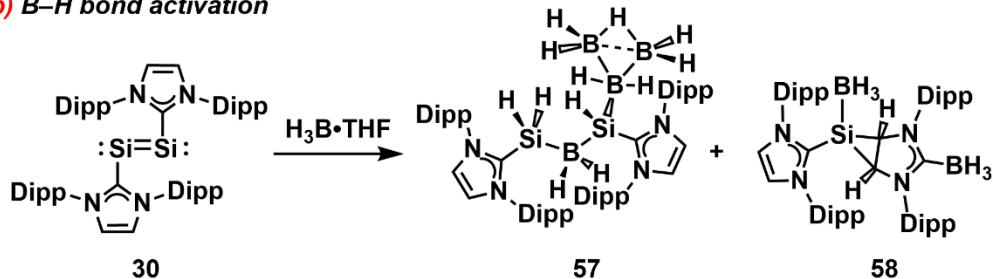
Since the dehydrogenation of amine-boranes is relevant to Chapter 3 in this Thesis, selected examples of N–H and B–H bond oxidative addition, as well as synergistic H⁺/H⁻ addition by highly reactive Si complexes is shown in Scheme 1.12.^{2,31,35} To start, N–H bond activation is shown in Scheme 1.12a, where the addition of ^tBuNH₂ to the cationic Si(II) Nacnac complex [^{Dipp}/NMe₂Nacnac}Si][Al(OR^F)₄] (**55**) [^{Dipp}/NMe₂Nacnac = {HC(Me₂NCNDipp)₂}⁻; R^F = C(CF₃)₃] afforded the salt

$[\{\text{Dipp}^{\text{NMe}_2}\text{Nacnac}\}\text{Si}(\text{H})\{\text{N}(\text{H})\text{tBu}\}][\text{Al}(\text{OR}^{\text{F}})_4]$ (**56**).^{35a} Using the aforementioned $\text{IPr}\cdot\text{Si}=\text{Si}\cdot\text{IPr}$ (**35**), addition of $\text{H}_3\text{B}\cdot\text{THF}$ allowed Robinson and co-workers to access $\text{IPr}\cdot\text{SiH}_2\text{-BH}_2\text{-SiH}(\text{B}_3\text{H}_7)\cdot\text{IPr}$ (**57**) *via* the formal insertion of a BH_2 unit into the Si–Si bond; a minor product (**58**) was also isolated from ligand backbone activation of *in-situ* generated $\text{IPr}\cdot\text{BH}_3$ (Scheme 1.12b).^{35b} Finally, the Si hydride complex $[(\text{Dipp}^{\text{Nacnac}})\text{SiH}\cdot\text{Ni}(\text{CO})_3]$ (**60**) ($\text{Dipp}^{\text{Nacnac}} = [(\text{HC}(\text{MeCNDipp})_2)^-]$) can be formed *via* the synergistic addition of H^+/H^- from ammonia-borane ($\text{H}_3\text{B}\cdot\text{NH}_3$) to $[\{\text{DippNC}(\text{Me})\text{CHC}(\text{=CH}_2)\text{NDipp}\}\text{Si}\cdot\text{Ni}(\text{CO})_3]$ (**59**) (Scheme 1.12c).^{35c} The dehydrogenation of $\text{H}_3\text{B}\cdot\text{NH}_3$ occurs as a result of polarized $\text{B}^{\delta+}\text{-H}^{\delta-}$ and $\text{N}^{\delta-}\text{-H}^{\delta+}$ linkages. $\text{H}_3\text{B}\cdot\text{NH}_3$ reacts with compound **59** *via* hydride transfer onto the electropositive Si center from the B–H linkage and nucleophilic attack by the olefin ($\text{H}_2\text{C}=\text{}$) unit in **59** onto the N–H site of ammonia-borane (Scheme 1.12c).^{35c} Presently, the use of silylenes (R_2Si) and germynes (R_2Ge) in stoichiometric and catalytic chemical transformations is emerging as a result of the preliminary reactivity discussed in this section. While section 1.1.4 will highlight the reactivity of silylenes (R_2Si) in more detail, the next section will expand on the synthesis of germynes (R_2Ge) and related Ge hydride complexes.

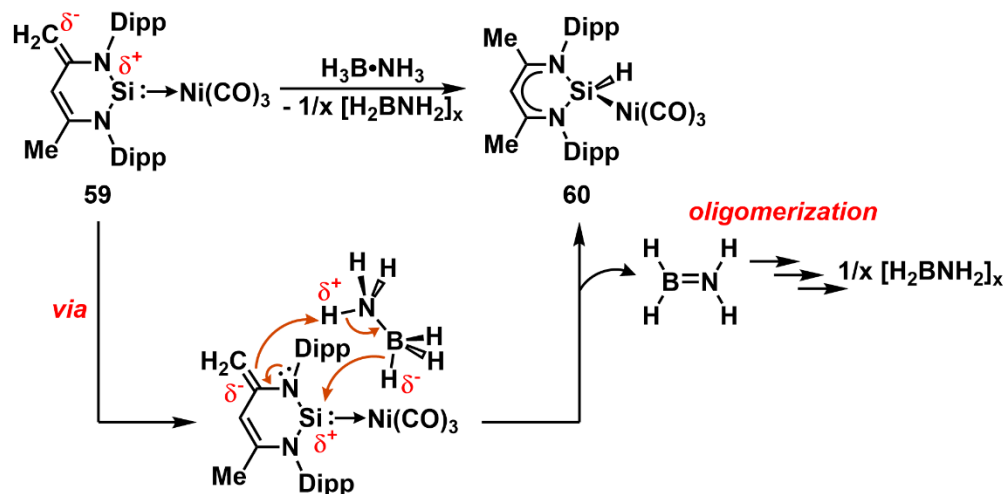
(a) N–H bond activation



(b) B–H bond activation



(c) Synergistic H⁺/H⁻ addition



Scheme 1.12. Selected examples of (a) N–H bond activation; (b) B–H bond activation or; (c) synergistic H⁺/H⁻ addition by silylenes and related low-oxidation state silicon species.

1.1.1.2. Synthesis of Germynes and Related Hydrides

In general, the synthetic routes to germynes (R_2Ge and related hydrides) are nearly identical to those already discussed above. However, easy access to commercially available Ge(II) sources, such as $Cl_2Ge \cdot$ dioxane and GeI_2 , simplifies these synthetic methods.^{2,31} Selected examples of germynes (61-70) relevant to this Thesis are shown in Figure 1.8, a portion of which are direct structural analogues to their silylene counterparts.^{2,29c,31,36}

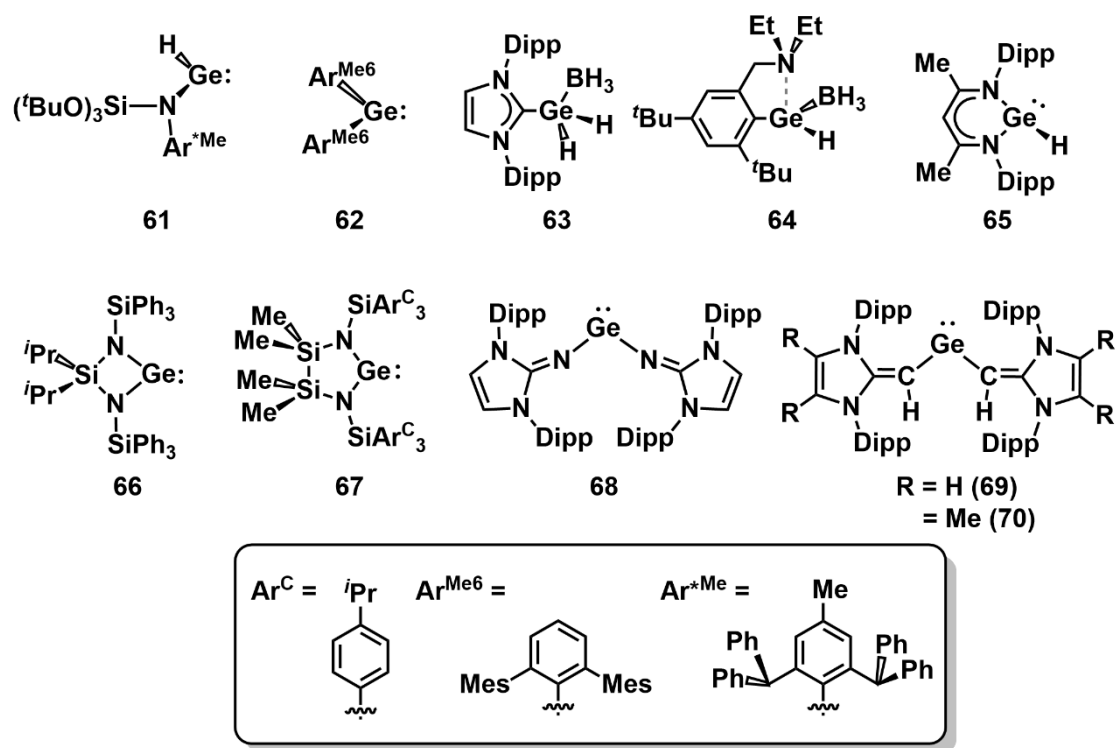
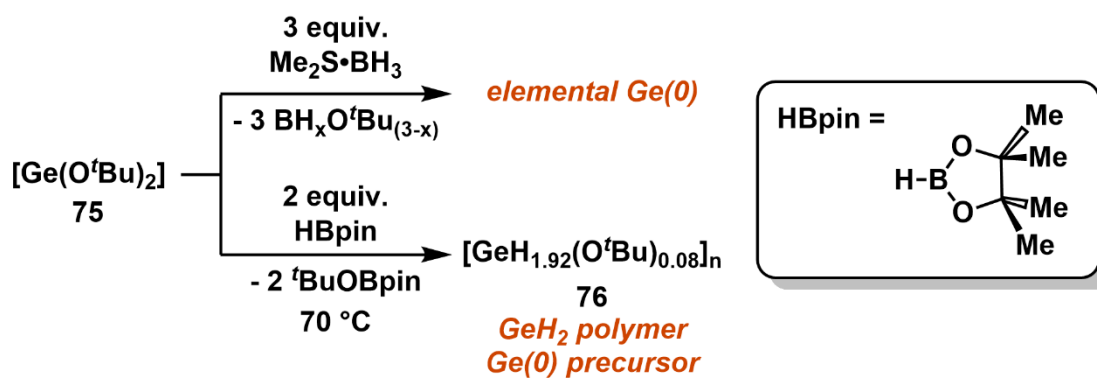
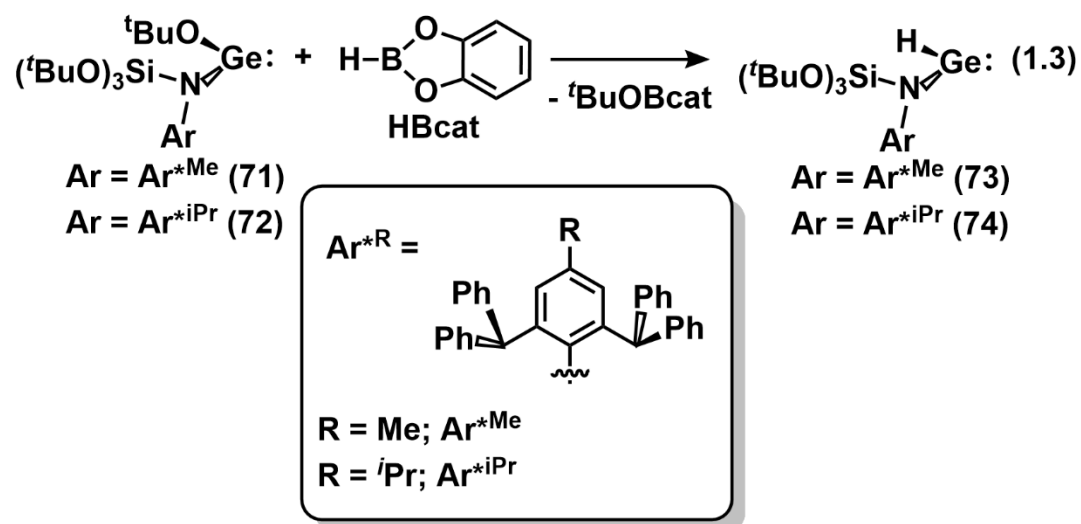


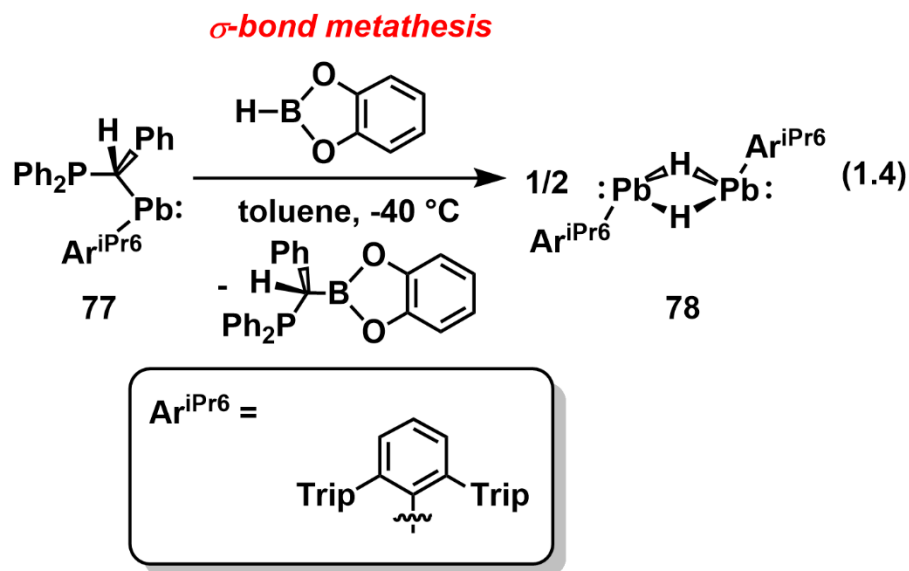
Figure 1.8. Selected examples of germynes (R_2Ge) and related low-oxidation state Ge(II) species (61-70).

A synthetic protocol involving σ -bond metathesis may be used to generate Ge hydrides, as reported by Jones and co-workers, where they combined highly bulky

amido-stabilized Ge(II) *tert*-butoxide precursors (**71**) and (**72**) with HBcat (HBcat = catecholborane) to afford $[\text{Ar}^{*\text{Me}}\{(\text{tBuO})_3\text{Si}\}\text{N}]\text{GeH}$ (**73**) ($\text{Ar}^{*\text{Me}} = 2,6,4\text{-(Ph}_2\text{CH)}_2\text{MeC}_6\text{H}_2$) and $[\text{Ar}^{*\text{iPr}}\{(\text{tBuO})_3\text{Si}\}\text{N}]\text{GeH}$ (**74**) ($\text{Ar}^{*\text{iPr}} = 2,6,4\text{-(Ph}_2\text{CH)}_2\text{iPrC}_6\text{H}_2$) (Equation 1.3).^{36g} Subsequent hydride transfer chemistry using pre-catalyst **74** will be discussed in the next two sections. Expanding into materials chemistry, a significant example of σ -bond metathesis with Ge hydrides was reported from the Rivard group involving $[\text{Ge}(\text{O}^t\text{Bu})_2]$ (**75**) (Scheme 1.13).³⁷ Whereas addition of $\text{Me}_2\text{S}\cdot\text{BH}_3$ to **75** induces the rapid release of elemental Ge (at 70 °C), the combination of excess (10 equiv.) HBpin (HBpin = pinacolborane) and **75** yields an orange metastable hydride with a chemical formula of $[\text{GeH}_{1.92}(\text{O}^t\text{Bu})_{0.08}]_x$ (**76**); this species is a suitable precursor to Ge films (Scheme 1.13).³⁷ Furthermore, the first structurally characterized Pb(II) hydride complex, $\text{Ar}^{\text{iPr}_6}\text{Pb}(\mu\text{-H})_2\text{PbAr}^{\text{iPr}_6}$ (**78**) was reported from a σ -bond metathesis (similar to Jones' route) between $\{\text{Ph}_2\text{PC(H)(Ph)}\}\text{Ar}^{\text{iPr}_6}\text{Pb}$: (**77**) and HBcat (Equation 1.14).³⁸ The isolation of compound **78** suggests that this synthetic protocol may allow for access to other thermally-sensitive Group 14 element-based species.



Scheme 1.13. Divergent reactivity of $[\text{Ge}(\text{O}^t\text{Bu})_2]$ (75) with $\text{Me}_2\text{S}\cdot\text{BH}_3$ or HBpin .

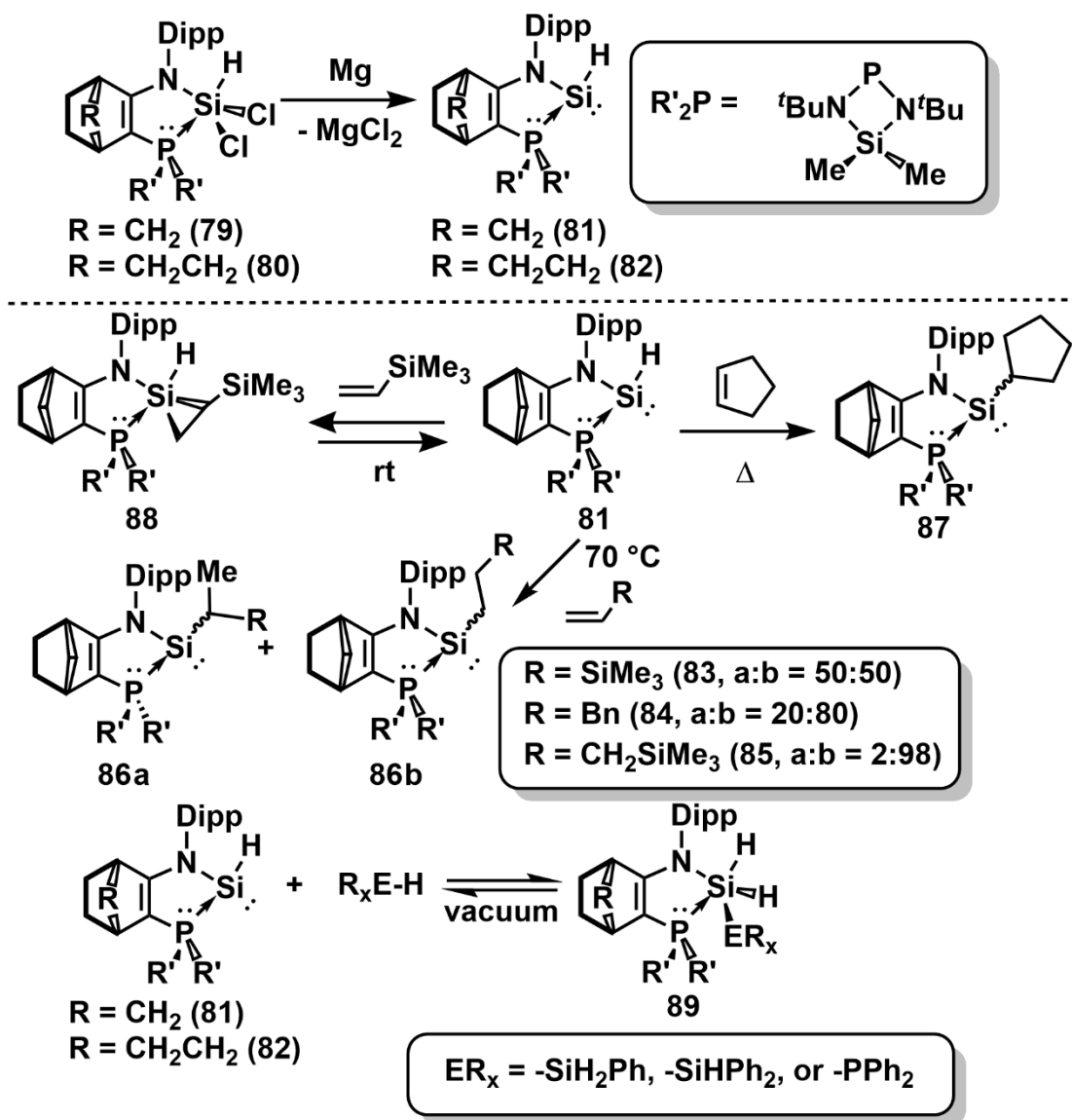


1.1.2 Small Molecule Activation Involving Group 14 Element Hydrides (Si and Ge)

The stoichiometric reactivity discussed in the next section will focus on hydrosilylation and hydrogermylation of alkenes and alkynes by hydridic Si(II) and Ge(II) species to highlight that effective hydride transfer is possible with small substrates; however, their reactivity is not limited to these examples and other chemical transformations (CO₂ reduction, hydrodefluorination, dehydrocoupling, and ring-opening polymerization) with Group 14 element hydrides (Si–Pb) have been reported in the literature.³¹ Selected examples will involve stoichiometric or catalytic reactivity where the tetrel center (often in a low-oxidation state) acts as a site for the observed transformation.

1.1.2.1. Stoichiometric Reactivity of Group 14 Element Tetrelenes and Related Hydrides (Si and Ge)

To demonstrate the high reactivity of low-oxidation state silicon centers in organic transformations,^{2,31} Kato, Baceiredo, and co-workers used amidophosphine ligands to synthesize $P_LSi(H)Cl_2$ precursors (P_L = amidophosphine donors, **79** and **80**) as shown in Scheme 1.14.^{31,39} Following the isolation of **79** and **80**, Mg metal reduction of **79** and **80** afforded the Si(II) hydride complexes $[\{Me_2Si(N^tBu)_2P\}(C_7H_{10})N(Dipp)]SiH$ (**81**) and $[\{Me_2Si(N^tBu)_2P\}(C_8H_{12})N(Dipp)]SiH$ (**82**), respectively (Scheme 1.14).³⁹ The combination of compound **81** with alkenes gave way to efficient hydrosilylation chemistry, albeit in a non-stereoselective fashion. In higher temperature (70 °C) reactions involving the α -olefins $RC(H)=CH_2$ ($R = SiMe_3, Bn, \text{ or } CH_2SiMe_3$), compound **81** readily forms mixtures of Markovnikov and anti-Markovnikov addition products (**83-86**); similarly, compound **81** and cyclopentene form diastereomeric products (**87**) derived from hydrosilylation onto the central olefinic unit.³⁹ At room temperature, reversible hydrosilylation occurs between compound **81** and $Me_3SiC(H)=CH_2$ to form a three-membered silirane (**88**).³⁹ Expanding on this reversible process, the combination of compounds **81** or **82** with phenylsilane ($PhSiH_3$), diphenylsilane (Ph_2SiH_2), or diphenylphosphine (Ph_2PH) leads to reversible Si-H or P-H activation, respectively, to form the hydrogenated compound **89**.³⁹



Scheme 1.14. Synthesis of the amidophosphine-ligated Si(II) complexes (**81** and **82**) and their reactivity with olefins, silanes, or phosphines.

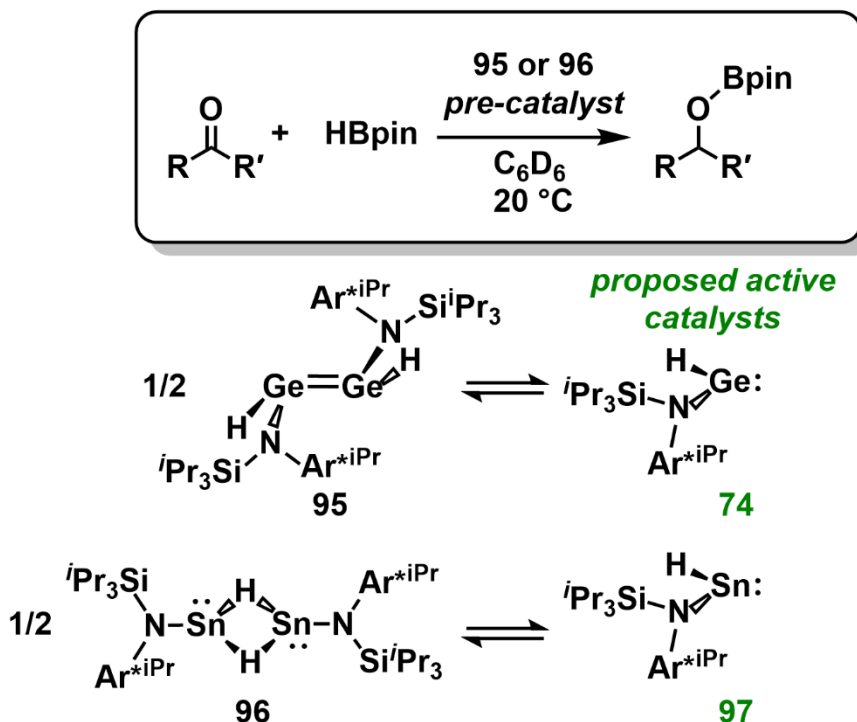
Returning to the bulky amido(hydrido)germylenes first reported by Jones and co-workers, $[\text{Ar}^*i\text{Pr}\{(\text{}^t\text{BuO})_3\text{Si}\}\text{N}]\text{GeH}$ (**74**) is able to undergo hydrogermylation reactions (Scheme 1.15) in a similar manner as demonstrated by Kato and Baccaredo, as outlined above.^{36g} Expanding from hydride transfer to terminal alkenes, the

tetrelenes in hydride transfer processes, largely focused on the two-coordinate amido(hydrido)germylenes developed by Jones and co-workers. Alongside mention of some related Sn and Pb species, the history/development of Group 14 element-mediated catalysis will be highlighted, the future of which is moving toward Si-based catalysts.

1.1.2.2. Catalytic Hydride Transfer (Hydroboration, Hydrosilylation, and Hydrocyanation)

The first well-defined examples of Group 14 element-mediated catalytic hydride transfer were reported in 2014 using the previously introduced bulky amido(hydrido)germylene $\{\text{Ar}^{\text{*iPr}}(\text{iPr}_3\text{Si})\text{N}\}\text{GeH}$ (**74**).^{36g,40,41} Of note, compound **74** is in equilibrium in solution with its dimeric analogue $[\{\text{Ar}^{\text{*iPr}}(\text{iPr}_3\text{Si})\text{N}\}\text{Ge}(\text{H})=\text{Ge}(\text{H})\{\text{N}(\text{Si}^{\text{iPr}}\text{Pr}_3)\text{Ar}^{\text{*iPr}}\}]$ (**95**) by NMR spectroscopy.⁴¹ In addition, a similar dimeric Sn(II) hydride $[\{\text{Ar}^{\text{*iPr}}(\text{iPr}_3\text{Si})\text{N}\}\text{Sn}(\mu\text{-H})_2\text{Sn}\{\text{N}(\text{Si}^{\text{iPr}}\text{Pr}_3)\text{Ar}^{\text{*iPr}}\}]$ (**96**) was used for hydride transfer catalysis, which also exhibited an equilibrium with the monomeric Sn(II) complex $\{\text{Ar}^{\text{*iPr}}(\text{iPr}_3\text{Si})\text{N}\}\text{SnH}$ (**97**).⁴¹ Once isolated, both E(II) compounds (Ge; **95**) and (Sn; **96**) were used as pre-catalysts for the effective hydroboration of ketones and aldehydes, with the lowest reported pre-catalyst loading of 0.05 mol % (per tetrel atom) (Scheme 1.16).⁴¹ Based on both computations and NMR spectroscopy,^{42,43} the active catalysts in these hydroborations were proposed to be the monomeric Ge(II) and Sn(II) complexes, **74** and **97**, respectively. Higher turnover frequencies (TOFs) are obtained with the Sn(II)

hydride catalysts (**96/97**), the highest of which was $> 13300 \text{ hr}^{-1}$ for the hydroboration of RC(O)H substrates (R = Et, *i*Pr, and Cy).⁴¹

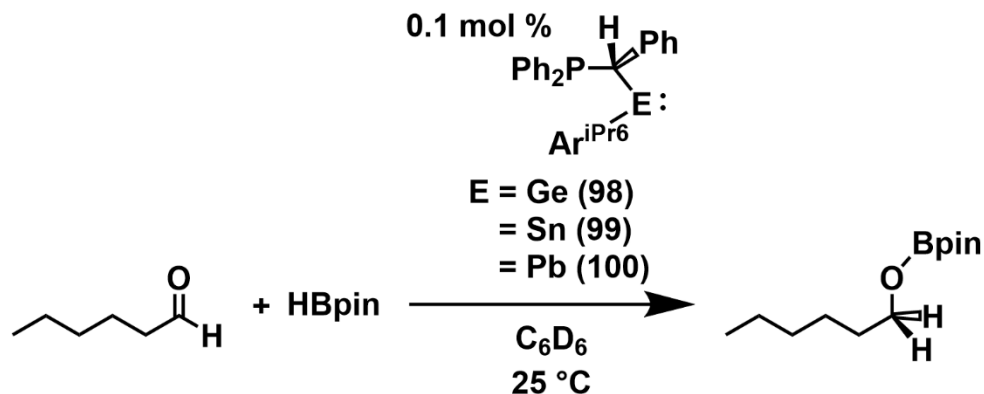


Scheme 1.16. Hydroboration of aldehydes and ketones with the pre-catalysts **95** and **96**.

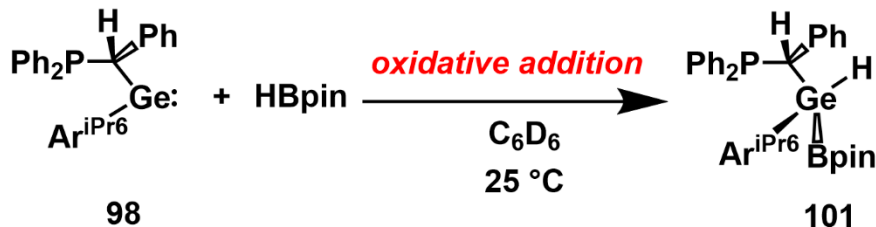
Another example of catalytic hydride transfer involves the hydroboration of ketones and aldehydes with HBpin using terphenyl-supported tetrelenes $\text{Ar}^{i\text{Pr}6}\text{E}-\text{C}(\text{H})\text{Ph}-\text{PPh}_2$ [E = Ge (**98**), Sn (**99**), and Pb (**100**)] (Scheme 1.17a).⁴⁴ Using identical reaction conditions (hexanal, HBpin, C_6D_6 , 25°C , 0.1 mol % loading of pre-catalyst), the Wesemann group was able to determine that the Pb(II) species (**100**) was the most active catalyst, as it showed quantitative formation of the intended hydroboration product ($\text{Me}(\text{CH}_2)_5\text{OBpin}$) after 7 min of reaction time.⁴⁴ In contrast, compounds **98**

and **99** required 30 min of reaction time to afford 79 % and 96 % yields of borylated product, according to NMR spectroscopy.⁴⁴ Focusing on the Ge(II) pre-catalyst (**98**), effective hydroborations were observed after 1 hr with ferrocenyl aldehyde [FcC(O)H], benzaldehyde, and acetophenone with a 1 mol % pre-catalyst loading of Ar^{iPr6}Ge-C(H)Ph-PPh₂ (**98**) in each case.⁴⁴ Furthermore, the active catalyst in hydroboration catalysis starting with **98** appears to be the hydridogermane [Ar^{iPr6}GeH{C(H)Ph-PPh₂} (Bpin)] (**101**), which was isolated upon stoichiometric addition of pinacolborane, HBpin, to compound **98** (Scheme 1.17b).⁴⁴ While these hydroboration pre-catalysts are not as active as Jones' amido(hydrido)germylenes (and stannylenes), Wesemann's report further confirms that Ge-H linkages can allow catalytic hydride transfer at room temperature.

(a) Catalytic hydroboration by E(II) species (E = Ge, Sn, Pb)



(b) Synthesis of active Ge(IV)–H catalyst

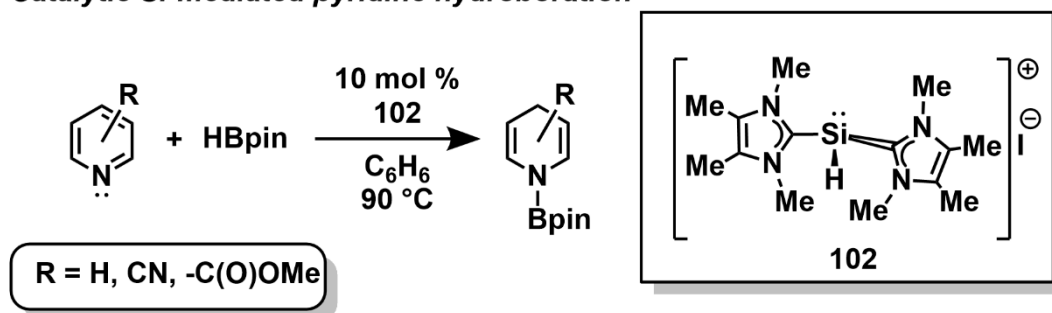


Scheme 1.17. (a) Catalytic hydroboration using the terphenyl-supported pre-catalysts (**98-100**); (b) stoichiometric oxidative addition of HBpin with **98** to form $[\text{Ar}^{\text{iPr}_6}\text{GeH}\{\text{C}(\text{H})\text{Ph}-\text{PPh}_2\}(\text{Bpin})]$ (**101**).

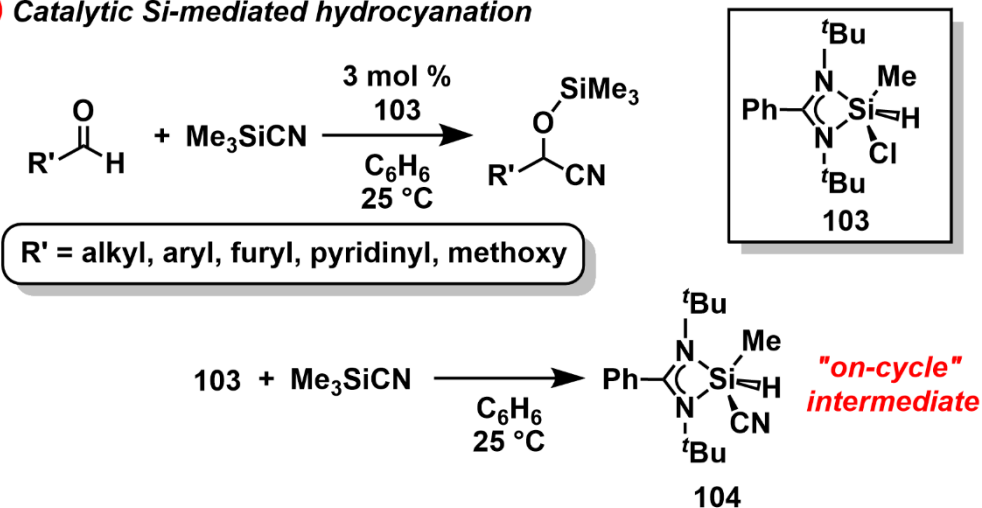
Thus far, discussion of catalytic hydride transfer in this Introduction has focused on compounds of Ge, Sn and Pb; however, important progress has also been made in the use of Si(II) catalysts in these chemical transformations (Scheme 1.18a).^{45a} As an example, the cationic carbene-supported Si(II) species $[(\text{ImMe}_4)_2\text{SiH}]\text{I}$ (**102**) [$\text{ImMe}_4 = (\text{MeCNMe})_2\text{C}:$] demonstrated significant hydroboration activity with pyridine substrates, in the presence of both HBpin and ketones/aldehydes at 90 °C (Scheme 1.18a).^{45a} Although the obtained TOF values using catalyst **102** were lower (0.4 to 116 hr^{-1}) than those found with Jones' Ge(II) (**95**) and Sn(II) (**96**) pre-catalysts, high

spectroscopic yields were observed (> 90%; 10 mol % loading of **102**), along with increased functional group tolerance, which allowed for the selective hydroboration of furanyl, thiophenyl, and olefinic-substituted substrates.^{45a}

(a) Catalytic Si-mediated pyridine hydroboration



(b) Catalytic Si-mediated hydrocyanation



Scheme 1.18. (a) Si-catalyzed pyridine hydroboration using a Si(II) species (**102**); (b) hydrocyanation of aldehydes by a Si(IV) hydride (**103**).

To demonstrate that catalytic hydride transfer reactivity is not limited to Si(II) species, a pentacoordinate silicon(IV) hydride catalyst [$\{\text{PhC}(\text{N}^t\text{Bu})_2\}\text{SiCl}(\text{H})\text{Me}$] (**103**) is shown in Scheme 1.18b; compound **103** (at a 3 mol % loading) was able to mediate the efficient hydrocyanation of aldehydes at 25 °C, albeit with low TOF values

of 3-6 hr⁻¹.^{45b} Similar to the catalytic behavior demonstrated by compound **102**, catalytic hydrocyanations using compound **103** showed high functional group tolerance by allowing efficient reaction with substrates that featured C(sp²)-X and -OMe linkages, furanyl/pyridinyl moieties, and olefinic groups.^{45b} Upon combination of [$\text{PhC}(\text{N}^t\text{Bu})_2\text{SiCl}(\text{H})\text{Me}$] (**103**) with Me₃SiCN, the cyanosilane [$\text{PhC}(\text{N}^t\text{Bu})_2\text{Si}(\text{CN})\text{H}(\text{Me})$] (**104**) formed, implicating compound **104** as an active “on-cycle” intermediate in hydrocyanation (Scheme 1.18b).^{45b}

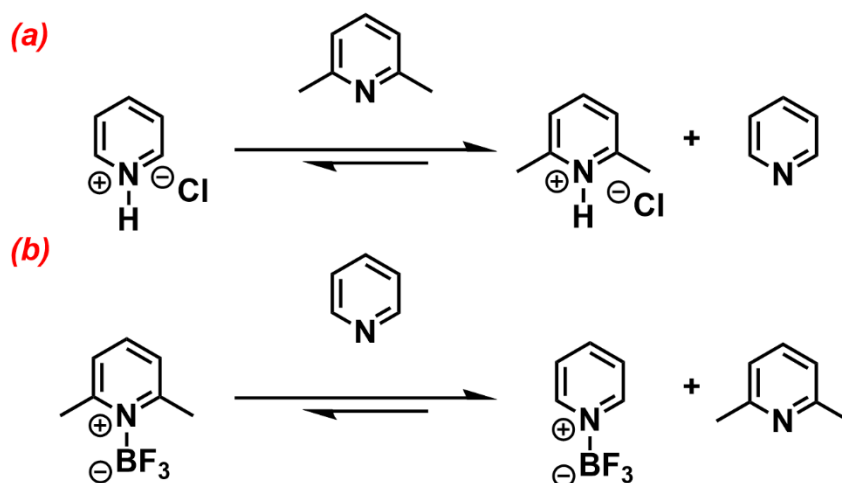
The stoichiometric and catalytic reactivity of Si and Ge compounds demonstrates that the activity of these catalysts is, thus far, not high enough to compete with transition metals, especially on an industrial scale; however, there is strong potential in this chemistry upon further ligand design and optimization. Fundamentally, these studies have shown that transient or isolable Si-H and Ge-H linkages can be crucial to the reactivity observed. Within Chapters 2 and 4 in this Thesis, hydridic and low-oxidation state Group 14 element complexes (Si and Ge) were targeted using frustrated Lewis pairs (FLPs) as ligands. Thus, the following section discusses the origin, history and current state of molecular FLPs in relevant chemical transformations.

1.2 Frustrated Lewis Pairs (FLPs): History and Chemistry

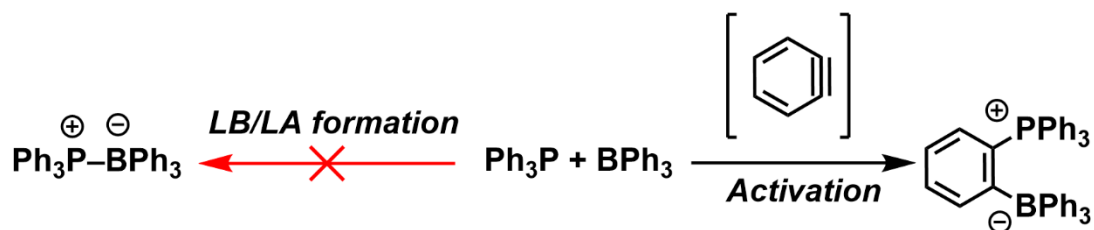
The term frustrated Lewis pairs (FLPs) was coined by the Stephan Group, to define a geometrically or sterically constrained Lewis base (LB)/Lewis acid (LA) pair that cannot form a coordinative single bond between the LB and LA sites, as opposed to classical zwitterionic LB-LA adduct formation.^{46,47} In many FLP-mediated transformations, boranes featuring fluorinated aryl groups, such as $B(C_6F_5)_3$,⁴⁸ are used as the highly acidic and bulky LAs, paired with commercially available R_3P ($R =$ aryl or alkyl) as their LB counterparts.^{46,47} In recent years, the term FLP has been expanded to include LB/LA pairs that exhibit single bonds in solution and/or in the solid-state (a so-called “closed” conformation), since the “open” conformation is kinetically accessible by an equilibrium derived dissociation of the LB-LA single bond in solution.^{46,47} Of added note, recent electron paramagnetic resonance (EPR) spectroscopic studies by the Melen, Slootweg and Müller groups show that the final addition products from the combination of FLPs with small substrates can be formed through either one- or two-electron transfers, opening the door to future radical-mediated FLP chemistry.⁴⁹ A clear model reaction for the divergent mechanisms was reported by the Stephan Group, which involved changing the substituents on R_3P ($R =$ Mes or t Bu) in the presence of $B(C_6F_5)_3$, as Ph_3SnH can be activated by either one- or two- electron transfer to form either $[Mes_3P-H][H-B(C_6F_5)_3]$ or $[tBu_3P-SnPh_3][H-B(C_6F_5)_3]$, respectively (Scheme 1.19).^{49a}

adducts. In particular, readily available amine-boranes ($\text{H}_3\text{B}\cdot\text{NHR}_2$) and phosphine-boranes ($\text{H}_3\text{B}\cdot\text{PHR}_2$) have garnered significant interest as their catalytic dehydropolymerization can yield processable polymers with attractive properties (see Section 1.4).⁵⁷

While the aforementioned examples are key to synthetic chemistry, separating the LB from the LA gives way to unquenched sites of reactivity that are requisite for FLP behavior.^{46,47} The first glimpses of FLP chemistry were noted by H. C. Brown and G. Wittig, both of which would later share the 1979 Nobel Prize in Chemistry for their work in the development of boron- and phosphorus-containing compounds.⁵⁸ In 1942, while studying the steric strain between boranes and 2,6-lutidine, H. C. Brown observed that no adduct formation was observed when BMe_3 was combined with 2,6-lutidine.⁵⁹ Furthermore, even though 2,6-lutidine is able to deprotonate pyridine hydrochloride to form 2,6-lutidine hydrochloride and free pyridine (Scheme 1.20), the displacement of 2,6-lutidine by pyridine in BF_3 adducts was observed to form free 2,6-lutidine and pyridine $\cdot\text{BF}_3$ (Scheme 1.20); this study highlighted the effect of steric hinderance in classical LB-LA adduct formation (or lack thereof).⁵⁹ These observations by Brown were followed by work in 1959 from G. Wittig, where the combination of *in-situ* formed benzyne with a $\text{Ph}_3\text{P}/\text{BPh}_3$ mixture afforded the addition product, *o*- $\text{Ph}_3\text{P}(\text{C}_6\text{H}_4)\text{BPh}_3$, instead of the $\text{Ph}_3\text{P}\cdot\text{BPh}_3$ adduct (Scheme 1.21).⁶⁰



Scheme 1.20. (a) Deprotonation of pyridine hydrochloride by 2,6-lutidine; (b) displacement of 2,6-lutidine by pyridine in the BF_3 -adduct.



Scheme 1.21. Cooperative activation of a benzyne by Ph_3P and BPh_3 .

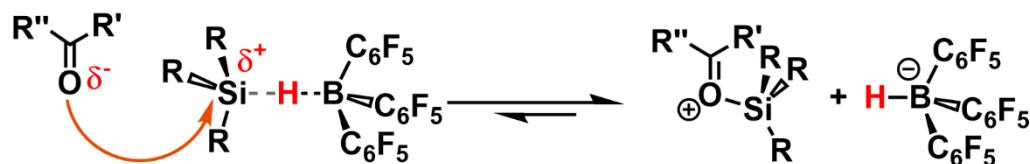
The subsequent emergence of FLPs as highly reactive species for catalytic and/or energetically uphill chemical transformations was the result of landmark work by the Piers and Stephan Groups starting in the 1990s.^{47,61} Piers' in-depth study of the $\text{B}(\text{C}_6\text{F}_5)_3$ -catalyzed hydrosilylation of ketones ($\text{R}'(\text{R}'')\text{C}=\text{O}$; R' and R'' = alkyl or aryl) revealed an "encounter complex" between the $\text{R}_3\text{Si}-\text{H}\cdots\text{B}(\text{C}_6\text{F}_5)_3$ units that makes the Si center more electropositive; subsequent concerted nucleophilic attack by ketones $\text{R}'(\text{R}'')\text{C}=\text{O}$ and hydride transfer by the $[\text{H}-\text{B}(\text{C}_6\text{F}_5)_3]^-$ anion generated yields the final $\text{R}'(\text{R}'')\text{C}(\text{H})-\text{OSiR}_3$ product (Scheme 1.22).⁶¹ Using 1–4 mol % $\text{B}(\text{C}_6\text{F}_5)_3$ and one equiv.

of Ph_3SiH with a variety of ketones at room temperature resulted in $> 76\%$ isolated yields of the hydrosilylated products with the highest turn-over frequency (TOF) being 637 hr^{-1} .⁶¹

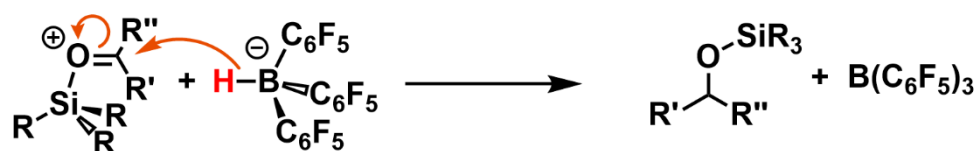
(a) Encounter complex formation



(b) Nucleophilic attack by $\text{R}_2\text{C=O}$



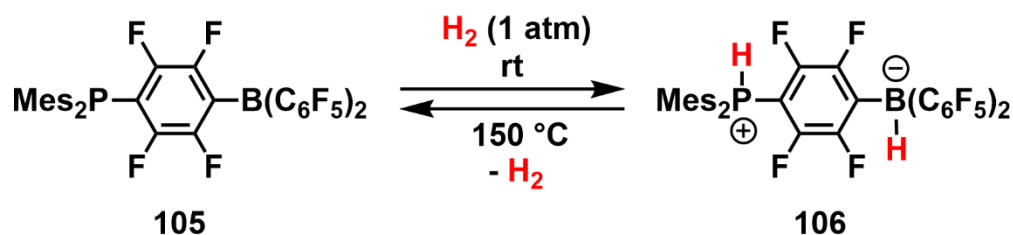
(c) Hydride transfer from $[\text{HB(C}_6\text{F}_5)_3]^-$



Scheme 1.22. (a) Initial activation of the $\text{R}_3\text{Si-H}$ bond by $\text{B(C}_6\text{F}_5)_3$; (b) nucleophilic attack onto R_3Si by a ketone; (c) final hydride transfer from $[\text{HB(C}_6\text{F}_5)_3]^-$ to form the hydrosilylated product, $\text{R}'(\text{R}'')(\text{H})\text{CO-SiR}_3$.

In 2006, the Stephan Group demonstrated that a C_6F_4 -bridged FLP, $\text{Mes}_2\text{P(C}_6\text{F}_4)\text{B(C}_6\text{F}_5)_2$ (**105**) could cleave the robust H-H single bond (bond dissociation enthalpy = 435.7 kJ/mol)⁶² at room temperature to afford the zwitterionic product $[\text{Mes}_2\text{HP(C}_6\text{F}_4)\text{BH(C}_6\text{F}_5)_2]$ (**106**) (Scheme 1.23).⁴⁷ By heating $[\text{Mes}_2\text{HP(C}_6\text{F}_4)\text{BH(C}_6\text{F}_5)_2]$ (**106**) at $150 \text{ }^\circ\text{C}$, regeneration of $\text{Mes}_2\text{P(C}_6\text{F}_4)\text{B(C}_6\text{F}_5)_2$ (**105**) was observed *via* H_2 gas evolution.⁴⁷ Prior to this work, the only examples of a Group 13 element involved in H_2 activation were from low temperature (10 to 200 K)

matrix or hot plasma experiments using BBr_3/H_2 , $\text{Cp}^*\text{Al}/\text{H}_2$, and vaporized Ga/H_2 mixtures.⁶³ While main group elements lack energetically accessible d -orbitals for the activation of dihydrogen,⁵ landmark work by the Stephan Group showed that synergistic (FLP) activation could be used as a substitute for d -orbital-based reactivity.⁴⁷ The following section highlights subsequent FLP work since the 2006 discovery.



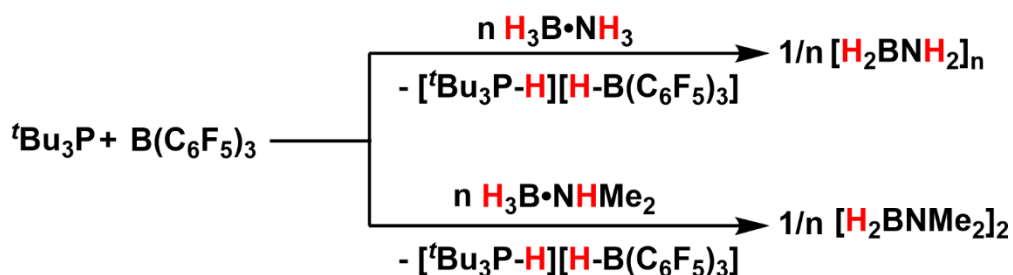
Scheme 1.23. Reversible dihydrogen activation by $\text{Mes}_2\text{P}(\text{C}_6\text{F}_4)\text{B}(\text{C}_6\text{F}_5)_2$ (**105**).

1.2.2 Cooperative Activation of Small Molecules *via* FLPs

Spurred by the H_2 activation described above, the range of chemical transformations accessible by FLPs has grown drastically, such that all examples cannot be discussed here; however, comprehensive and recent reviews are listed as part of references 46 and 47. To gain an understanding of the specific work outlined in this Thesis (particularly in Chapter 3), related examples of FLPs in dehydrocoupling and transfer hydrogenations using amine-boranes as sources of H_2 will be discussed.

Stoichiometric examples of FLP-mediated dehydrocoupling began in 2010 with work by the Miller and the Manners Groups.^{64,65} The Miller Group used an intermolecular FLP, tBu_3P and $\text{B}(\text{C}_6\text{F}_5)_3$, to induce the dehydrocoupling of the ammonia-borane $\text{H}_3\text{B}\cdot\text{NH}_3$ and $\text{H}_3\text{B}\cdot\text{NHMe}_2$ at room temperature (Scheme 1.24).⁶⁴ By

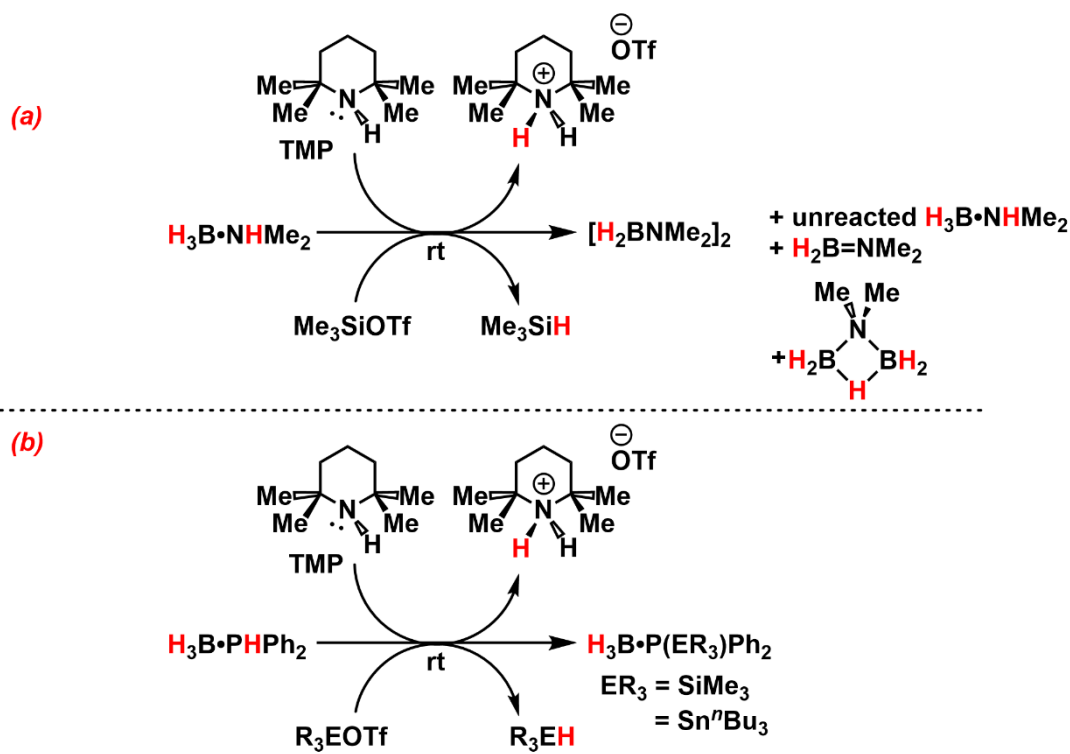
combining a mixture of $t\text{Bu}_3\text{P}/\text{H}_3\text{B}\cdot\text{NHMe}_2$ with $\text{B}(\text{C}_6\text{F}_5)_3$, the nearly quantitative formation of $[\text{tBu}_3\text{PH}][\text{HB}(\text{C}_6\text{F}_5)_3]$ and $[\text{H}_2\text{BNMe}_2]_2$ was observed according to multinuclear (^1H , ^{31}P , ^{11}B) NMR spectroscopy.⁶⁴ In the same manner, the combination of $t\text{Bu}_3\text{P}/\text{B}(\text{C}_6\text{F}_5)_3$ with $\text{H}_3\text{B}\cdot\text{NH}_3$ afforded $[\text{tBu}_3\text{PH}][\text{HB}(\text{C}_6\text{F}_5)_3]$ and $[\text{H}_2\text{BNH}_2]_n$ (according to ^{11}B NMR spectroscopy).⁶⁴



Scheme 1.24. Stoichiometric dehydrocoupling of amine-boranes using $t\text{Bu}_3\text{P}/\text{B}(\text{C}_6\text{F}_5)_3$ mixtures.

Moving towards mixed Group 14/15 element-based FLPs, the Manners Group used intermolecular Sn/N- and Si/N-containing pairs for the dehydrocoupling of both $\text{H}_3\text{B}\cdot\text{NHMe}_2$ and $\text{H}_3\text{B}\cdot\text{PPh}_2$ (Scheme 1.25).⁶⁵ Combining the FLP $\text{Me}_3\text{SiOTf}/\text{TMP}$ (TMP = 2,2,6,6-tetramethylpiperidine) with $\text{H}_3\text{B}\cdot\text{NHMe}_2$ proved to be less controlled than in the examples by Miller,⁶⁴ affording a mixture of $[\text{H}_2\text{BNMe}_2]_2$, $\text{H}_2\text{B}=\text{NMe}_2$, and $[\text{H}_2\text{B}(\mu\text{-NMe})(\mu\text{-H})\text{BH}_2]$ alongside the expected Me_3SiH and $[\text{TMP-H}][\text{OTf}]$ by-products (Scheme 1.25a).⁶⁵ In an attempt to dehydrocouple $\text{H}_3\text{B}\cdot\text{PPh}_2$, $\text{Me}_3\text{SiOTf}/\text{TMP}$ and $n\text{Bu}_3\text{SnOTf}/\text{TMP}$ were tested as FLPs, and gave the P–H bond activation products $\text{H}_3\text{B}\cdot\text{P}(\text{ER}_3)\text{Ph}_2$ ($\text{ER}_3 = \text{SiMe}_3$ or Sn^nBu_3) (Scheme 1.25b),⁶⁵ the products formed suggested that the competing concerted P–H deprotonation/E–O substitution process is more favorable than dehydrocoupling. The difficulty in the

attempted FLP-mediated P–H/B–H dehydrocoupling by Manners is consistent with previous reports of slower dehydropolymerization of phosphine-borane adducts in comparison to the amine-borane complexes in the presence of transition metal-based catalysts.⁵⁷



Scheme 1.25. (a) Stoichiometric dehydrocoupling of dimethylamine-borane into a mixture of products; (b) attempted dehydrocoupling of diphenylphosphine-borane by the FLPs R_3EOTf/TMP ($ER_3 = SiMe_3$ or Sn^nBu_3).

Expanding into catalytic amine-borane dehydrogenation, many examples of catalysis mediated by intramolecular FLPs have been reported (Figure 1.9, **107-110**).⁶⁶⁻

⁶⁹ Upon exposure to 10 mol % *trans*- $Mes_2P(H)C=C(Me)B(C_6F_5)_2$ (**107**), transfer hydrogenation was possible between $H_3B•NH_3$ and an enamine, forming the cyclic

borazine (HBNH)₃ by-product alongside the amine derived from hydrogenation (Figure 1.9, **107**).⁶⁶ It should be noted that compound **107** is unable to activate H₂ directly, so H₃B•NH₃ is used as a source of H⁺/H⁻ in this reaction.⁶⁶ Subsequent collaborative work by Slootweg, Uhl and co-workers showed that a germinal FLP Mes₂P(Al^tBu₂)C=C(H)Ph (**108**) (0.4 mol %) can dehydrocouple neat H₂B•NHMe₂ into [H₂BNMe₂]₂ with a 77 % isolated yield (Figure 1.9).⁶⁷ Furthermore, by using a xanthene-based FLP catalyst, **109** (Figure 1.9), the Aldridge Group demonstrated the catalytic dehydrocoupling of H₂B•NHMe₂ at 55 °C into [H₂B(μ-NMe)(μ-H)BH₂] and H₃B•NH₃ or H₃B•NH₂Me into their corresponding borazine trimers.⁶⁸ Mechanistic studies showed that the stoichiometric complex, [109{H₂BNH₂}], is an unreactive “off-cycle” species for dehydrocoupling; this observation is further reinforced by related FLP-aminoborane work discussed in Chapter 3.⁶⁸ Of particular relevance to this Thesis, Bourissou and co-workers explored the reactivity of the phosphine-borane intramolecular FLP, *o*-ⁱPr₂P(C₆H₄)B(Fxyl)₂ (Fxy1 = 3,5-(F₃C)₂C₆H₃) (**110**), which is in equilibrium between closed and open conformations (ΔG = +1.6 kcal/mol from closed to open).⁶⁹ Specifically, compound **110** can effectively dehydrocouple acyclic and cyclic amine-boranes as well as diamine-boranes at temperatures below 100 °C (Figure 1.9).⁶⁹ As will be discussed further in this Thesis (Chapters 2-4), related ⁱPr₂P(C₆H₄)BR₂ compounds can exhibit equilibria between closed and open forms, which can greatly affect their reactivity; in addition, they can participate in similar dehydrogenation reactivity with amine-boranes.

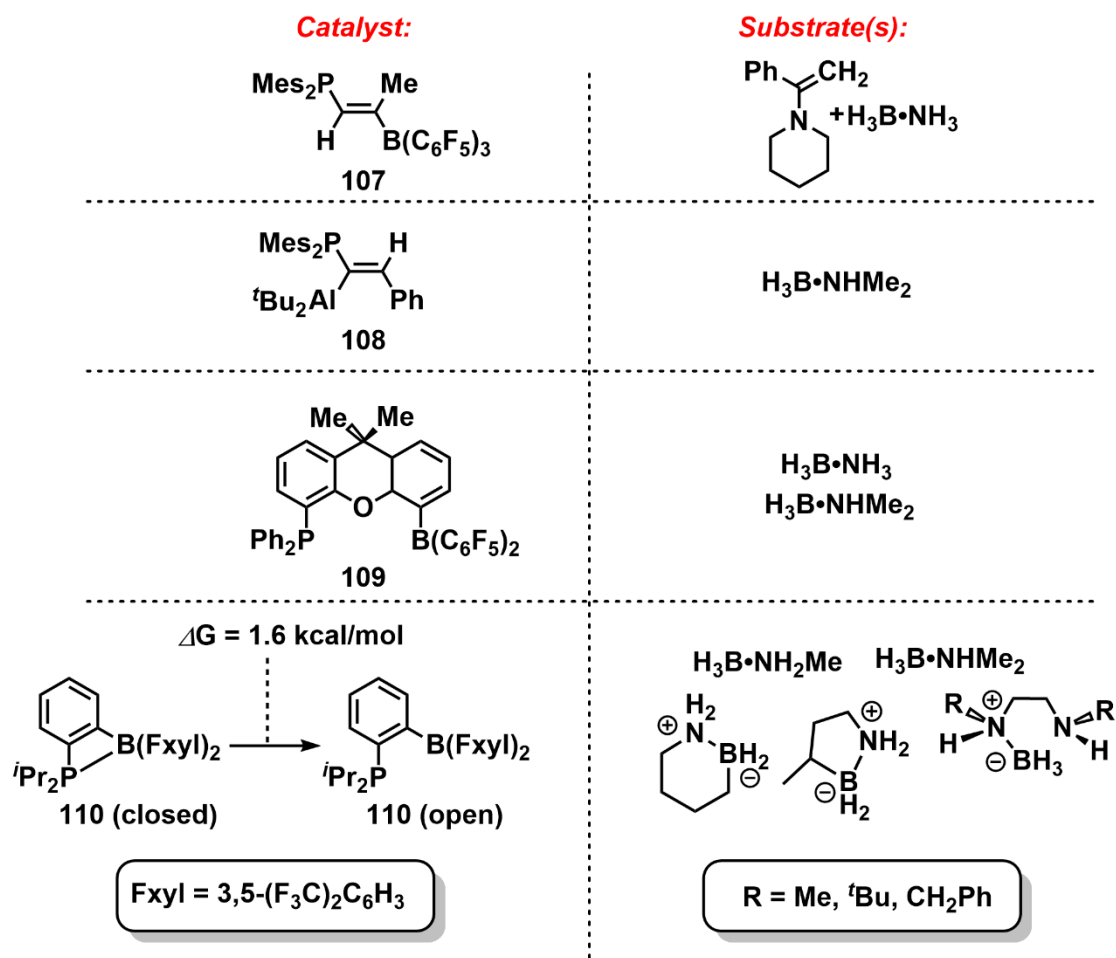
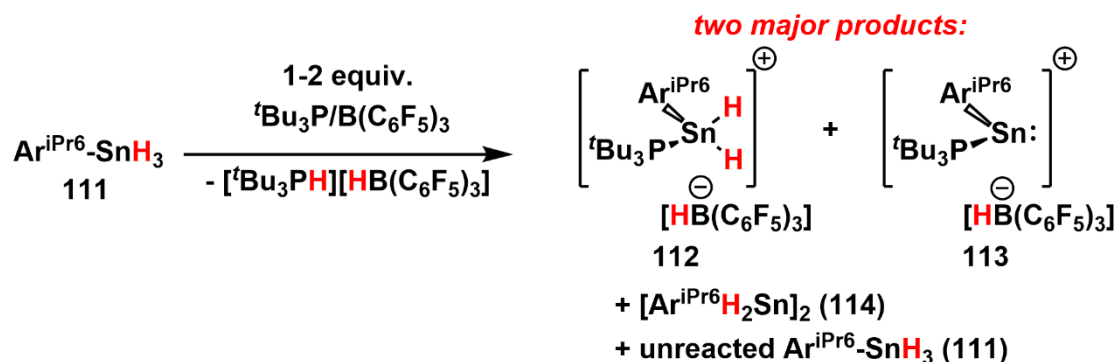


Figure 1.9. Selected examples of amine-borane dehydrocoupling FLP catalysts (**107-110**), including structures of the amine-borane substrates tested.

The FLP-mediated dehydrocoupling strategies have also been extended to include Group 14 element hydrides, as shown by recent work from the Wesemann group,⁷⁰ where they demonstrated the dehydrogenation of Ar^{iPr6}SnH₃ (**111**) by the ^tBu₃P/B(C₆F₅)₃ FLP to yield a mixture of cationic products, [Ar^{iPr6}SnH₂(P^tBu₃)]⁺ (**112**) and [Ar^{iPr6}Sn(P^tBu₃)]⁺ (**113**), alongside [^tBu₃PH]⁺ and [HB(C₆F₅)₃]⁻ ions in varying ratios, depending on the number of FLP equiv. used and reaction time (Scheme 1.26).⁷⁰

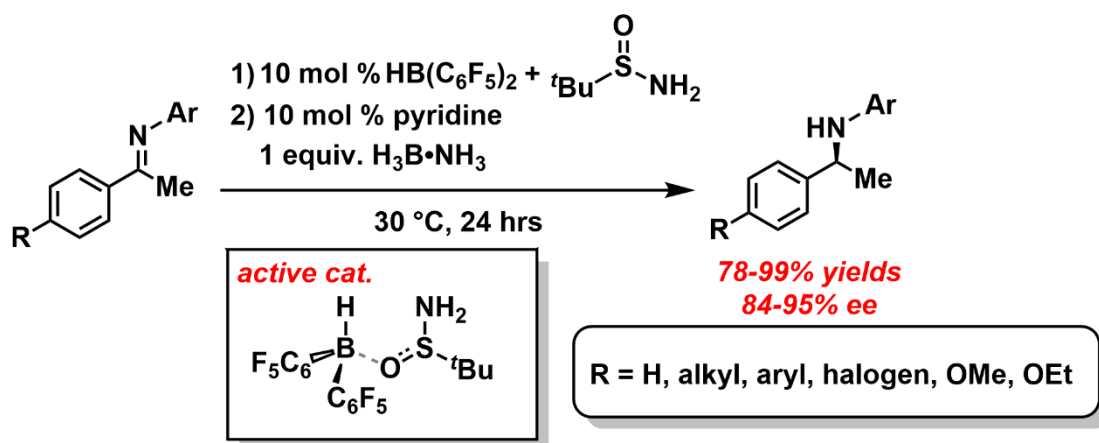
Minor amounts of the intended dehydrocoupled distannane $[\text{Ar}^{\text{iPr6}}\text{H}_2\text{Sn}]_2$ (**114**) were observed, suggesting that tuning of the FLP system may be possible to induce more controlled homoatomic dehydrocoupling.⁷⁰



Scheme 1.26. Attempted dehydrocoupling of $\text{Ar}^{\text{iPr6}}\text{SnH}_3$ (**111**) by a mixture of $^t\text{Bu}_3\text{P/B(C}_6\text{F}_5)_3$.

Building from the observed H_2 splitting and dehydrocoupling chemistry of FLPs, catalytic asymmetric transfer hydrogenation using a 10 mol % mixture of $\text{HB(C}_6\text{F}_5)_2$ (Piers' borane)/(*R*)-*tert*-butylsulfonamide ($^t\text{Bu}_3\text{S(O)NH}_2$), pyridine (10 mol %) as an additive and $\text{H}_3\text{B}\cdot\text{NH}_3$ as a H_2 source has been reported for a variety of imines, as summarized in Scheme 1.27.⁷¹ By performing control reactions and mechanistic studies (*via* NMR spectroscopy), the active catalyst was revealed to be an encounter complex with a central contact between the $\text{B}\cdots\text{O}=\text{S}$ unit, similar to the one observed in Piers' catalytic hydrosilylation of ketones discussed earlier (Scheme 1.22). Using the FLP $\text{HB(C}_6\text{F}_5)_2$ /*R*- $^t\text{Bu}_3\text{S(O)NH}_2$, 78-99 % yields with 84-95 % ee (ee = enantiomeric excess) were achieved for aryl-substituted imines, with a high tolerance for electron-withdrawing or electron-donating groups noted.⁷¹ Not only can the combination of H_2

or amine-boranes (either as substrates or sources of H₂) and FLPs offer new insight into dehydrocoupling processes, it has also opened the door for asymmetric hydrogenation-based routes to pharmaceutically relevant compounds, that were generally obtained with transition metal catalysts.



Scheme 1.27. Asymmetric transfer hydrogenation of imines using a borane/sulfinamide FLP system.

1.3 Silicon (Si) and Germanium (Ge) Films

1.3.1 Properties and Applications

So far in this Introduction, the importance and properties of silicon and germanium as semi-conductors have gone largely unmentioned. For example, the incorporation of semi-conducting silicon has been a major focus in the field of photovoltaics, although lead halide perovskite cells are gaining attention as components of solar cells as well.²⁰ Lead halide perovskite APbX₃ solar cells (typically A⁺ = MeNH₃; X⁻ = Cl-I)⁷² have been able to achieve 25.7 % power conversion efficiencies

(PCEs) as of 2021;⁷³ however, they are based on the element lead, which presents long-term supply issues (natural abundance of 14 mg/kg in the Earth's crust)⁶² and toxicity concerns, the latter is heightened by solar cell instability leading to lead leaching.⁷² In contrast to lead, silicon is *ca.* 20,000 times more abundant in the Earth's crust,⁶² is non-toxic, and is generally highly stable within photovoltaic systems.^{62, 20} Motivated by its advantages, bulk silicon has been studied extensively, particularly after the discovery of the Czochralski method for pulling pure monocrystalline silicon crystals.⁷⁴ With a similar band gap to silicon (1.1 eV),²⁰ germanium (band gap = 0.8 eV) has also been tested in solar cells, while GeO₂ has been used in fiber optic cables.⁷⁵ However, the low natural abundance of Ge (1.5 mg/kg)⁶² has limited its use in comparison to silicon.²⁰ Regardless, both silicon and germanium films have been studied thoroughly in light-emitting diodes (LEDs) and transistors.²⁰ To cover all applications of silicon and germanium in electronics within this Thesis would be impossible. Instead, the ubiquitous industrial-scale method of Si and Ge film growth, chemical vapor deposition (CVD), is discussed below to highlight the motivation behind the low temperature Si and Ge film deposition protocols described in Chapter 2.

In general, CVD can be simply described as follows:^{76,77} gaseous reactants are introduced into a heated reactor at a controlled gas flow rate (Figure 1.10a). Inside the reactor, reactants undergo either: (1) gas diffusion into the boundary layer and subsequent adsorption onto the substrate surface (Figures 1.10b and c); or (2) they can react in the gas phase above the substrate surface (Figure 1.10d), followed by diffusion/adsorption onto the substrate. Whether the reactant gases undergo reaction in

the gas phase (Figure 1.10d) or on the substrate surface (Figure 1.10e), intermediates and by-products are released which undergo desorption to escape the reactor (Figure 1.10f). Subsequently, heterogeneous reactions between the reactant gas and the substrate leads to controlled film growth on the surface (Figure 1.10e). For greater control, film thicknesses are monitored over time, such that the desired thickness can be selected with the correct reaction time. Once the desired film thickness has been achieved, high vacuum can be introduced to remove intermediates and left-over by-products. The film-covered substrate can be recovered and fully characterized to measure its physical and electronic properties, such as roughness or conductivity. CVD can allow for controlled tuning of film properties, as the introduction of added energy (plasma, hot wire, laser, etc...) or changes in loading method, reactant gas identity and concentration, substrate, temperature differentials, pressure, gas flow rate, and reaction time can all be used to optimize the desired film conditions.⁷⁶ The high degree of control makes CVD a powerful technique, albeit at the cost of expensive equipment and the use of toxic/reactive gaseous precursors.⁷⁶

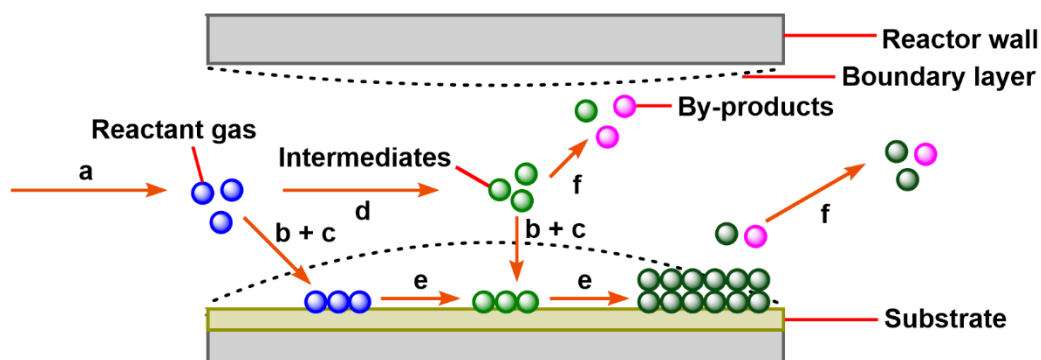


Figure 1.10. Representative schematic for a typical CVD process, depicting: (a) mass transport; (b) gas diffusion; (c) adsorption; (d) gas phase reaction; (e) heterogeneous/surface reaction; (f) desorption and mass transport. Adapted from Figure 1 in ref. 76.

Post-World War II, the demand for silicon-based computer chips led to the development of new CVD methods for semi-conducting films, allowing plasma/photo/laser-assisted CVD (PCVD) and hot filament/wire CVD (HF-CVD) methods to emerge.⁷⁶ In PCVD, an intense energy source (plasma, high intensity lamp or laser) is used to instigate CVD, which allows for lower reaction temperatures but increases the equipment cost and complexity.⁷⁶ Alternatively, HF-CVD uses a metallic filament (often W, Ta, or Mo) that is heated to temperatures much higher than the reactor temperature above the substrate, such that the input gases begin to react along the filament, adsorb onto the substrate and react at lower reactor temperatures overall.⁷⁶ The following sections (1.3.2 and 1.3.3) describe selected examples of Si and Ge CVD precursors.

1.3.2 Chemical Vapor Deposition (CVD) for the Growth of Si Films

Generally, examples of silicon thin film CVD precursors can be broken down into four categories: halosilanes, mixed halo/hydridosilanes, hydridosilanes, and organosilanes (Figure 1.11). Starting with the halosilanes and mixed halo/hydridosilanes (generally called Si-H-Cl systems due to the addition of H₂ and release of HCl), the deposition of amorphous Si thin films is possible above *ca.* 450 °C using either SiCl₄^{78a} or Si₂Cl₆,^{78b} although the film growth is slow below 800 °C. In order to obtain silicon in high purity, the presence of H₂ gas is required since the SiCl₂ intermediate (produced *via* the gas-phase reaction $\text{SiCl}_4 + \text{H}_2 \rightarrow \text{SiCl}_2 + 2 \text{HCl}$) can introduce structural defects by attacking the film surface of deposited silicon without another equiv. of H₂ to react with (*vide infra*).⁷⁸ After SiCl₂ gas generation, the surrounding H₂ environment allows for the formation of other H_xSiCl_y species (*via* release of HCl) and then hydrogenated SiH_{1,2,3,4} (Si₂H₄, Si₂H₆, etc...) intermediates which undergo the final degradation step into elemental Si and elimination of H₂ gas.⁷⁸ The related mixed halo/hydridosilanes, HSiCl₃,^{78c} and H₂SiCl₂,^{78a} exhibit nearly identical CVD behavior (Figures 1.11a and b).

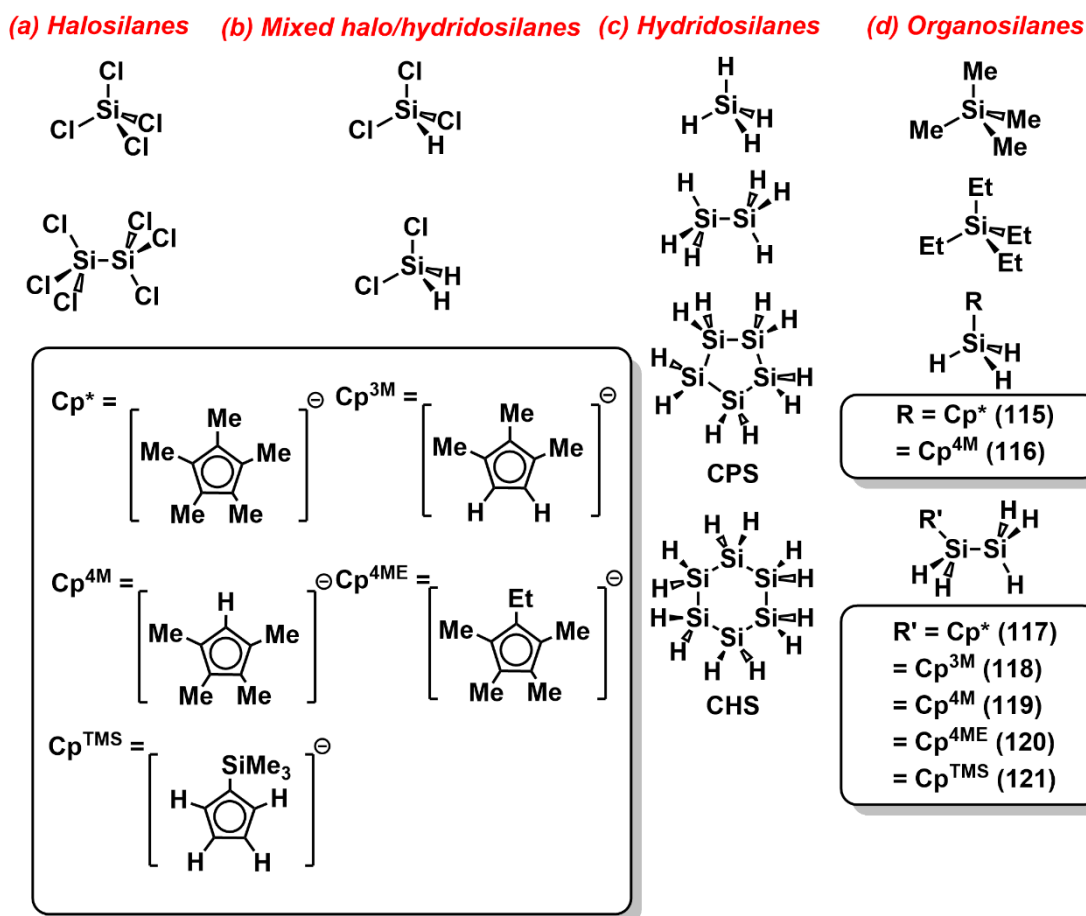


Figure 1.11. Selected examples of elemental Si film CVD precursors: (a) halosilanes; (b) mixed halo/hydridosilanes; (c) hydridosilanes; (d) organosilanes.

The most popular precursors for industrial Si CVD film growth are hydridosilanes SiH_4 ⁷⁹ or Si_2H_6 ⁸⁰; these compounds can be used as a pure feedstock or they can be diluted and even mixed with controlled amounts of NH_3 gas (or N_2H_4),^{78d} light hydrocarbons^{79b} or even diluted O_2 ^{79c} to provide silicon nitride (Si_3N_4), silicon carbide (SiC) or SiO_2 thin films, respectively (Figure 1.11c). Both hydridosilanes, SiH_4 or Si_2H_6 , require heating above 600 °C to induce effective Si deposition in traditional CVD methods and *ca.* > 400 °C in more complicated approaches (*e.g.*, PCVD). Si

deposition below 600 °C often yields hydrogenated amorphous Si (*a*-Si:H) film surfaces (5-20 % hydrogen content within *ca.* 200-600 °C) which are typically used in solar cell devices as the presence of surface Si–H bonds increases the overall efficiency.²⁰ However, both hydridosilanes SiH₄ or Si₂H₆ are extremely pyrophoric and can autoignite under ambient conditions, leading to safety risks upon accidental gas leakage.

As mentioned above, the lowest temperature used for CVD of Si films is *ca.* 400 °C with added equipment complexity. To further lower the required deposition temperatures in film growth and increase the ease of precursor handling, higher hydridosilanes, such as cyclopentasilane^{81b,c} (CPS or [H₂Si]₅), have been studied as liquid precursors for Si film growth (Figure 1.11c). In particular, CPS can undergo polymerization to give [H₂Si]_n oligomers upon heating above *ca.* 100 °C, upon extended exposure to ambient light, or more rapidly upon irradiation at 405 nm with a lamp.^{81b} These [H₂Si]_n oligomers were highly branched, with number average molecular weights (M_n) of 2.6 kDa and a polydispersity index (PDI) above 2.^{81b} The high processability of CPS allows for drop-casting, spin-coating, and ink-jet printing methods to first deposit a CPS layer, which can then be thermally dehydrogenated above 540 °C to give *a*-Si:H films (*ca.* 19-50 nm thick).^{81b,c} These *a*-Si:H films can subsequently be exposed to a high energy 308 nm XeCl laser (345 mJ/cm²) to induce a change from *a*-Si into highly polycrystalline Si films (confirmed by transmission electron microscopy, TEM).^{81b,c} Furthermore, ink-jet printing allows for deposition of bulk *a*-Si (30-40 μm) from CPS in specific pre-programmed detailed patterns in a similar manner to photolithography.^{81b,c} While the transistor devices tested using CPS as a Si precursor

currently exhibit poor performance as a result of surface defects, these oligomeric silanes offer high potential as Si thin film precursors with higher processability at similar deposition temperatures compared to the traditional SiH₄/H₂ CVD methods. A related liquid oligomeric silane, cyclohexasilane (CHS or [H₂Si]₆), has been reported^{81d} for which preliminary studies suggested full decomposition into elemental Si occurs at 170 °C. Recently, CHS was used in a similar drop-casting route as for CPS^{81b,c} to form 60 nm *a*-Si:H films, although temperatures above 550 °C were required.^{81e}

The thermal behavior of silanes suggests usage of any precursor (liquid or gaseous) with pre-installed Si–Si and Si–H linkages may still lead to the formation of light-weight and pyrophoric intermediates, but this phenomenon may be minimized by stabilization from carbon-based ligands. Careful monitoring of elemental composition in Si films derived from the CVD of carbon-ligated precursors must be performed to confirm minimal carbon content for pure amorphous or crystalline Si surfaces. Carbon-substituted CVD precursors fall within the organosilanes category and have been studied to increase the degree of safety associated with handling the reactants. Selected examples of organosilane precursors include: SiMe₄,^{82a} SiEt₄,^{82b} RSiH₃^{82c} (R = Cp* (115), Cp^{4M} (116); Cp^{4M} = [C₅Me₄H][−]) and disilanes RSi₂H₅^{82d,e} (R' = Cp* (117), Cp^{3M} (118), Cp^{4M} (119), Cp^{4ME} (120), Cp^{TMS} (121); Cp^{3M} = [C₅Me₃H₂][−], Cp^{4ME} = [C₅Me₄Et][−], Cp^{TMS} = [C₅(Me₃Si)H₄][−]) (Figure 1.11d). Of note, SiMe₄ and SiEt₄ are commonly used to deposit amorphous silicon carbide (SiC) films, but the carbon content can be minimized (< 5 %) upon added annealing at 425 °C in the presence of H₂ gas, such that its composition is primarily *a*-Si (according to XPS, Raman and FT-IR).^{82a,b}

The Cp-based silanes (**115-121**) isolated by Jutzi and co-workers are safe to handle and require temperatures above 550 °C in CVD for nm-scale high-purity *a*-Si film growth.^{82c,d,e} Fundamentally, these Cp*-stabilized silanes have been useful in confirming the release of SiH₂ and SiH₃ intermediates at temperatures above 400 °C by mass spectrometry (MS) monitoring of the desorbed gases generated during CVD.^{82c} This is consistent with previously mentioned results from cold matrices of laser-ablated Si in the presence of H₂ gas that show formation of SiH_{1,2,3} intermediates by IR spectroscopy (see above).^{21a}

Since the CVD of SiO₂ films is crucial to the function of current silicon chips (as an insulating layer),^{20,76} selected examples of SiO₂ film precursors are shown in Figure 1.12, depicting the structures of tetraethylorthosilicate [TEOS or Si(OEt)₄],⁸³ hexamethylcyclotrisiloxane ([Me₂SiO]₃ or D₃),^{84a} octamethylcyclotetrasiloxane ([Me₂SiO]₄ or D₄),^{84a} and hexamethyldisiloxane (HMDSO or Me₃SiOSiMe₃).^{84b} For TEOS, traditional CVD methods require temperatures above 700 °C for the deposition of amorphous SiO₂ films and these high temperatures are not compatible for deposition of SiO₂ onto most solar cell junctions; however, the mixture of TEOS/O₃ can lower the CVD temperatures to a suitable magnitude (400 °C) to afford amorphous SiO₂ films ranging in thickness from 200 nm to 1 μm, depending on the feedstock ratio and deposition time.⁸³ Both cyclic siloxanes D₃ and D₄ can be used as SiO₂ precursors at filament temperatures above 800 °C (HF-CVD), yielding amorphous SiO₂ films with an average thickness of 150 nm; this film thickness is not yet within the desired range for computer chips (*ca.* 1-5 nm).^{84a} Alternatively, HMDSO/O₂ mixtures can be used in

a Ar plasma (> 5000 °C local temperatures) CVD set-up with the reactor itself heated to near $200\text{--}300$ °C to deposit 2-8 nm thick amorphous SiO_2 films.^{84b} These siloxane precursors are safer to handle than mixtures of hydridosilanes with O_2 , despite the need for expensive equipment (*e.g.*, Ar plasma). Once deposited, these Si thin films often exhibit amorphous character; however, recrystallization from *a*-Si to polycrystalline Si is possible by thermal annealing for extended time (> 20 hrs) near *ca.* 450 °C or shorter time (4 min at *ca.* 700 °C per step) depending on the desired properties.^{20,79c} Ideally, silicon CVD precursors should be safe to handle, able to withstand long-term storage, and with low deposition temperatures (*ca.* < 200 °C) to minimize energy costs, which inspired the motivation behind work in Chapter 2 within this Thesis.

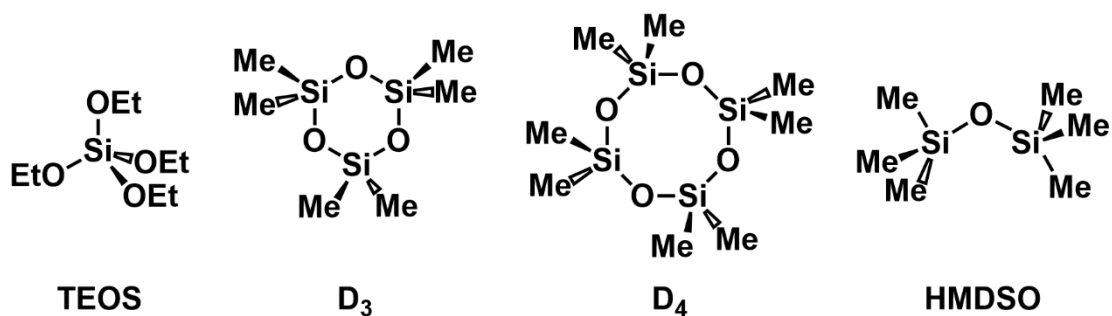


Figure 1.12. Selected examples of siloxanes used in SiO_2 film CVD.

1.3.3 Chemical Vapor Deposition (CVD) for the Growth of Ge Films

Thus far, the development of precursors for the CVD of Ge films is similar to those for silicon, with typical precursors including halogermanes, hydridogermanes, and organogermanes (Figure 1.13). Out of the three categories, the use of halogermane precursors for the deposition of elemental germanium is the earliest. In 1887, Winkler

studied the heating of GeCl_4 inside a glass bulb, which he noted resulted in a “germanium mirror”, although the exact temperature and by-products were not specified.^{85a} A more detailed example was reported by Voegelen in 1921 using GeCl_4 and H_2 gas that was generated from a mixture of zinc and sulfuric acid.^{85b} The combination of *in-situ* formed H_2 and GeCl_4 generated volatile gases (likely GeH_4 and/or H_xGeCl_y species) which deposited bulk germanium as it passed through the heated glass tube (temperature not reported).^{85b} In a similar manner to the deposition of halosilanes, halogermanes undergo reduction reactions at temperatures above 400 °C in the presence of H_2 gas (*e.g.*, $\text{GeCl}_4 + \text{H}_2 \rightarrow \text{GeCl}_2 + 2 \text{HCl}$); subsequently, the GeCl_2 intermediate is proposed to react with more H_2 to give short-lived $\text{GeH}_{1,2,3}$ and $\text{Ge}_2\text{H}_2/\text{Ge}_2\text{H}_4$ species, which then deposit bulk Ge and regenerate H_2 gas.^{21b,85,86} Further disproportionation (*via* $2 \text{GeCl}_2 \rightleftharpoons \text{Ge} + \text{GeCl}_4$) is a possible reaction pathway; however, this equilibrium was found to favor the formation of GeCl_2 at temperatures above 350 °C in the 1970s.^{86d} In fact, sublimation of GeCl_2 (and polymeric $[\text{GeCl}_2]_x$) can be achieved by the reduction of GeCl_4 with elemental Ge above 350 °C (*e.g.*, $\text{GeCl}_4 + \text{Ge} \rightarrow 2 \text{GeCl}_2$).^{86c} Common sources of halogermanes in CVD film growth include GeCl_4 and GeI_2 (Figure 1.13a).⁸⁶ The CVD of GeCl_4 occurs in the presence of H_2 at temperatures greater than > 460 °C to form 100-700 nm thick monocrystalline Ge films.^{86a,c} In contrast, the deposition mechanism from GeI_2 relies accessing the following equilibrium in order to proceed: $2 \text{GeI}_2 \rightleftharpoons \text{Ge} + \text{GeI}_4$; deposition of polycrystalline Ge films from GeI_2 has been observed to occur at temperatures ranging from 210 °C to 260 °C inside a sublimation chamber at 330 mTorr.^{86b} Furthermore,

GeI₂/GeI₄ mixtures have recently been microwave-heated in the presence of RNH₂ (R = alkyl) capping ligands to release [RNH₃]I and yield Ge nanoparticles.⁸⁷ The exact mechanism of Ge nanoparticle formation through this route is not yet known since disproportionation, redox and radical-based reaction pathways have all been implicated.⁸⁷

Hydridogermanes, such as GeH₄ and Ge₂H₆, are toxic yet ubiquitously used precursors for the industrial preparations of Ge *via* CVD (Figure 1.13b).⁸⁸ For GeH₄, reactor temperatures ranging from 250 to 350 °C are sufficient for low-pressure (300–600 mTorr) CVD of *ca.* 20 nm thick polycrystalline Ge films.^{88a} Using much lower pressures (< 10⁻⁵ mTorr) and GeH₄ as a feedstock, the controlled formation of nm-scale Ge films can be achieved such that amorphous Ge can be deposited at temperatures below 225 °C, monocrystalline Ge can be deposited from 225 °C to 400 °C, and polycrystalline Ge can be deposited above 450 °C.^{88b} Similarly, using Ge₂H₆, the low-pressure CVD (< 3 × 10⁻³ mTorr) of amorphous (< 300 °C) or monocrystalline (< 500 °C) Ge films has been achieved.^{88d}

To address safety concerns and increase the ease of handling, organogermanes have been reported in recent years that are less volatile, less dangerous to handle, and more soluble than their halo- or hydrido- analogues.⁸⁹ Selected examples of organogermanes in CVD film growth include GeR₄ [R = Me, Et, HC=CH₂], R'₂GeH₂ [R' = Cp^{4M} (**122**), Cp* (**123**)], R''GeH₃ [R'' = ^tBu (**124**), Cp^{4M} (**125**), Cp* (**126**)] (Figure 1.13c).⁸⁹ In the case of GeEt₄, CVD of nm-scale polycrystalline Ge films was achieved at ambient pressures (760 Torr) and a 500–560 °C temperature range.^{89b} Interestingly,

the onset of decomposition for GeEt₄ is reduced from *ca.* 450 °C to *ca.* 350 °C in the presence of H₂ gas *vs.* He is used as a carrier gas.^{89b} The inclusion of H₂ gas also has an influence on the by-products released, according to gas chromatography: CVD GeEt₄/He mixtures show the formation of ethylene (C₂H₄) upon increasing deposition time, while GeEt₄/H₂ mixtures show both C₂H₄ and ethane (C₂H₆), from olefin hydrogenation of C₂H₄ by H₂ at high temperatures. D₂ labelling experiments revealed the following β-hydride elimination pathway occurs: GeEt₄ → Ge + 4 C₂H₄ + 2 H₂.^{89b} While β-hydride elimination has been consistently reported as a major pathway in the Ge deposition using GeEt₄, a gas chromatography-supported methyl radical-based mechanism has been implicated for GeMe₄, with the overall reaction: GeMe₄ → 2 C₂H₆ + Ge.^{89g} Full consumption of Ge(HC=CH₂)₄ in CVD has been observed at temperatures above 700 °C; however, the crystallinity or thickness of these Ge films were not reported.^{89c} The ambient pressure (760 Torr) CVD of R'₂GeH₂ (**122** and **123**) exhibited temperature ranges (*ca.* 275-400 °C) for the deposition of 100-200 nm thick amorphous Ge films; the deposited films could be annealed into polycrystalline Ge films by irradiating with a 514.5 nm Ar laser (used for Raman spectroscopy).^{89e} Similarly, the CVD of ^tBuGeH₃ (**124**) occurred at 320 °C (30 Torr), affording 30 nm thick amorphous Ge films.^{89d}

The CVD behavior of the R''GeH₃ complexes (**124–126**) was studied by Jutzi and co-workers, and is similar to that of Cp*SiH₃ (**115**), where ambient pressure CVD near *ca.* 350 °C yields 20 nm thick amorphous Ge films.^{82c} Since the MS chamber attached to the reactor vessel for the CVD of compound **126** showed a significant

increase in the $^{76}\text{GeH}_2$ m/z peak upon heating over time, the formation of GeH_2 as an intermediate in the thermolysis (above $200\text{ }^\circ\text{C}$) was postulated.^{89f} According to MS, the m/z peaks for $\text{Cp}^*\text{-H}$ species was also observed to increase over time, and is proposed to be the result of hydride transfer onto the Cp^* group from the GeH_3 unit in **126**.^{89f} By combining this observation with the formation of GeH_2 from laser-ablated Ge/H_2 mixtures by the Andrews Group,^{21b} the generation of a GeH_2 intermediate in the release of elemental Ge and H_2 gas from GeH_4 or other organogermanes (**122-126**) has some experimental support.

(a) Halogermanes (b) Hydridogermanes (c) Organogermanes

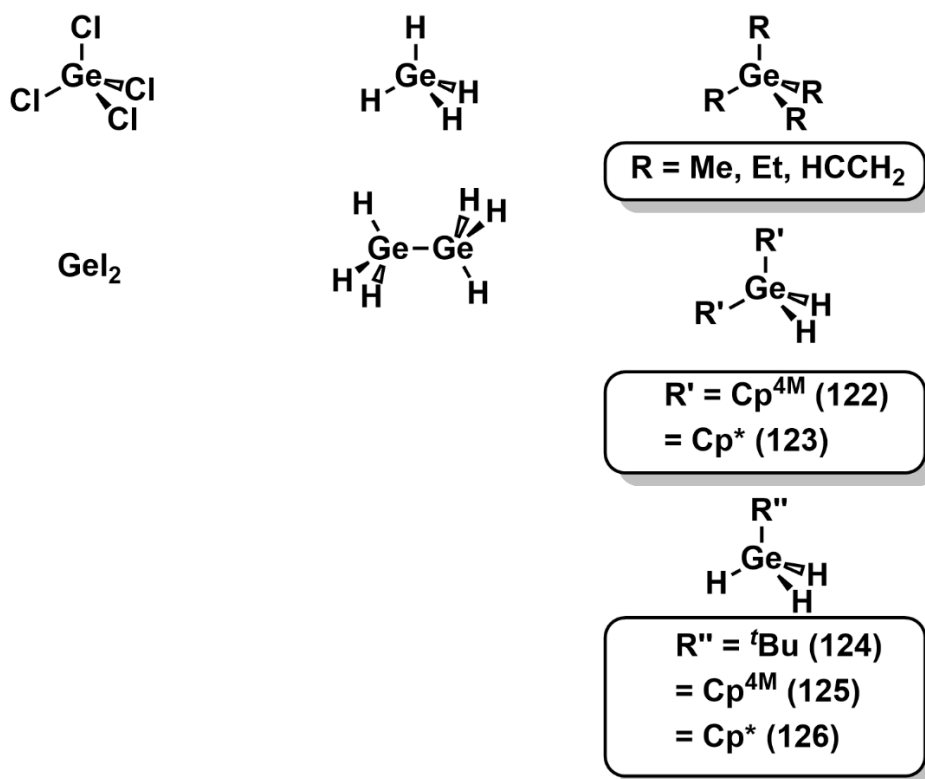


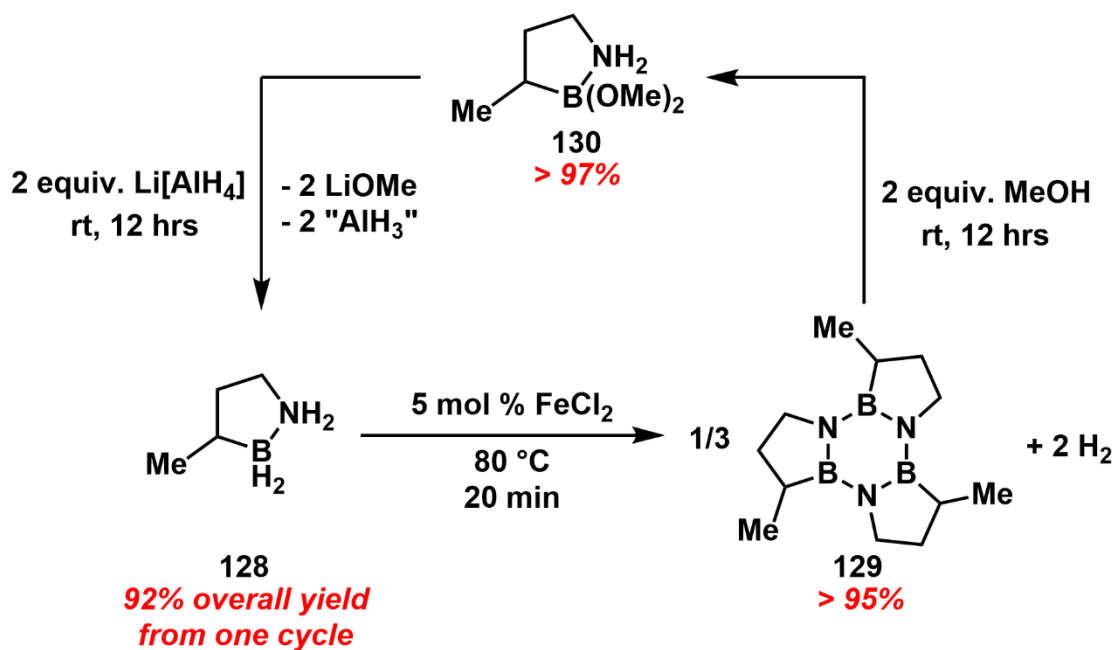
Figure 1.13. Selected examples of Ge CVD film precursors: (a) halogermanes; (b) hydridogermanes; (c) organogermanes.

In exploring the kinetic stabilization of GeH_2 , several examples of low temperature, solution-based Ge film deposition without the need for CVD equipment have been reported.^{37,90} In particular, the GeH_2 complex $\text{ImMe}_2 \cdot \text{GeH}_2 \cdot \text{BH}_3$ [**127**; $\text{ImMe}_2 = (\text{HCNMe})_2\text{C} \cdot$]⁹⁰ and $[\text{Ge}(\text{O}^t\text{Bu})_2]$ (**75**)³⁷ (see Section 1.1.2.2). were both used in the Rivard Group to deposit bulk germanium (as aggregates or thin films) upon heating in toluene at 110 °C (**127**) or at 70 °C (**75**) upon addition of $\text{H}_3\text{B} \cdot \text{SMe}_2$.^{37,90} Motivated by recent progress in the field of main group element chemistry, FLPs have been studied as ligands for the development of new precursors (such as stabilized SiH_2 and GeH_2 complexes) and this work is discussed in Chapter 2.

1.4 BN-Containing Polymers and Precursors to Bulk Boron Nitride

Compared to the analogous polyolefins $[\text{H}_2\text{C}-\text{C}(\text{H})\text{R}]_n$ ($\text{R} = \text{alkyl or aryl}$), polyaminoboranes with the general formula $[\text{H}_2\text{B}-\text{NHR}]_n$ have historically been understudied despite being first observed nearly 90 years ago by Schlesinger and Burg.⁵⁷ Without solubilizing groups, these polyaminoboranes are highly insoluble, as observed in the parent $[\text{H}_2\text{B}-\text{NH}_2]_x$, which was identified *via* solid-state ^{11}B NMR and IR spectroscopy.⁵⁷ Another challenge is the attainment of kinetic/thermodynamic control over the formation of linear polymers *vs.* cyclic dehydrogenated products.^{57,91} Despite these challenges, amine-borane monomers and their resulting polymers remain of high interest for hydrogen storage applications due to their high hydrogen weight % (*i.e.*, 19.6 % for the parent ammonia-borane $\text{H}_3\text{B} \cdot \text{NH}_3$).^{57,91,92} Of note, a related cyclic

amine-borane species **128** (Scheme 1.28), an air-stable and moisture-stable liquid, was shown to be able to undergo catalytic dehydrogenation in the presence of inexpensive FeCl_2 ($< 5 \text{ mol } \%$) at mild temperatures ($< 80 \text{ }^\circ\text{C}$) to yield the dehydrogenated product **129**.^{93a} Regeneration (by returning from **129** to **128**) required addition of two equiv. of MeOH to form a methoxy-containing intermediate **130**.^{93a} Cleavage of the B–O bonds in compound **130** was achieved using two equiv. of $\text{Li}[\text{AlH}_4]$ to afford the monomer **128** in a 92 % overall yield.^{93a} Thus, this reversible hydrogenation/dehydrogenation route is high yielding and based on commercially available precursors.^{93a} Other related cyclic amine-borane precursors are currently emerging as promising fuels for hydrogen-based transportation.⁹³

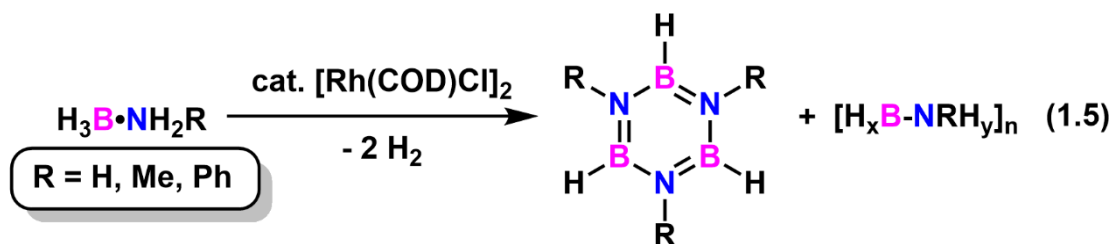


Scheme 1.28. Dehydrogenation and regeneration of a cyclic amine-borane (**128**) in search of regeneratable hydrogen storage materials.

1.4.1 BN-Containing Polymers: Properties and Applications

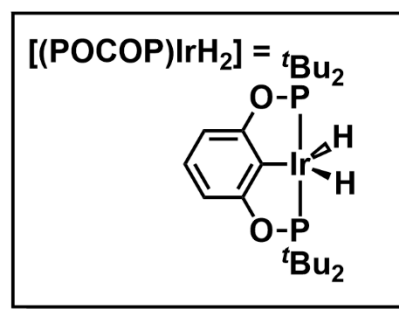
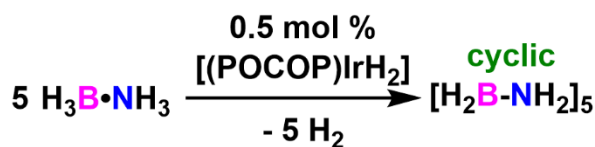
Over the last two decades, pioneering work by the Manners Group has accessed polyaminoboranes through the discovery of new dehydrocoupling catalysts and the underlying mechanisms to achieve control over polymer growth.⁵⁷ Landmark work by the Manners Group was reported in the early 2000s, where well-defined dehydrocoupling of $\text{H}_3\text{B}\cdot\text{NH}_2\text{R}$ ($\text{R} = \text{H}, \text{Me}, \text{or Ph}$) was first observed using 0.5 mol % $[\text{Rh}(\text{COD})\text{Cl}]_2$ ($\text{COD} = 1,5\text{-cyclooctadiene}$) to produce cyclic borazines $[\text{HBNR}]_3$ ($\text{R} = \text{H}, \text{Me}, \text{or Ph}$) and insoluble oligomeric mixtures $[\text{H}_x\text{B-NRH}_y]_n$ (Equation 1.5).^{94a-c} This work inspired further examination of other transition metal catalysts for the controlled dehydropolymerization of amine-boranes. In this regard, Goldberg, Heinekey and co-workers first showed that the parent ammonia-borane, $\text{H}_3\text{B}\cdot\text{NH}_3$ could be dehydropolymerized into the cyclic pentamer, $[\text{H}_2\text{B-NH}_2]_5$, by a Brookhart-type iridium catalyst $[(\text{POCOP})\text{IrH}_2]$ ($\text{POCOP} = [1,3\text{-}(\text{tBu}_2\text{PO})_2\text{C}_6\text{H}_3]^-$) at room temperature (Scheme 1.29a).^{94d} Although the cyclic pentamer $[\text{H}_2\text{B-NH}_2]_5$ is highly insoluble (thus, difficult to characterize), the dehydropolymerization of $\text{H}_3\text{B}\cdot\text{NH}_3$ was corroborated by Manners and co-workers using lower catalyst loadings of $[(\text{POCOP})\text{IrH}_2]$ (0.3 mol %) and higher monomer concentrations (10 M) (Scheme 1.29b).^{94e} Furthermore, Manners' dehydropolymerization protocol ($[(\text{POCOP})\text{IrH}_2]$, 0.3 mol %, 10 M monomer concentration) was extended to the primary amine-boranes $\text{H}_3\text{B}\cdot\text{NH}_2\text{R}$ ($\text{R} = \text{Me}$ or ^nBu) to form their respective soluble homopolymers $[\text{H}_2\text{B-NHR}]_n$ ($\text{R} = \text{Me}$ or ^nBu), and copolymers from mixtures of monomers $\text{H}_3\text{B}\cdot\text{NH}_3$, $\text{H}_3\text{B}\cdot\text{NH}_2\text{Me}$ and $\text{H}_3\text{B}\cdot\text{NH}_2^i\text{Bu}$, M_n

(M_n = number average molecular weight) values ranging from 47 kDa (*e.g.*, a 1:1 [H_2B-NH_2] $_x$ [$H_2B-NHMe$] $_y$ co-polymer) to 405 kDa (*e.g.*, homopolymer [H_2B-NH^iBu] $_n$).^{94e}

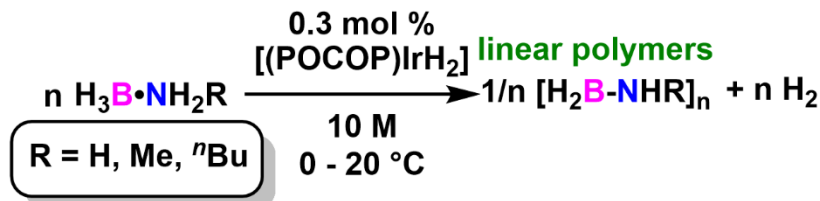


Ir-catalyzed dehydropolymerization of:

(a) *Ammonia-borane*



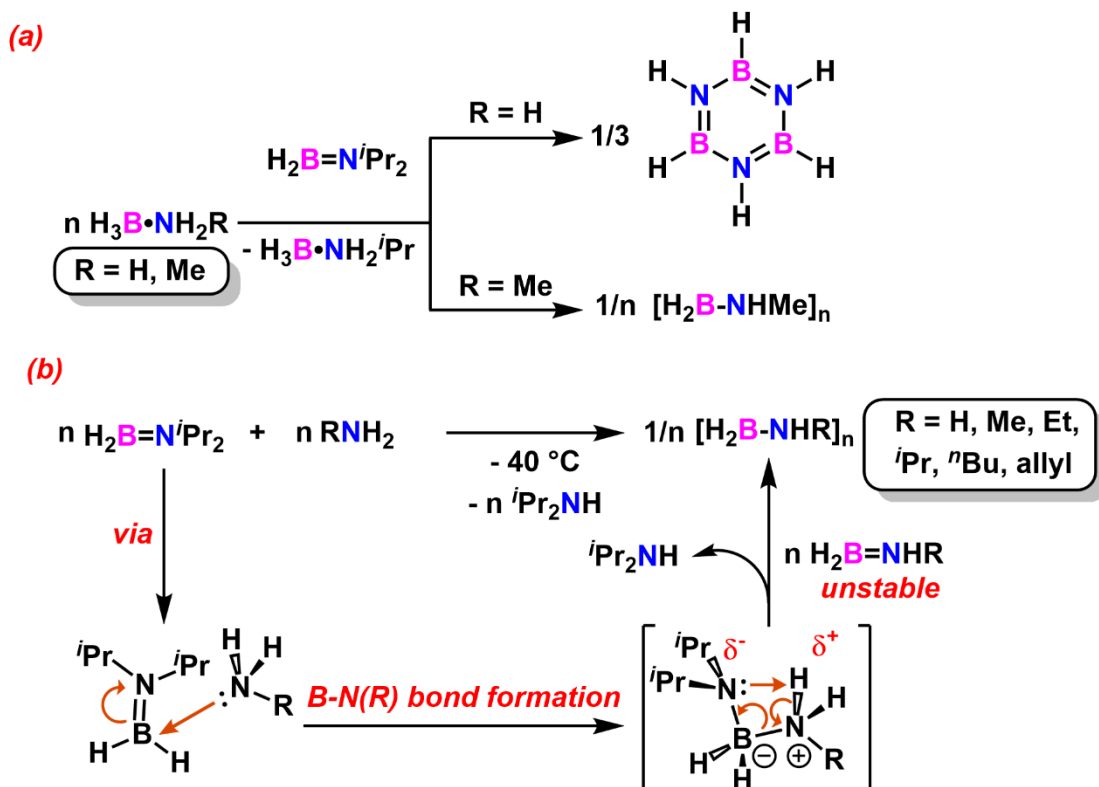
(b) *Primary amine-borane adducts*



Scheme 1.29. Ir-catalyzed dehydropolymerization of: (a) ammonia-borane; (b) primary amine-borane adducts.

As a result of early investigations on Ir-catalyzed dehydropolymerization, the catalytic dehydrocoupling of primary ($H_3B\cdot NH_2R$) and secondary ($H_3B\cdot NHR_2$) amine-boranes by way of transition metals (either *via* heterogeneous or homogenous pathways) has been realized to access mono-substituted polyaminoboranes and cyclic oligomers, respectively.^{57,91} As noted in Section 1.2.2., FLPs can induce

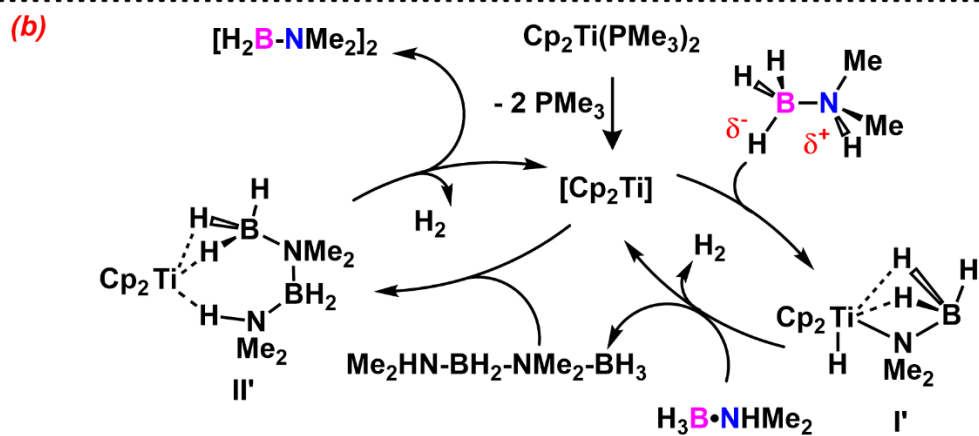
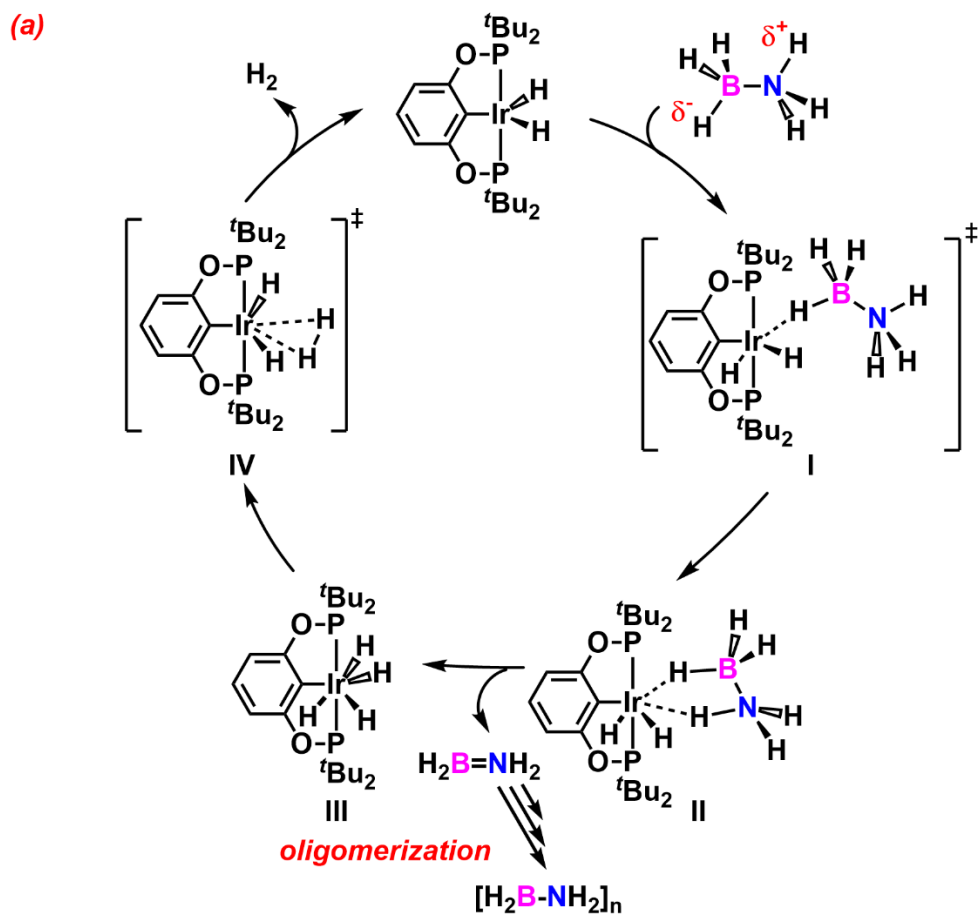
dehydrocoupling and may one day be catalysts of choice for dehydropolymerization. Metal-free dehydrocoupling of amine-boranes is also possible by the use of other B-N-containing species or even amines.^{95,96} For example, the synergistic transfer of H⁺/H⁻ units from H₃B•NHR (R = H or Me) can be induced by the addition of iminoborane H₂B=N^{*i*}Pr₂ to generate H₃B•NH^{*i*}Pr₂ and the dehydrogenation by-products [HBNH]₃ and [H₂B-NHMe]_n, respectively (Scheme 1.30a).⁹⁵ As an extension of this work, Alcaraz and co-workers demonstrated that the BH₂ unit within H₂B=N^{*i*}Pr₂ could be exchanged (in a formal sense) upon the addition of primary amines RNH₂ at -40 °C (R = H, Me, Et, ^{*i*}Pr, ^{*n*}Bu, or allyl) to afford the polymers [H₂B-NHR]_n and loss of ^{*i*}Pr₂NH.⁹⁶ The isolated yields for these BN-containing polymers were above 48 %, with M_n values ranging from 17 kDa to *ca.* 2000 kDa (Scheme 1.30b).⁹⁶ However, these polymers exhibited highly variable polydispersity indices (PDIs) ranging from 1.2 to 10.2, reflecting a lack of controlled polymer growth in many cases. Of note, the isolation of the allyl-substituted polymer [H₂B-NH(allyl)]_n (48 % yield, M_n = 580 kDa) using this protocol suggests higher functional group tolerance compared to traditional catalytic dehydrocoupling methods since the extruded H₂ from the latter route would hydrogenate the allyl unit in [H₂B-NH(allyl)]_n if metal catalysts were present.⁹⁶ The BH₂ transfer between H₂B=N^{*i*}Pr₂ and RNH₂ likely occurs as shown in Scheme 1.30b, with the initial formation of a B-N(R) bond (and loss of B-N double bond character), then subsequent loss of ^{*i*}Pr₂NH due to removal of N-H proton from -N(H)R unit.⁹⁶



Scheme 1.30. (a) Synergistic H⁺/H⁻ exchange between primary amine-boranes and the iminoborane H₂B=N^{*i*Pr}₂; (b) low temperature (-40 °C) amine-induced dehydropolymerization of primary amine-boranes.

While catalytic dehydrocoupling mechanisms for both primary (H₃B•NH₂R) and secondary (H₃B•NHR₂) amine-boranes can feature similar overall transformations, the exact steps can differ depending on the precise environment on the transition metal center and its coordination/ligand environment (*e.g.*, Ir, Rh, Ru, Ti, etc...).^{57,91} Scheme 1.31 depicts two representative catalytic cycles for the dehydropolymerization of ammonia-borane by [(POCOP)IrH₂] (Scheme 1.31a);^{97a} and the dehydrocoupling of H₃B•NHMe₂ by *in-situ* formed [Cp₂Ti]^{97b} into the cyclic dimer [H₂B-NMe₂]₂ (*via* Me₂HN-BH₂-NMe₂-BH₃) (Scheme 1.31b). Starting with the dehydropolymerization of

$\text{H}_3\text{B}\cdot\text{NH}_3$ (Scheme 1.31a), the mechanism begins with initial reorganization from $[(\text{POCOP})\text{IrH}_2]$ to transition state **I** due to attractive electrostatic forces between the electropositive Ir center in $[(\text{POCOP})\text{IrH}_2]$ and the hydridic $\text{B}^{\delta+}-\text{H}^{\delta-}$ linkages within $\text{H}_3\text{B}\cdot\text{NH}_3$.^{97a} Subsequently, the H^+/H^- unit within $\text{H}_3\text{B}\cdot\text{NH}_3$ binds to the Ir center to give complex **II** ($[(\text{POCOP})\text{IrH}_2\cdot\text{H}_3\text{BNH}_3]$), which allows for the dehydrogenation of the $\text{H}_3\text{B}\cdot\text{NH}_3$ unit and formation of **III**, a tetrahydride $[(\text{POCOP})\text{IrH}_4]$ complex.^{97a} Intermediate **III** is not stable over time (*vide infra*) and releases H_2 gas to regenerate $[(\text{POCOP})\text{IrH}_2]$ after proceeding through a $\eta^2\text{-H}_2$ [Ir] transition state (**IV**).^{97a} Thus, this dehydropolymerization mechanism suggests that the metal center is predominantly involved in the initial dehydrogenation of $\text{H}_3\text{B}\cdot\text{NH}_3$ and subsequent polymer growth is based on the instability of the transient iminoborane, $\text{H}_2\text{B}=\text{NH}_2$.^{97a} It is worth noting that this mechanism is supported by DFT computations (using a less bulky model of $[(\text{POCOP})\text{IrH}_2]$ with flanking PMe_2 groups) that demonstrated reasonable energy barriers (ΔE^\ddagger) for the first step ($[(\text{POCOP})\text{IrH}_2]$ to **I**; 8.7 kcal/mol) and the final step (**IV** to $[(\text{POCOP})\text{IrH}_2]$; 9.5 kcal/mol).^{97a} In addition, intermediate **III** was detected as a major species by kinetic NMR spectroscopy experiments; the independent syntheses of $[(\text{POCOP})\text{IrH}_4]$ (**III**) by Brookhart and co-workers corroborate that this species is highly unstable and cannot be isolated in pure form due to constant extrusion of H_2 under ambient conditions.^{97a,c}

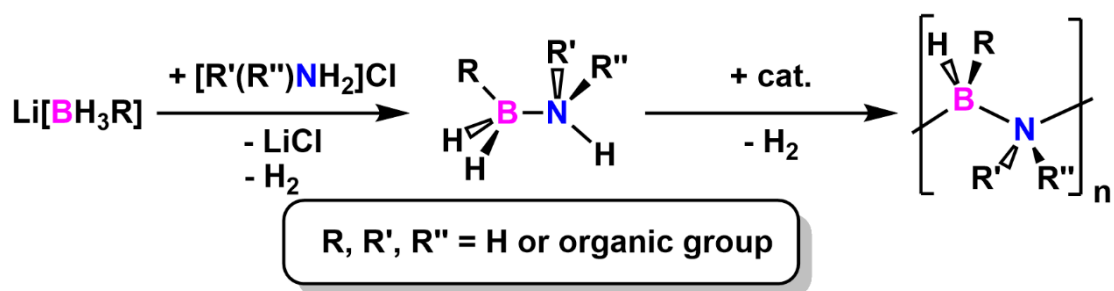


Scheme 1.31. Catalytic dehydrocoupling mechanisms for: (a) the polymerization of parent ammonia-borane using $[(\text{POCOP})\text{IrH}_2]$; (b) the formation of cyclic dimer $[\text{H}_2\text{B-NMe}_2]_2$ from $[\text{Cp}_2\text{Ti}]$. Adapted from Schemes 5.7 and 5.14 in ref 57.

The mechanism for dehydrocoupling of $\text{H}_3\text{B}\cdot\text{NHMe}_2$ by $[\text{Cp}_2\text{Ti}]$ into the cyclic dimer $[\text{H}_2\text{B-NMe}_2]_2$ is different to that of Ir-catalyzed dehydropolymerization (Scheme 1.31b). Once the active catalyst is formed, the Ti center initially removes a proton from the NMe_2 unit on $\text{H}_3\text{B}\cdot\text{NHMe}_2$ to form intermediate **I'**.^{97b} Subsequently, another molecule of $\text{H}_3\text{B}\cdot\text{NHMe}_2$ approaches intermediate **I'**, and the Ti center acts as a mediator for dehydrogenation and oligomerization of $\text{H}_3\text{B}\cdot\text{NHMe}_2$ into the linear complex $\text{Me}_2\text{HN-BH}_2\text{-NMe}_2\text{-BH}_3$.^{97b,d} This step re-forms the $[\text{Cp}_2\text{Ti}]$ catalyst, which in turn binds the newly generated $\text{Me}_2\text{HN-BH}_2\text{-NMe}_2\text{-BH}_3$ to form intermediate **II''**.^{97b,d} In an identical fashion to intermediates **II** and **I'**, polarized $\text{B}^{\delta+}\text{-H}^{\delta-}$ linkages allow for the stabilization of the Ti metal environment within intermediate **II''**.^{97b,d} Finally, simultaneous dehydrogenation of $\text{Me}_2\text{HN-BH}_2\text{-NMe}_2\text{-BH}_3$ yields the observed product $[\text{H}_2\text{B-NMe}_2]_2$.^{97b,d} Although the intermediates **I'** and **II''** have not been isolated, the depicted pathway was concluded to be the most favorable by DFT computations and the structure of intermediates (**I'** and **II''**) are similar to isolated $[(^i\text{Bu}_3\text{P})_2\text{Rh}\{\text{H}_3\text{B-NHMe}_2\}]^+[\text{BAR}^{\text{F}}_4]^-$ [$\text{Ar}^{\text{F}} = 3,5\text{-(F}_3\text{C)}_2\text{C}_6\text{H}_3$]^{91b} salts formed in other dehydrocoupling studies.⁵⁷

As will be discussed in Chapter 3, catalytic dehydrogenation can be effectively shut down by decreased hydridic character within the B–H unit in isolated aminoborane complexes, which is consistent with mechanistic studies that propose initial $\text{B}^{\delta+}\text{-H}^{\delta-}$ bond activation is crucial to dehydropolymerization (Scheme 1.31).⁹¹ Currently, mono-substituted polyaminoboranes (*e.g.*, $[\text{H}_2\text{B-NHMe}]_n$) can now be accessed in processable amounts (multi-gram scale, *ca.* > 50 kDa) through catalytic dehydrogenation of

commercially available amine-boranes, representing a major advancement in this field.^{57,91} For the preparation of less common amine-boranes, salt metathesis between $\text{Li}[\text{BH}_2\text{R}]$ ($\text{R} = \text{H}$ or organic group) and $[\text{R}'(\text{R}'')\text{NH}_2]\text{Cl}$ ($\text{R}, \text{R}', \text{R}'' = \text{H}$ or organic group) has been used (Scheme 1.32).^{57,91}



Scheme 1.32. General route to a variety of amine-boranes by salt metathesis and subsequent dehydropolymerization.

Once isolated, organo-substituted polyaminoboranes generally display amorphous character (as seen in $[\text{H}_2\text{B}-\text{N}(\text{H})\text{R}]_n$ where $\text{R} = \text{alkyl}$ or aryl), in contrast to the parent $[\text{H}_2\text{B}-\text{NH}_2]_n$ polymer which was confirmed by wide-angle X-ray scattering (WAXS) to be semi-crystalline.^{96,97} Furthermore, the solid-state packing of these repeating B–N units often results in glass transition temperature (T_g) values that can range from *ca.* 50-90 °C,⁹⁸ meaning the polymers behave as brittle glasses at room temperature. While the brittleness of polyaminoboranes may limit their use in applications that require flexible films, they could be employed in a similar manner as polycarbonates, which are used ubiquitously as high resistance glass panes or lenses.⁹⁸ Controlled tuning of carbon-based commodity polymers has been studied extensively to afford either flexible films (low T_g 's) or brittle glasses (high T_g 's) primarily *via*

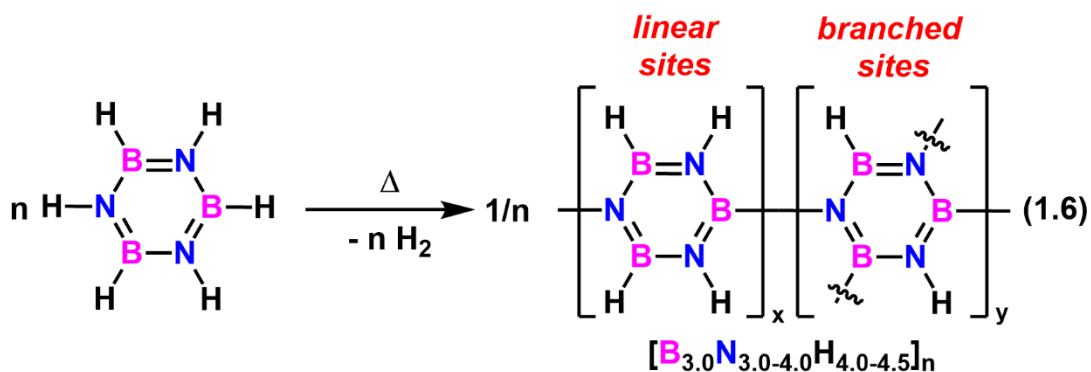
changes to the polymer backbone, but this has not yet been achieved with the same degree of control with polyaminoboranes.^{57,91,99} Compared to polyolefins, organic-substituted polyaminoboranes generally have better solubility for drop-casting or solution-based processing, such that they could be used in molds for polymer shaping.^{57,91,99} A general comparison between polypropylene [H₂C-C(H)Me]_n and poly(*N*-methylaminoborane) [H₂B-N(H)Me]_n demonstrates this solubility trend, as well as thermal stability and chemical stability differences (Table 1.1).^{57,91,96} The lower thermal decomposition temperature for poly(*N*-methylaminoborane) (< 160 °C) may allow for use of polyaminoboranes as boron nitride (BN) ceramic precursors (see below for preliminary studies).⁹⁶

Table 1.1. Comparison of polypropylene [H₂C-C(H)Me]_n and poly(*N*-methylaminoborane) [H₂B-N(H)Me]_n. Adapted from Table 1 in ref. 96b.

Polymer	Solvents	T _{decomp.}	Relative stability
[H ₂ C-C(H)Me] _n	Xylene	> 400 °C	Air-/Water-stable
[H ₂ B-N(H)Me] _n	THF, CH ₂ Cl ₂ , CHCl ₃ , DMSO	> 160 °C	Slow decomp. (air)

Testing polyaminoboranes as BN preceramics, the Manners Group reported the pyrolysis of [H₂B-NH₂]_n and [H₂B-N(H)Me]_n. Heating polymers [H₂B-NH₂]_n or [H₂B-N(H)Me]_n above 1000 °C resulted in divergent thermal behavior depending on the substrate used. On Si wafers, amorphous hexagonal BN (*h*-BN) nanostructures could be observed from either [H₂B-NH₂]_n or [H₂B-N(H)Me]_n; however, on Al₂O₃ wafers, the formation of Al₅BO₉ could be observed and thermolysis conditions could be tuned to form Al₅BO₉ nanowires.¹⁰⁰

A related BN-containing material, polyborazylene, is derived from the parent borazine (HBNH)₃ and features a cyclic B-N backbone instead of the linear B-N environment seen in polyaminoboranes (Equation 1.6).¹⁰¹ Thus far, polyborazylene (and its partially N-functionalized variants) have seen more success for use as BN ceramics than polyaminoboranes.¹⁰¹ Upon heating borazine (HBNH)₃ at 70 °C under vacuum for extended times (48 hrs) or > 45 °C in a Ar-filled autoclave, polyborazylene can be prepared with the general formula, [B_{3.0}N_{3.0-4.0}H_{4.0-4.5}]_n as a result of linear and branched repeating units (Equation 1.6).¹⁰¹ The syntheses of polyborazylene offers high potential for low temperature methods to boron nitride (BN) since the parent borazine (HBNH)₃ is highly volatile and polymerizable at temperatures below 100 °C, and the resulting polyborazylene exhibits low viscosity for spin-coating.¹⁰¹ In the presence of Ar or NH₃ gas at 900-1450 °C, polyborazylene can yield amorphous BN (*a*-BN) with high ceramic yields (> 80 %).¹⁰¹ The following section (1.4.2) discusses the attractive properties of bulk BN to highlight why the development of gentler routes to bulk BN are under active study.



1.4.2 Bulk BN: Properties and Applications

Depending on the solid-state phases, boron nitride (BN) can exhibit different physical and electronic properties (Table 1.2).^{102,103} The forms discussed here include: amorphous BN (*a*-BN), hexagonal (*h*-BN) and cubic (*c*-BN), which are the most common in materials applications; however, a wurtzite (*w*-BN) phase exists as a metastable material produced at very high pressures (> 11 GPa).¹⁰² The related rhombohedral (*r*-BN) phase is not as well-studied as the *c*-BN or *h*-BN phases but recent DFT computations suggest it is the more stable phase compared to *h*-BN under CVD conditions (> 1100 °C, > 1 kPa).¹⁰⁴

Table 1.2. Structural data and properties for boron nitride phases.

Forms	Unit cell dimension a [Å]	Unit cell dimension c [Å]	E _g [eV] ^a	Hardness [GPa]	Thermal conductivity. ^b [W/m·K]
<i>a</i> -BN	-	-	5.05	10 ^c	3
<i>h</i> -BN	2.50428(5)	6.6562(10)	5.2	1.3-1.5 ^d	600
<i>c</i> -BN	3.6153(1)	-	6.4	45 ^c	740

^aelectronic bandgap; ^bthermal conductivity; ^cKnoop hardness; ^dVickers hardness.

Focusing on properties, all three selected forms in Table 1.2, show wide band gap values (E_g > 5 eV; indirect for *c*-BN, direct for *h*-BN), with both *h*-BN and *c*-BN phases showing excellent thermal conductivity (> 600 W/m·K). For reference, diamond leads the field in thermal conductivity under ambient conditions at 2000 W/m·K.¹⁰⁵⁻¹⁰⁷ In addition, the *c*-BN exhibits hardness values that are roughly one order of magnitude higher than *h*-BN, classifying it as a “superhard” material, second only to

diamond.^{103,105,106} Although diamond can be extracted from mining, supply issues necessitate the synthesis and manufacturing of diamond under high temperatures (> 1000 °C) and/or high pressures (> 2 GPa); even the explosive detonation of graphite has been used to access diamond.¹⁰⁵⁻¹⁰⁸ Of added note for tooling and drilling applications, *c*-BN can survive oxidation in air near 1200 °C whereas diamond is stable up to 600 °C in air.¹⁰⁹

It should also be mentioned that *h*-BN has been studied in the field of optoelectronic materials, particularly as part of UV-light emitting diodes and piezoelectric materials.¹⁰³ In addition, BN-based nanomaterials have also found their place in biomedical applications, as they exhibit favorable dispersion/wetting behavior towards water alongside high biocompatibility for implants or drug delivery.¹⁰³ In recent years, lower temperature syntheses of BN (discussed in detail in Section 1.4.3.) have been explored to make BN more accessible over diamond.

1.4.3 Known Preparations of Bulk Boron Nitride

One of the earliest preparations for BN was performed in 1842 where the combination of molten (> 240 °C) boric acid [B(OH)₃] and potassium cyanide (KCN) yielded a white powder with a 1:1 B:N composition.¹¹⁰ Since then, many synthetic routes to BN have been developed, the majority of which are based combining B(OR)₃/NH₃ mixtures at high temperatures (> 900 °C).¹¹¹ A notable contribution by Wentorf reported well-defined “borazon”, the cubic form of BN (*c*-BN), by heating mixtures of boron and nitrogen at temperatures above 1350 °C and pressures above 6

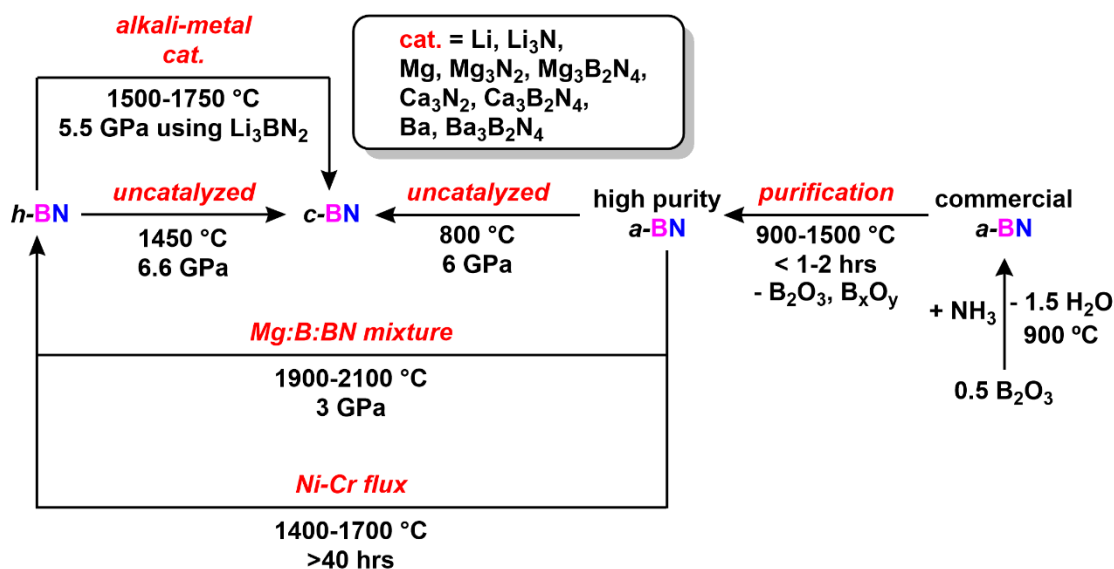
GPa; although it should be noted that the exact conditions and reagents of the original preparation were not reported, only the final properties of *c*-BN were described by Wentorf.¹¹²

To gain an overview of BN synthetic protocols, selected examples of the bulk preparations for crystalline *h*-BN and *c*-BN, along with an industrial route to *a*-BN, are shown in Scheme 1.33.^{109,111} The preparation of crystalline *h*-BN and *c*-BN is necessary for their incorporation in optoelectronics, whereas *a*-BN and microcrystalline BN exhibit large grain sizes with inconsistent roughness that hinders its attractive properties, such as increased thermal conductivity and charge carrier mobilities, and efficient luminescence. In contrast, large single crystals of *h*-BN or *c*-BN feature smooth crystal faces that allow for optimal properties in photovoltaics.^{109,111} Commercially, *a*-BN can be made by a solid-state protocol called the HT-HP (high temperature-high pressure) method using inexpensive reagents, such as B₂O₃ and NH₃.¹¹² If needed, purification of commercial *a*-BN to remove B₂O₃ (and other B_xO_y oxides) at temperatures ranging from 900-1500 °C for short time (1-2 hrs) under Ar can be performed.¹⁰⁹ This purification process can yield high purity *a*-BN.^{109,111} Although annealing of *a*-BN into *c*-BN or *h*-BN may be possible above > 800 °C, it does not produce the well-defined and large-domained crystalline BN material needed for optoelectronics. Furthermore, there are even a few reports of purifying *a*-BN from B_xO_y using extreme temperatures (2000 °C) for 2 hr under dynamic vacuum (exact pressure not specified).^{109,111} The “uncatalyzed” routes shown in Scheme 1.33 are HT-HP methods that have been explored to access *c*-BN from either *a*-BN or *h*-BN.^{109,111}

The motivation behind the development of “catalyzed” routes [including the Ni-Cr flux and a mixture of elemental Mg, B and *a*-BN (Mg:B:BN) methods; see below] shown in Scheme 1.33 is to access large-size (mm-scale), single crystals of either *h*-BN or *c*-BN, which notoriously prefer to form semi-crystalline and/or multi-crystalline materials.^{109,111} In these “catalyzed” methods, a solvent/catalyst, such as alkali metal nitrides, is used that can mediate more controlled nucleation and growth of BN single crystals. These catalysts are often composed of alkali metal nitrides (shown as “cat.” in Scheme 1.33), which in turn leads to long-term safety risks since small amounts of dispersed and heated alkali metal (*e.g.*, lithium or barium) are flammable in air. For this reason, these “catalyzed” methods must be rigorously kept air-free.^{109,111}

To bypass the need for a strict air-free methodology, both transition metal alloys (*e.g.*, Ni-Cr) and less air-sensitive mixtures (*e.g.*, Mg-B-BN mixtures generated from solid Mg, B and BN) have been studied (Scheme 1.33). In the Ni-Cr flux example, Hoffman and co-workers used a mixture of Ni:Cr (53 wt. % Cr) powders in a 1:20 ratio with *a*-BN loaded under N₂ inside a BN crucible. At near ambient pressures (860 Torr), the temperature inside the furnace chamber is ramped up to either 1600 °C or 2000 °C (depending on the batch), then cooled to 1200 °C and held for extended time (< 48 hrs) to generate slowly highly pure, crystalline *h*-BN (40 μM to 5 mm).¹⁰⁹ In the Mg-B-BN system, a mixture of magnesium flakes, amorphous B and *a*-BN were ground together (1:1.2:0.1) inside a boron nitride crucible and heated to 1900-2100 °C under high pressure (3 GPa) for < 2 hrs to produce *h*-BN single crystals, up to 2.5 mm in size.¹⁰⁹ While both of the specified examples produced moderately-sized single crystals of *h*-

BN, optimization of these systems is still underway since they still require higher temperatures than those used in the HT-HP routes ($> 1900\text{ }^{\circ}\text{C}$) and/or prolonged reaction times ($> 40\text{ hrs}$).^{109,111} In addition to the synthetic routes of bulk BN discussed above, explosive shock detonations of *h*-BN (similarly to that used to yield diamond) have been used to induce a phase change into *c*-BN or *w*-BN.¹¹³



Scheme 1.33. Selected examples of routes to bulk crystalline BN forms (*h*-BN or *c*-BN) using *a*-BN as a reagent.

Presently, the largest (mm-sized) and highest purity single crystals of both *h*-BN and *c*-BN are produced by a specific alkali-metal/nitride catalyzed route developed by Taniguchi and Watanabe at the National Institute of Materials Science (Tsukuba, Japan); the resulting batches are in turn shared collaboratively with research laboratories around the world.¹¹⁴ For *h*-BN, their synthetic protocol involves extended annealing (20-80 hrs) of oxide-purified *h*-BN in the presence of $\text{Ba}_3\text{B}_2\text{N}_4$ at temperatures of $1500\text{--}1750\text{ }^{\circ}\text{C}$ with pressures ranging from $4.0\text{--}5.5\text{ GPa}$.¹¹⁴ Similarly,

the growth of large *c*-BN single crystals was reported by Taniguchi and Watanabe using similar reaction conditions with Li_3BN_2 as their catalyst/solvent.¹¹⁴

The development of *h*-BN or *c*-BN thin films is currently underway. The deposition of BN thin films allows access to controlled surfaces that can be used as thermally conductive films or wide band gap semi-conducting layers in transistors. Largely, this field is focused on uncovering lower temperature methods for obtaining high purity BN thin films *via* CVD, which have been reported using expensive instrumentation (see below).^{109,111} For both *h*-BN and *c*-BN thin film deposition, a suitable substrate with a similar lattice structure is often required for the proper nucleation and growth of well-defined BN thin films. In this regard, diamond and/or Si(001) surfaces are often used as substrates since both lattices are nearly identical to that of *c*-BN. Alternatively, the substrate of choice for *h*-BN thin films is often sapphire (Al_2O_3 ; hexagonal).¹⁰⁹

A notable example of *c*-BN film CVD was reported by Bello and co-workers, wherein they used a specific PCVD technique, electron-cyclotron-resonance microwave plasma (ECR-MP) of a He-Ar- N_2 - BF_3 - H_2 gas mixture to yield crystalline *c*-BN thin films ranging from 200 nm to 2 μm .¹¹⁵ Briefly, ECR-MP CVD describes a CVD reactor in which reactant gases (in this case, N_2 , BF_3 , and H_2) are introduced at a constant flow into a heated chamber filled with a high energy plasma (Ar or He) and microwave frequencies (in resonance with electron cyclotron systems; *ca.* 2 GHz) to afford the slow, controlled growth of well-defined thin films. In their investigation, Bello and co-workers used a He/Ar plasma with a 1400 W microwave source at a

reduced pressure of 2×10^{-3} Torr with a constant flow of $\text{N}_2:\text{BF}_3:\text{H}_2$ (1:1:1) at a reactor temperature of 950°C .¹¹⁵ Overall, the lowest reported CVD temperature for crystalline *c*-BN thin films is 430°C using an Ar plasma discharge with a N_2 :elemental B ratio of 1:1 as the reagent gas mixture to yield $1.5\ \mu\text{m}$ -thick films.¹⁰⁹

For the generation of crystalline *h*-BN thin films, a straight-forward example was reported by Lin, Jiang and co-workers, where *ca.* $1\ \mu\text{m}$ -thick films were grown onto sapphire substrates from CVD of NH_3 and BEt_3 at temperatures $> 1300^\circ\text{C}$ and ambient pressures.¹¹⁶ A major disadvantage of this route is the need for the initial CVD of buffer layer of 10-20 nm BN or AlN onto the sapphire substrate at $600\text{-}800^\circ\text{C}$ prior to CVD of the *h*-BN film.¹¹⁶ The lowest reported CVD temperature for accessing crystalline *h*-BN thin films is 850°C , although it should be noted that these films were polycrystalline with a very slow growth rate ($150\ \text{\AA}/\text{hr}$) from NH_3 :elemental B (1:1) mixtures using a high energy electron beam at low pressures (10^{-3} Torr).¹¹⁷ Thus far, CVD methods of *c*-BN or *h*-BN are still limited by the need for high temperatures and/or high pressures, along with the need for substrates with similar lattices or buffer layers (*e.g.*, BN or AlN) for the controlled growth of crystalline BN films.¹⁰⁹

1.5 Thesis Objectives

As noted in the sections pertaining to Si/Ge films or bulk BN syntheses, much of the work in these areas rely on synthetic routes that can be harsh, both in terms of the temperatures and/or pressures required, as well as risks associated with handling of corrosive starting materials (*e.g.*, BF_3). Since FLPs can mediate a variety of chemical

transformations (*e.g.*, dehydrocoupling, hydrogen transfer), the integration of FLPs as precursors in materials chemistry should be explored to lower the need for harsh conditions by using easier-to-handle FLP-based precursors. In addition, FLP-main group element complexes have been largely unexplored thus far, as the focus of FLPs has historically been centered on the catalysis of organic substrates. The main objective in this Thesis is to demonstrate that FLPs can be used as suitable ligands for the stabilization of fundamentally valuable main group element moieties, with subsequent low temperature deposition of industrially relevant materials. Specifically, Chapter 2 in this Thesis outlines the isolation of FLP-Group 14 element complexes, which can deposit semi-conducting Si or Ge films at low (< 110 °C) temperatures. Subsequently, Chapter 3 describes the access to rare main group element moieties (such as HBNH) using phosphine-borane FLPs. Finally, the work in Chapter 4 reports the unexpected ligand activation that may occur in intramolecular phosphine-borane FLP-methylene complexes, as well as new modified ligand backbones for the future development of FLP main group element complexes.

1.6 References

1. R. West, *Polyhedron* **2002**, *21*, 467–472.
2. T. J. Hadlington, M. Driess, C. Jones, *Chem. Soc. Rev.* **2018**, *47*, 4176–4197.
3. P. W. N. M. van Leeuwen, ed., *Homogeneous Catalysis*, 1st ed. (Internet Version, Springer Science and Business, Dordrecht, The Netherlands, **2004**).
4. P. Kalck, C. Le Berre, P. Serp, *Coord. Chem. Rev.* **2020**, *402*, 213078 and references therein.
5. P. P. Power, *Nature* **2010**, *463*, 171–177.
6. P. Jutzi, *Angew. Chem. Int. Ed. Engl.* **1975**, *14*, 232–245.
7. P. J. Davidson, M. F. Lappert, *J. Chem. Soc., Chem. Commun.* **1973**, 317a.
8. A. G. Brook, F. Abdesaken, B. Gutekunst, G. Gutekunst, R. K. Kallury, *J. Chem. Soc., Chem. Commun.* **1981**, 191–192.
9. a) R. West, M. J. Fink, J. Michl, *Science* **1981**, *214*, 1343–1344; b) M. J. Fink, M. J. Michalczyk, K. J. Haller, R. West, J. Michl, *J. Chem. Soc., Chem. Commun.* **1983**, 1010–1011.
10. M. Yoshifuji, I. Shima, N. Inamoto, K. Hirotsu, T. Higuchi, *J. Am. Chem. Soc.* **1981**, *103*, 4587–4589.
11. J.-E. Siewert, A. Schumann, C. Hering-Junghans, *Dalton Trans.* **2021**, *50*, 15111–15117.
12. P. Jutzi, D. Kanne, C. Krüger, *Angew. Chem. Int. Ed. Engl.* **1986**, *25*, 164.
13. D. J. Liptrot, P. P. Power, *Nat. Rev. Chem.* **2017**, *1*, 0004.
14. F. S. Kipping, J. E. Sands, *J. Chem. Soc., Trans.* **1921**, *119*, 830–847.

15. a) A. G. Moiseev, W. J. Leigh, *Organometallics* **2007**, *26*, 6268–6276; b) A. G. Moiseev, W. J. Leigh, *Organometallics* **2007**, *26*, 6277–6289.
16. R. C. Fischer, P. P. Power, *Chem. Rev.* **2010**, *110*, 3877–3923.
17. H. B. Wedler, P. Wendelboe, P. P. Power, *Organometallics* **2018**, *37*, 2929–2936.
18. a) M. Driess, H. Grützmacher, *Angew. Chem. Int. Ed. Engl.* **1996**, *35*, 828–856 and references therein; b) Y. Apeloig, R. Pauncz, M. Karni, R. West, W. Steiner, D. Chapman, *Organometallics* **2003**, *22*, 3250–3256.
19. S. Fujimori, S. Inoue, *Eur. J. Inorg. Chem.* **2020**, 3131–3142.
20. a) R. Fornari, *Handbook of Crystal Growth: Thin Films and Epitaxy*; T. Kauch, Ed.; Elsevier B. V.; Amsterdam, The Netherlands, **2015**, *3*, 1–49; b) H. Ibach, H. Lüth, eds., *Solid-State Physics: An Introduction to Principles for Materials Science*, 4th ed. (Internet Version, Springer-Verlag Berlin, Heidelberg, **2009**).
21. a) L. Andrews, X. Wang, *J. Phys. Chem. A* **2002**, *106*, 7696–7702; b) X. Wang, L. Andrews, G. P. Kushto, *J. Phys. Chem. A* **2002**, *106*, 5809–5816.
22. E. Rivard, *Dalton Trans.* **2014**, *43*, 8577–8586.
23. M. J. S. Gynane, D. H. Harris, M. F. Lappert, P. P. Power, P. Rivière, M. Rivière-Baudet, *J. Chem. Soc., Dalton Trans.* **1977**, 2004–2009.
24. a) V. Nesterov, D. Reiter, P. Bag, P. Frisch, R. Holtzner, A. Porzelt, S. Inoue, *Chem. Rev.* **2018**, *118*, 9678–9842; b) M. Melaimi, R. Jazzar, M. Soleilhavoup, G. Bertrand, *Angew. Chem. Int. Ed.* **2017**, *56*, 10046–10068.

25. a) Y. Wang, Y. Xie, P. Wei, R. B. King, H. F. Schaefer III, P. v. R. Schleyer, G. H. Robinson, *Science* **2008**, *321*, 1069–1071; b) A. Sidiropoulos, C. Jones, A. Stasch, S. Klein, G. Frenking, *Angew. Chem. Int. Ed.* **2009**, *48*, 9701–9704.
26. C. Jones, *Nat. Rev. Chem.* **2017**, *1*, 0059.
27. a) S. Yao, Y. Xiong, A. Saddington, M. Driess, *Chem. Commun.* **2021**, *57*, 10139–10153 and references therein; b) J. Xu, S. Pan, S. Yao, G. Frenking, M. Driess, *Angew. Chem. Int. Ed.* **2022**, e202209442.
28. M. Denk, R. Lennon, R. Hayashi, R. West, A. V. Belyakov, H. P. Verne, A. Haaland, M. Wagner, N. Metzler, *J. Am. Chem. Soc.* **1994**, *116*, 2691–2692.
29. a) R. S. Ghadwal, H. W. Roesky, S. Merkel, J. Henn, D. Stalke, *Angew. Chem. Int. Ed.* **2009**, *48*, 5683–5686; b) A. C. Filippou, O. Chernov, G. Schnakenburg, *Angew. Chem. Int. Ed.* **2009**, *48*, 5687–5690; c) M. M. D. Roy, S. R. Baird, E. Dornsiepen, L. A. Paul, L. Miao, M. J. Ferguson, Y. Zhou, I. Siewert, E. Rivard, *Chem. Eur. J.* **2021**, *27*, 8572–8579.
30. a) F. Meyer-Wegner, A. Nadj, M. Bolte, N. Auner, M. Wagner, M. C. Holthausen, H.-W. Lerner, *Chem. Eur. J.* **2011**, *17*, 4715–4719; b) J. I. Schweizer, A. G. Sturm, T. Porsch, M. Berger, M. Bolte, N. Auner, M. C. Holthausen, *Z. Anorg. Allg. Chem.* **2018**, *644*, 982–988; c) R. S. Ghadwal, K. Pröpper, B. Dittrich, P. G. Jones, H. W. Roesky, *Inorg. Chem.* **2011**, *50*, 358–364.
31. M. M. D. Roy, A. A. Omaña, A. S. S. Wilson, M. S. Hill, S. Aldridge, E. Rivard, *Chem. Rev.* **2021**, *121*, 12784–12965.

32. S. M. I. Al-Rafia, A. C. Malcolm, R. McDonald, M. J. Ferguson, E. Rivard, *Chem. Commun.* **2012**, *48*, 1308–1310.
33. S. M. I. Al-Rafia, A. C. Malcolm, R. McDonald, M. J. Ferguson, E. Rivard, *Angew. Chem. Int. Ed.* **2011**, *50*, 8354–8357.
34. a) A. V. Protchenko, K. H. Birj Kumar, D. Dange, A. D. Schwarz, D. Vidovic, C. Jones, N. Kaltsoyannis, P. Mountford, S. Aldridge, *J. Am. Chem. Soc.* **2012**, *134*, 6500–6503; b) B. D. Reken, T. M. Brown, J. C. Fettinger, H. M. Tuononen, P. P. Power, *J. Am. Chem. Soc.* **2012**, *134*, 6504–6507; c) D. Wendel, A. Porzelt, F. A. D. Herz, D. Sarkar, C. Jandl, S. Inoue, B. Rieger, *J. Am. Chem. Soc.* **2017**, *139*, 8134–8137; d) R. Holzner, D. Reiter, P. Frisch, S. Inoue, *RSC Adv.* **2020**, *10*, 3402–3406; e) A. V. Protchenko, A. D. Schwarz, M. P. Blake, C. Jones, N. Kaltsoyannis, P. Mountford, S. Aldridge, *Angew. Chem. Int. Ed.* **2013**, *52*, 568–571.
35. a) A. Meltzer, S. Inoue, C. Präsang, M. Driess, *J. Am. Chem. Soc.* **2010**, *132*, 3038–3046; b) M. Y. Abraham, Y. Wang, Y. Xie, P. Wei, H. F. Schaefer III, P. v. R. Schleyer, G. H. Robinson, *J. Am. Chem. Soc.* **2011**, *133*, 8874–8876; c) M. Stoelzel, C. Präsang, S. Inoue, S. Enthaler, M. Driess, *Angew. Chem. Int. Ed.* **2012**, *51*, 399–403.
36. a) Y. Ding, H. Hao, H. W. Roesky, M. Noltemeyer, H.-G. Schmidt, *Organometallics* **2001**, *20*, 4806–4811; b) L. W. Pineda, V. Jancik, K. Starke, R. B. Oswald, H. W. Roesky, H. W. *Angew. Chem. Int. Ed.* **2006**, *45*, 2602–2605; c) Y. Peng, J.-D. Guo, B. D. Ellis, Z. Zhu, J. C. Fettinger, S. Nagase, P. P. Power, *J. Am. Chem. Soc.* **2009**, *131*, 16272–16282; d) S. M. I. Al-Rafia, P. A. Lummis, M. J. Ferguson, R. McDonald, E. Rivard, *Inorg. Chem.* **2010**, *49*, 9709–9717; e) S. K. Liew, S. M. I. Al-Rafia, J. T.

Goettel, P. A. Lummis, S. M. McDonald, L. J. Miedema, M. J. Ferguson, R. McDonald, E. Rivard, *Inorg. Chem.* **2012**, *51*, 5471–5480; f) M. W. Lui, C. Merten, M. J. Ferguson, R. McDonald, Y. Xu, E. Rivard, *Inorg. Chem.* **2015**, *54*, 2040–2049; g) T. J. Hadlington, B. Schwarze, E. I. Izgorodina, C. Jones, *Chem. Commun.* **2015**, *51*, 6854–6857; h) C. Hering-Junghans, P. Andreiuk, M. J. Ferguson, R. McDonald, E. Rivard, *Angew. Chem. Int. Ed.* **2017**, *56*, 6272–6275; i) J. Tremmel, J. Tydlitát, L. Dostál, A. Ružička, X. Deraet, J. Turek, R. Jambor, *Chem. Eur. J.* **2020**, *26*, 6070–6075.

37. J. Sinclair, W. Medroa del Pino, K. Aku-Dominguez, Y. Minami, A. Kiran, M. J. Ferguson, M. Yasuda, E. Rivard, *Dalton Trans.* **2021**, *51*, 17688–17696.

38. J. Schneider, C. P. Sindlinger, K. Eichele, H. Schubert, L. Wesemann, *J. Am. Chem. Soc.* **2017**, *139*, 6542–6545.

39. a) R. Rodriguez, Y. Contie, R. Nougúé, A. Baceiredo, N. Saffon-Merceron, J. M. Sotiropoulos, T. Kato, T. *Angew. Chem. Int. Ed.* **2016**, *55*, 14355–14358; b) R. Rodriguez, D. Gau, Y. Contie, T. Kato, N. Saffon-Merceron, A. Baceiredo, *Angew. Chem. Int. Ed.* **2011**, *50*, 11492–11495.

40. a) L. Zhao, M. Hermann, C. Jones, G. Frenking, *Chem. Eur. J.* **2016**, *22*, 11728–11735; b) T. J. Hadlington, M. Hermann, G. Frenking, C. Jones, *Chem. Sci.* **2015**, *6*, 7249–7257.

41. T. J. Hadlington, M. Hermann, G. Frenking, C. Jones, *J. Am. Chem. Soc.* **2014**, *136*, 3028–3031.

42. J. Li, C. Schenk, C. Goedecke, G. Frenking, C. Jones, *J. Am. Chem. Soc.* **2011**, *133*, 18622–18625.

43. T. J. Hadlington, M. Hermann, J. Li, G. Frenking, C. Jones, *Angew. Chem. Int. Ed.* **2013**, *52*, 10199–10203.
44. J. Schneider, C. P. Sindlinger, S. M. Freitag, H. Schubert, L. Wesemann, *Angew. Chem. Int. Ed.* **2017**, *56*, 333–337.
45. a) B.-X. Leong, J. Lee, Y. Li, M.-C. Yang, C.-K. Siu, M.-D. Su, C.-W. So, *J. Am. Chem. Soc.* **2019**, *141*, 17629–17636; b) V. S. V. S. N. Swamy, M. K. Bisai, T. Das, S. S. Sen, *Chem. Commun.* **2017**, *53*, 6910–6913.
46. For selected articles on molecular frustrated Lewis pairs (FLPs), see: a) D. W. Stephan, G. Erker, *Angew. Chem. Int. Ed.* **2010**, *49*, 46–76; b) D. W. Stephan, G. Erker, *Angew. Chem. Int. Ed.* **2015**, *54*, 6400–6441; c) D. W. Stephan, *Science* **2016**, *354*, aaf7229; d) F.-G. Fontaine, D. W. Stephan, *Phil. Trans. R. Soc. A.* **2017**, *375*, 20170004; e) D. W. Stephan, *J. Am. Chem. Soc.* **2021**, *143*, 20002–20014 and references therein.
47. G. C. Welch, R. R. San Juan, J. D. Masuda, D. W. Stephan, *Science* **2006**, *314*, 1124–1126.
48. a) W. E. Piers, T. Chivers, *Chem. Soc. Rev.* **1997**, *26*, 345–354; b) G. Erker, *Dalton Trans.* **2005**, 1883–1890; c) J. R. Lawson, R. L. Melen, *Inorg. Chem.* **2017**, *56*, 8627–8643.
49. For selected articles on one-electron transfer involving FLPs: a) L. L. Liu, L. L. Cao, Y. Shao, G. Ménard, D. W. Stephan, *Chem.* **2017**, *3*, 259–267; b) F. Holtrop, A. R. Jupp, B. J. Kooij, N. P. van Leest, B. de Bruin, J. C. Slootweg, *Angew. Chem. Int. Ed.* **2020**, *59*, 22210–22216; c) F. Holtrop, A. R. Jupp, N. P. Van Leest, M. Paradiz

Dominguez, R. M. Williams, A. M. Brouwer, B. De Bruin, A. W. Ehlers, J. C. Slootweg, *Chem. Eur. J.* **2020**, *26*, 9005–9011; d) Y. Soltani, A. Dasgupta, T. A. Gazis, D. M. C. Ould, E. Richards, B. Slater, K. Stefkova, V. Y. Vladimirov, L. C. Wilkins, D. Wilcox, R. L. Melen, *Cell Rep. Phys. Chem.* **2020**, *1*, 10016; e) A. Dasgupta, E. Richards, R. L. Melen, *Angew. Chem. Int. Ed.* **2021**, *60*, 53–65; f) A. Merk, H. Großekappenberg, M. Schmidtman, M.-P. Luecke, C. Lorent, M. Driess, M. Oestreich, H. F. T. Klare, T. Müller, *Angew. Chem. Int. Ed.* **2018**, *57*, 15267–15271.

50. a) M. Wang, F. Nudelman, R. R. Matthes, M. P. Shaver, *J. Am. Chem. Soc.* **2017**, *139*, 14232–14236; b) L. Chen, R. Liu, Q. Yan, *Angew. Chem. Int. Ed.* **2018**, *57*, 9336–9340; c) L. Chen, R. Liu, X. Hao, Q. Yan, *Angew. Chem. Int. Ed.* **2019**, *58*, 264–268; d) U. Yolsal, M. Wang, J. R. Royer, M. P. Shaver, *Macromolecules* **2019**, *52*, 3417–3425; e) B. Adelizzi, P. Chidchob, N. Tanaka, B. A. G. Lamers, S. C. J. Meskers, S. Ogi, A. R. A. Palmans, S. Yamaguchi, E. W. Meijer, *J. Am. Chem. Soc.* **2020**, *142*, 16681–16689; f) U. Yolsal, T. A. R. Horton, M. Wang, M. P. Shaver, *J. Am. Chem. Soc.* **2021**, *143*, 12980–12984; g) T. A. R. Horton, M. Wang, M. P. Shaver, *Chem. Sci.* **2022**, *13*, 3845–3850.

51. For selected articles on FLP-containing nanomaterials: a) J. L. Fiorio, R. V. Gonçalves, E. Teixeira-Neto, M. A. Ortuño, N. López, L. M. Rossi, *ACS Catal.* **2018**, *8*, 3516–3524; b) K. Mentoer, L. Twigge, J. W. H. Niemantsverdriet, J. C. Swarts, E. Erasmus, *Inorg. Chem.* **2021**, *60*, 55–69; c) A. Palazzolo, S. Carencio, *Chem. Mater.* **2021**, *33*, 7914–7922. For selected articles on surface-bound FLPs: d) H. Lee, Y. M. Choi, D.-W. Lim, M. M. Rahman, Y.-I. Kim, I. H. Cho, H. W. Kang, J.-H. Seo, C. Jeon,

K. B. Yoon, *Angew. Chem. Int. Ed.* **2015**, *54*, 13080–13084; e) K. C. Szeto, W. Sahyoun, N. Merle, J. L. Castelbou, N. Popoff, F. Lefebvre, J. Raynaud, C. Godard, C. Claver, L. Delevoye, R. M. Gauvin, M. Taoufik, *Catal. Sci. Technol.* **2016**, *6*, 882–889; f) J.-Y. Xing, J.-C. Buffet, N. H. Rees, P. Nørby, D. O’Hare, *Chem. Commun.* **2016**, *52*, 10478–10481; g) J. L. Fiorio, N. López, L. M. Rossi, *ACS Catal.* **2017**, *7*, 2973–2980.

52. a) J. Bauer, H. Braunschweig, R. D. Dewhurst, K. Radacki, *Chem. Eur. J.* **2013**, *19*, 8797–8805; b) Y. Jiang, O. Blacque, T. Fox, H. Berke, *J. Am. Chem. Soc.* **2013**, *135*, 7751–7760; c) S. J. K. Forrest, J. Clifton, N. Fey, P. G. Pringle, H. A. Sparkes, D. F. Wass, *Angew. Chem. Int. Ed.* **2015**, *54*, 2223–2227; d) J. Campos, *J. Am. Chem. Soc.* **2017**, *139*, 2944–2947; e) N. Hidalgo, J. J. Moreno, M. Pérez-Jiménez, C. Maya, J. López-Serrano, J. Campos, *Organometallics* **2020**, *39*, 2534–3544; f) N. Hidalgo, J. J. Moreno, M. Pérez-Jiménez, C. Maya, J. López-Serrano, J. Campos, *Chem. Eur. J.* **2020**, *26*, 5982–5993; g) H. Tinnermann, C. Fraser, R. D. Young, *Dalton Trans.* **2020**, *49*, 15184–15189; h) E. S. Osipova, E. S. Gulyaeva, E. I. Gutsul, V. A. Kirkina, A. A. Pavlov, Y. V. Nelyubina, A. Rossin, M. Peruzzini, L. M. Epstein, N. V. Belkova, O. A. Filippov, E. S. Shubina, *Chem. Sci.* **2021**, *12*, 3682–3692.

53. X. Sun, W. Su, K. Shi, Z. Xie, C. Zhu, *Chem. Eur. J.* **2020**, *26*, 5354–5359.

54. a) J. T. O’Brien, E. R. Williams, *J. Phys. Chem. A.* **2011**, *115*, 14612–14619; b) H. Ohtaki, T. Radnai, *Chem. Rev.* **1993**, *93*, 1157–1204.

55. a) T. V. O’Halloran, *Science* **1993**, *261*, 715–725; b) A. M. Pyle, *J. Biol. Inorg. Chem.* **2002**, *7*, 679–690.

56. a) R. W. Schaeffer, B. C. Chan, S. R. Marshall, B. Blasiolo, N. Khan, K. L. Yoder, M. E. Trainer, C. H. Yoder, *J. Chem. Educ.* **2000**, *77*, 509–510; b) R. Barlag, F. Nyasulu, *J. Chem. Educ.* **2011**, *88*, 643–645.
57. A. Staubitz, A. P. M. Robertson, M. E. Sloan, I. Manners, *Chem. Rev.* **2010**, *110*, 4023–4078 and references therein.
58. E. Vedejs, *Science* **1980**, *207*, 42–44.
59. H. C. Brown, H. I. Schlesinger, S. Z. Cardon, *J. Am. Chem. Soc.* **1942**, *64*, 325–329.
60. G. Wittig, E. Benz, *Chem. Ber.* **1959**, *92*, 1999–2013.
61. a) D. J. Parks, W. E. Piers, *J. Am. Chem. Soc.* **1996**, *118*, 9440–9441; b) S. Rendler, M. Oestreich, *Angew. Chem. Int. Ed.* **2008**, *47*, 5997–6000.
62. J. R. Rumble, ed., *CRC Handbook of Chemistry and Physics*, 100th ed. (Internet Version, CRC Press/Taylor & Francis, Boca Raton, Florida, **2019**).
63. a) A. Moroz, R. L. Sweany, *Inorg. Chem.* **1992**, *31*, 5236–5242; b) H.-J. Himmel, J. Vollet, *Organometallics* **2002**, *21*, 5972–9577; c) Z. L. Xiao, R. H. Hauge, J. L. Margrave, *Inorg. Chem.* **1993**, *32*, 642–646.
64. A. J. M. Miller, J. E. Bercaw, *Chem. Commun.* **2010**, *46*, 1709–1711.
65. G. R. Whittell, E. I. Balmond, A. P. M. Robertson, S. K. Patra, M. F. Haddow, I. Manners, *Eur. J. Inorg. Chem.* **2010**, 3967–3975.
66. D. W. Stephan, G. Erker, *Angew. Chem. Int. Ed.* **2009**, *49*, 46–76.
67. C. Appelt, J. C. Slootweg, K. Lammertsma, W. Uhl, *Angew. Chem. Int. Ed.* **2013**, *52*, 4256–4259.

68. Z. Mo, A. Rit, J. Campos, E. L. Kolychev, S. Aldridge, *J. Am. Chem. Soc.* **2016**, *138*, 3306–3309.
69. M. Boudjelel, E. D. Sosa-Carrizo, S. Mallet-Ladeira, S. Massou, K. Miqueu, G. Bouhadir, D. Bourissou, *ACS Catal.* **2018**, *8*, 4459–4464.
70. C. P. Sindlinger, F. S. W. Aicher, H. Schubert, L. Wesemann, *Angew. Chem. Int. Ed.* **2017**, *56*, 2198–2202.
71. S. Li, G. Li, W. Meng, H. Du, *J. Am. Chem. Soc.* **2016**, *138*, 12956–12962.
72. N. Kumar, J. Rani, R. Kurchania, *Mater. Today: Proc.* **2021**, *46*, 5570–5574.
73. a) H. Min, D. Y. Lee, J. Kim, G. Kim, K. S. Lee, J. Kim, M. J. Paik, Y. K. Kim, K. S. Kim, M. G. Kim, T. J. Shin, S. Il Seok, *Nature* **2021**, *598*, 444–450; b) National Renewable Energy Laboratory Energy Efficiencies Chart (as of August 2022): <https://www.nrel.gov/pv/assets/pdfs/best-research-cell-efficiencies-rev220630.pdf>
74. a) J. Czochralski, *Z. Phys. Chem.* **1918**, *92*, 219–221; b) J. Evers, P. Klüfers, R. Staudigl, P. Stallhofer, *Angew. Chem. Int. Ed.* **2003**, *42*, 5684–5698.
75. U. J. Gibson, L. Wei, J. Ballato, *Nat. Commun.* **2021**, *12*, 3990.
76. L. Sun, G. Yuan, L. Gao, J. Yang, M. Chhowalla, M. H. Gharahcheshmeh, K. K. Gleason, Y. S. Choi, B. H. Hong, Z. Liu, *Nat. Rev. Methods Primers* **2021**, *1*, 5.
77. R. Gordon, *J. Non-Cryst. Solids* **1997**, *218*, 81–91.
78. a) J. Bloem, W. A. P. Claassen, W. G. J. N. Valkenburg, *J. Cryst. Growth* **1982**, *57*, 177–184; b) R. C. Taylor, B. A. Scott, S.-T. Lin, F. LeGoues, J. C. Tsang, *MRS Online Proceedings Library* **1986**, *77*, 709–714; c) W. A. P. Claassen, J. Bloem, *J. Cryst.*

Growth **1980**, *50*, 807–815; d) Y. Ron, A. Raveh, U. Carmi, A. Inspektor, A. Avni, *Thin Solid Films* **1983**, *107*, 181–189.

79. a) K. Toshikawa, A. Yokotani, K. Kurosawa, *Jpn. J. Appl. Phys.* **2005**, *44*, 7785–7788; b) D. E. Carlson, C. R. Wronski, *Appl. Phys. Lett.* **1976**, *28*, 671–673; c) N. Herlin, M. Lefebvre, M. Péalat, J. Perrin, *J. Phys. Chem.* **1992**, *96*, 7063–7072; d) S. M. Han, E. S. Aydil, *J. Vac. Sci. Technol.* **1996**, *14*, 2062–2070; e) R. Kakkad, J. Smith, W. S. Lau, S. J. Fonash, R. Kerns, *J. Appl. Phys.* **1989**, *65*, 2069–2072.

80. Y. Mishima, M. Hirose, Y. Osaka, K. Nagamine, Y. Ashida, N. Kitagawa, K. Isogaya, *Jpn. J. Appl. Phys.* **1983**, *22*, L46–L48.

81. a) H. Kanoh, O. Sugaira, M. Matsumura, *Jpn. J. Appl. Phys.* **1993**, *32*, 2613–2619; b) T. Shimoda, Y. Matsuki, M. Furusawa, T. Aoki, I. Yudasaka, H. Tanaka, H. Iwasawa, D. Wang, M. Miyasaka, Y. Takeuchi, *Nature* **2006**, *440*, 783–786; c) M. Gerwig, A. S. Ali, D. Neubert, S. Polster, U. Böhme, G. Franze, M. Rosenkranz, A. Popov, I. Ponomarev, M. P. M. Jank, C. Viehweger, E. Brendler, L. Frey, P. Kroll, E. Kroke, *Adv. Electron. Mater.* **2021**, *7*, 2000422; d) M. Gerwig, U. Böhme, M. Friebe, F. Gründler, G. Franze, M. Rosenkranz, H. Schmidt, E. Kroke, *ChemistryOpen* **2020**, *9*, 762–773 and references therein; e) G. R. S. Iyer, E. K. Hobbie, S. Guruvenket, J. M. Hoey, K. J. Anderson, J. Lovaasen, C. Gette, D. L. Schulz, O. F. Swenson, A. Elangovan, P. Boudjouk, *ACS Appl. Mater. Interfaces* **2012**, *4*, 2680–2685.

82. a) A. Grill, V. Patel, *J. Appl. Phys.* **1999**, *85*, 3314–3318; b) S. Guruvenket, S. Andrie, M. Simon, K. W. Johnson, R. A. Sailer, *Plasma Process. Polym.* **2011**, *8*, 1126–1136; c) J. Dahlhaus, P. Jutzi, H.-J. Frenck, W. Kulisch, *Adv. Mater.* **1993**, *5*, 377–380;

- d) A. Klipp, F. Hamelmann, G. Haindl, J. Hartwich, U. Kleineberg, P. Jutzi, U. Heinzmann, *Chem. Vap. Deposition* **2000**, *6*, 63–66; e) A. Klipp, S. H. A. Petri, B. Neumann, H.-G. Stammler, P. Jutzi, *J. Organomet. Chem.* **2001**, *620*, 20–31.
83. K. Fujino, Y. Nishimoto, N. Tokumasu, K. Maeda, *J. Electrochem. Soc.* **1990**, *137*, 2883–2887.
84. a) H. G. Pryce Lewis, T. B. Casserly, K. K. Gleason, *J. Electrochem. Soc.* **2001**, *148*, F212–F220; b) V. Raballand, J. Benedikt, S. Hoffmann, M. Zimmermann, A. von Keudell, *J. Appl. Phys.* **2009**, *105*, 083304.
85. a) C. Winkler, *J. Prakt. Chem.* **1887**, *36*, 177–209; b) E. Voegelen, *Z. Anorg. Chem.* **1902**, *30*, 325–330.
86. a) H. Ishii, Y. Takahashi, *J. Electrochem. Sci.* **1988**, *135*, 1539–1543; b) D. T. Restrepo, K. E. Lynch, K. Giesler, S. M. Kuebler, R. G. Blair, *Mater. Res. Bull.* **2012**, *47*, 3484–3488; c) J.-S. Park, M. Curtin, C. Major, S. Bengtson, M. Carroll, A. Lochtefeld, *Electrochem. Solid-State Lett.* **2007**, *10*, H313–H316; d) J. Satgé, M. Massol, P. Rivière, *J. Organomet. Chem.* **1973**, *56*, 1–39; e) G. Jonkers, S. M. Van der Kerk, C. A. De Lange, *Chem. Phys.* **1982**, *70*, 69–75.
87. a) E. Muthuswamy, A. S. Iskandar, M. M. Amador, S. M. Kauzlarich, *Chem. Mater.* **2013**, *25*, 1416–1422; b) K. Tabatabaei, A. L. Holmes, K. A. Newton, E. Muthuswamy, R. Sfadia, S. A. Carter, S. M. Kauzlarich, *Chem. Mater.* **2019**, *31*, 7510–7521.
88. a) Z. Meng, Z. Jin, B. A. Gururaj, P. Chu, H. S. Kwok, M. Wong, *J. Electrochem. Soc.* **1997**, *144*, 1423–1429; b) V. Sorianello, L. Colace, N. Armani, F. Rossi, C. Ferrari, C. Lazzarini, L. Lazzarini, G. Assanto, *Opt. Mater. Express* **2011**, *1*, 856–865; c) G.

Dushaq, M. Rasras, A. Nayfeh, *Thin Solid Films* **2017**, *636*, 585–592; d) F. Gencarelli, B. Vincent, L. Souriau, O. Richard, W. Vandervorst, R. Loo, M. Caymax, M. Heyns, *Thin Solid Films* **2012**, *520*, 3211–3215; e) J. Pola, J. P. Parsons, R. Taylor, *J. Chem. Soc., Faraday Trans.* **1992**, *88*, 1637–1641.

89. a) M. Jakoubová, Z. Bastl, P. Fiedler, J. Pola, *Infrared. Phys. Technol.* **1994**, *35*, 633–635; b) J. E. Boucham, F. Maury, R. Morancho, *J. Anal. Appl. Pyrol.* **1997**, *44*, 153–165; c) P. G. Harrison, C. de Cointet, D. Ograb, D. M. Podesta, *Chem. Mater.* **1994**, *6*, 1620–1626; d) K. Suda, T. Kijima, S. Ishihara, N. Sawamoto, H. Machida, M. Ishikawa, H. Sudoh, Y. Ohsita, A. Ogura, *ECS J. Solid State Sci. Technol.* **2015**, *4*, P152–P154; e) R. Fritzsche, D. R. Zahn, M. Mehring, *J. Mater. Sci.* **2021**, *56*, 9274–9286; f) K. Ditmar, P. Jutzi, J. Schmalhorst, G. Reiss, *Chem. Vap. Deposition* **2001**, *7*, 193–195; g) J. E. Taylor, T. S. Milazzo, *J. Phys. Chem.* **1978**, *82*, 847–852.

90. J. Sinclair, G. Dai, R. McDonald, M. J. Ferguson, A. Brown, E. Rivard, *Inorg. Chem.* **2020**, *59*, 10996–11008.

91. a) E. M. Leitao, T. Jurca, I. Manners, *Nat. Chem.* **2013**, *5*, 817–829 and references therein; b) T. M. Douglas, A. B. Chaplin, A. S. Weller, *J. Am. Chem. Soc.* **2018**, *130*, 14432–14433.

92. Y. Zhang, M. A. Hopkins, D. J. Liptrot, H. Khanbareh, P. Groen, X. Zhou, D. Zhang, Y. Bao, K. Zhou, C. R. Bowen, D. R. Carbery, *Angew. Chem. Int. Ed.* **2020**, *59*, 7808–7812.

93. a) W. Luo, P. G. Campbell, L. N. Zakharov, S.-Y. Liu, *J. Am. Chem. Soc.* **2011**, *133*, 19326–19329; b) C. W. Yoon, L. G. Sneddon, *J. Am. Chem. Soc.* **2006**, *128*,

13992–13993; c) W. Luo, L. N. Zakharov, S.-Y. Liu, *J. Am. Chem. Soc.* **2011**, *133*, 13006–13009; d) G. Chen, L. N. Zakharov, M. E. Bowden, A. J. Karkamkar, S. M. Whittemore, E. B. III, Garner, T. C. Mikulas, D. A. Dixon, T. Autrey, S.-Y. Liu, *J. Am. Chem. Soc.* **2015**, *137*, 134–137; e) Y. Dai, X. Zhang, Y. Liu, H. Yu, W. Su, J. Zhou, Q. Ye, Z. Huang, *J. Am. Chem. Soc.* **2022**, *144*, 8434–8438.

94. a) C. A. Jaska, K. Temple, I. Manners, *Chem. Commun.* **2001**, 962–963; b) C. A. Jaska, K. Temple, I. Manners, *J. Am. Chem. Soc.* **2003**, *125*, 9424–9434; c) C. A. Jaska, I. Manners, *J. Am. Chem. Soc.* **2004**, *126*, 9776–9785; d) M. C. Denney, V. Pons, T. J. Hebden, D. M. Heinekey, K. I. Goldberg, *J. Am. Chem. Soc.* **2006**, *128*, 12048–12049; e) A. Staubitz, A. P. Soto, I. Manners, *Angew. Chem. Int. Ed.* **2008**, *47*, 6212–6215; f) A. Staubitz, M. E. Sloan, A. P. M. Robertson, A. Friedrich, S. Schneider, P. J. Gates, J. R. Schmedt auf der Günne, I. Manners, *J. Am. Chem. Soc.* **2010**, *132*, 13332–13345.

95. A. P. M. Robertson, E. M. Leitao, I. Manners, *J. Am. Chem. Soc.* **2011**, *133*, 19322–19325.

96. a) C. A. De Albuquerque Pinheiro, C. Roiland, P. Jehan, G. Alcaraz, *Angew. Chem. Int. Ed.* **2018**, *57*, 1519–1522; b) A. Staubitz, *Angew. Chem. Int. Ed.* **2018**, *57*, 5990–5992.

97. a) A. Paul, C. B. Musgrave, *Angew. Chem. Int. Ed.* **2007**, *46*, 8153–8156; b) M. E. Sloan, A. Staubitz, T. J. Clark, C. A. Russell, G. C. Lloyd-Jones, I. Manners, *J. Am. Chem. Soc.* **2010**, *132*, 3831–3841; c) I. Göttker-Schnetmann, P. S. White, M. Brookhart, *Organometallics* **2004**, *23*, 1766–1776; d) Y. Luo, K. Ohno, *Organometallics* **2007**, *26*, 3597–3600.

98. C. N. Brodie, T. M. Boyd, L. Sotorríos, D. E. Ryan, E. Magee, S. Huband, J. S. Town, G. C. Lloyd-Jones, D. M. Haddleton, S. A. Macgregor, A. S. Weller, *J. Am. Chem. Soc.* **2021**, *143*, 21010–21023.
99. I. Amer, A. Van Reenen, T. Mokrani, *Mater. Sci.* **2016**, *22*, 381–389 and references therein.
100. V. A. Du, T. Jurca, G. R. Whittell, I. Manners, *Dalton Trans.* **2016**, *45*, 1055–1062.
101. S. Bernard, P. Miele, *Materials* **2014**, *7*, 7436–7459 and references therein.
102. a) P. B. Mirkarimi, K. F. McCarty, D. L. Medlin, *Mater. Sci. Eng.* **1997**, *R21*, 47–100 and references therein; b) A. V. Kurdyumov, V. L. Solozhenko, W. B. Zelyavski, *J. Appl. Cryst.* **1995**, *28*, 540–545.
103. Z. Zheng, M. Cox, B. Li, *J. Mater. Sci.* **2018**, *53*, 66–99 and references therein.
104. H. Pedersen, B. Alling, H. Högberg, A. Ektarawong, *J. Vac. Sci. Tech. A* **2019**, *37*, 040603.
105. A. Pakdel, Y. Bando, D. Golberg, *Chem. Soc. Rev.* **2014**, *43*, 934–959.
106. R. Riedel, *Adv. Mater.* **1994**, *6*, 549–560.
107. F. P. Bundy, W. A. Bassett, M. S. Weathers, R. J. Hemley, H. U. Mao, A. F. Concharov, *Carbon* **1996**, *34*, 141–153.
108. a) P. S. DeCarli, J. C. Jamieson, *Science* **1961**, *133*, 1821–1822; b) S. J. Turneaure, S. M. Sharma, T. J. Volz, J. M. Winey, Y. M. Gupta, *Sci. Adv.* **2017**, *3*, eaao3561.
109. N. Izyumskaya, D. O. Demchenko, S. Das, Ü. Özgür, V. Avrutin, H. Morkoç, *Adv. Electron. Mater.* **2017**, *3*, 1600485.

110. W. H. Balmain, *J. Prakt. Chem.* **1842**, 27, 422–430.
111. a) Z. Zhao, B. Xu, Y. Tian, *Annu. Rev. Mater. Res.* **2016**, 46, 383–406; b) Y. Tian, B. Xu, D. Yu, Y. Ma, Y. Wang, Y. Jiang, W. Hu, C. Tang, Y. Gao, K. Luo, Z. Zhao, L.-M. Wang, B. Wen, J. He, Z. Liu, *Nature* **2013**, 493, 385–388; c) R. T. Paine, C. K. Narula, *Chem. Rev.* **1990**, 90, 73–91; d) A.-K. Wolfrum, B. Matthey, A. Michaelis, M. Herrmann, *Materials* **2018**, 11, 255.
112. R. H. Wentorf, *J. Chem. Phys.* **1957**, 26, 956.
113. L. Vel, G. Demazeau, J. Etourneau, *Mater. Sci. Eng. B* **1991**, 10, 149–164.
114. a) M. Zastrow, *Nature* **2019**, 572, 429–432; b) T. Taniguchi, T. Teraji, S. Koizumi, K. Watanabe, S. Yameoka, *Jpn. J. Appl. Phys.* **2002**, 41, L109–L111; c) K. Watanabe, T. Taniguchi, H. Kanda, *Nat. Mater.* **2004**, 3, 404–409.
115. W. Zhang, I. Bello, Y. Lifshitz, K. M. Chan, X. Meng, Y. Wu, C. Y. Chan, S.-T. Lee, *Adv. Mater.* **2004**, 16, 1405–1408.
116. R. Dahal, J. Li, S. Majety, B. N. Pantha, X. K. Cao, J. Y. Lin, H. X. Jiang, *Appl. Phys. Lett.* **2011**, 98, 211110.
117. V. K. Gupta, C. C. Wamsley, M. W. Koch, G. W. Wicks, *J. Vac. Sci. Technol. B* **1999**, 17, 1246–1248.

Chapter 2 – Frustrated Lewis Pair Chelation as a Vehicle for Low Temperature Semi-conductor Element and Polymer Deposition

2.1 Introduction

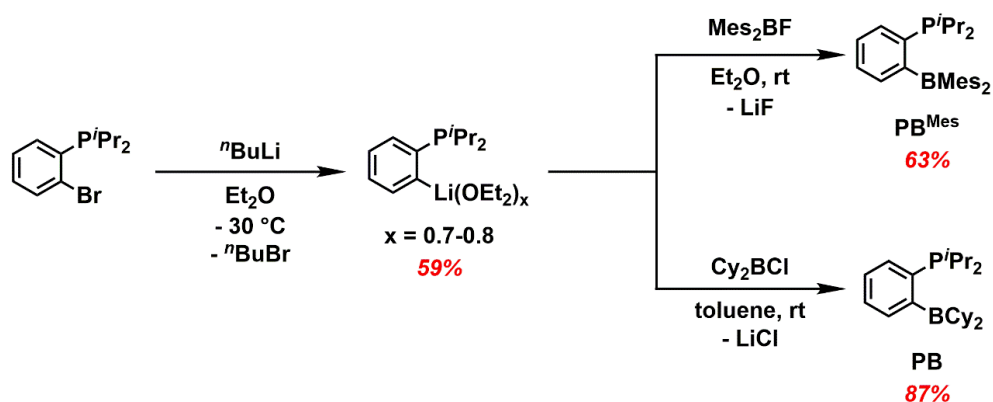
Main group element chemistry represents one of the pillars of molecular synthesis, with the ongoing discovery of new inorganic multiple bonds, non-metal-mediated catalytic transformations, and even the recent fixation of nitrogen by the light element boron receiving widespread attention.¹ Despite such breakthroughs, it is rare that modern synthetic chemistry makes a deep impact in the realm of materials science, a field that often relies upon decades-to-centuries old methods and harsh reaction conditions for synthesis. In this Chapter, a general, solution-based route to semi-conducting Si or Ge films and a σ -conjugated polysilane is reported that harnesses labile frustrated Lewis pair (FLP) chelation² to access the storable precursors [FLP{ER₂}] (E = Si or Ge; R = H or Me).

Frustrated Lewis pairs (FLPs) contain unquenched Lewis basic and acidic sites, leading to the cooperative activation of typically inert substrates, such as H₂, CO, or CO₂.² Furthermore, FLPs are being explored as next generation main group element-based catalysts.³ In this Chapter, the intramolecular FLP ⁱPr₂P(C₆H₄)BCy₂ (**PB**; Cy = cyclohexyl)⁴ was explored to stabilize silicon(II) and germanium(II) dihydrides, with the expectation that the singlet EH₂ units (E = Si or Ge) would engage in synergistic donor-acceptor interactions with **PB**.⁵ Knowing that the Ge(II) dihydride donor-acceptor complex Ph₃PCMe₂•GeH₂•BH₃ can afford luminescent Ge nanoparticles from

solution, albeit at high temperature of 190 °C under microwave irradiation,⁶ it was anticipated that the new [PB{EH₂}] chelates would release bulk Si or Ge and H₂ (*via* free EH₂) at much lower temperatures, enabling the eventual recycling of **PB**. This Chapter documents the success of this approach, leading to the low temperature (≤ 110 °C) deposition of semi-conducting Si and Ge films onto substrates from solution. In addition, the storable dialkylsilicon(II) adduct⁷ [PB{SiMe₂}] was prepared and used to generate polydimethylsilane [SiMe₂]_n, an inorganic polymer precursor to silicon carbide.⁸

2.2 Results and Discussion

As a starting point, a previously reported FLP, ⁱPr₂P(C₆H₄)BMe₂ (**PB^{Mes}**; Mes = 2,4,6-Me₃C₆H₂)⁹ was explored initially for this study; however, **PB^{Mes}** did not exhibit any reactivity with a variety of Ge(II), Sn(II) and Pb(II) sources; thus, ⁱPr₂P(C₆H₄)BCy₂ (**PB**) became the main ligand for this study. First reported by Bourissou and co-workers for the isolation of monomeric transition metal complexes,⁴ **PB** was chosen in this study since its high degree of steric bulk should allow for effective kinetic stabilization of main group element moieties. **PB** was obtained *via* a modification of a previous procedure by.⁴ In order to obtain **PB** in high purity, the precursor *o*-ⁱPr₂P(C₆H₄)Br was lithiated using ^tBuLi and the corresponding salt, [ⁱPr₂P(C₆H₄)Li(OEt₂)_x] (x = 0.7-0.8) was isolated and characterized by single-crystal X-ray crystallography (Scheme 2.1 and Figure 2.1). Notably, **PB^{Mes}** was synthesized in a similar manner *via* initial isolation of [ⁱPr₂P(C₆H₄)Li(OEt₂)_x] and subsequent addition of Mes₂BF (Scheme 2.1).



Scheme 2.1. Step-wise syntheses of **PB^{Mes}** and **PB**.

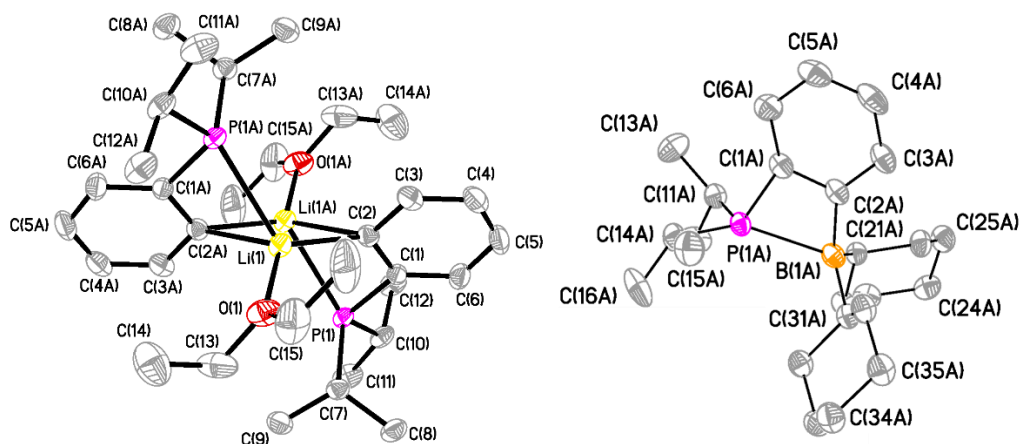


Figure 2.1. Molecular structure of $[{}^i\text{Pr}_2\text{P}(\text{C}_6\text{H}_4)\text{Li}(\text{OEt}_2)]_2$ (left) and **PB** (right) with thermal ellipsoids at a 30 % probability level. All hydrogen atoms have been omitted for clarity. Selected bond lengths [\AA] and angles [$^\circ$], with values corresponding to a second molecule in the asymmetric unit in square brackets: $[{}^i\text{Pr}_2\text{P}(\text{C}_6\text{H}_4)\text{Li}(\text{OEt}_2)]_2$: P1–C1 1.8337(16), P1–C7 1.8685(16), P1–C10 1.8535(16), P1–Li1A 2.652(3), O1–C13 1.474(3), O1–C15 1.405(3), O1–Li1 1.954(3), Li1A–C1 2.784(3), Li1–C2 2.185(3); C1–P1–C7 100.91(7), C7–P1–Li1A 120.01(7). **PB**: Only C31A to C36A atoms are shown on the disordered cyclohexyl ring attached to B(1A). Selected bond lengths [\AA] and angles [$^\circ$]: P1A–B1A 2.2771(14) [2.1964(13)], P1A–C1A 1.8015(12) [1.8033(12)], B1A–C2A 1.6265(16) [1.6317(16)]; C1A–P1A–B1A 73.06(5) [74.63(5)], P1A–B1A–C2A 77.17(7) [78.48(6)].

Upon addition of ClBCy₂ to [ⁱPr₂P(C₆H₄)Li(OEt₂)_x] (x = 0.7-0.8) in toluene, **PB** can be isolated as a spectroscopically pure oil in a 87 % yield. In addition, X-ray quality crystals of **PB** were isolated upon cooling a solution of **PB** in Et₂O to -30 °C, confirming the presence of an elongated P–B bond in the solid-state, with a length of 2.2771(14) Å (Figure 2.1). Although **PB** exhibits weak intramolecular P–B bonding in the solid-state, it could still react with Cl₂E sources (E = Si, Ge) (Figures 2.1 and 2.2). The solid-state structure of **PB**^{Mes} exhibits a P⋯B distance of 3.203(4) Å, confirming a trigonal planar boron center (sum of bond angles = 359.9(12)°); thus, no appreciable P–B intramolecular bonding is present. However, the high steric bulk from the flanking mesityl rings hinders any cooperative FLP trapping of Cl₂E (E = Si, Ge).

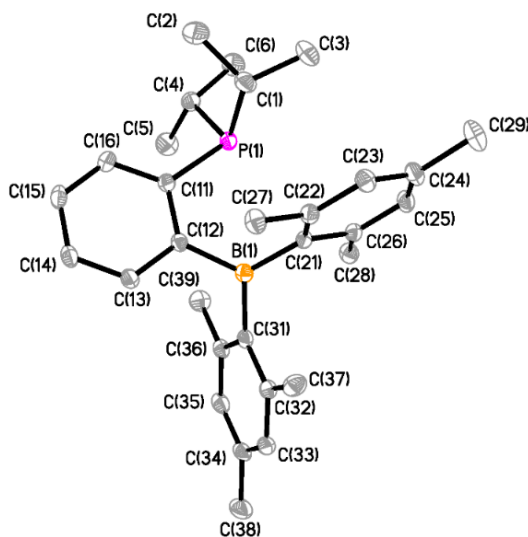
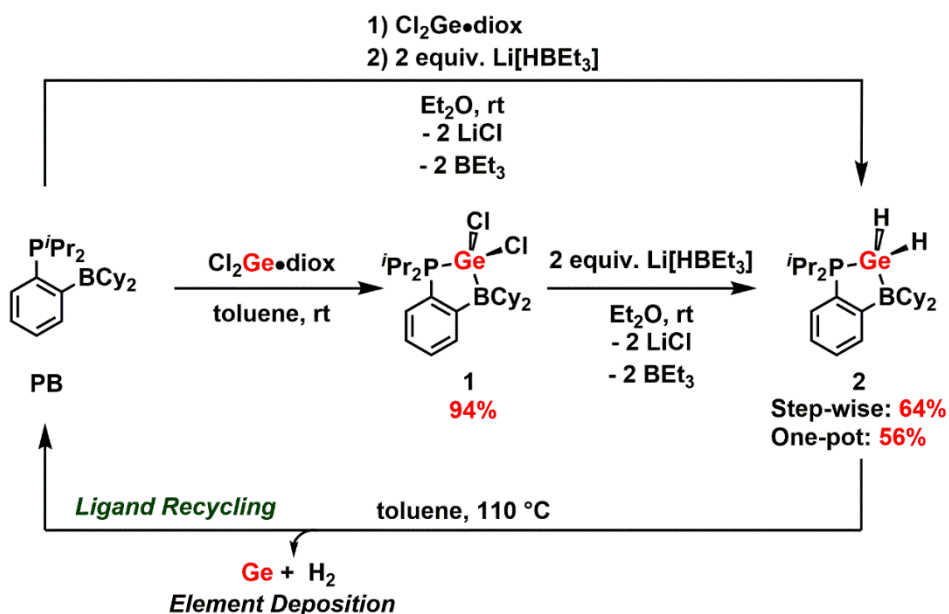


Figure 2.2. Molecular structure of **PB**^{Mes} with thermal ellipsoids at a 30 % probability level. All hydrogen atoms have been omitted for clarity. Selected bond lengths [Å] and angles [°]: P1–C1 1.868(2), P1–C4 1.8584(19), P1–C11 1.8468(18), B1–C12 1.578(3), B1–C21 1.580(3), B1–C31 1.582(3); C1–P1–C4 105.56(9), C1–P1–C11 100.45(9), B1–C11–C12 125.37(15), C12–B1–C21 121.93(15).

Addition of $\text{Cl}_2\text{Ge}\cdot\text{dioxane}$ to **PB** in toluene afforded the FLP adduct $[\text{PB}\{\text{GeCl}_2\}]$ (**1**), which was then converted into the target Ge(II)-dihydride adduct $[\text{PB}\{\text{GeH}_2\}]$ (**2**) upon treatment of **1** with two equiv. of $\text{Li}[\text{HBEt}_3]$ in Et_2O (Scheme 2.2); Compound **2** can also be synthesized in a one-pot procedure starting from **PB**.



Scheme 2.2. Step-wise and one-pot syntheses of $[\text{PB}\{\text{GeH}_2\}]$ (**2**).

As expected, $[\text{PB}\{\text{GeH}_2\}]$ (**2**) gave a $^{11}\text{B}\{^1\text{H}\}$ NMR resonance at 2.9 ppm in C_6D_6 , consistent with a four-coordinate boron environment. For comparison, the three-coordinate boron center in free **PB** in C_6D_6 solution resonates at 75.6 ppm. The GeH_2 unit in **2** yields a ^1H NMR signal at 3.80 ppm and a $\nu(\text{Ge-H})$ IR band at 1990 cm^{-1} .¹⁰ The solid-state structures of $[\text{PB}\{\text{GeCl}_2\}]$ (**1**) and **2** have been determined by single-crystal X-ray crystallography and are depicted in Figure 2.3. The Ge–P distance in **2** [2.3447(3) Å] is the same within experimental error as the coordinative Ge–P length in Marschner’s disilylgermylene adduct $\text{Me}_3\text{P}\cdot[\text{Ge}\{\text{Si}(\text{SiMe}_3)_3\}_2]$ [2.3484(6) Å].¹¹ The

Ge–B distance in **2** [2.1490(15) Å] is slightly longer than in the corresponding Ge–B bond in Kinjo's (boryl)germylene $\text{Me}_3\text{P}\cdot[\text{GeB}(\text{Mes})\text{N}(\text{Ad})\text{CH}=\text{CHC}(\text{SiMe}_3)_2]$ [2.121(2) Å] (Ad = adamantyl).¹²

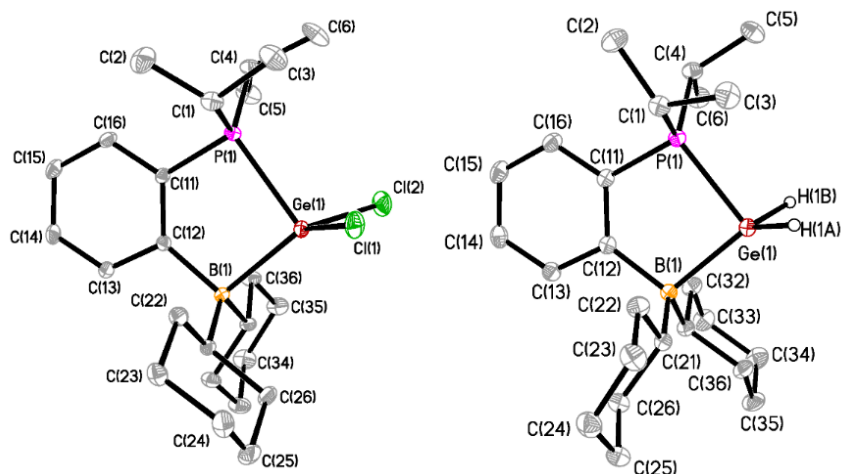
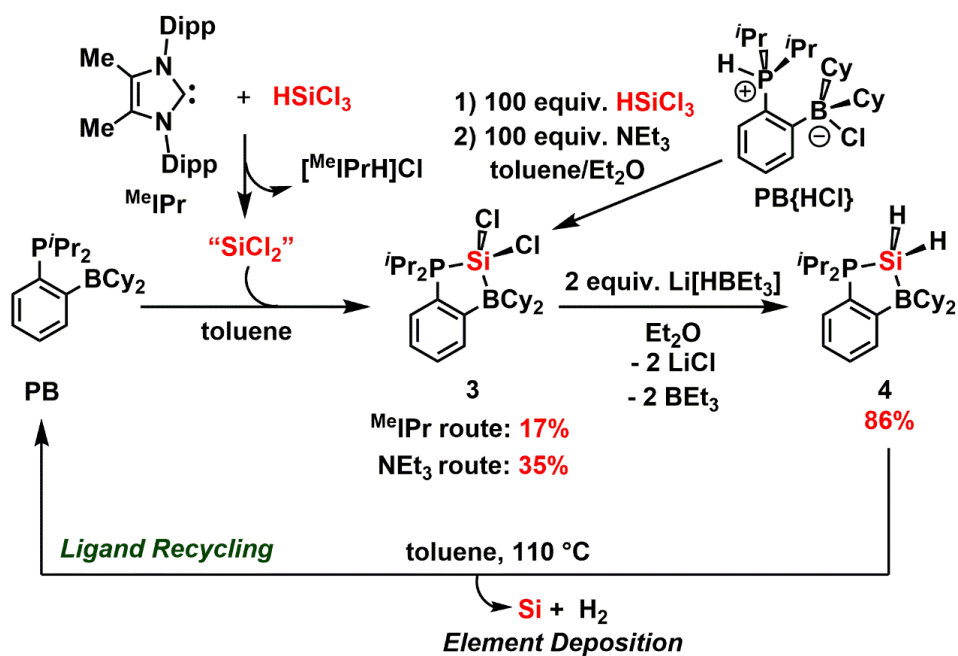


Figure 2.3. Molecular structure of $[\text{PB}\{\text{GeCl}_2\}]$ (**1**) (left) and $[\text{PB}\{\text{GeH}_2\}]$ (**2**) (right) with thermal ellipsoids at a 30 % probability level. All hydrogen atoms have been omitted for clarity. Selected bond lengths [Å] and angles [°]: **1**: Ge1–P1 2.3942(5), Ge1–B1 2.198(2), Ge1–C11 2.2023(7), Ge1–C12 2.1975(7); P1–Ge1–B1 94.62(6), C11–Ge1–C12 99.16(3), C11–Ge1–P1 94.85(7), Ge1–B1–C12 100.28(13). **2**: Ge1–P1 2.3447(3), Ge1–B1 2.1490(15), Ge1–H1A 1.49(2), Ge1–H1B 1.58(2); P1–Ge1–B1 92.32(4), H1A–Ge1–H1B 102.99(11).

Two routes to the Si(II)-FLP complex $[\text{PB}\{\text{SiCl}_2\}]$ (**3**) were developed, each involving the *in-situ* generation of SiCl_2 (Scheme 2.3).¹³ The highest isolated yield of pure **3** was 35 % starting from ${}^i\text{Pr}_2\text{P}(\text{H})(\text{C}_6\text{H}_4)\text{BCy}_2(\text{Cl})$ $[\text{PB}\{\text{HCl}\}]$ (solid-state structure shown in Figure 2.4) and 100 equiv. of both Et_3N and HSiCl_3 ; $[\text{PB}\{\text{HCl}\}]$ is prepared by independent synthesis from **PB** and HCl (see Section 2.4.2.). The solid-state structure of $[\text{PB}\{\text{SiCl}_2\}]$ (**3**) was confirmed by single-crystal X-ray

crystallography (Figure 2.5). Conversion of **3** into the Si(II) dihydride [PB{SiH₂}] (**4**) was accomplished in a 86 % isolated yield *via* the addition of two equiv. of Li[HBEt₃] in Et₂O (Scheme 2.3).



Scheme 2.3. Syntheses of [PB{SiH₂}] (**4**) using different SiCl₂ sources; MeIPr = (MeCNDipp)₂C; Dipp = 2,6-ⁱPr₂C₆H₃.

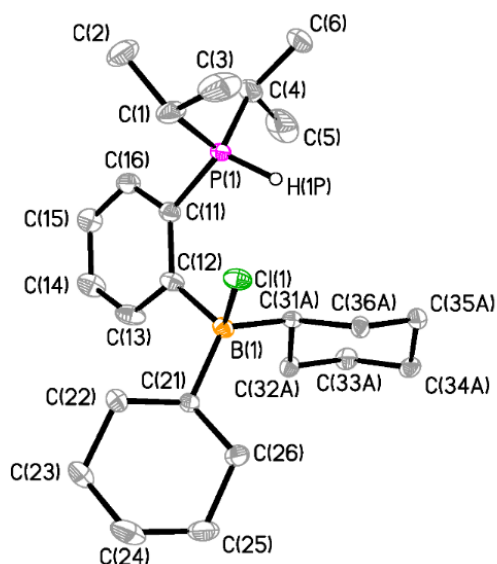


Figure 2.4. Molecular structure of $[\text{PB}\{\text{HCl}\}]$ with thermal ellipsoids at a 30 % probability level. All hydrogen atoms, except the one at P(1) have been omitted for clarity. Only C31A to C36A atoms are shown on the disordered cyclohexyl ring attached to B1. Selected bond lengths [\AA] and angles [$^\circ$]: C11–B1 2.014(2), P1–H(1P) 1.26(3), P1–C1 1.822(3), B1–C12 1.644(3); C1–P1–C4 112.58(13), C1–P1–H(1P) 109.8(12), C11–P1–H(1P) 111.4(12), C11–B1–C12 108.09(12), C11–B1–C21 103.96(12).

The NMR spectra of $[\text{PB}\{\text{SiH}_2\}]$ (**4**) are consistent with the assigned structure, including the presence of a diagnostic triplet ^{29}Si NMR resonance at -80.4 ppm [$^1J_{\text{SiH}} = 158$ Hz]. The SiH_2 unit appears as a $\nu(\text{Si-H})$ IR band at 2107 cm^{-1} .¹⁴ The solid-state structure of **4** is depicted in Figure 2.5 (right), which shows a similar C_2PBSi heterocyclic structure as in **3**. The coordinative Si–P bond in **4** [2.2787(5) \AA] is slightly shorter than in Baceiredo’s silicon(II) hydride $[(\text{Me}_2\text{Si}(\text{N}^t\text{Bu})_2)\text{P}](\text{C}_8\text{H}_{10})\text{N}(\text{Dipp})\text{SiH}$ [2.318(15) \AA].^{1b} While the Si–B distance in **4** [2.0769(15) \AA] is longer than in Cui’s

Si(II)-hydride adduct $\text{ImMe}_4 \cdot \text{Si}(\text{H})[\{\text{N}(\text{Boryl})\text{CH}_2\}_2]$ (Boryl = $[\text{B}(\text{NDippCH}_2)_2]$;
 $\text{ImMe}_4 = (\text{MeCNMe})_2\text{C}:$) [2.014(5) Å].¹⁵

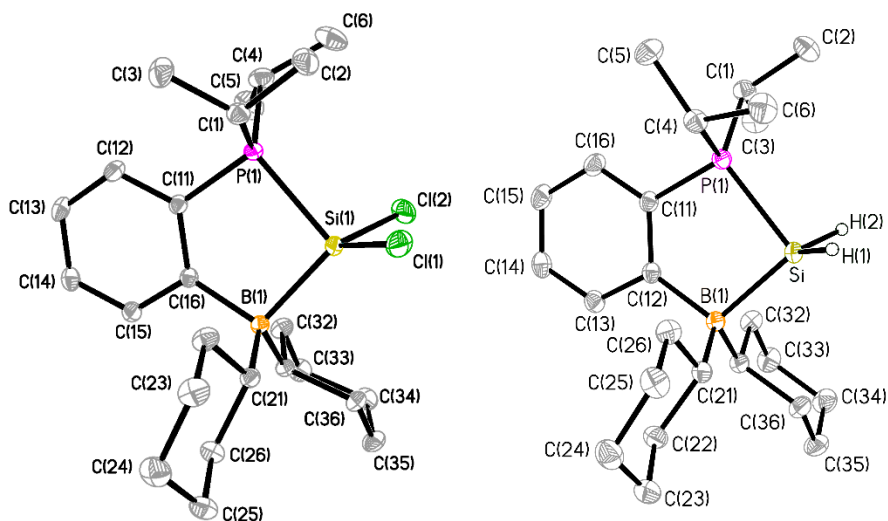


Figure 2.5. Molecular structure of $[\text{PB}\{\text{SiCl}_2\}]$ (**3**) (left) and $[\text{PB}\{\text{SiH}_2\}]$ (**4**) (right) with thermal ellipsoids at a 30 % probability level. All hydrogen atoms have been omitted for clarity. Selected bond lengths [Å] and angles [°]: **3**: Si1–P1 2.3058(4), Si1–B1 2.0597(13), Si1–C11 2.0777(5), Si1–C12 2.0818(5); P1–Si1–B1 96.94(4), C11–Si1–C12 102.79(2), C11–Si1–P1 95.03(4), Si1–B1–C12 101.49(7). **4**: Si1–P1 2.2787(5), Si1–B1 2.0769(15), Si1–H1 1.414(19), Si1–H2 1.415(19); P1–Si1–B1 94.09(4), H1–Si1–H2 102.9(11).

A major goal of this study was to use the newly prepared FLP-EH₂ complexes (**2** and **4**) as single-source precursors for the deposition of the bulk semi-conductors Ge and Si. To start, $[\text{PB}\{\text{GeH}_2\}]$ (**2**) was subjected to thermal gravimetric analysis (TGA), which showed an onset of decomposition at 115 °C, with a residual mass after heating to 550 °C of 15 wt. % (Figure 2.6); this value corresponds very well to the expected wt.

% Ge of 16 % in **2**. For [PB{SiH₂}] (**4**), the onset of decomposition was significantly lower (67 °C), with 14 wt. % remaining after heating to 550 °C (Figure 2.7). The expected remaining weight % of Si in **4** is *ca.* 7 %, suggesting incomplete degradation of **4** in the solid-state and/or partial oxidation of the reactive Si(0) surface. To confirm that the free **PB** ligand would volatilize upon heating, a TGA on **PB** was conducted (Figure 2.8), which showed an onset of volatilization (temperature at which 99.5 % weight loss is observed) at 134 °C, with a 3 wt. % residual mass after heating to 550 °C.

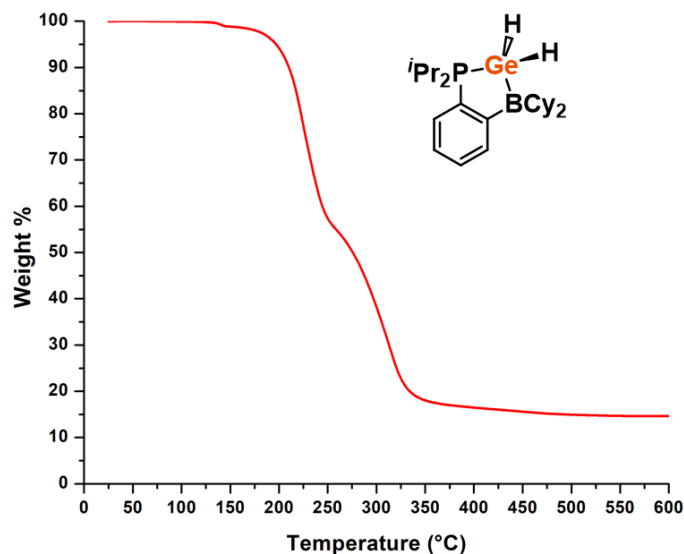


Figure 2.6. TGA profile of [PB{GeH₂}] (**2**), ranging from 25 °C to 600 °C in a N₂ atmosphere at a heating rate of 10 °C/min.

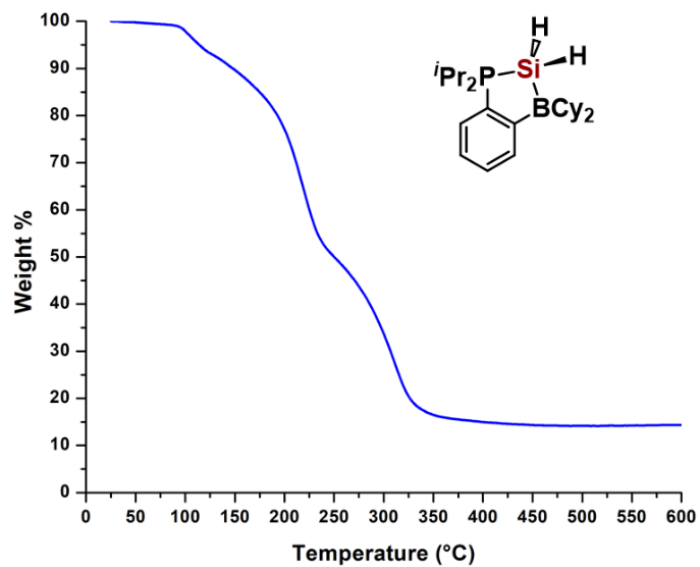


Figure 2.7. TGA profile of [PB{SiH₂}] (**4**), ranging from 25 °C to 600 °C in a N₂ atmosphere at a heating rate of 10 °C/min.

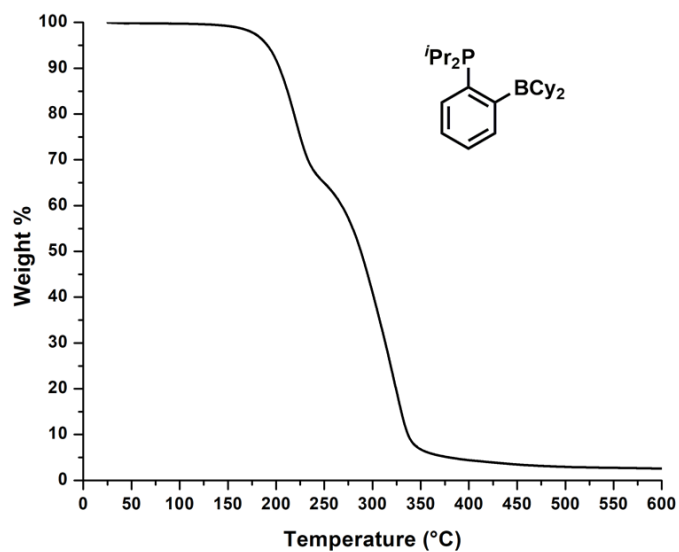


Figure 2.8. TGA profile of **PB**, ranging from 25 °C to 600 °C in a N₂ atmosphere at a heating rate of 10 °C/min.

Encouraged by the low decomposition temperatures for the [PB{EH₂}] adducts **2** and **4**, two possible general thermolytic pathways for the decomposition of **2** or **4** into

PB, E(solid) and H₂ were evaluated computationally at a M06-2X¹⁶/cc-pVTZ¹⁷ level of theory (Figures 2.9 and 2.10). Decomposition of these hydrides into **PB**, E (solid) and H₂ was calculated to be exergonic (ΔG) in toluene by -25.5 kcal/mol (Ge) and -13.7 kcal/mol (Si) through either Pathway 1 (direct dehydrogenation; Figure 2.9) or Pathway 2 (initial loss of EH₂; Figure 2.10). The toluene-solvated computations suggest that direct dehydrogenation (Pathway 1) is favored over loss of EH₂ (Pathway 2) by 3.8 kcal/mol for **4** and 7.7 kcal/mol for **2** (Figures 2.9 and 2.10).

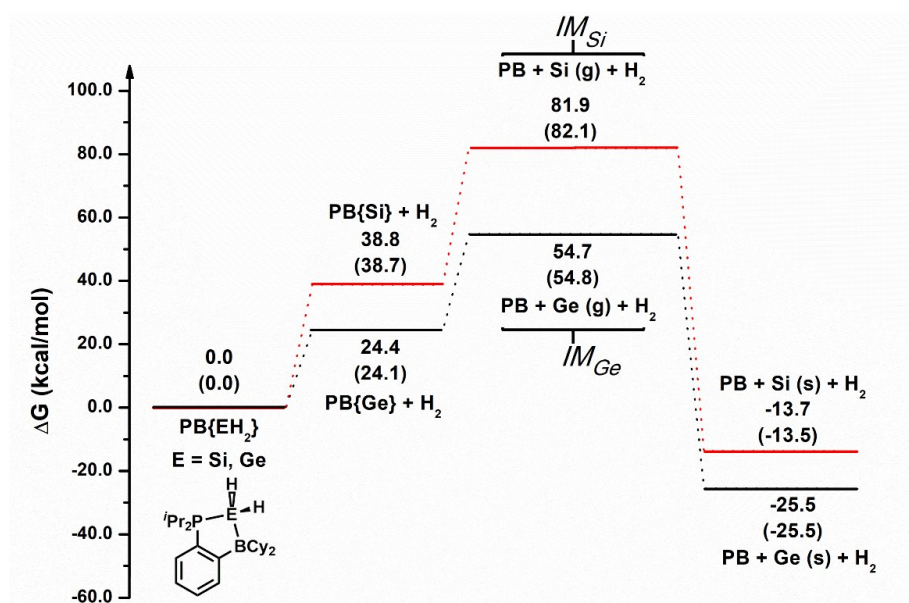


Figure 2.9. Computed relative Gibbs free energies in kcal/mol for Pathway 1 in the thermolysis of [PB{EH₂}] (E = Si (red lines) and Ge (black lines)) in the gas phase; values in parentheses correspond to those obtained with a toluene polarizable continuum model (PCM). Pathway 1 involves E–H bond cleavage and loss of H₂ with subsequent E–P and E–B bond breakage to release H₂, **PB** and E (E= Si and Ge). For *IM*_{Si} (**PB** + Si_(g) + H₂), silicon was optimized as a triplet state in the gas phase. Likewise, for *IM*_{Ge} (**PB** + Ge_(g) + H₂), germanium was optimized as a triplet state in the gas phase. No transition states could be located; attempts to locate transition states optimized to intermediate structures (**PB**, PB{E}, [PB{EH₂]}). Thus, the P–E/E–B bond breakage may be a barrierless concerted process. Gibbs free energy formation for germanium and silicon are included in the last step, as obtained from the NIST.¹⁸

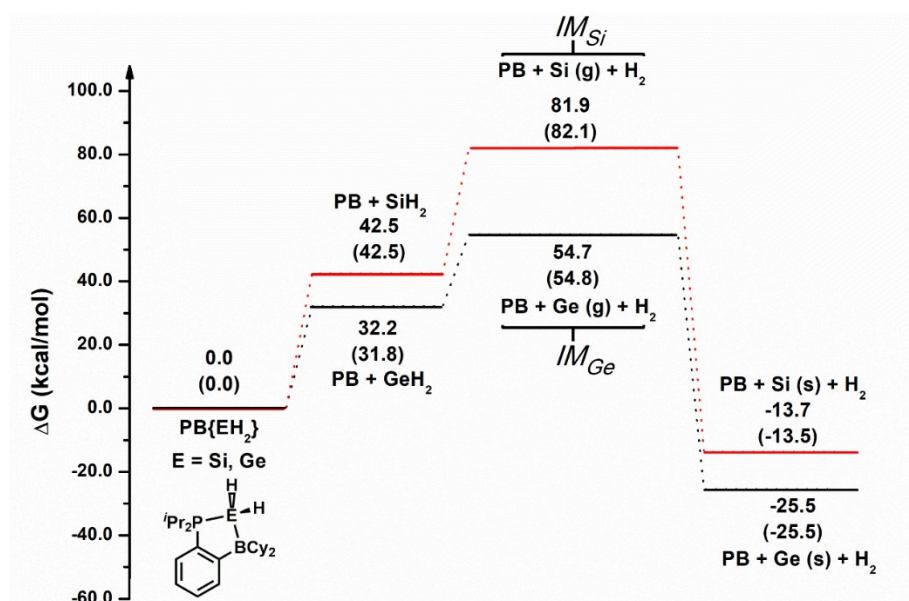


Figure 2.10. Computed relative Gibbs free energies in kcal/mol for Pathway 2 in the thermolysis of [PB{EH₂}] (E = Si (red lines) and Ge (black lines)) in the gas phase; values in parentheses correspond to those obtained with a toluene polarizable continuum model (PCM). Pathway 2 involves P–E and E–B bond cleavage, leading to loss of EH₂ with subsequent E–H bond breakage to release H₂, **PB** and E (E= Si and Ge). For IM_{Si} (**PB** + Si_(g) + H₂), silicon was optimized as a triplet state in the gas phase. Likewise, for IM_{Ge} (**PB** + Ge_(g) + H₂), germanium was optimized as a triplet state in the gas phase. No transition states could be located; attempts to locate transition states optimized to intermediate structures (**PB**, PB{E}, [PB{EH₂}]). Thus, the P–E/E–B bond breakage may be a barrierless concerted process. Gibbs free energy formation for germanium and silicon are included in the last step, as obtained from the NIST.¹⁸

Heating solutions of **2** or **4** inside a J-Young NMR tube in toluene-*d*₈ to 110 °C (8 hrs) deposited Ge or Si on the glass surface, respectively, with the sole species detected by multinuclear NMR spectroscopy (¹H, ¹¹B, ³¹P) in solution being dissolved H₂ and the free ligand, **PB**. When element deposition was conducted on a preparative

scale, *ca.* 70 % of **PB** could be recovered and re-used, thus forming a “closed loop” cycle for element deposition (Schemes 2.2 and 2.3). Notably, the solution-phase deposition of Si from **4** at 110 °C represents, to my knowledge, the lowest temperature deposition of this ubiquitous semi-conductor from a storable single-source molecular precursor.¹⁹

To characterize the morphology and elemental composition of the deposited bulk Ge (and films) from the thermolysis of [PB{GeH₂}] (**2**), SEM imaging and EDX maps were obtained (Figures 2.11 - 2.14). Figure 2.11 confirms deposition of bulk Ge with a globular morphology, similarly to the previously reported thermolysis of Ph₃PCMe₂•GeH₂•BH₃ to deposit bulk Ge.^{6b} EDX mapping (Figures 2.12 and 2.13) further corroborates that the bulk sample composition is largely Ge (from the detected Ge L α emission) with minimal oxidation (Figure 2.13(d)) observed.

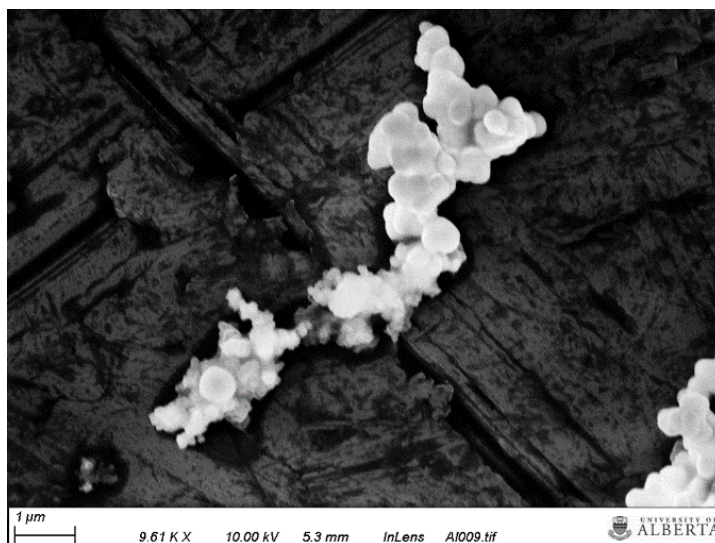


Figure 2.11. Secondary-electron SEM image showing Ge from the thermolysis of **2** on top of an aluminum stub.

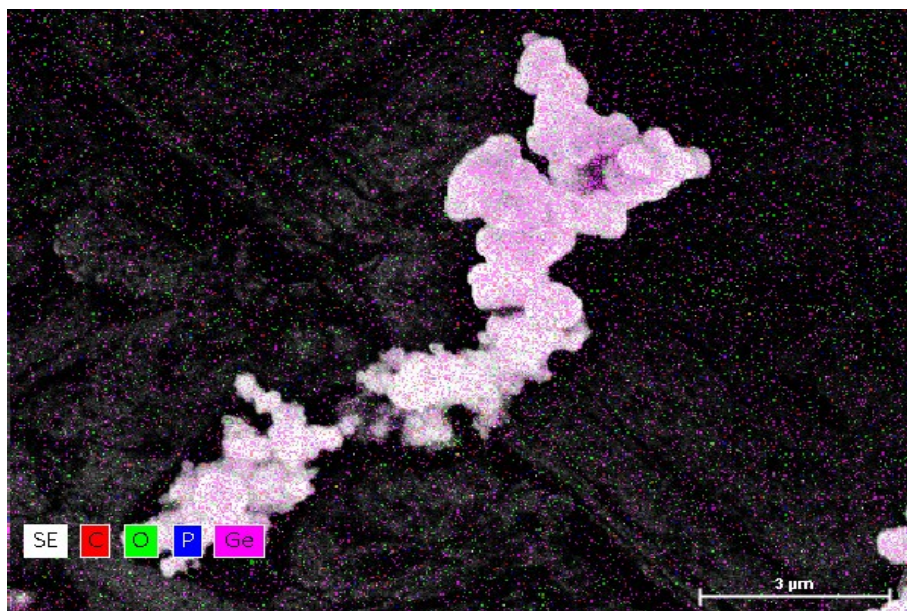


Figure 2.12. An overlaid energy dispersive X-ray (EDX) map showing the distribution of C, O, P and Ge in a sample of deposited Ge (same sample as in Figure 2.11).

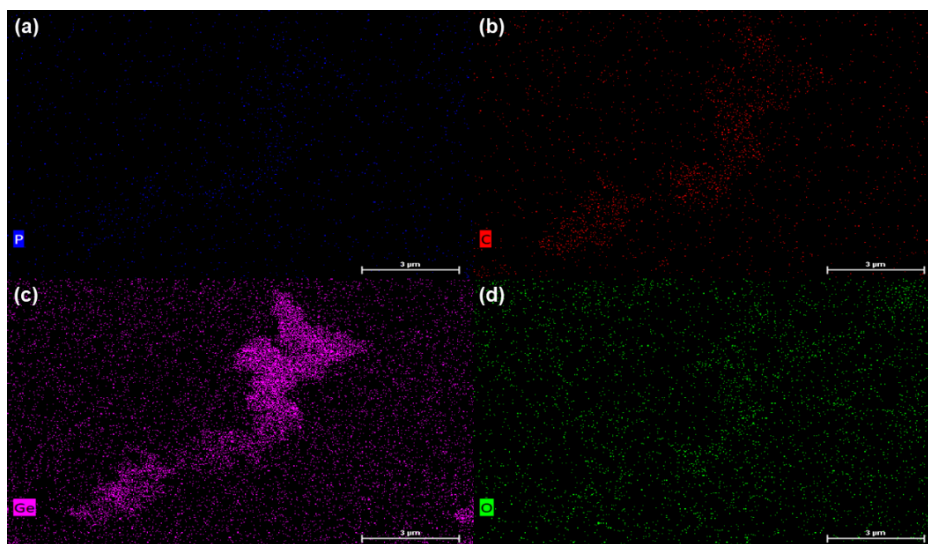


Figure 2.13. EDX mapping images that show the spatial distribution of (a) P; (b) C; (c) Ge; (d) O in a deposited sample of Ge (same as in Figures 2.11 and 2.12).

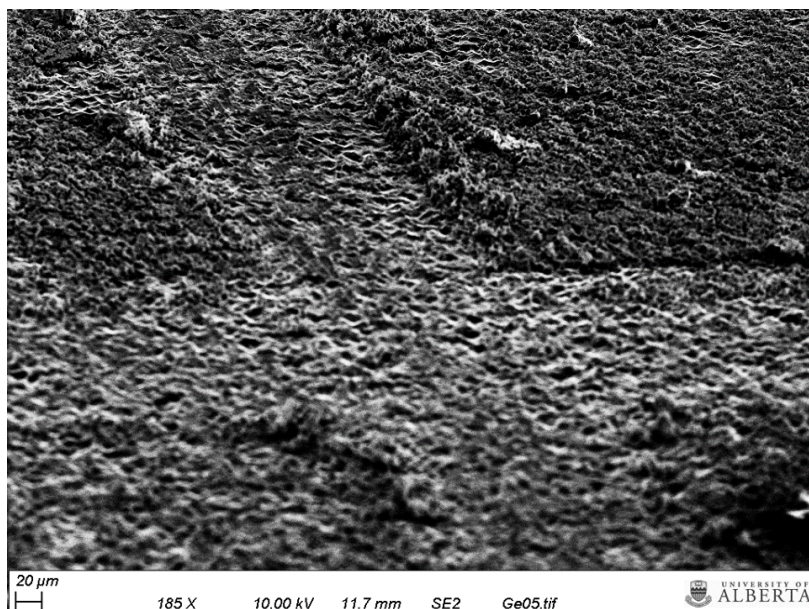


Figure 2.14. Angled (54°) secondary-electron SEM image of a Ge film deposited onto a Si wafer *via* thermolysis of **2** in toluene (1.06×10^{-2} M, 20 hrs, 110°C). The “X” pattern in the film was scratched using the tip of a stainless steel (1.2 mm diameter) needle.

In the same manner, SEM imaging and EDX mapping was performed on bulk Si (and films) derived from the thermolysis of $[\text{PB}\{\text{SiH}_2\}]$ (**4**) (Figures 2.15 to 2.20). In contrast to bulk Ge samples deposited from **2**, the bulk Si samples often showed sample charging, which required the use of carbon tape as the substrate to minimize imaging distortion (Figure 2.15). Regardless, high quality SEM/EDX imaging could be collected, confirming the formation of fused Si nanoparticle clusters with minimal oxidation, alongside strong Si $\text{K}\alpha$ emission in EDX (Figures 2.16 and 2.17).

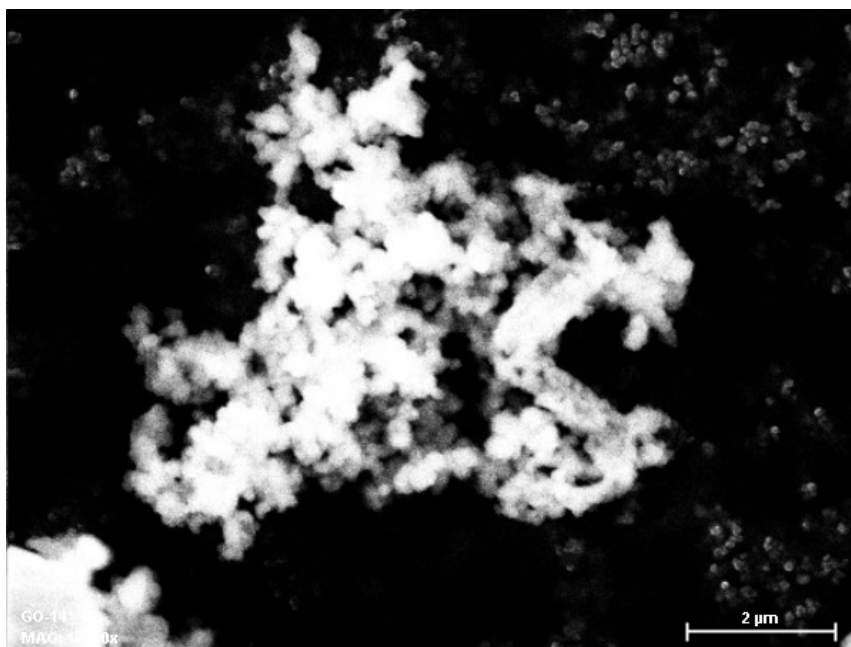


Figure 2.15. Secondary-electron SEM image showing Si deposited from the thermolysis of **4** onto carbon tape.

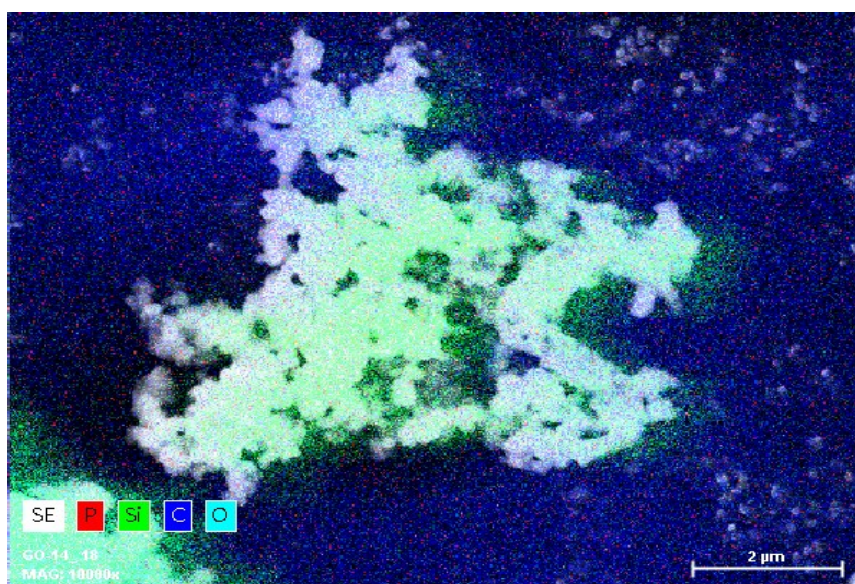


Figure 2.16. An overlaid energy dispersive X-ray (EDX) map showing the distribution of C, O, P and Si in a sample of deposited Si (same sample as in Figure 2.15).

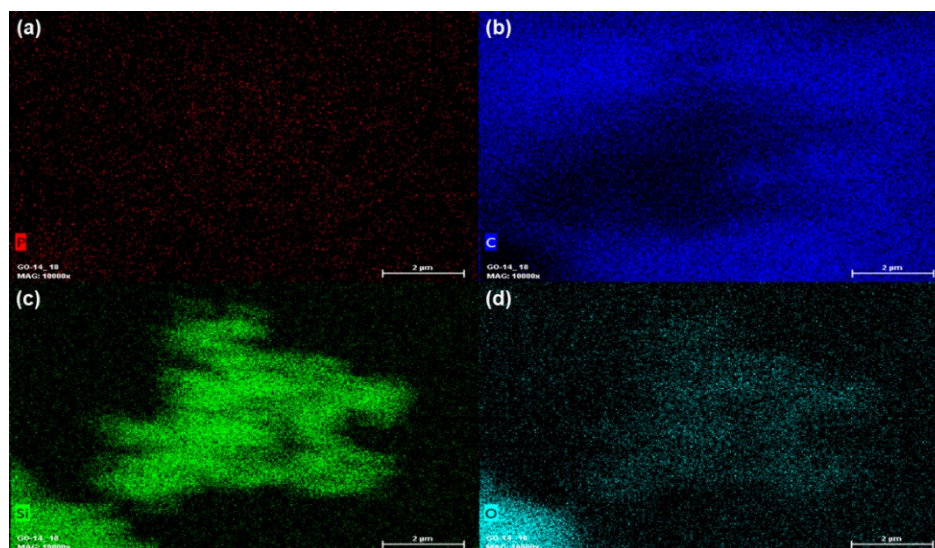


Figure 2.17. EDX mapping images that show the spatial distribution of (a) P; (b) C; (c) Si; (d) O (same sample as in Figures 2.15 and 2.16 above).

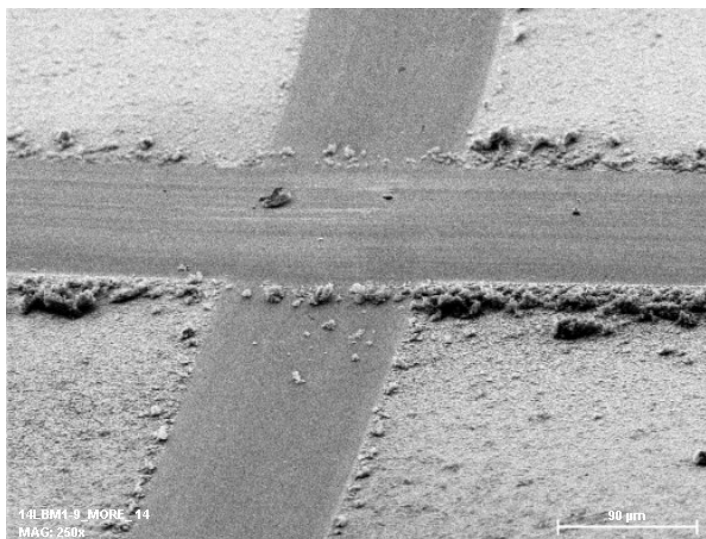


Figure 2.18. Angled (52°) secondary-electron SEM image of a Si film deposited onto a Ge wafer *via* thermolysis of **4** in toluene (3.22×10^{-2} M, 20 hrs, 110°C). The “X” pattern was scratched into the film using the tip of a stainless steel (1.2 mm diameter) needle.

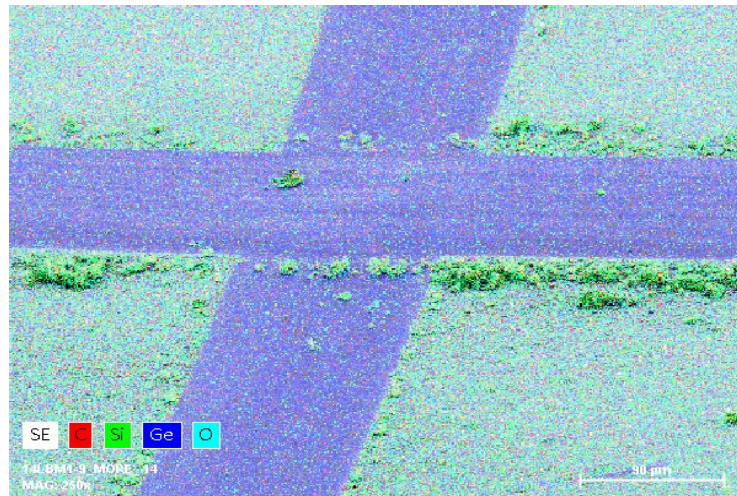


Figure 2.19. An overlaid EDX map of patterned Si film on a Ge wafer, showing the distribution of C, O, Ge and Si (same sample as in Figure 2.18).

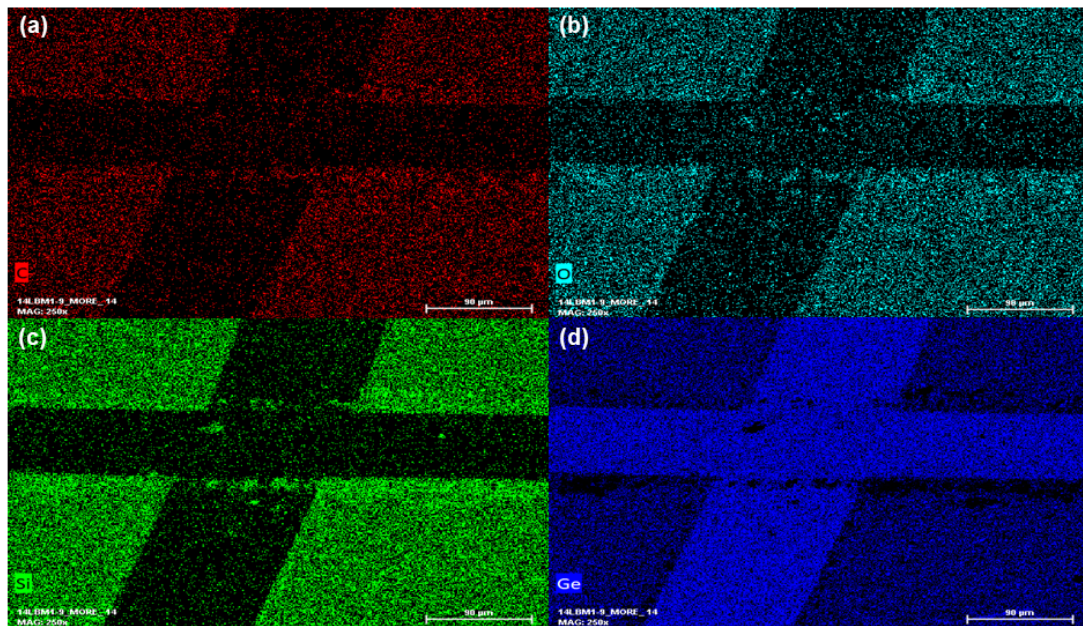


Figure 2.20. EDX mapping images to show the spatial distribution of (a) C; (b) O; (c) Si; (d) Ge (same sample as in Figures 2.18 and 2.19 above).

When element deposition was repeated onto Si or Ge wafers from solution, SEM revealed the presence of Si and Ge films with thicknesses of 110(15) nm and 14(4) μm , respectively (Figures 2.14 (Ge), and 2.18-2.20 (Si)). In all collected EDX imaging, EDX showed negligible P atom content in all cases, thus sample contamination with **PB** or starting $\text{PB}[\{\text{EH}_2\}]$ complex (E = Si or Ge) was minimal. The oxidation state of the deposited Si and Ge was probed by XPS, which showed both Ge(0) and Ge(II) environments for the Ge films (Figures 2.21 and 2.22), while only one Si(0) environment was shown for the Si films (Figures 2.23 and 2.24). Oxidation of deposited Ge is likely due to brief exposure to air during sample transfer.²⁰

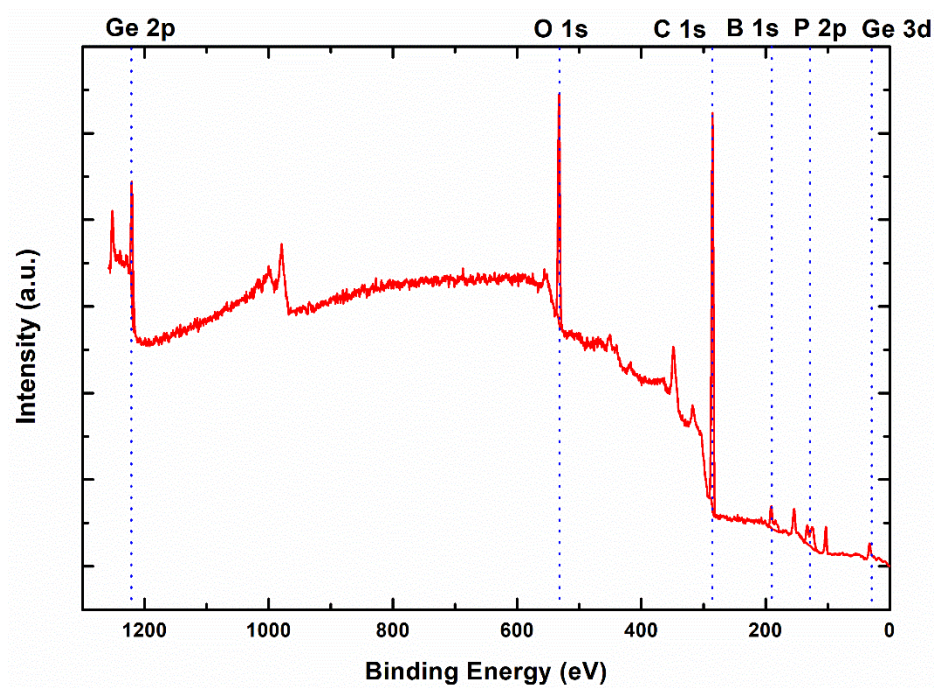


Figure 2.21. Survey XPS spectra of deposited Ge. Sample preparation required temporary exposure of Ge to atmosphere prior to XPS analysis, resulting in partial oxidation of Ge. Although the B 1s and P 2p peaks have been identified using the CasaXPS (VAMAS) software, the B 1s and P 2p peaks are too close to the instrument baseline for reliable interpretation.

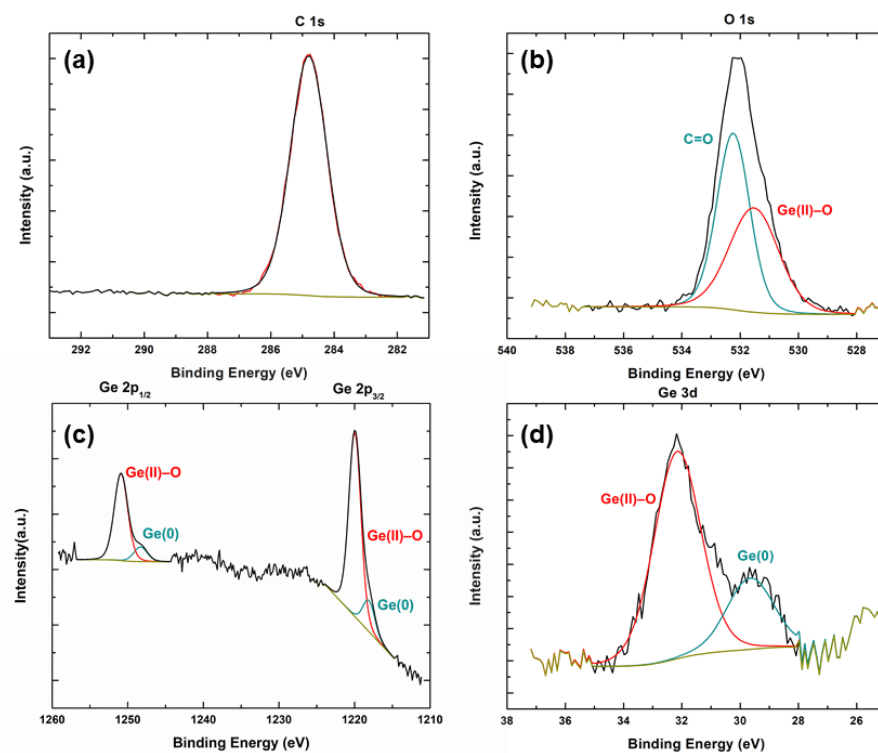


Figure 2.22. High-resolution XPS spectra of a sample of bulk Ge with (a) C 1s; (b) O 1s; (c) Ge 2p; (d) Ge 3d regions shown.

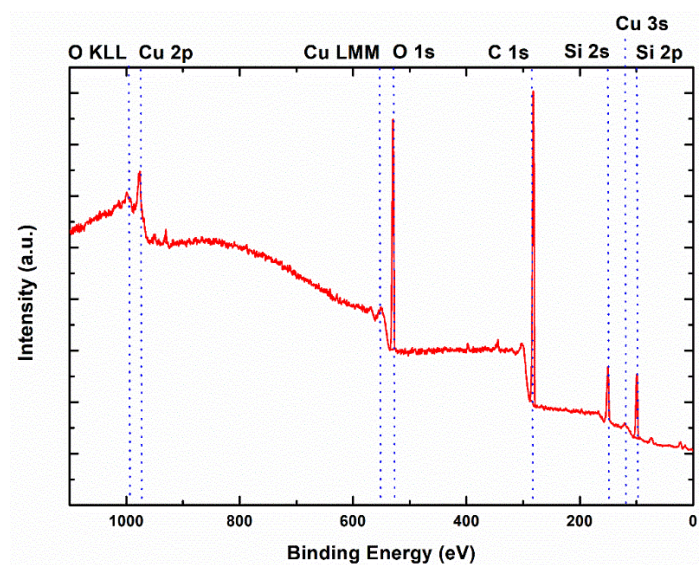


Figure 2.23. Survey XPS spectrum of deposited Si.

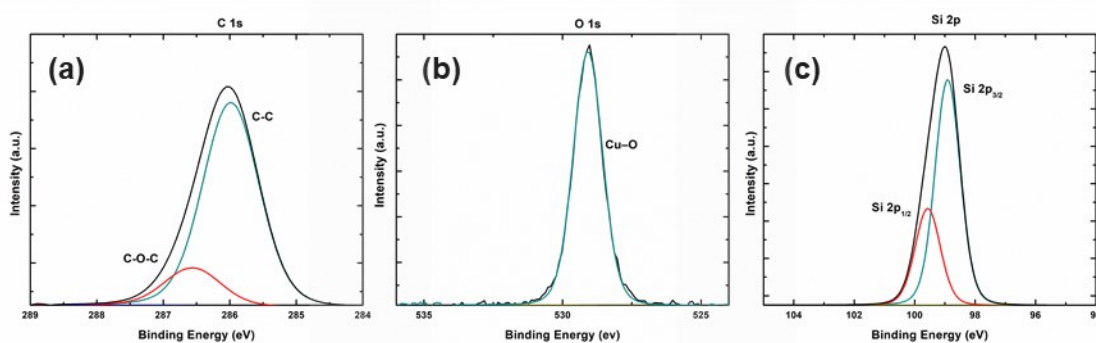


Figure 2.24. High-resolution XPS spectra of bulk Si with (a) C 1s; (b) O 1s; (c) Si 2p regions shown (Si 2p_{3/2} and Si 2p_{1/2} peaks are separated by 0.68 eV). Note: The O 1s peaks matched well with previously reported surface and lattice Cu–O environments from the copper stubs.²¹

Raman spectroscopy was performed on bulk Ge (from the thermolysis of **2**) and bulk Si (from the thermolysis of **4**) to probe the degree of crystallinity in their respective Raman spectra. (Figures 2.25 and 2.26). To minimize oxidation, Raman spectra were collected on Ge and Si samples that were packed into flame-sealed melting point tubes under N₂ for analysis. While crystalline Ge and Si samples exhibit well-defined Ge–Ge peaks at 300 cm⁻¹ and Si–Si peaks at 520 cm⁻¹,²² the deposited Ge and Si samples exhibited broad Ge–Ge (280 cm⁻¹) (Figure 2.25) and Si–Si (485 cm⁻¹) peaks (Figure 2.26), which are well in accordance with previously reported Raman spectra of amorphous Ge²³ and Si.²⁴

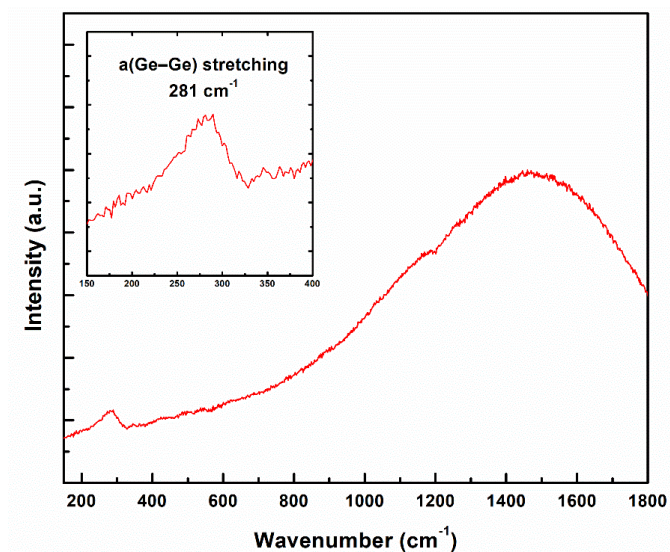


Figure 2.25. Raman spectrum of deposited Ge using a 632.8 nm laser at 100 % power (5 mW) in static mode (10 seconds, 18 accumulations), showing the expected broad amorphous Ge–Ge stretching near 280 cm⁻¹. The large broad peak at higher wavenumbers is due to background fluorescence of the sample.

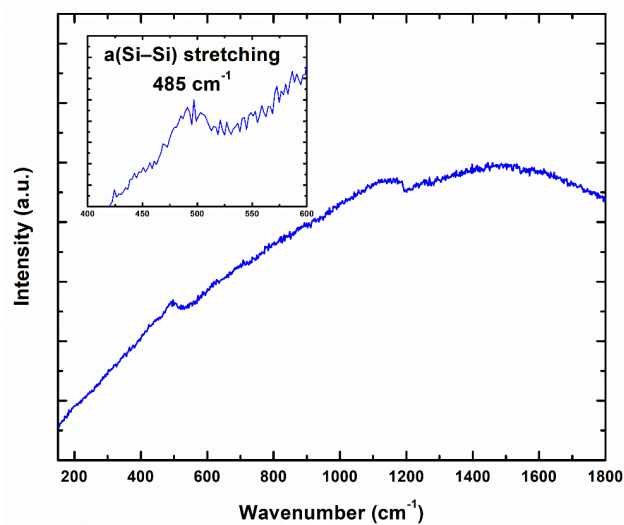


Figure 2.26. Raman spectrum of deposited Si using Ge using a 632.8 nm diode laser at 100 % power (5 mW) in static mode (10 seconds, 15 accumulations), showing the expected broad amorphous Si–Si stretching near 485 cm⁻¹. The large broad peak at higher wavenumbers is due to background fluorescence of the sample.

The reported FLP chelation strategy also enables the formation of a FLP-diorganosilylene complex, as demonstrated by the synthesis of $[\text{PB}\{\text{SiMe}_2\}]$ (**5**) in a 70 % yield from the reaction between $[\text{PB}\{\text{SiCl}_2\}]$ (**3**) and two equiv. of MeLi (Equation 2.1). The single-crystal X-ray structure of **5** (Figure 2.27) exhibits a similar P–Si–B bite angle ($93.63(5)^\circ$) as in **4** ($94.09(4)^\circ$), as well as an elongated Si–P bond length ($2.3055(6)$ Å) vs. the value of $2.2787(5)$ Å in **4**, suggesting that low temperature release of the $[\text{SiMe}_2]$ moiety should be possible.

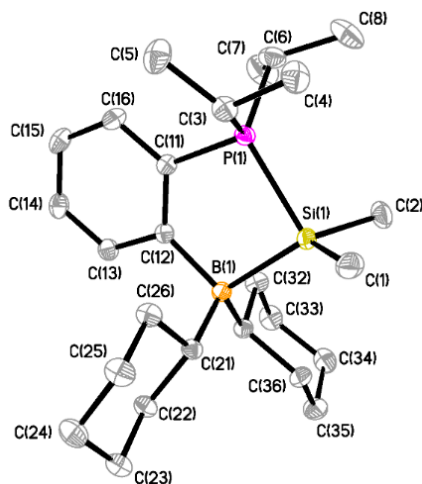
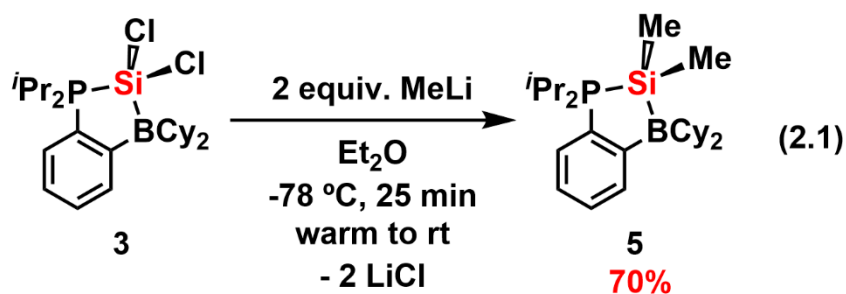


Figure 2.27. Molecular structure of $[\text{PB}\{\text{SiMe}_2\}]$ (**5**) with thermal ellipsoids at a 30 % probability level. All hydrogen atoms have been omitted for clarity. Selected bond lengths [Å] and angles [$^\circ$]: Si1–P1 $2.3055(6)$, Si1–B1 $2.0746(17)$, Si1–C1 $1.890(2)$, Si1–C2 $1.8902(19)$; P1–Si1–B1 $93.63(5)$, C1–Si1–C2 $104.21(10)$.

Heating **5** in toluene at 110 °C for 15 hrs yielded predominantly free **PB** (by $^{31}\text{P}\{^1\text{H}\}$ NMR) and an orange mixture. Dissolution of the products in THF and precipitation into cold (-30 °C) pentane afforded polydimethylsilane $[\text{SiMe}_2]_n$ as a white solid, which was identified using FT-IR (Figure 2.28)^{25,26}, ^1H - ^{29}Si HSQC/HMBC NMR spectroscopies (Figure 2.29),²⁷ and gel permeation chromatography (Figure 2.30).

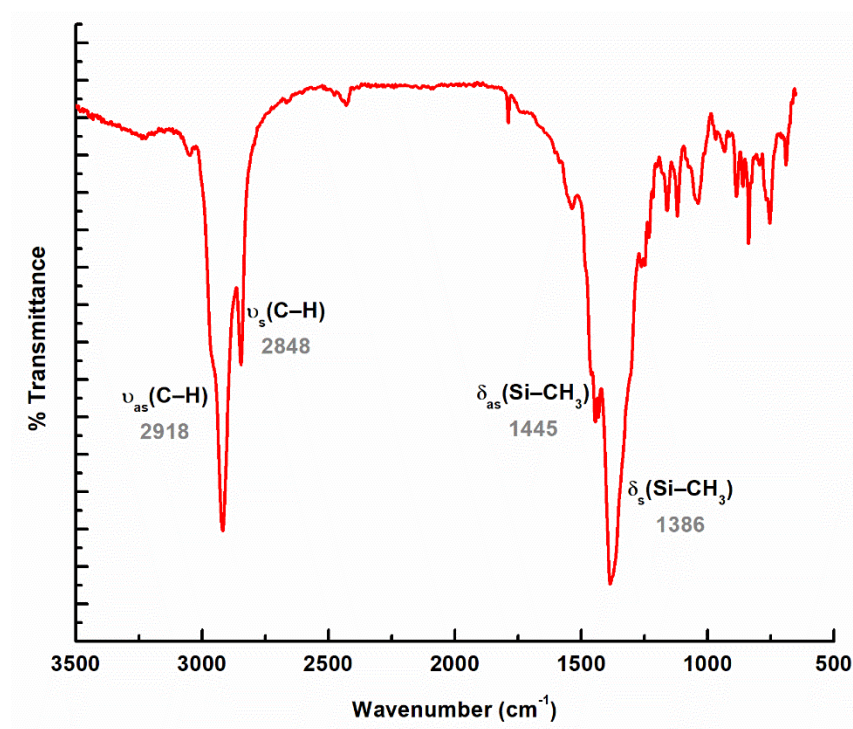


Figure 2.28. FT-IR spectrum for deposited polydimethylsilane $[\text{SiMe}_2]_n$ after precipitation from cold methanol and dried under high vacuum. ν = stretching mode; δ = deformation; as = asymmetric; s = symmetric. Assignments were made *via* comparison with previously reported polysilanes.^{25,26}

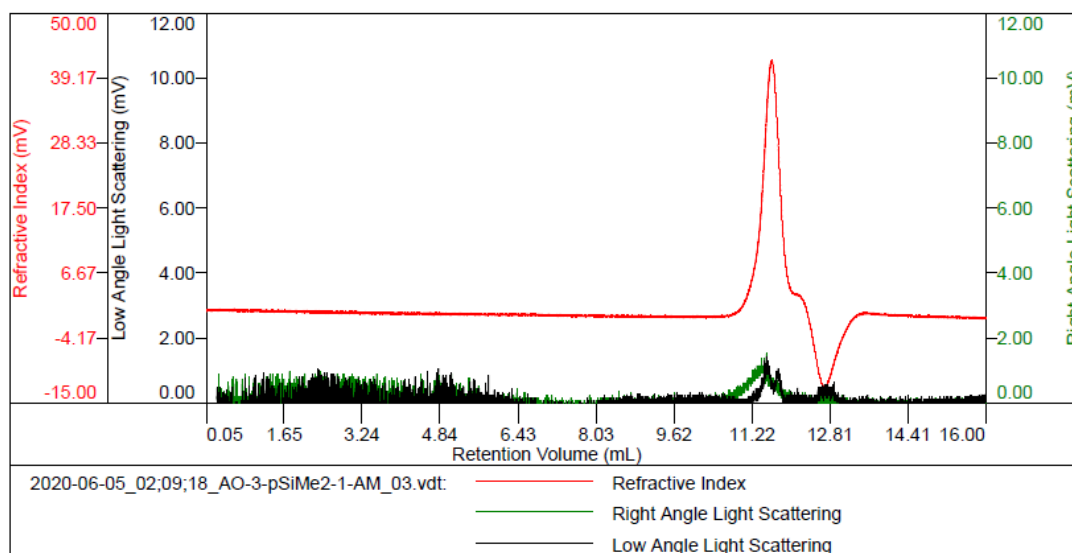


Figure 2.29. GPC elution profile for deposited polydimethylsilane $[\text{SiMe}_2]_n$. Note that negative peaks in the refractive index (RI) detector are artifacts of sample injection.

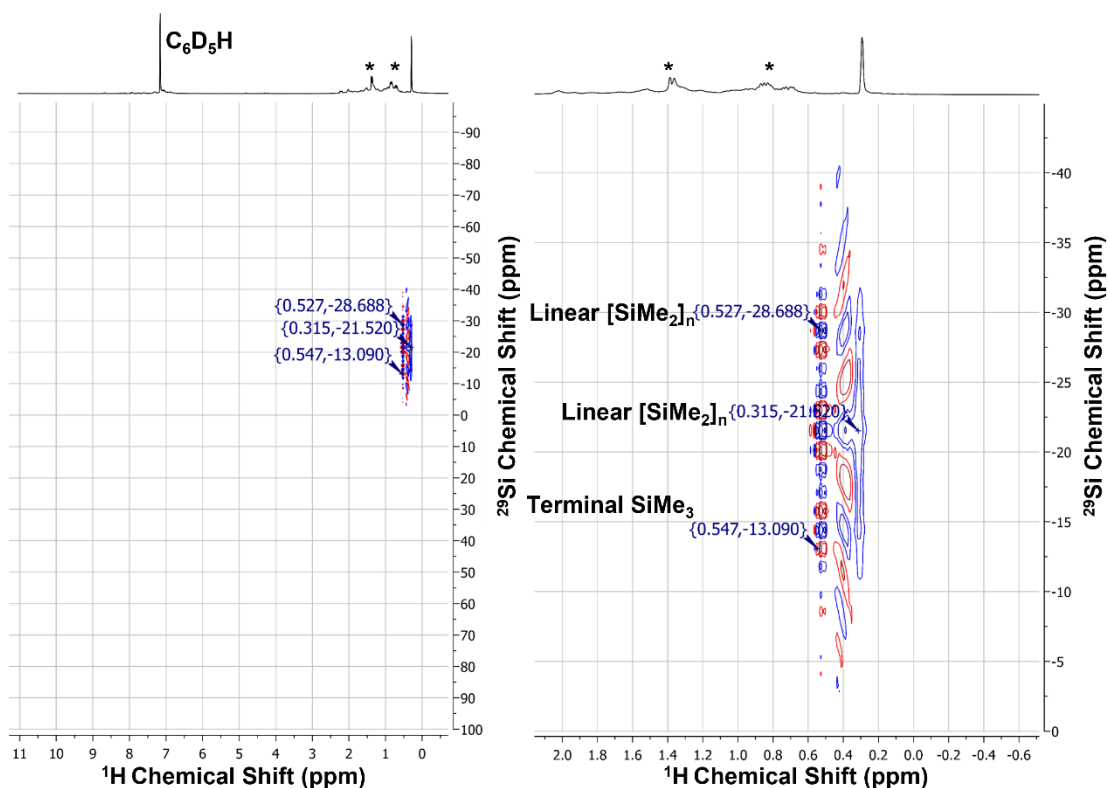


Figure 2.30. ^1H - ^{29}Si HMBC 2D NMR spectrum of deposited polydimethylsilane $[\text{SiMe}_2]_n$ in C_6D_6 .²⁷ Peaks labelled with an asterisk (*) are due to residual pentane.

^1H - ^{29}Si HMBC analysis is consistent with a predominantly linear polymer structure,²⁸ while GPC data shows unimodal distribution with a number average molecular weight (M_n) of 2.7 kDa (45 repeat units), and a polydispersity index (PDI) of 2.2. Zybill and co-workers have previously observed the extrusion of oligomeric $[\text{SiMe}_2]_x$ (molecular weight = 550 ± 10 Da by cryoscopy) upon heating their silicon-iron adduct $[(\text{Me}_2\text{N})_3\text{PO} \cdot \text{Me}_2\text{Si} \cdot \text{Fe}(\text{CO})_4]$ to 120 °C, releasing toxic $\text{OP}(\text{NMe}_2)_3$ and metal carbonyls in the process.²⁹ The current route to $[\text{SiMe}_2]_n$, a demonstrated precursor to silicon carbide,⁸ is a promising new direction for FLP chemistry. The synthetic protocol introduced here should provide future access to a wide range of poly(diorganotetrelanes) $[\text{GeR}_2]_n$ and $[\text{SiR}_2]_n$ of tuneable composition, where R = alkyl or aryl groups; this includes R groups that are incompatible with pre-existing harsh Wurtz coupling routes to poly(diorganotetrelanes), such as alkynyl groups.

2.3 Conclusions

This Chapter introduces the FLP-stabilized dihydrotetrelene adducts $[\text{PB}\{\text{GeH}_2\}]$ (**2**) and $[\text{PB}\{\text{SiH}_2\}]$ (**4**), and the diorganosilylene complex $[\text{PB}\{\text{SiMe}_2\}]$ (**5**). The E(II) dihydride complexes represent bottleable single-source precursors for the deposition of bulk Ge and Si upon mild heating in solution. Another hallmark of this work is the ability to isolate/recycle the FLP ligand (**PB**) after element deposition. To my knowledge, the deposition of Si at 110 °C from the single-source molecular Si(II) dihydride precursor **4** in solution represents the lowest temperature for such a process.

Finally, polydimethylsilane $[\text{SiMe}_2]_n$ (a precursor to silicon carbide) can be deposited from the diorganosilylene adduct $[\text{PB}\{\text{SiMe}_2\}]$ (**5**). Future work will involve development of new FLP-chelated substrates for low temperature deposition of other industrially relevant materials, such as boron nitride (BN).

2.4 Experimental Details

2.4.1 General Considerations

All reactions were performed using Schlenk and glovebox (Innovative Technology, Inc.) techniques. All solvents (except hexamethyldisiloxane and petroleum ether) were dried using a solvent purification system provided by Innovative Technology, Inc., degassed (freeze-pump-thaw method), and stored under nitrogen prior to use. Hexamethyldisiloxane and petroleum were refluxed over calcium hydride overnight under a N_2 atmosphere, distilled, and stored over 4 Å molecular sieves prior to use. Chlorodicyclohexylborane (ClBCy_2), chlorodiisopropylphosphine (ClIPr_2), $\text{Li}[\text{HBET}_3]$ (1.0 M solution in THF), Mes_2BF ($\text{Mes} = 2,4,6\text{-Me}_3\text{C}_6\text{H}_2$), trichlorosilane, MeLi (1.6 M solution in Et_2O), HCl (2.0 M solution in Et_2O), and $\text{Cl}_2\text{Ge}\cdot\text{dioxane}$ were obtained from Sigma-Aldrich and used as received. 1,2-Dibromobenzene was obtained from Oakwood Chemicals and used as received. $n\text{BuLi}$ (2.5 M solution in hexanes) was obtained from Sigma-Aldrich and titrated with *N*-benzyl benzamide prior to use.³⁰ Triethylamine was obtained from Sigma-Aldrich, degassed *via* three freeze-pump-thaw cycles, and stored in a Teflon-capped Schlenk flask over 4 Å molecular sieves prior to use. 1-1-Diisopropylphosphine-2-bromobenzene^{31,32} and MeIPr^{33} $[(\text{MeCNDipp})_2\text{C};$

Dipp = 2,6- $\text{Pr}_2\text{C}_6\text{H}_3$] were made according to literature procedures. ^1H , ^{11}B , $^{13}\text{C}\{^1\text{H}\}$, ^{29}Si and ^{31}P NMR spectra were recorded at room temperature using a Varian Inova-400, VNMRS-500, or VNMRS-700 spectrometer and referenced to Me_4Si (^1H , $^{13}\text{C}\{^1\text{H}\}$, ^{29}Si), 85 % H_3PO_4 (^{31}P), and 15 % $\text{F}_3\text{B}\cdot\text{OEt}_2$ (^{11}B). Chemical shifts are reported in parts per million (ppm) and coupling constants (J) are reported in Hertz (Hz). Elemental analyses and thermal gravimetric analyses were performed at the Analytical and Instrumentation Laboratory at the University of Alberta using the Thermo Flash 2000 Elemental Analyzer and the Perkin Elmer Pyris 1, respectively. Melting points were measured in sealed glass capillaries under nitrogen using MelTemp apparatus. Infrared (IR) spectra were recorded as Nujol mulls on a Nicolet IR100 FTIR spectrometer for **PB**, **2**, and **4**. FT-IR spectra of deposited polydimethylsilane $[\text{SiMe}_2]_n$ samples were recorded as solids with a Thermo Nicolet 8700 FTIR Spectrometer and Continuum Microscope. Raman spectroscopy on deposited Ge and Si was performed by analysis of the samples in sealed melting point tubes (20 \times objective lens) using a Renishaw inVia Raman microscope (laser excitation source was RL633 5 mW HeNe laser). Raman spectral acquisition settings were 632.8 nm laser, at 100 % power (5 mW), in static mode (10 seconds, with 18 accumulations for the deposited Ge Raman spectra and 15 accumulations for the deposited Si Raman spectra). All spectra were normalized for power, time and intensity. Raman data was acquired using Wire 3.4 software and plots were prepared using Origin 2020 software without the use of baseline correction.

Scanning electron microscopy (SEM) was carried out with a JEOL 6301F field emission SEM operated at an acceleration voltage of 5 kV. SEM samples of deposited Ge were prepared by drop-casting a slurry (~ 2 mg/mL) of the bulk element in hexanes onto an aluminum stub under N_2 , followed by evaporation of the solvent under vacuum. SEM samples of deposited Si were prepared by drop-casting a slurry of Si in hexanes onto carbon tape, followed by insertion of tape into SEM stage and removal of the hexanes under vacuum. SEM of samples of Ge or Si films were prepared by thermolysis of **2** or **4** in a sealed microwave tube at 110 °C in toluene for 20 hrs; specific details regarding sample preparation and purification can be found in Section 2.4.2. X-ray photoelectron spectroscopy (XPS) was performed using the following parameters: Kratos Axis Ultra instrument, 210 W, 10^{-7} Pa operating chamber pressure, with a monochromatic Al K source ($\lambda = 8.34$ Å) at an electron takeoff angle of 90°. XPS samples were prepared by drop-casting the bulk elements from slurries (~ 2 mg/mL) in petroleum ether onto copper stubs. All XPS spectra were processed using the CasaXPS (VAMAS) software package and referenced to advantageous carbon at C 1s = 284.8 eV. After calibration, a Shirley-type background correction was applied to all high-resolution peaks, except for the Ge 2p peaks, which were interpreted using a linear background. Gel permeation chromatography (GPC) was performed with a Viscotek VE 2001 autosampler, Viscotek T6000M column and a GPC 270 Max dual and Viscotek VE 3580 detectors [right and low angle light scattering and refractive index detection] using THF as an eluent at a flow rate of 0.5 mL/min. GPC calibration was performed before every sample batch with 99 kDa and 235 kDa polystyrene standards

obtained from Malvern. GPC analysis was performed using the OmniSEC 4.6 software package.

2.4.2 Synthetic Procedures

Synthesis of [$i\text{Pr}_2\text{P}(\text{C}_6\text{H}_4)\text{Li}(\text{OEt}_2)_x$]. This compound was made according to a modified literature procedure.⁴ $n\text{BuLi}$ (2.5 M solution in hexanes, 4.98 mL, 12 mmol) was added drop-wise to a solution of 1-diisopropylphosphino-2-bromobenzene (3.293 g, 12.05 mmol) in 10 mL of Et_2O at room temperature, resulting in a dark red solution. After stirring for 10 min at room temperature, the mixture was cooled to $-30\text{ }^\circ\text{C}$ for 16 hrs. This afforded [$i\text{Pr}_2\text{P}(\text{C}_6\text{H}_4)\text{Li}(\text{OEt}_2)_2$] as yellow X-ray quality crystals, which yielded a final Et_2O solvate content of [$i\text{Pr}_2\text{P}(\text{C}_6\text{H}_4)\text{Li}(\text{OEt}_2)_{0.72}$] after drying the crystals to constant weight (1.807 g, 59 %). ^1H NMR spectroscopy was used to determine the amount of coordinated Et_2O present; typical values of x in the formula above ranged from 0.7 to 0.8 equiv. The NMR data for [$i\text{Pr}_2\text{P}(\text{C}_6\text{H}_4)\text{Li}(\text{OEt}_2)_x$] matched those in the literature.⁴

Synthesis of $i\text{Pr}_2\text{P}(\text{C}_6\text{H}_4)\text{BMes}_2$ (PB^{Mes}).⁹ $n\text{BuLi}$ (2.80 M solution in hexanes, 3.50 mL, 9.80 mmol) was added drop-wise to a solution of 1-diisopropylphosphino-2-bromobenzene (2.703 g, 9.895 mmol) dissolved in 5 mL of Et_2O , cooled to $-40\text{ }^\circ\text{C}$. This resulted in a dark red-brown solution over a white precipitate. After decanting away the supernatant, the remaining solid, containing $i\text{Pr}_2\text{P}(\text{C}_6\text{H}_4)\text{Li}$, was dissolved in 5 mL of Et_2O , and a solution of Mes_2BF (2.768 g, 10.32 mmol) in 5 mL of Et_2O was added to

the reaction mixture at room temperature. After stirring the mixture for 8 hrs, the volatiles were removed under vacuum, the crude product was combined with 8 mL of toluene, and the mixture filtered through Celite. Removal of the solvent from the filtrate under vacuum yielded ${}^i\text{Pr}_2\text{P}(\text{C}_6\text{H}_4)\text{BMes}_2$ (**PB^{Mes}**) as a yellow solid (2.872 g, 63 %). X-ray quality crystals were grown by dissolving **PB^{Mes}** in hexanes, followed by cooling to $-30\text{ }^\circ\text{C}$ for 16 hrs. ${}^1\text{H}$ NMR spectra were collected at $-30\text{ }^\circ\text{C}$ to minimize rotational broadening from Mes groups; NMR spectra at room temperature matched those reported previously:⁹ ${}^1\text{H}$ NMR (399.9 MHz, $-30\text{ }^\circ\text{C}$, CDCl_3): $\delta = 7.51$ (d, ${}^3J_{\text{HH}} = 7.2$ Hz, 1H, ArH), 7.34-7.37 (m, 1H, ArH), 7.22-7.26 (m, 1H, ArH), 7.16-7.18 (m, 1H, ArH), 6.79 (s, 2H, Mes-CH), 6.75 (s, 1H, Mes-CH), 6.63 (s, 1H, Mes-CH), 2.29 (s, 3H, Mes- CH_3), 2.25 (s, 3H, Mes- CH_3), 2.22 (s, 3H, Mes- CH_3), 2.14 (s, 3H, Mes- CH_3), 2.00 (s, 3H, Mes- CH_3), 1.68 (s, 3H, Mes- CH_3), 1.27-1.32 (m, 2H, $\text{CH}(\text{CH}_3)_2$), 1.06 (dd, ${}^3J_{\text{HH}} = 6.4$ Hz, ${}^3J_{\text{HP}} = 13.9$ Hz, 3H, $\text{CH}(\text{CH}_3)_2$), 0.93-0.96 (m, 3H, $\text{CH}(\text{CH}_3)_2$), 0.77 (dd, ${}^3J_{\text{HH}} = 6.8$ Hz, ${}^3J_{\text{HP}} = 13.6$ Hz, 3H, $\text{CH}(\text{CH}_3)_2$), 0.49 (dd, ${}^3J_{\text{HH}} = 7.2$ Hz, ${}^3J_{\text{HP}} = 16.5$ Hz, 3H, $\text{CH}(\text{CH}_3)_2$). ${}^{13}\text{C}\{{}^1\text{H}\}$ NMR (100.6 MHz, $-30\text{ }^\circ\text{C}$, CDCl_3 ; assignments made *via* 2D ${}^1\text{H}$ - ${}^{13}\text{C}$ HSQC and HMBC experiments): $\delta = 157.8$ (d, ${}^1J_{\text{CP}} = 40.6$ Hz, $\text{C}_{\text{ipso-P}}$), 144.3 (s, $\text{C}_{\text{ipso-B}}$), 143.3 (s, CMes-B), 141.8 (s, MesC), 141.7 (s, MesC), 141.6 (s, MesC), 140.7 (d, $J_{\text{PC}} = 3.1$ Hz, ArC), 140.1 (s, MesC), 139.5 (s, MesC), 138.9 (d, $J_{\text{CP}} = 8.6$ Hz, ArC), 132.5 (s, ArC), 132.4 (s, ArC), 131.1 (d, $J_{\text{CP}} = 1.8$ Hz, ArC), 128.9 (s, ArC), 128.2 (s, MesCH), 128.1 (s, MesCH), 128.0 (s, MesCH), 127.8 (s, MesCH), 25.6 (d, ${}^1J_{\text{CP}} = 15.7$ Hz, $\text{CH}(\text{CH}_3)_2$), 24.5 (d, ${}^2J_{\text{CP}} = 5.4$ Hz, $\text{CH}(\text{CH}_3)_2$), 23.9 (s, Mes CH_3), 23.2 (d, ${}^1J_{\text{CP}} = 10.1$ Hz, $\text{CH}(\text{CH}_3)_2$), 22.6 (s, Mes CH_3), 22.5 (s, Mes CH_3), 22.3 (s, Mes CH_3), 21.9 (s,

MesCH₃), 21.8 (s, MesCH₃), 20.8 (d, ²J_{CP} = 12.2 Hz, CH(CH₃)₂), 20.6 (d, ²J_{CP} = 17.0 Hz, CH(CH₃)₂), 16.6 (s, CH(CH₃)₂). ³¹P{¹H} NMR (161.9 MHz, -30 °C, CDCl₃): δ = 3.9 (s, ⁱPr₂P) [Note: this resonance shifts to 5.5 ppm at room temperature]. ¹¹B{¹H} NMR (128.3 MHz, -30 °C, CDCl₃; FWHM = 50 Hz): δ = -12.4 (s, Mes₂B) [Note: this resonance shifts to 75.6 ppm at room temperature]. Anal. Calcd. for C₃₀H₄₀PB (%): C 81.44, H 9.11; Found: C 80.24, H 9.01. M.p. 139-142 °C.

Synthesis of ⁱPr₂P(C₆H₄)BCy₂ (PB). This ligand was prepared according to a modified literature procedure.⁴ Chlorodicyclohexylborane (1.718 mL, 7.839 mmol) was added drop-wise over 5 min at room temperature to a solution of [ⁱPr₂P(C₆H₄)Li(Et₂O)_x] (x = 0.72, 1.807 g, 7.1 mmol) in 10 mL of toluene, and the reaction mixture was stirred for 8 hrs at room temperature before removing the volatiles under vacuum. The product was extracted into 20 mL of Et₂O and the mixture was filtered through Celite. The solvent from the filtrate was then removed under vacuum to afford **PB** as a colorless air- and moisture-sensitive oil (2.29 g, 87 %). The NMR data for **PB** matched those reported previously.⁴ Colorless crystals of **PB** of suitable quality for single-crystal X-ray crystallography were grown from a concentrated solution of cold (-30 °C) Et₂O.

Synthesis of [PB{GeCl₂}] (1). A solution of Cl₂Ge•dioxane (144.3 mg, 0.6229 mmol) in 10 mL of toluene was added to a solution of ⁱPr₂P(C₆H₄)BCy₂ (**PB**) (230.6 mg, 0.6226 mmol) in 5 mL of toluene. After stirring the mixture for 12 hrs at room temperature, the volatiles were removed under vacuum. The resulting product was washed with 2 × 2

mL of petroleum ether and dried under vacuum to give [PB{GeCl₂}] (**1**) as a white solid (0.3013 g, 94 %). Colorless X-ray quality crystals of **1** were grown from a concentrated solution in cold (-30 °C) hexanes. ¹H NMR (699.8 MHz, C₆D₆): δ = 7.51 (dd, ³J_{HH} = 7.7 Hz, ³J_{HP} = 4.8 Hz, 1H, ArH), 7.21 (virtual t of d, ³J_{HH} = 7.8 Hz, ⁴J_{HP} = 1.4 Hz, 1H, ArH), 6.86-6.95 (m, 2H, ArH), 2.22 (d of septets, ³J_{HH} = 6.9 Hz, ²J_{HP} = 11.2 Hz, 2H, CH(CH₃)₂), 2.13-2.15 (m, 2H, H_{Cy}), 1.75-1.86 (m, 8H, H_{Cy}), 1.48-1.54 (m, 2H, H_{Cy}), 1.35-1.44 (m, 10H, H_{Cy}), 0.97 (dd, ³J_{HH} = 6.9 Hz, ³J_{HP} = 17.5 Hz, 6H, CH(CH₃)₂), 0.86 (dd, ³J_{HH} = 6.9 Hz, ³J_{HP} = 16.1 Hz, 6H, CH(CH₃)₂). ¹³C {¹H} NMR (100.6 MHz, C₆D₆): δ = 133.8 (d, J_{CP} = 10.4 Hz, ArC), 131.2 (d, J_{CP} = 4.3 Hz, ArC), 131.1 (d, J_{CP} = 2.6 Hz, ArC), 125.2 (d, J_{CP} = 7.7 Hz, ArC), 124.5 (s, ArC), 123.9 (s, ArC), 34.4 (s, BCy₂), 33.4 (br, BCy₂), 32.1 (s, BCy₂), 29.6 (s, BCy₂), 29.1 (s, BCy₂), 27.9 (s, BCy₂), 24.9 (d, ¹J_{CP} = 19.8 Hz, CH(CH₃)₂), 17.9 (s, CH(CH₃)₂), 17.6 (s, CH(CH₃)₂). ³¹P {¹H} NMR (161.9 MHz, C₆D₆): δ = -2.1 (s, ⁱPr₂P). ¹¹B {¹H} NMR (128.3 MHz, C₆D₆): δ = 17.7 (s, Cy₂B; FWHM = 22 Hz). Anal. Calcd. for C₂₄H₄₀BCl₂GeP (%): C 56.09, H 7.85; Found: C 56.01, H 7.78. M.p. 119-122 °C.

Synthesis of ⁱPr₂P(H)(C₆H₄)BCy₂(Cl) or [PB{HCl}]: A solution of HCl (2.0 M solution in Et₂O, 270 μL, 0.54 mmol) was added drop-wise to a solution of **PB** (205.7 mg, 0.5554 mmol) in 20 mL of toluene while stirring at -78 °C. After the reaction mixture was stirred at -78 °C for 1 hr, the mixture was warmed to room temperature, and the volatiles were removed under vacuum. The resulting solid was washed with 2 × 5 mL of petroleum ether and dried to give [PB{HCl}] as a white solid (0.1572 g, 70

%). Colorless X-ray quality crystals were grown from a concentrated solution of [PB{HCl}] in cold (-30 °C) hexanes. ¹H NMR (699.8 MHz, CDCl₃): δ = 8.22 (br d, ¹J_{PH} = 518 Hz, 1H, PH), 7.53-7.55 (m, 1H, ArH), 7.33-7.35 (m, 1H, ArH), 7.14-7.18 (m, 1H, ArH), 7.07-7.09 (m, 1H, ArH), 2.72 (br, 2H, CH(CH₃)₂), 1.71-1.74 (m, 2H, H_{Cy}), 1.50-1.59 (m, 6H, CH(CH₃)₂), 1.38-1.40 (m, 6H, CH(CH₃)₂), 1.22-1.29 (m, 6H, H_{Cy}), 1.10-1.14 (m, 4H, H_{Cy}), 0.99-1.02 (m, 2H, H_{Cy}), 0.87-0.89 (m, 4H, H_{Cy}), 0.78-0.80 (m, 4H, H_{Cy}). ¹³C{¹H} NMR (175.9 MHz, CDCl₃): δ = 136.1 (br, ArC), 130.9 (br, ArC), 130.3 (br, ArC), 124.2 (d, J_{CP} = 13.2 Hz, ArC), 119.3 (s, ArC), 118.9 (s, ArC), 34.6 (br, BCy₂), 30.5 (br, BCy₂), 29.2 (br, BCy₂), 27.9 (s, BCy₂), 23.9 (br d, ¹J_{CP} = 42.5 Hz, CH(CH₃)₂), 19.0 (br, CH(CH₃)₂), 17.7 (br, CH(CH₃)₂). ³¹P NMR (161.9 MHz, CDCl₃): δ = 30.5 (d, ¹J_{HP} = 526 Hz, ⁱPr₂PH). ¹¹B{¹H} NMR (128.3 MHz, CDCl₃): δ = 12.2 (br, Cy₂BCl; FWHM = 42 Hz). Anal. Calcd. for C₂₄H₄₁BPCl (%): C 70.86, H 10.16; Found: C 69.99, H 10.17. M.p. 162-164 °C.

Syntheses of [PB{GeH₂}] (2):

Step wise route to [PB{GeH₂}] (2), starting from 1. Li[HBET₃] (1.0 M solution in THF, 147.8 μL, 0.1 mmol) was added to a solution of [PB{GeCl₂}] (1) (30.8 mg, 0.0599 mmol) in 10 mL of Et₂O, resulting in a color change from colorless to orange. The reaction mixture was stirred for 1 hr at room temperature before the volatiles were removed under vacuum. The crude reaction mixture was then combined with 5 mL of hexanes, the mixture filtered through Celite, and the filtrate concentrated to a volume of 2 mL. Storage of this concentrated solution at -30 °C for 16 hrs gave [PB{GeH₂}]

(2) as a white microcrystalline solid (0.0197 g, 59 %). Colorless X-ray quality crystals of 2 were grown from a concentrated solution of cold (-30 °C) Me₃SiOSiMe₃. ¹H NMR (399.9 MHz, C₆D₆): δ = 7.82 (dd, ³J_{HH} = 7.8 Hz, J_{HP} = 3.2 Hz, 1H, ArH), 7.26-7.30 (m, 1H, ArH), 6.96-7.00 (m, 1H, ArH), 6.87-6.90 (m, 1H, ArH), 3.81 (s, 2H, GeH₂), 2.19-2.22 (m, 2H, H_{Cy}), 1.83 (septet, partially buried, ³J_{HH} = 7.1 Hz, 2H, CH(CH₃)₂), 1.81-1.96 (m, 8H, H_{Cy}), 1.24-1.65 (m, 10H, H_{Cy}), 1.00-1.12 (m, 2H, H_{Cy}), 0.85 (dd, ³J_{HH} = 7.3 Hz, ³J_{HP} = 16.2 Hz, 6H, CH(CH₃)₂), 0.72 (dd, ²J_{HH} = 7.3 Hz, ³J_{HP} = 16.2 Hz, 6H, CH(CH₃)₂). ¹³C{¹H} NMR (125.7 MHz, C₆D₆): δ = 135.2 (d, J_{CP} = 13.8 Hz, ArC), 130.6 (d, J_{CP} = 2.5 Hz, ArC), 129.8 (d, J_{CP} = 6.3 Hz, ArC), 129.5 (s, ArC), 128.9 (s, ArC), 124.7 (d, J_{CP} = 7.5 Hz, ArC), 35.4 (s, BCy₂), 34.2 (br, BCy₂), 32.8 (s, BCy₂), 30.0 (s, BCy₂), 29.8 (s, BCy₂), 28.6 (s, BCy₂), 24.8 (d, ¹J_{CP} = 22.6 Hz, CH(CH₃)₂), 18.7 (s, CH(CH₃)₂), 18.4 (s, CH(CH₃)₂). ³¹P{¹H} NMR (161.9 MHz, C₆D₆): δ = 34.1 (s, ⁱPr₂P). ¹¹B{¹H} NMR (128.3 MHz, C₆D₆): δ = 2.8 (br, Cy₂B; FWHM = 51 Hz). IR (Nujol mull, cm⁻¹): 1990 (s, νGe-H). Anal. Calcd. for C₂₄H₄₂BGeP (%): C 64.78, H 9.51; Found: C 64.96, H 9.49. M.p. 98-99 °C.

One-pot procedure to [PB{GeH₂}] (2), starting from PB. A solution of Cl₂Ge•dioxane (316.8 mg, 1.367 mmol) in 10 mL of Et₂O was added to a solution of 1,2-ⁱPr₂P(C₆H₄)BCy₂ (PB) (505.4 mg, 1.365 mmol) in 300 mL of Et₂O. The reaction mixture was stirred for 12 hrs and then Li[HBET₃] (1.0 M solution in THF, 2.75 mL, 2.7 mmol) was added drop-wise. After stirring the mixture at room temperature for 3 hrs, the precipitate was allowed to settle for 30 min and the mother liquor was decanted and

filtered through a Celite-packed frit. The volatiles were removed from the filtrate under vacuum, and the resulting solid was then washed 3×2 mL of cold (-30 °C) hexanes to yield $[\text{PB}\{\text{GeH}_2\}]$ (**2**) as a white powder (0.2354 g, 39 %). NMR data for this product matched that obtained in the step wise procedure described above.

Syntheses of $[\text{PB}\{\text{SiCl}_2\}]$ (**3**):

Procedure A (from PB and $^{\text{Me}}\text{IPr}/\text{HSiCl}_3$). HSiCl_3 (41.5 μL , 0.411 mmol) was added to a rapidly stirring solution containing $^i\text{Pr}_2\text{P}(\text{C}_6\text{H}_4)\text{BCy}_2$ (**PB**) (152.0 mg, 0.4104 mmol) and $^{\text{Me}}\text{IPr}$ (171.1 mg, 0.4110 mmol) in 18 mL of toluene, resulting in the immediate precipitation of $[\text{MeIPrH}]\text{Cl}$. After 15 min, 0.5 g of pre-dried silica gel was added and the mixture was stirred for 5 min. The precipitate/silica gel was allowed to settle and the mother liquor was filtered through a 2 cm plug of silica gel in a glass fiber-packed pipette. The volatiles were removed from the filtrate to give $[\text{PB}\{\text{SiCl}_2\}]$ (**3**) as an analytically pure white solid (0.0328 g, 17 %). Colorless X-ray quality crystals of $[\text{PB}\{\text{SiCl}_2\}]$ (**3**) were grown from a concentrated solution of cold (-30 °C) hexanes. ^1H NMR (399.9 MHz, C_6D_6): $\delta = 7.78$ (dd, $^3J_{\text{HH}} = 7.6$ Hz, $J_{\text{HP}} = 4.0$ Hz, 1H, *ArH*), 7.23-7.26 (m, 1H, *ArH*), 6.90-6.92 (m, 1H, *ArH*), 6.84-6.86 (m, 1H, *ArH*), 2.00-2.15 (m, 4H, $\text{CH}(\text{CH}_3)_2$ and H_{Cy}), 1.86-1.94 (m, 8H, H_{Cy}), 1.66-1.74 (m, 4H, H_{Cy}), 1.35-1.61 (m, 5H, H_{Cy}), 1.08-1.32 (m, 3H, H_{Cy}), 0.86 (dd, $^3J_{\text{HH}} = 6.8$ Hz, $^3J_{\text{HP}} = 16.0$ Hz, 6H, $\text{CH}(\text{CH}_3)_2$), 0.82 (dd, $^3J_{\text{HH}} = 7.2$ Hz, $^3J_{\text{HP}} = 16.0$ Hz, 6H, $\text{CH}(\text{CH}_3)_2$). $^{13}\text{C}\{^1\text{H}\}$ NMR (175.9 MHz, C_6D_6): $\delta = 135.6$ (d, $J_{\text{CP}} = 11.4$ Hz, *ArC*), 131.2 (d, $J_{\text{CP}} = 2.8$ Hz, *ArC*), 130.4 (d, $J_{\text{CP}} = 6.2$ Hz, *ArC*), 129.1 (s, *ArC*), 128.5 (s, *ArC*), 124.5 (d, $J_{\text{CP}} = 8.6$ Hz, *ArC*), 34.5 (s,

BCy₂), 32.8 (br, BCy₂), 32.0 (s, BCy₂), 30.1 (s, BCy₂), 29.7 (s, BCy₂), 28.5 (s, BCy₂), 24.2 (d, ¹J_{CP} = 24.5 Hz, CH(CH₃)₂), 17.8 (s, CH(CH₃)₂), 17.5 (s, CH(CH₃)₂). ³¹P{¹H} NMR (161.9 MHz, C₆D₆): δ = -5.4 (s, ⁱPr₂P). ¹¹B{¹H} NMR (128.3 MHz, C₆D₆): δ = -4.3 (br, Cy₂B; FWHM = 163 Hz). ²⁹Si{¹H} (79.4 MHz, C₆D₆): δ = 53.8 (d, ¹J_{PSi} = 117 Hz, SiCl₂). Anal. Calcd. for C₂₄H₄₀BCl₂SiP (%): C 61.42, H 8.59; Found: C 62.19, H 8.81. M.p. 111-113 °C.

Procedure B (from [PB{HCl}] and excess Et₃N/HSiCl₃). HSiCl₃ (5.14 mL, 50.8 mmol) was added at room temperature to a solution of ⁱPr₂P(H)(C₆H₄)BCy₂(Cl) [PB{HCl}] (206.8 mg, 0.5083 mmol) in 100 mL of a 1:4 toluene:Et₂O mixture. Then, Et₃N (7.10 mL, 50.9 mmol) was added quickly to the reaction mixture, leading to the precipitation of a yellow solid over the span of 10 min. After stirring at room temperature for another 8 hrs, the reaction mixture was subjected to cannula filtration to give a colorless solution. The volatiles were removed from the filtrate under vacuum, then the product was extracted with 2 × 5 mL of toluene, followed by 2 × 5 mL of Et₂O. The extracts were combined and the solvents were then removed under vacuum to give a white solid. This product was dissolved in 10 mL of hexanes, filtered, and then the filtrate was concentrated to a final volume of 1 mL. Cooling this solution for 16 hrs at -30 °C gave colorless crystals of [PB{SiCl₂}] (**3**) (0.0832 g, 35 %). The NMR data for [PB{SiCl₂}] (**3**) synthesized using this procedure (B) matched the data listed above for Procedure A.

Synthesis of [PB{SiH₂}] (4). Li[HBET₃] (1.0 M solution in THF, 81.0 μ L, 0.081 mmol) was added to a stirring solution of [PB{SiCl₂}] (3) (19.0 mg, 0.0405 mmol) in 10 mL of Et₂O, resulting in the formation of a white precipitate after 5 min. The reaction mixture was then stirred for another 1 hr and the volatiles were removed under vacuum. 5 mL of hexanes was then added and the mixture was filtered through Celite. The filtrate was concentrated to a volume of 2 mL and cooled to -30 °C for 16 hrs to yield [PB{SiH₂}] (4) as colorless crystals of suitable quality for single-crystal X-ray crystallography (0.0139 g, 86 %). ¹H NMR (399.9 MHz, C₆D₆): δ = 7.87 (dd, ³J_{HH} = 7.6 Hz, J_{HP} = 2.8 Hz, 1H, ArH), 7.28-7.31 (m, 1H, ArH), 6.97-6.99 (m, 1H, ArH), 6.84-6.86 (m, 1H, ArH), 3.59 (d, ²J_{HP} = 3.6 Hz with ²⁹Si-¹H satellites ¹J_{Hsi} = 161 Hz, 2H, SiH₂), 2.19-2.22 (m, 2H, H_{Cy}), 1.81-2.00 (m, 10H, CH(CH₃)₂ and H_{Cy}), 1.60-1.69 (m, 2H, H_{Cy}), 1.24-1.55 (m, 6H, H_{Cy}), 1.08-1.23 (m, 4H, H_{Cy}), 0.81 (dd, ³J_{HH} = 7.2 Hz, ³J_{HP} = 16.0 Hz, 6H, CH(CH₃)₂), 0.72 (dd, ³J_{HH} = 7.2 Hz, ³J_{HP} = 16.4 Hz, 6H, CH(CH₃)₂). ¹³C{¹H} NMR (175.9 MHz, C₆D₆): δ = 135.7 (d, J_{CP} = 14.8 Hz, ArC), 130.8 (d, J_{CP} = 2.8 Hz, ArC), 129.7 (s, ArC), 129.5 (d, J_{CP} = 6.9 Hz, ArC), 129.1 (br, ArC), 124.7 (d, J_{CP} = 8.4 Hz, ArC), 35.7 (s, BC_{y2}), 34.3 (br, BC_{y2}), 33.1 (s, BC_{y2}), 30.2 (s, BC_{y2}), 30.0 (s, BC_{y2}), 28.7 (s, BC_{y2}), 24.3 (d, ¹J_{CP} = 26.7 Hz, CH(CH₃)₂), 18.5 (s, CH(CH₃)₂), 18.0 (s, CH(CH₃)₂). ³¹P{¹H} NMR (161.9 MHz, C₆D₆): δ = 29.7 (s, ⁱPr₂P). ¹¹B{¹H} NMR (128.3 MHz, C₆D₆): δ = -4.2 (br, Cy₂B; FWHM = 106 Hz). ²⁹Si (79.4 MHz, C₆D₆): δ = -84.0 (t, ¹J_{Hsi} = ca. 158 Hz, SiH₂). IR (Nujol mull, cm⁻¹): 2107 (s, ν Si-H). Anal. Calcd. for C₂₄H₄₂BSiP (%): C 71.98, H 10.57; Found: C 71.63, H 10.42. M.p. 93-95 °C.

Synthesis of [PB{SiMe₂}] (5). MeLi (1.6 M solution in Et₂O, 187 μ L, 0.29 mmol) was added to a solution of [PB{SiCl₂}] (3) (70.2 mg, 0.149 mmol) in 50 mL of Et₂O at -78 °C, resulting in a small amount of white precipitate. The reaction mixture was stirred for 25 min at -78 °C before warming up to room temperature. At this point, the volatiles were removed (under vacuum) from the white slurry. The crude reaction mixture was combined with 5 mL of hexanes and filtered through Celite; the filtrate was then concentrated to a volume of 2 mL. Storage of this concentrated solution at -30 °C for 16 hrs gave [PB{SiMe₂}] (5) as a white microcrystalline solid (0.0446 mg, 70 %). X-ray quality crystals of 5 were grown from a concentration solution in cold (-30 °C) hexanes. ¹H NMR (399.9 MHz, C₆D₆): δ = 7.94 (dd, ³J_{HH} = 7.6 Hz, J_{HP} = 2.8 Hz, 1H, ArH), 7.28-7.32 (m, 1H, ArH), 6.97-7.00 (m, 1H, ArH), 6.89-6.93 (m, 1H, ArH), 1.88-2.00 (m, 12H, H_{Cy} and CH(CH₃)₂), 1.51-1.64 (m, 4H, H_{Cy}), 1.40-1.46 (m, 2H, H_{Cy}), 1.29-1.36 (m, 3H, H_{Cy}), 0.88-0.97 (m, 3H, H_{Cy}), 0.79 (dd, ³J_{HH} = 6.4 Hz, ³J_{HP} = 17.6 Hz, 6H, CH(CH₃)₂), 0.78 (dd, ³J_{HH} = 6.8 Hz, ³J_{HP} = 15.6 Hz, 6H, CH(CH₃)₂), 0.56 (d, ³J_{HP} = 9.9 Hz, 6H, Si(CH₃)₂). ¹³C {¹H} NMR (175.9 MHz, C₆D₆): δ = 135.7 (d, J_{CP} = 13.4 Hz, ArC), 130.2 (s, ArC), 129.8 (d, J_{CP} = 5.9 Hz, ArC), 128.9 (s, ArC), 128.5 (s, ArC), 123.9 (d, J_{CP} = 8.1 Hz, ArC), 35.4 (s, BCy₂), 34.1 (s, BCy₂), 32.8 (s, BCy₂), 30.5 (s, BCy₂), 30.1 (s, BCy₂), 28.9 (s, BCy₂), 24.2 (d, ¹J_{CP} = 22.5 Hz, CH(CH₃)₂), 18.6 (s, CH(CH₃)₂), 18.1 (s, CH(CH₃)₂), 0.4 (d, ²J_{CP} = 8.1 Hz, Si(CH₃)₂). ³¹P {¹H} NMR (161.9 MHz, C₆D₆): δ = 10.2 (br, ⁱPr₂P). ¹¹B {¹H} NMR (128.3 MHz, C₆D₆): δ = -9.0 (br, Cy₂B; FWHM = 60 Hz). ²⁹Si {¹H} (79.4 MHz, C₆D₆): δ = 15.9 (br, Si(CH₃)₂). Anal. Calcd. for C₂₆H₄₆BSiP (%): C 72.88, H 10.82; Found: C 71.58, H 10.31. M.p. 165-167 °C.

Thermolysis of [PB{GeH₂}] (2):

Procedure A – For SEM/EDX/IR/Raman analysis of bulk Ge(0). A sample of [PB{GeH₂}] (2) (23.1 mg, 0.0449 mmol) was dissolved in 600 μ L of toluene. Then, the solution was transferred into a Teflon-capped J-Young NMR tube, sealed under N₂ and heated to 110 °C using an oil bath. After 10 hrs, the reaction mixture was examined by ³¹P{¹H} NMR to confirm full conversion from [PB{GeH₂}] (2) to **PB**. Afterwards, the mixture was transferred to a vial, and a further 3 \times 5 mL of hexanes was used to extract the slurried contents of the NMR tube. The extracts were combined and the precipitate allowed to settle. The mother liquor (containing **PB**) was decanted away from the deposited Ge(0), and the remaining precipitate was further washed with 2 \times 5 mL of hexanes (allowing the precipitate to settle for 30 min in between washes). Drying under high vacuum gave bulk Ge(0) as a light brown solid. Recovery of **PB** from combined organic fractions: 14.3 mg, 74 %. Mass of Ge(0) recovered: 3.4 mg, 90 %.

Procedure B – For SEM/EDX analysis of Ge films: A sample of [PB{GeH₂}] (2) (23.6 mg, 0.0530 mmol) was dissolved in 5.00 mL of toluene in a glovebox. The resulting solution of **2** (1.06×10^{-2} M) was filtered through a piece of glass fiber filter paper into a microwave tube containing a <100> oriented N-type Si wafer substrate (University Wafer, 4” size, 500 μ m thickness with surface oxide). The microwave tube was then sealed with a Teflon cap, brought outside of the glovebox and heated to 110 °C for 20 hrs using an oil bath. Once cooled to room temperature, the microwave tube

was brought inside of the glovebox, unsealed and the mother liquor decanted. The remaining Ge-coated Si substrate was washed with 3×5 mL of hexanes (to remove residual **PB**) and dried under high vacuum. The surface of the Ge-covered Si wafer was then scratched with an “X” pattern using the tip of a stainless steel (1.2 mm diameter) needle.

Thermolysis of [PB{SiH₂}] (4):

Procedure A – For SEM/EDX/IR analysis of bulk Si(0): A sample of [PB{SiH₂}] (4) (21.6 mg, 0.0490 mmol) was dissolved in 0.600 mL of toluene in a glovebox. The solution was then transferred into to a Teflon-capped J-Young NMR tube and heated to 110 °C using an oil bath. After 10 hrs, the reaction mixture was analyzed by ³¹P{¹H} NMR to confirm full conversion of [PB{SiH₂}] (4) to **PB**. Afterwards, the contents of the NMR tube were transferred into a vial in a glovebox; further extraction of the material in the NMR tube was accomplished using 3×5 mL of hexanes. The extracts were combined and the precipitate was allowed to settle. The mother liquor was decanted away (to separate **PB** from the deposited Si(0)), and the precipitate was washed again with 2×5 mL of hexanes, each time allowing 30 min for the Si(0) precipitate to settle. The sample of Si(0) was then dried under high vacuum to give Si(0) as a light yellow solid. Recovery of **PB** from the organic fractions: 13.3 mg, 73 %. Mass of Si(0) recovered: 1.1 mg, 80 %.

Procedure B – For SEM/EDX analysis of Si films. A sample of [PB{SiH₂}] (**4**) (42.5 mg, 0.114 mmol) was dissolved in 3.00 mL of toluene in a glovebox. The solution (3.22 × 10⁻² M) was filtered through a piece of glass fiber filter paper into a microwave tube containing a <100> oriented P-type Ge wafer substrate (University Wafer, 4” size, 175 μm thickness with surface oxide). The microwave tube was sealed with a Teflon cap, brought outside of the glovebox and heated to 110 °C for 20 hrs using an oil bath. Once cooled to room temperature, the microwave tube was brought inside of the glovebox, unsealed and the remaining solution decanted away from the Si-coated wafer. The wafer was washed with 3 × 5 mL of hexanes (solvent filtered beforehand through a pipette packed with Celite on top of a piece of glass fiber filter paper) in order to remove residual **PB**, and the Si-covered Si wafer was dried under high vacuum. Lastly, the Si-covered wafer was scratched with an “X” pattern using the tip of a stainless steel (1.2 mm diameter) needle.

Thermolysis of [PB{SiMe₂}] (5**).** A solution of [PB{SiMe₂}] (**5**) (46.3 mg, 0.108 mmol) in 0.600 mL of toluene was prepared in a glovebox and transferred into a Teflon-capped J-Young NMR tube. The sample was then heated to 110 °C using an oil bath, after 15 hrs, the mixture was analyzed by ³¹P{¹H} NMR spectroscopy, which showed a 77 % conversion of [PB{SiMe₂}] (**5**) into **PB**. Afterwards, the yellow mixture in the tube was slurried together and transferred to a vial in a glovebox, followed by the removal of the volatiles under vacuum. The remaining solid in the vial was washed with 3 × 5 mL of hexanes in order to remove **PB** and any remaining/unreacted [PB{SiMe₂}]

(5). The remaining precipitate, containing $[\text{SiMe}_2]_n$, was dissolved in 1 mL of THF and the polymer was into 20 mL of rapidly stirring pentane at $-30\text{ }^\circ\text{C}$. Drying the isolated precipitate under vacuum gave $[\text{SiMe}_2]_n$ as a white solid (0.0018 g, 29 %). ^1H NMR (399.9 MHz, C_6D_6): $\delta = 0.55$ (br, terminal $\text{Si}(\text{CH}_3)_3$), 0.53 (br, linear $\text{Si}(\text{CH}_3)_2$), 0.31 (br, linear $\text{Si}(\text{CH}_3)_2$). $^{29}\text{Si}\{^1\text{H}\}$ (79.4 MHz, C_6D_6): $\delta = -11.8$ to -16.7 (br, terminal $\text{Si}(\text{CH}_3)_3$), -18.5 to -24.2 (br, linear $\text{Si}(\text{CH}_3)_2$), -26.0 to -31.3 (br, linear $\text{Si}(\text{CH}_3)_2$); these resonances were detected by a 2D ^1H - ^{29}Si HMBC experiment. IR (neat, cm^{-1}): 2918 (s, $\nu_{\text{as}}\text{C-H}$), 2848 (m, $\nu_{\text{s}}\text{C-H}$), 1445 (m, $\delta_{\text{as}}\text{Si-CH}_3$), 1386 (s, $\delta_{\text{s}}\text{Si-CH}_3$). GPC (in THF): $M_n = 2.7$ kDa (45 repeat units), PDI = 2.2.

2.4.3 X-ray Crystallography

Appropriate X-ray quality crystals were coated with a small amount of hydrocarbon oil (Paratone-N) and removed from the glovebox in a vial. Crystals were quickly mounted onto a glass fiber and placed in a low temperature stream of nitrogen on the X-ray diffractometer. All data was collected using a Bruker APEX II CCD detector/D8 or PLATFORM diffractometer using Mo $\text{K}\alpha$ (0.71073 Å) or Cu $\text{K}\alpha$ (1.54178 Å) radiation, with the crystals cooled to $-80\text{ }^\circ\text{C}$ or $-100\text{ }^\circ\text{C}$. The data was corrected for absorption through Gaussian integration from the indexing of crystal faces.³⁴ Crystal structures were solved using intrinsic phasing (SHELXT)³⁵ and refined using SHELXL-2014.³⁶ The assignment of hydrogen atom positions are based on the sp^2 - or sp^3 -hybridization geometries of their attached carbon atoms and were given thermal parameters 20 % greater than those of their parent atoms. Molecular structures

are shown with thermal ellipsoids at a 30 % probability level and have been generated using SHELXP.

Table 2.1. X-ray crystallographic data for [ⁱPr₂P(C₆H₄)Li(OEt₂)₂], **PB^{Mes}** and **PB**.

Compound	[ⁱ Pr ₂ P(C ₆ H ₄)Li(OEt ₂) ₂]	PB^{Mes}	PB
Formula	C ₃₂ H ₅₆ Li ₂ O ₂ P ₂	C ₃₀ H ₄₀ BP	C ₂₄ H ₄₀ BP
Formula weight	548.58	442.40	370.34
Crystal system	Monoclinic	Monoclinic	Monoclinic
Space group	<i>P2₁/c (No.14)</i>	<i>P2₁/c (No. 14)</i>	<i>P2₁/c (No.14)</i>
Crystal dimensions (mm)	0.37×0.30×0.19	0.35×0.20×0.06	0.21×0.24×0.34
<i>a</i> (Å)	9.7585(12)	19.8298(7)	23.2790(5)
<i>b</i> (Å)	15.3613(19)	8.0265(3)	9.7656(2)
<i>c</i> (Å)	12.4399(16)	17.8198(6)	21.3411(4)
α (°)	90	90	90
β (°)	109.819(2)	108.756(3)	111.8493(8)
γ (°)	90	90	90
<i>V</i> (Å ³)	1754.3(4)	2685.65(17)	4503.04(16)
<i>Z</i>	2	4	8
ρ (g/cm ³)	1.039	1.094	1.093
Abs coeff (mm ⁻¹)	0.147	0.990	1.085
<i>T</i> (°C)	-80	-100	-100
2 θ_{\max} (°)	106.52	140.10	148.32
Total data	15724	16110	23449
Unique data	4054 (0.0262)	5117 (0.0489)	9153 (0.0179)
Obs data [<i>I</i> >2 σ (<i>I</i>)] ^a	3367	4080	8643
Params	172	295	524 ^b
<i>R</i> ₁ [<i>I</i> >2 σ (<i>I</i>)] ^a	0.0464	0.0447	0.0382
<i>wR</i> ₂ [all data] ^a	0.1372	0.1214	0.1061
Max/min $\Delta\rho$ (e ⁻ Å ⁻³)	0.369/-0.340	0.257/-0.250	0.302/-0.235

^a $R_1 = \frac{\sum||F_o| - |F_c||}{\sum|F_o|}$; $wR_2 = [\frac{\sum w(F_o^2 - F_c^2)^2}{\sum w(F_o^4)}]^{1/2}$.

^bDue to disorder in the cyclohexyl rings, C31C–C32C, C32C–C33C, C33C–C34C, C34C–C35C, C35C–C36C, C36C–C31C were restrained to be approximately the same as C31A–C32A, C32A–C33A, C33A–C34A, C34A–C35A, C35A–C36A, C36A–C31A by use of SHELXL **SAME** instruction (total of twelve restraints). In addition, C31C to C36C were refined isotropically.

Table 2.2. X-ray crystallographic data for [PB{HCl}], [PB{GeCl₂}] (1) and [PB{GeH₂}] (2).

Compound	[PB{HCl}]	[PB{GeCl ₂ }] (1)	[PB{GeH ₂ }] (2)
Formula	C ₂₄ H ₄₁ BClP	C ₂₄ H ₄₀ BCl ₂ GeP	C ₂₄ H ₄₂ BGeP
Formula weight	444.94	513.83	444.94
Crystal system	Orthorhombic	Orthorhombic	Orthorhombic
Space group	<i>Pbca</i> (No. 61)	<i>P2₁2₁2₁</i> (No. 19)	<i>Pbca</i> (No. 61)
Crystal dimensions (mm)	0.23×0.14×0.05	0.35×0.20×0.06	0.23×0.14×0.05
<i>a</i> (Å)	21.4197(5)	10.3795(3)	21.4197(5)
<i>b</i> (Å)	9.6386(2)	13.8844(4)	9.6386(2)
<i>c</i> (Å)	23.2674(6)	17.6615(5)	23.2674(6)
α (°)	90	90	90
β (°)	90	90	90
γ (°)	90	90	90
<i>V</i> (Å ³)	4803.69(19)	2545.25(13)	4803.69(19)
<i>Z</i>	8	4	8
ρ (g/cm ³)	1.230	1.341	1.230
Abs coeff (mm ⁻¹)	2.381	4.208	2.381
<i>T</i> (°C)	-100	-100	-100
$2\theta_{\max}$ (°)	144.79	147.78	144.79
Total data	31381	11116	31381
Unique data	4747 (0.0194)	4981 (0.0265)	4747 (0.0194)
Obs data [<i>I</i> >2 σ (<i>I</i>)] ^a	4496	4916	4496
Params	252 ^b	262	252
<i>R</i> ₁ [<i>I</i> >2 σ (<i>I</i>)] ^a	0.0242	0.0222	0.0242
<i>wR</i> ₂ [all data] ^a	0.0703	0.0572	0.0703
Max/min $\Delta\rho$ (e ⁻ Å ⁻³)	0.314/-0.338	0.453/-0.650	0.314/-0.338

$$^a R_1 = \frac{\sum ||F_o| - |F_c||}{\sum |F_o|}; wR_2 = \left[\frac{\sum w(F_o^2 - F_c^2)^2}{\sum w(F_o^4)} \right]^{1/2}.$$

^bThe B1–C31A and B1–C31B distances were restrained to be approximately the same by use of the SHELXL **SADI** instruction.

Table 2.3. X-ray crystallographic data for [PB{SiCl₂}] (3), [PB{SiH₂}] (4), and [PB{SiMe₂}] (5).

Compound	[PB{SiCl ₂ }] (3)	[PB{SiH ₂ }] (4)	[PB{SiMe ₂ }] (5)
Formula	C ₂₄ H ₄₀ BCl ₂ SiP	C ₂₄ H ₄₂ BSiP	C ₂₆ H ₄₆ BSiP
Formula weight	469.33	400.44	428.50
Crystal system	Monoclinic	Orthorhombic	Monoclinic
Space group	<i>P2₁/n</i> (No.14)	<i>Pbca</i> (No.61)	<i>P2₁/n</i> (No.14)
Crystal dimensions (mm)	0.22×0.20×0.16	0.21×0.09×0.05	0.13×0.13×0.04
<i>a</i> (Å)	9.8646(2)	21.3338(4)	9.8524(2)
<i>b</i> (Å)	15.4576(3)	9.6408(2)	15.3657(3)
<i>c</i> (Å)	17.0757(4)	23.2679(5)	17.3786(4)
α (°)	90	90	90
β (°)	102.3442 (10)	90	100.8580(10)
γ (°)	90	90	90
<i>V</i> (Å ³)	2543.56(9)	4785.62(17)	2583.83(9)
<i>Z</i>	4	8	4
ρ (g/cm ³)	1.226	1.112	1.102
Abs coeff (mm ⁻¹)	3.390	1.517	1.433
<i>T</i> (°C)	-100	-80	-100
2 θ _{max} (°)	148.13	148.44	140.68
Total data	110565	151723	17029
Unique data	5110 (0.0341)	4792 (0.1072)	4928 (0.0345)
Obs data [<i>I</i> >2 σ (<i>I</i>)] ^a	4866	4154	4237
Params	266	256	264
<i>R</i> ₁ [<i>I</i> >2 σ (<i>I</i>)] ^a	0.0275	0.0339	0.0382
w <i>R</i> ₂ [all data] ^a	0.0741	0.0917	0.1082
Max/min $\Delta\rho$ (e ⁻ Å ⁻³)	0.297/-0.384	0.275/-0.309	0.344/-0.265

$$^aR_1 = \frac{\sum||F_o| - |F_c||}{\sum|F_o|}; wR_2 = [\frac{\sum w(F_o^2 - F_c^2)^2}{\sum w(F_o^4)}]^{1/2}.$$

2.5 References and Notes

1. For recent advances and reviews, see: a) P. P. Power, *Nature* **2010**, *463*, 171–177; b) R. Rodriguez, D. Gau, Y. Contie, T. Kato, N. Saffon-Merceron, A. Baceiredo, *Angew. Chem. Int. Ed.* **2011**, *50*, 11492–11495; c) S. Yao, Y. Xiong, M. Driess, *Acc. Chem. Res.* **2017**, *50*, 2026–2037; d) V. Nesterov, D. Reiter, P. Bag, P. Frisch, R. Holzner, A. Porzelt, S. Inoue, *Chem. Rev.* **2018**, *118*, 9678–9842; e) J. Hicks, P. Vasko, J. M. Goicoechea, S. Aldridge, *Nature* **2018**, *557*, 92–95; f) R. Kobayashi, S. Ishida, T. Iwamoto, *Angew. Chem. Int. Ed.* **2019**, *58*, 9425–9428; g) M.-A. Légaré, M. Rang, G. Bélanger-Chabot, J. I. Schweizer, I. Krummenacher, R. Bertermann, M. Arrowsmith, M. C. Holthausen, H. Braunschweig, *Science* **2019**, *363*, 1329–1332; h) W. Lu, Y. Li, R. Kinjo, *J. Am. Chem. Soc.* **2019**, *141*, 5164–5168; i) K. M. Marczenko, J. A. Zurakowski, K. L. Bamford, J. W. M. MacMillan, S. S. Chitnis, *Angew. Chem. Int. Ed.* **2019**, *58*, 18096–18101; j) T. Sugahara, J.-D. Guo, D. Hashizume, T. Sasamori, N. Tokitoh, *J. Am. Chem. Soc.* **2019**, *141*, 2263–2267; k) S. Kurumada, S. Takamori, M. Yamashita, *Nat. Chem.* **2020**, *12*, 36–39; l) M. M. D. Roy, A. A. Omaña, A. S. S. Wilson, M. S. Hill, S. Aldridge, E. Rivard, *Chem. Rev.* **2021**, *121*, 12784–12965.
2. a) R. Dobrovetsky, D. W. Stephan, *J. Am. Chem. Soc.* **2013**, *135*, 4974–4977; b) D. W. Stephan, *Science* **2016**, *354*, aaf7229; c) J. Li, C. G. Daniliuc, G. Kehr, G. Erker, *Angew. Chem. Int. Ed.* **2019**, *58*, 6737–6741.
3. a) C. B. Caputo, L. J. Hounjet, R. Dobrovetsky, D.W. Stephan, *Science* **2013**, *341*, 1374–1377; b) M.-A. Légaré, M.-A. Courtemanche, É. Rochette, F.-G. Fontaine, *Science* **2015**, *349*, 513–516.

4. S. Bontemps, G. Bouhadir, K. Miqueu, D. Bourissou, *J. Am. Chem. Soc.* **2006**, *128*, 12056–12057.
5. For early studies on donor-acceptor (LB/LA) stabilization, see: a) T. J. Marks, *J. Am. Chem. Soc.* **1971**, *93*, 7090–7091; b) W. Petz, *Chem. Rev.* **1986**, *86*, 1019–1047; c) U. Vogel, A. Y. Timoshkin, M. Scheer, *Angew. Chem. Int. Ed.* **2001**, *40*, 4409–4412; d) P. A. Rupar, M. C. Jennings, P. J. Ragona, K. M. Baines, *Organometallics* **2007**, *26*, 4109–4111; e) S. M. I. Al-Rafia, A. C. Malcolm, S. K. Liew, M. J. Ferguson, E. Rivard, *J. Am. Chem. Soc.* **2011**, *133*, 777–779; f) S. M. I. Al-Rafia, A. C. Malcolm, R. McDonald, M. J. Ferguson, E. Rivard, *Angew. Chem. Int. Ed.* **2011**, *50*, 8354–8357; g) A. K. Swarnakar, C. Hering-Junghans, K. Nagata, M. J. Ferguson, R. McDonald, N. Tokitoh, E. Rivard, *Angew. Chem. Int. Ed.* **2015**, *54*, 10666–10669; h) H. P. Hickox, Y. Wang, Y. Xie, P. Wei, H. F. Schaefer III, G. H. Robinson, *J. Am. Chem. Soc.* **2016**, *138*, 9799–9802.
6. a) T. K. Purkait, A. K. Swarnakar, G. B. De Los Reyes, F. A. Hegmann, E. Rivard, J. G. C. Veinot, *Nanoscale* **2015**, *7*, 2241–2244; b) A. K. Swarnakar, S. M. McDonald, K. C. Deutsch, P. Choi, M. J. Ferguson, R. McDonald, E. Rivard, *Inorg. Chem.*, **2014**, *53*, 8662–5671.
7. For selected studies on SiR₂ generation and complexation, see: a) H. Gilman, S. Gust Cottis, W. H. Atwell, *J. Am. Chem. Soc.* **1964**, *86*, 1596–1599; b) T. J. Drahnak, J. Michl, R. West, *J. Am. Chem. Soc.* **1979**, *101*, 5427–5428; c) D. H. Pae, M. Xiao, M. Y. Chiang, P. P. Gaspar, *J. Am. Chem. Soc.* **1991**, *113*, 1281–1288; d) H. Tobita, H. Kurita, H. Ogino, *Organometallics* **1998**, *17*, 2850–2856; e) R. Waterman, P. G. Hayes,

- T. D. Tilley, *Acc. Chem. Res.* **2007**, *40*, 712–719; f) A. Tahara, S. Nagino, Y. Sunada, R. Haige, H. Nagashima, *Organometallics* **2018**, *37*, 2531–2543.
8. a) S. Yajima, J. Hayashi, M. Omori, *Chem. Lett.* **1975**, *4*, 931–934; b) T. S. Radhakrishnan, *J. Appl. Polym. Sci.* **2006**, *99*, 2679–2686 and references therein.
9. M. W. P. Bebbington, S. Bontemps, G. Bouhadir, D. Bourissou, *Angew. Chem. Int. Ed.* **2017**, *46*, 3333–3336.
10. K. C. Thimer, S. M. I. Al-Rafia, M. J. Ferguson, R. McDonald, E. Rivard, *Chem. Commun.* **2009**, 7119–7121.
11. M. Walewska, J. Baumgartner, C. Marschner, *Chem. Commun.* **2015**, *51*, 276–278.
12. B. Rao, R. Kinjo, *Angew. Chem. Int. Ed.* **2019**, *58*, 18150–18153.
13. a) R. S. Ghadwal, R. Azhakar, H. W. Roesky, *Acc. Chem. Res.* **2013**, *46*, 444–456; b) J. Teichmann, M. Wagner, *Chem. Commun.* **2018**, *54*, 1397–1412 and references therein.
14. S. M. I. Al-Rafia, A. C. Malcolm, R. McDonald, M. J. Ferguson, E. Rivard, *Chem. Commun.* **2012**, *48*, 1308–1310.
15. L. Zhu, J. Zhang, C. Cui, *Inorg. Chem.* **2019**, *58*, 12007–12010.
16. Y. Shao, D. Truhlar, *Theor. Chem. Acc.* **2008**, *120*, 215–241.
17. T. H. Dunning Jr., *J. Chem. Phys.* **1989**, *90*, 1007–1023.
18. NIST Chemistry Webbook. <http://webbook.nist.gov/chemistry/>
19. Oligosilanes also extrude H₂ upon strong UV-irradiation at room temperature to yield amorphous hydride-terminated Si: M. Haas, V. Christopoulos, J. Radebner, M.

- Holthausen, T. Lainer, L. Schuh, H. Fitzek, G. Kothleitner, A. Torvisco, R. Fischer, O. Wunnicke, H. Stueger, *Angew. Chem. Int. Ed.* **2017**, *56*, 14071–14074.
20. Similar surface oxidation of Ge nanofilms deposited from the precursor $\text{ImMe}_2 \cdot \text{GeH}_2 \cdot \text{BH}_3$ ($\text{ImMe}_2 = (\text{HCNMe}_2)_2\text{C}:$) was found. While the temperature of deposition ($100\text{ }^\circ\text{C}$) was similar to that used in this Chapter, this approach could not be applied for the deposition of Si, nor could the donor- and acceptor-ligands involved be recycled: J. M. Sinclair, G. Dai, R. McDonald, M. J. Ferguson, A. Brown, E. Rivard, *Inorg. Chem.* **2020**, *59*, 10996–11008.
21. L. Armelao, D. Barreca, G. Bottaro, S. Gross, A. Gasparotto, C. Maragno, E. Tondello, A. Zattin, *Surf. Sci. Spect.* **2015**, *10*, 137–142.
22. D. Bermejo, M. Cardona, *J. Non-Cryst. Solids* **1979**, *32*, 405–419.
23. M. Wihl, M. Cardona, J. Tauc, *J. Non-Cryst. Solids* **1972**, *8*, 172–178.
24. R. L. C. Vink, G. T. Barkema, W. F. van der Weg, *Phys. Rev. B: Condens. Matter Phys.* **2001**, *63*, 115210.
25. J. P. Wesson, T. C. Williams, *J. Polym. Sci., Polym. Chem. Ed.* **1979**, *17*, 2833–2843.
26. A. L. Smith, *Spectrochim. Acta* **1960**, *16*, 87–105.
27. W. R. Schmidt, L. V. Interrante, R. H. Doremus, T. K. Trout, P. S. Marchetti, G. E. Maciel, *Chem. Mater.* **1991**, *3*, 257–267.
28. a) H. Kaji, F. Horii, *Macromolecules* **2007**, *40*, 5420–5423; b) K. Deller, B. Rieger, *RSC Adv.* **2015**, *5*, 87445–87455.

29. C. Zybail, D. L. Wilkinson, C. Leis, G. Müller, *Angew. Chem. Int. Ed. Engl.* **1989**, *28*, 203–205.
30. A. F. Burchat, M. J. Chong, N. Nielsen, *J. Org. Chem.* **1997**, *542*, 281–283.
31. J. C. DeMott, W. Gu, B. J., McCulloch, D. E. Herbert, M. D. Goshert, J. R. Walensky, J. Zhou, O. V. Ozerov, *Organometallics* **2015**, *34*, 3930–3933.
32. M. Sircoglou, Étude des modes de coordination des ligands amphiphiles PE (E = B, Al, Ga). Université Paul Sabatier: Toulouse, Doctoral Thesis **2009**.
33. E. Hupf, F. Kaiser, P. A. Lummis, M. M. D. Roy, R. McDonald, M. J. Ferguson, F. E. Kühn, E. Rivard, *Inorg. Chem.* **2020**, *59*, 1592–1601.
34. R. H. Blessing, *Acta. Cryst.* **1995**, *A51*, 33–38.
35. G. M. Sheldrick, *Acta. Cryst.* **2015**, *A71*, 3–8.
36. G. M. Sheldrick, *Acta. Cryst.* **2015**, *C71*, 3–8.

Chapter 3 – Frustrated Lewis Pair Chelation and Reactivity of Complexed Parent Iminoborane and Aminoborane

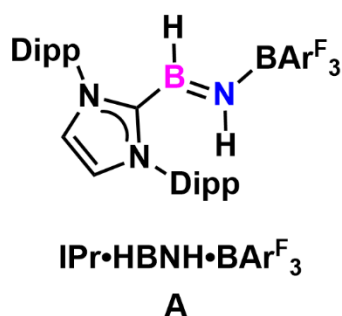
3.1 Introduction

Boron nitride (BN) is of great interest due to its enhanced hardness (in its cubic form, *c*-BN), thermal conductivity, electronically insulating properties, and thermal stability compared to its corresponding isoelectronic carbon allotropes, such as diamond.¹ Unfortunately, most syntheses of BN involve extreme synthetic conditions,^{2,3} such as temperatures above 900 °C, which make these protocols incompatible with most device fabrication methods (Scheme 3.1a). As a result, the synthesis of new precursors to bulk boron nitride under milder conditions is of great value, with the generation of reactive BN units through dehydrogenation⁴ of pre-formed HBNH complexes as a possible strategy (Scheme 3.1). Free HBNH contains highly polarized B-N σ - and π -linkages, thus, rapid oligomerization of this parent species occurs under non-cryogenic conditions.^{5,6} In 2015, the first formal complex of HBNH, $\text{IPr}\cdot\text{HBNH}\cdot\text{BAr}^{\text{F}}_3$ was reported (**A** in Scheme 3.1b; $\text{IPr} = (\text{HCNDipp})_2\text{C}$; ; $\text{Dipp} = 2,6\text{-}^i\text{Pr}_2\text{C}_6\text{H}_3$; $\text{Ar}^{\text{F}} = 3,5\text{-(F}_3\text{C)}_2\text{C}_6\text{H}_3$), although attempts to yield a molecular BN complex *via* dehydrogenation failed.⁷ More recently, frustrated Lewis pair (FLP)⁸ chelation by a phosphine-borane ligand $^i\text{Pr}_2\text{P}(\text{C}_6\text{H}_4)\text{BCy}_2$ or **PB** was used as a means to intercept low-oxidation state element hydride complexes of SiH_2 and GeH_2 (**B** and **C**; Scheme 3.1c; see Chapter 2), demonstrating that these complexes were viable precursors for the mild (< 100 °C) deposition of films of silicon and germanium, respectively.^{9,10}

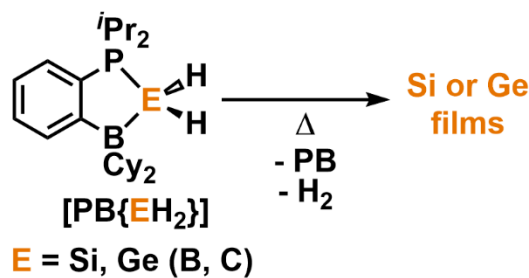
(a) Large-scale synthesis of BN:



(b) First HBNH complex:



(c) Initial FLP work:



Scheme 3.1. (a) Large-scale synthesis of boron nitride (BN); (b) first isolated complex of HBNH (**A**); (c) previous work using FLP-chelated EH₂ (Si, Ge) complexes (**B** and **C**) and their use to deposit films of silicon and germanium, respectively.

Herein, the formation of related FLP-chelates, [PB{H₂BNH₂}] and [PB{HBNH}],¹¹ is documented along with experimental efforts to yield boron nitride *via* dehydrogenation. The reactivity of the iminoborane complex [PB{HBNH}], towards nucleophilic and electrophilic reagents is examined. Finally, the chelating ability of an FLP with alternate (geometrically constrained) alkyl substituents at the Lewis acidic boron center is investigated.

3.2 Results and Discussion

Access to the unsaturated B–N systems in this Chapter began with combining the intramolecular FLP **PB**^{8b,9} with one equiv. of H₃B•NH₃ in THF for 12 hrs, leading to the loss of H₂ and formation of the aminoborane adduct [PB{H₂BNH₂}] (**1**) in a 75 % isolated yield (Equation 3.1).¹¹ The formation of **1** parallels the known frustrated Lewis pair (FLP)-instigated dehydrogenation of ammonia-borane by the groups of Aldridge and Slootweg to yield FLP{H₂BNH₂} complexes and dihydrogen.^{4b,8e} This transformation is proposed to proceed through the protio–hydrido complex [ⁱPr₂P{H}(C₆H₄)B{H}Cy₂], [PB{H₂}]]; however, this species could not be detected *in-situ* by NMR tracking of the reaction progress, nor did this species form from the direct reaction of **PB** with H₂ gas. The single-crystal X-ray structure of **1** (Figure 3.1) features a B–N single bond length of 1.573(2) Å for the H₂B–NH₂ moiety, which is identical, within experimental error to the dative B–N bond length in H₃B•NH₃ [1.599(8) Å].¹²

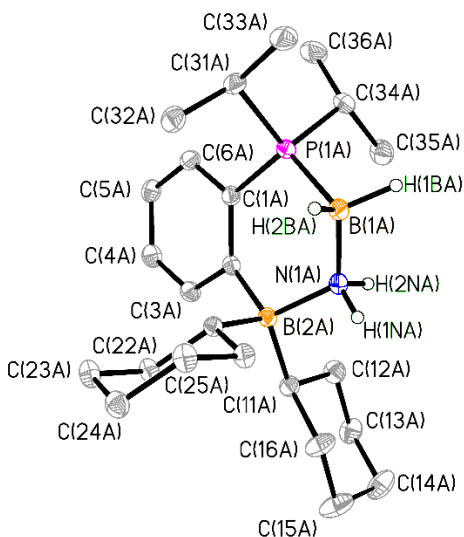
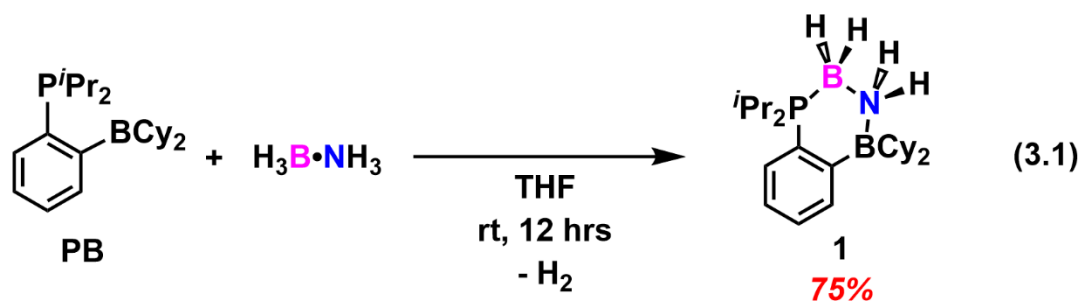


Figure 3.1. Molecular structure of [PB{H₂BNH₂}] (**1**) with thermal ellipsoids at a 30 % probability level. The asymmetric unit of **1** contains two molecules (A and B); only molecule A is shown above. All carbon-bound hydrogen atoms have been omitted for clarity. H atoms bound to boron and nitrogen were located in the difference Fourier maps and refined isotropically. Selected bond lengths [Å] and angles [°] for molecules A and [B]: **1**: P1A–C1A 1.8022(16) [1.8019(16)], P1A–B1A 1.9418(19) [1.9425(19)], N1A–B1A 1.573(2) [1.574(2)], N1A–B2A 1.630(2) [1.626(2)], C2A–B2A 1.649(2) [1.650(2)], N1A–H1NA 0.95(2) [0.89(2)], N1A–H2NA 0.91(2) [0.88(2)], B1A–H1BA 1.17(2) [1.145(19)], B2A–H2BA 1.122(19) [1.139(19)]; C1A–P1A–B1A 111.76(7) [111.71(7)], B1A–N1A–B2A 120.45(12) [120.98(12)], B1A–N1A–H1NA 108.3(12) [106.8(12)].

To better understand the underlying mechanism behind the formation of **1**, the energetics associated with the formation of [PB{H₂BNH₂}] (**1**) from **PB** and H₃B•NH₃ were examined *via* computations at the M06-2X¹³/cc-pVTZ¹⁴ level with a THF polarized continuum model (PCM). The initial dehydrogenation event to yield monomeric (transient) H₂B=NH₂ and the hydrogenated FLP [Pr₂P{H}(C₆H₄)B{H}Cy₂], [PB{H₂}] (Scheme 3.2) was computed to be endergonic [$\Delta G = 6.8$ kcal/mol]. However, subsequent loss of H₂ from [PB{H₂}] provides added free energy impetus, as evidenced by a computed ΔG of -14.9 kcal/mol for this process; this data is in line with the failed attempts to directly hydrogenate **PB** into [PB{H₂}] with molecular H₂ (1-4 atm). The final step in the formation of **1**, coordination of H₂B=NH₂ with **PB** to give [PB{H₂BNH₂}] (**1**) is exergonic by -23.1 kcal/mol, making the overall dehydrogenation process to yield **1** from **PB** and H₃B•NH₃ exergonic with $\Delta G = -31.2$ kcal/mol. While efforts to find a transition state in the dehydrogenation of H₃B•NH₃ with **PB** have not been successful so far, other groups have postulated the direct and synergistic transfer of H⁻/H⁺ units from H₃B•NH₂R to the respective Lewis basic and acidic centers of an FLP as a favorable path towards amine-borane dehydrogenation.¹⁵

% yield as a colorless solid. Thus, it appears that elevated temperatures facilitate Lewis base exchange of ammonia in $\text{H}_3\text{B}\cdot\text{NH}_3$ with the Lewis basic $-\text{P}^i\text{Pr}_2$ site in **PB** (likely *via* initial B–N bond cleavage in $\text{H}_3\text{B}\cdot\text{NH}_3$), in a similar fashion as the reported displacement of the ammonia from $\text{H}_3\text{B}\cdot\text{NH}_3$ in the presence of 1,4-diazabicyclo[2.2.2]octane (DABCO).¹⁶

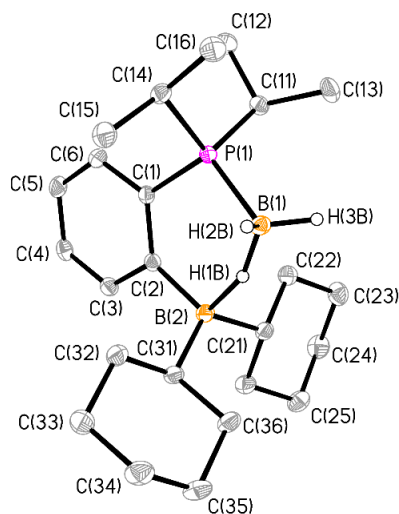
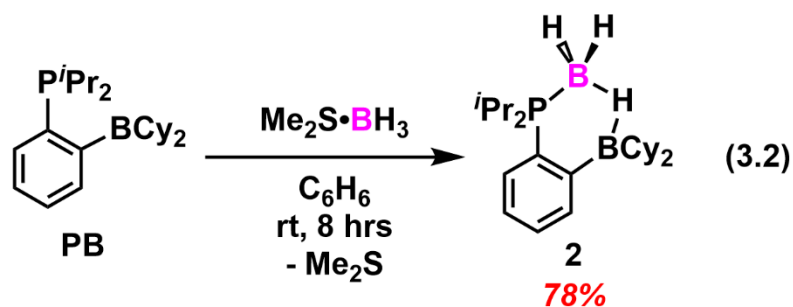


Figure 3.2. Molecular structure of $[\text{PB}\{\text{BH}_3\}]$ (**2**) with thermal ellipsoids at a 30 % probability level. All carbon-bound hydrogen atoms have been omitted for clarity. The H atoms bound to boron located in the difference Fourier maps and refined isotropically. Selected bond lengths [\AA] and angles [$^\circ$]: P1–C1 1.8092(10), P1–B1 1.9309(12), C2–B2 1.6058(15), B1–H1B 1.156(15), B1–H2B 1.100(16), B1–H3B 1.101(16), H1B–B2 1.156(15); C1–P1–B1 108.33(5), C2–B2–C21 116.61(9).

To examine the effect of added steric hinderance on the binding of aminoboranes with the FLP chelate, **PB** was combined with $\text{H}_3\text{B}\cdot\text{NH}_2\text{Me}$ in THF at room temperature. After 24 hrs, formation of the expected adduct $[\text{PB}\{\text{H}_2\text{BN}(\text{Me})\text{H}\}]$ (**3**) occurred, and this species was isolated as colorless crystals of suitable quality for a single-crystal X-ray diffraction (61 % yield, Equation 3.3, Figure 3.3). Overall, the metrical parameters of $[\text{PB}\{\text{H}_2\text{BN}(\text{Me})\text{H}\}]$ (**3**) are similar to those observed previously for $[\text{PB}\{\text{H}_2\text{BNH}_2\}]$ (**1**) with an internal B-N distance [B2-N1] of 1.581(2) Å, and a dative B-N distance involving the $-\text{BCy}_2$ unit [B1-N1] of 1.662(2) Å; notably, the latter B-N bond length in $[\text{PB}\{\text{H}_2\text{BN}(\text{Me})\text{H}\}]$ (**3**) is *ca.* 0.03 Å longer than in the corresponding adduct $[\text{PB}\{\text{H}_2\text{BNH}_2\}]$ (**1**) [1.628(3) Å, *avg.* of two independent molecules in the unit cell], reflecting the steric impact of the methyl group at N in **3**. Since it was observed that a longer reaction time was needed to afford **3** in similar yields to **1** (24 hrs vs. 12 hrs¹¹), the formation of $[\text{PB}\{\text{H}_2\text{BN}(\text{Me})\text{H}\}]$ (**3**) from the combination of **PB** and $\text{H}_3\text{B}\cdot\text{NH}_2\text{Me}$ was explored computationally at a M06-2X¹³/cc-pVTZ¹⁴ level of theory with a THF polarized continuum model. As with the formation of **1** from **PB** and $\text{H}_3\text{B}\cdot\text{NH}_3$ (Scheme 3.2), the initial dehydrogenation event to yield the mono-substituted aminoborane $\text{H}_2\text{B}=\text{NHMe}$ and the hydrogenated FLP $[\text{Pr}_2\text{P}\{\text{H}\}(\text{C}_6\text{H}_4)\text{B}\{\text{H}\}\text{Cy}_2]$ $[\text{PB}\{\text{H}_2\}]$ was computed to be endergonic [$\Delta G = 8.5$ kcal/mol]. The second step in the proposed mechanism, loss of H_2 from $[\text{PB}\{\text{H}_2\}]$, was already computed to be $\Delta G = -14.9$ kcal/mol (see above), however, the final step in the formation of **3**, coordination of $\text{H}_2\text{B}=\text{NHMe}$ with **PB** to give $[\text{PB}\{\text{H}_2\text{BN}(\text{Me})\text{H}\}]$ (**3**) is now significantly less exergonic [$\Delta G = -14.7$ kcal/mol] than the coordination of

$\text{H}_2\text{B}=\text{NH}_2$ to **PB** [$\Delta G = -23.1$ kcal/mol] (Scheme 3.2). Thus, the overall formation of **3** from **PB** and $\text{H}_3\text{B}\cdot\text{NH}_2\text{Me}$ is less exergonic [$\Delta G = -22.8$ kcal/mol; Scheme 3.3] as compared to the computed formation of **1** from **PB** and $\text{H}_3\text{B}\cdot\text{NH}_3$ [$\Delta G = -31.2$ kcal/mol] (Scheme 3.2).

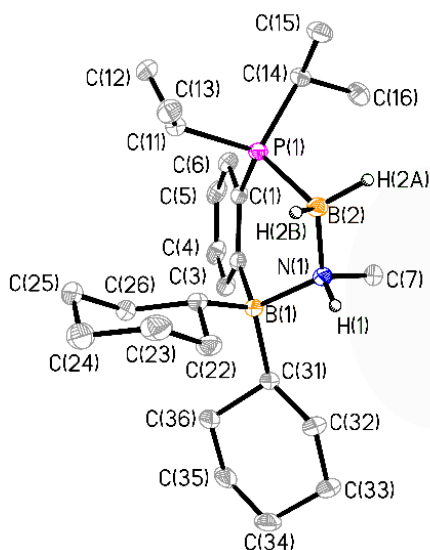
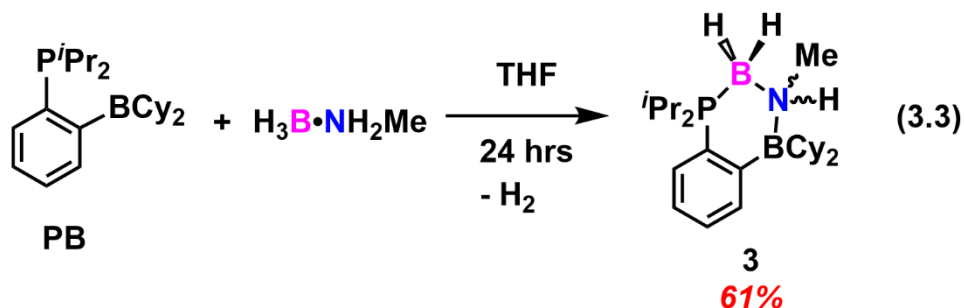
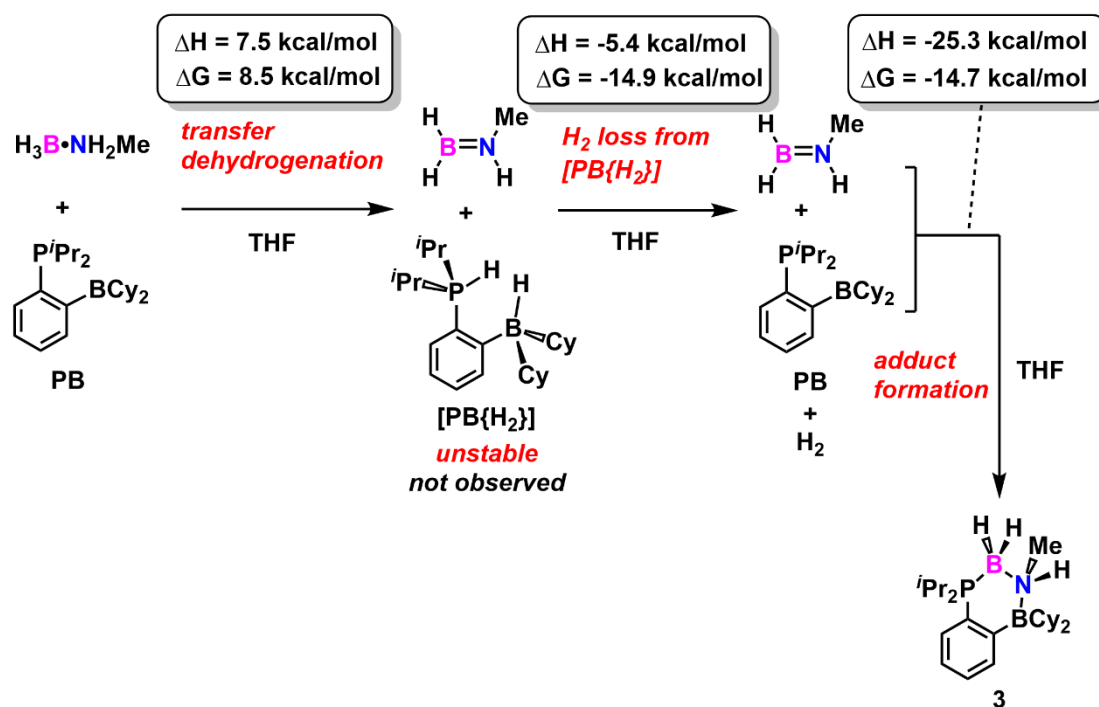


Figure 3.3. Molecular structure of $[\text{PB}\{\text{H}_2\text{BN}(\text{Me})\text{H}\}]$ (**3**) with thermal ellipsoids at a 30 % probability level. All carbon-bound hydrogen atoms have been omitted for clarity. H atoms bound to boron and nitrogen were located in the difference Fourier maps and refined isotropically. Selected bond lengths [\AA] and angles [$^\circ$]: P1–C1 1.8075(15), P1–B2 1.9784(17), N1–C7 1.4924(19), N1–B1 1.662(2), N1–B2 1.581(2); P1–B2–N1 108.82(10), C7–N1–B1 112.26(12), C7–N1–B2 111.48(12).



Scheme 3.3. Proposed reaction sequence leading to the formation of $[\text{PB}\{\text{H}_2\text{BN}(\text{Me})\text{H}\}]$ (**3**) and computed energetics (THF polarized continuum model, M06-2X/cc-pVTZ).

Given that the aminoborane adduct $[\text{PB}\{\text{H}_2\text{BNH}_2\}]$ (**1**) formally bears hydridic B–H and acidic N–H hydrogen atoms, it was hoped that dehydrogenation could be induced to form the target iminoborane adduct $[\text{PB}\{\text{HBNH}\}]$. Thus, $[\text{PB}\{\text{H}_2\text{BNH}_2\}]$ (**1**) was subjected to a series of known catalytic dehydrocoupling protocols, including combining **1** with 5 mol % (per metal atom) of $[\text{Rh}(\text{COD})\text{Cl}]_2$, $[\text{Rh}(\text{COD})\text{Cl}]_2/2 \text{Li}[\text{HBEt}_3]$, $[(\text{dppp})\text{Rh}(\text{CH}_2\text{Ph})]$, $\text{Cp}_2\text{TiCl}_2/2 \text{ }^n\text{BuLi}$, $[\text{Ir}(\text{COE})\text{Cl}]_2/2 \text{Li}[\text{HBEt}_3]$, 10 mol % $\text{Ph}_3\text{P}/\text{B}(\text{C}_6\text{F}_5)_3$ and $[\text{CpFe}(\text{CO})_2\text{I}]/\text{hv}$ in toluene with heating to 110 °C (COD = 1,5-cyclooctadiene; COE = cyclooctene; dppp = *bis*(diphenylphosphino)propane); in all

cases, no reaction was observed by *in-situ* ^{11}B and ^{31}P NMR spectroscopic analysis. These observations were surprising given that related conditions easily convert the amine-boranes $\text{H}_3\text{B}\cdot\text{NH}_2\text{R}$ (R = aryl or alkyl groups) into cyclic dehydrogenated products, such as borazanes $[\text{H}_2\text{B-NHR}]_3$, borazines $[\text{HBNR}]_3$, and linear polymers $[\text{H}_2\text{B-NHR}]_n$.¹⁷ Computations provide a partial reason for the failed dehydrogenation of **1**, since the dehydrogenation of $[\text{PB}\{\text{H}_2\text{BNH}_2\}]$ (**1**) to give H_2 and $[\text{PB}\{\text{HBNH}\}]$ was computed to be unfavorable in a THF polarized continuum model [$\Delta\text{H} = 16.1$ kcal/mol; $\Delta\text{G} = 7.9$ kcal/mol; M06-2X¹³/cc-pVTZ¹⁴]. To probe further the effect of substitution on FLP amine-borane adduct dehydrogenation, $[\text{PB}\{\text{H}_2\text{BN}(\text{Me})\text{H}\}]$ (**3**) was also combined with 5 mol % $[\text{Rh}(\text{COD})\text{Cl}]_2$ in THF. After stirring the mixture at room temperature for 8 hrs, no reaction was observed by NMR spectroscopy; however, heating the same mixture at 60 °C for 8 hrs led to the partial formation of **PB**, $[\text{HBNMe}]_3$ and $[\text{H}_2\text{B-NHMe}]_3$. The control reaction, heating a THF solution of **3** at 60 °C for 8 hrs in the absence of a possible dehydrocoupling catalyst, produced nearly identical ^{31}P and ^{11}B NMR spectral profiles; thus, the dehydrogenation of **3** is not accelerated to any substantial degree in the presence of the metal complexes investigated. While the desired iminoborane adduct $[\text{PB}\{\text{HBNMe}\}]$ was not isolated, these results are encouraging as it shows that release of B-N products from the FLP chelate may be possible under mild heating, a process that would be eventually required in the formation/release of bulk boron nitride from an FLP-chelated molecular precursor. As a final test of amine-borane dehydrogenation, **PB** was combined with $\text{H}_3\text{B}\cdot\text{NH}^i\text{Pr}_2$ in THF. After stirring the reagents at room temperature for 2 days, only a

ca. 9 % conversion of **PB** to [PB{BH₃}] (**2**) could be observed by ¹H NMR spectroscopy. Furthermore, combining the monomeric aminoborane H₂B=N^{*i*}Pr₂ with **PB** at room temperature in THF for 8 hrs followed by analysis by multinuclear (¹H, ³¹P, ¹¹B) NMR spectroscopy indicated that no reaction transpired, thus, there is a clear steric limitation for the complexation of H₂B=NR₂ (R = alkyl) species with **PB**.

Motivated by the recent publication of an intramolecular FLP bearing a sterically constrained bicyclic 9-borabicyclo(3.3.1)nonane (BBN) unit, [^{*i*}Pr₂P(C₆H₄)BBN], by Bontemps and co-workers,¹⁸ this ligand (termed herein as **P9B**) was combined with one equiv. of H₃B•NH₃ in THF. As expected, the target aminoborane adduct [P9B{H₂BNH₂}] (**4**) was obtained as a colorless solid in a 93 % isolated yield (Equation 3.4); *in-situ* NMR spectroscopy also showed that the borane adduct [P9B(BH₃)] (**5**) was also formed in a 5 % yield. Spectroscopically pure **5** can be made in a 98 % yield by combining Me₂S•BH₃ with **P9B** in THF for 8 hrs at room temperature. It should be noted that conversion of **P9B** to **4** requires heating to 65 °C in C₆H₆, while **PB** can activate H₃B•NH₃ at room temperature, likely due to the enhanced intramolecular P–B bonding within **P9B**.¹⁸ Specifically, a substantially shielded ¹¹B{¹H} NMR resonance for free **P9B** is observed in solution at 28.7 ppm in C₆D₆, while the -BCy₂ environment in **PB** appears at 75.6 ppm.¹¹ Furthermore, intramolecular P–B coordination was noted in the solid-state structure of **P9B** [P–B distance = 2.181(3) Å].¹⁸ The solid-state molecular structure of [P9B{H₂BNH₂}] (**4**) is depicted in Figure 3.4, which features a B2–N1 bond length of 1.5721(15) Å within the H₂BNH₂ unit,

which is identical within experimental error to the corresponding B–N single bond within the H₂B–NH₂ array in **1** [1.573(2) Å].¹¹

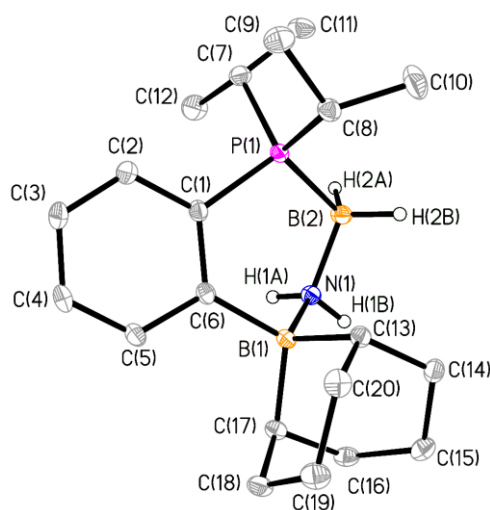
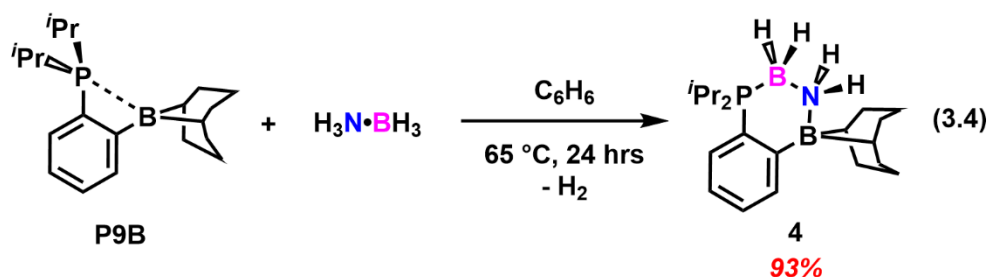


Figure 3.4. Molecular structure of [P9B{H₂BNH₂}] (**4**) with thermal ellipsoids at a 30 % probability level. All carbon-bound hydrogen atoms have been omitted for clarity. H atoms bound to boron and nitrogen were located in the difference Fourier maps and refined isotropically. Selected bond lengths [Å] and angles [°]: P1–C1 1.8086(1), P1–B2 1.9658(13), N1–B1 1.6319(14), N1–B2 1.5721(15), B1–H2A 1.130(5), B1–H2B 1.104(15), N1–H1A 0.905(16), N1–H1B 0.886(16), B1–C6 1.6484(16); C1–P1–B2 109.07(5), P1–B2–N1 108.64(7), B2–N1–B1 118.65(8), N1–B1–C6 103.72(8).

A major reason for targeting the synthesis of [P9B{H₂BNH₂}] (**4**) was that the presence of the less hindered Lewis acidic BBN group in relation to the -BCy₂ unit in

[PB{H₂BNH₂}] (**1**) might encourage favorable metal-mediated dehydrogenation chemistry. However, all attempts to promote the catalytic dehydrogenation of [P9B{H₂BNH₂}] (**4**) using 3 (metal atom) mol % of [Rh(COD)Cl]₂ or 0.6 mol % of [(dppp)Rh(CH₂Ph)] led to no reaction after heating the mixtures to 65 °C in THF for 8 hrs. This lack of reactivity can be traced (partly) to the neutral computed¹⁹ charge at the boron-bound hydrogen atoms in the -BH₂-NH₂- unit in **4** BH₂ [Q_{NPA} = -0.00] (Figure 3.5). Of added note, computations show that the negative Q_{NPA} values exist at the *ipso*-carbon atoms of the BBN unit in **4**, each -0.49, hinting at possible nucleophilic character within the -BR₂ unit (*vide infra*).

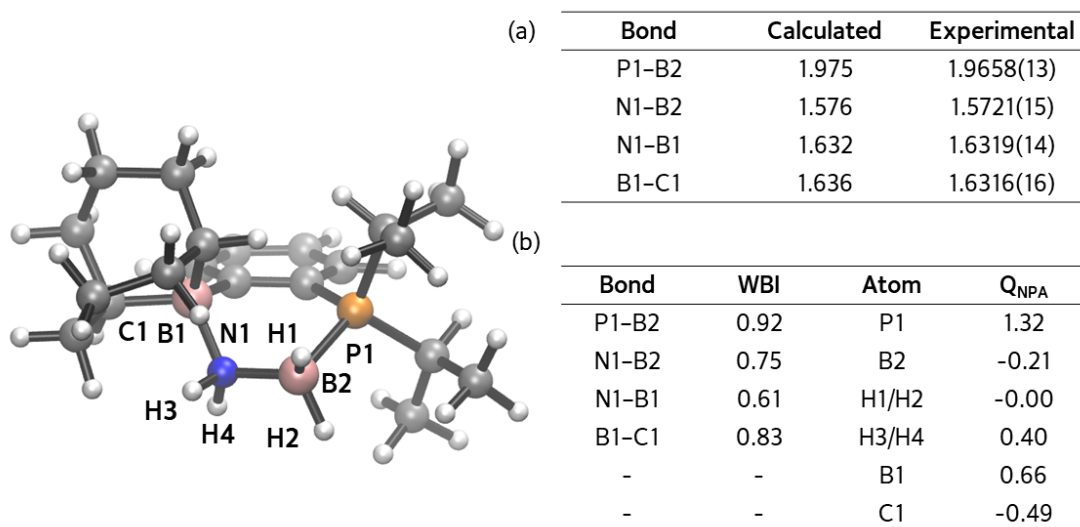
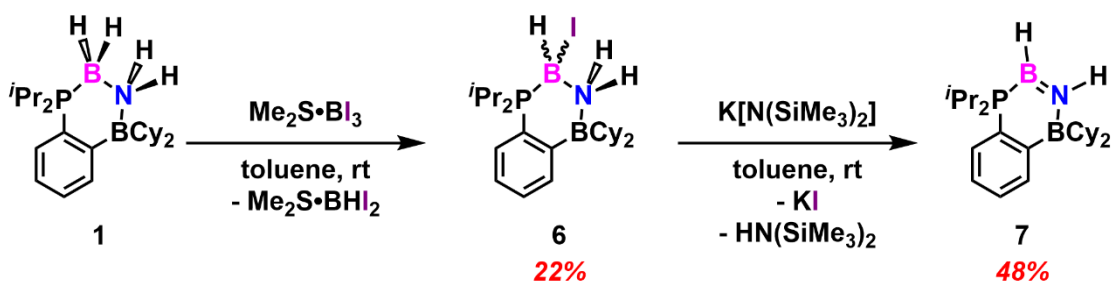


Figure 3.5. Optimized gas phase geometry of [P9B{H₂BNH₂}] (**4**) computed at a M06-2X¹³/cc-pVTZ¹⁴ level of theory with (a) calculated and experimental bond lengths [Å], and (b) Wiberg bond indices (WBI)¹⁹ and natural charges (Q_{NPA}).

Returning to the search for an FLP-chelated HBNH, an alternate halogenation/dehydrohalogenation route was explored to access a molecular complex

of HBNH using **PB**. As a first step, H/I exchange at boron was accomplished by treating [PB{H₂BNH₂}] (**1**) with Me₂S•BI₃,²⁰ leading to the iodoborane complex [PB{H(I)BNH₂}] (**6**) as colorless crystals in a 22 % isolated yield (Scheme 3.4). The low isolated yield for **6** was due to the persistence of the Me₂S•BI₂H by-product, which had to be removed *via* fractional crystallization, as both this by-product and **6** are soluble in hexanes and pentane. The solid-state structure of **6** features a four-coordinate boron center with typical B–I and B–H bond lengths of 2.290(7) Å and 1.03(6) Å, respectively. (Figure 3.6).



Scheme 3.4. Synthesis of [PB{HBNH}] (**7**) from [PB{H₂BNH₂}] (**1**) *via* B–H/B–I exchange and subsequent dehalogenation with K[N(SiMe₃)₂].

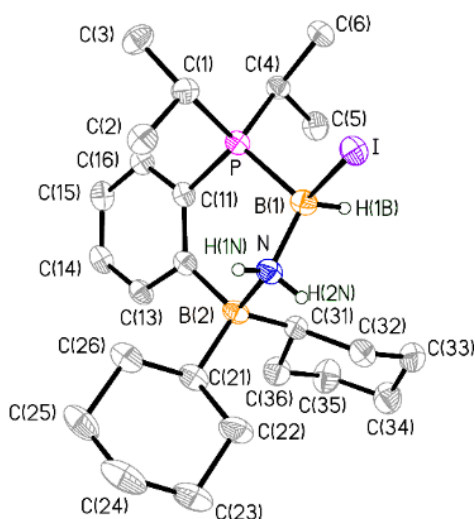


Figure 3.6. Molecular structure of $[PB\{H(I)BNH_2\}]$ (**6**) with thermal ellipsoids at a 30 % probability level. All carbon-bound hydrogen atoms have been omitted for clarity. H atoms bound to boron and nitrogen were located in the difference Fourier maps and refined isotropically. Selected bond lengths [\AA] and angles [$^\circ$]: P–C11 1.807(5), P–B1 1.944(7), B1–H1B 1.03(6), I–B1 2.290(7), N–B1 1.523(7), N–B2 1.657(8), C12–B2 1.633(8); C11–P–B1 107.5(3), B1–N–B2 118.1(4), I–B1–P 110.7(3).

After treating BI_3 with Me_2S in hexanes, $Me_2S \cdot BI_3$ was isolated as a colorless solid in a 65 % yield. By cooling ($-35\text{ }^\circ\text{C}$) a hexanes solution of $Me_2S \cdot BI_3$ for 16 hrs, colorless X-ray quality crystals of $Me_2S \cdot BI_3$ were obtained (Figure 3.7). While the solid-state structure of $Me_2S \cdot BI_3$ was first reported in 1987,²¹ detailed characterization of $Me_2S \cdot BI_3$ by multinuclear NMR, elemental analysis, and a high-quality crystallography structure refinement was not reported prior to this work (see Section 3.4.2. and Figure 3.7).

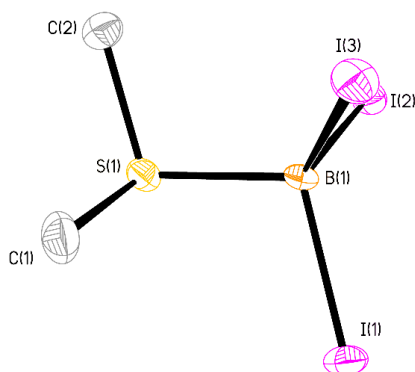


Figure 3.7. Molecular structure of $\text{Me}_2\text{S}\cdot\text{BI}_3$ with thermal ellipsoids at a 30 % probability level. All carbon-bound hydrogen atoms have been omitted for clarity. Selected bond lengths [\AA] and angles [$^\circ$]: I1–B1 2.232(5), I2–B1 2.219(5), I3–B1 2.212(5), S1–C1 1.803(6), S1–B1 1.937(6); C1–S1–C2 100.8(3), C1–S1–B1 105.2(3), S1–B1–I2 104.5(2).

With $[\text{PB}\{\text{H(I)BNH}_2\}]$ (**6**) in hand, dehydrohalogenation of **6** with $\text{K}[\text{N}(\text{SiMe}_3)_2]$ proceeded smoothly to give the target iminoborane complex $[\text{PB}\{\text{HBNH}\}]$ (**7**) as colorless crystals in a 48 % yield (Scheme 3.4). In contrast to the structure of $\text{IPr}\cdot\text{HB}=\text{NH}\cdot\text{BAr}^{\text{F}}_3$ (Scheme 3.1b),⁷ compound **7** adopts a *cis*-HBNH configuration, contained within a nearly planar $\text{C}_2\text{B}_2\text{NP}$ heterocycle (Figure 3.8). The formally dative P1–B2 and N1–B1 linkages in **7** are both shorter than the corresponding bonds in **1** [1.927(2) and 1.579(3) vs. 1.9418(19) and 1.630(2) \AA], reflecting the change in N and B hybridization from sp^3 in $[\text{PB}\{\text{H}_2\text{BNH}_2\}]$ (**1**) to sp^2 in $[\text{PB}\{\text{HBNH}\}]$ (**7**).

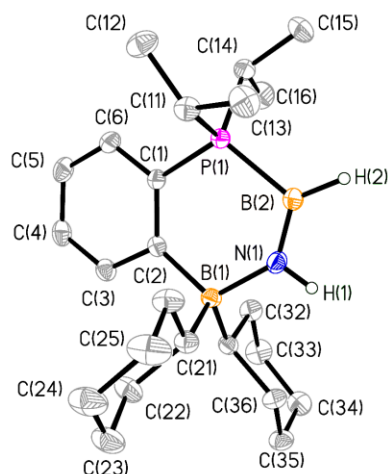


Figure 3.8. Molecular structure of [PB{HBNH}] (**7**) with thermal ellipsoids at a 30 % probability level. All carbon-bound hydrogen atoms have been omitted for clarity. H atoms bound to boron and nitrogen were located in the difference Fourier maps and refined isotropically. Selected bond lengths [Å] and angles [°]: P1–C1 1.7945(18), P1–B2 1.927(2), B2–N1 1.347(3), B2–H2 1.13(2), N1–H1 0.88(3), B1–N1 1.579(3), B1–C2 1.645(3); C1–P1–B2 108.35(9), N1–B1–C2 111.29(14), B1–N1–B2 133.91(17), P1–B2–N1 114.80(15).

The B2–N1 distance [1.347(3) Å] in **7** is elongated compared to that of gas phase HB=NH (1.2381 Å, as determined by IR diode laser spectroscopy),^{5b} and only slightly shorter than the B=N bond in IPr•HB=NH•BAr^F₃ [1.364(2) Å].⁷ The FT-IR spectrum of **7** (as a powder) showed well-defined N–H and B–H stretching bands at 3343 cm⁻¹ and 2465 cm⁻¹, respectively, which are lower in wavenumber by 27 cm⁻¹ (N–H) and 46 cm⁻¹ (B–H) compared to the corresponding vibrations in IPr•HB=NH•BAr^F₃⁷ (Figure 3.9, red trace). This trend suggests that stronger N–H and B–H bonds are present in IPr•HB=NH•BAr^F₃ compared to those in **7**, which may be promising for the catalytic dehydrogenation of H–B/N–H bonds in **7** to afford the target [PB{BN}] complex. Since

B=N stretching modes can range from 1100 cm^{-1} to 1500 cm^{-1} , the B=N stretching band in **7** has been tentatively assigned at 1443 cm^{-1} by comparison with the computed IR spectrum for **7** at a M06-2X¹³/cc-pVTZ¹⁴ level of theory (Figure 3.9, black trace).²² The B=N stretching band for **7** could not be compared to that found in $\text{IPr}\cdot\text{HB}=\text{NH}\cdot\text{BAr}^{\text{F}_3}$,⁷ as the reported IR spectrum for the latter species was collected in Nujol, which has IR stretches in this region. Notably, the B=N stretching for **7** (1443 cm^{-1}) was significantly shifted by *ca.* 200 cm^{-1} from that of gas phase $\text{HB}\equiv\text{NH}$ (1770 cm^{-1}),^{5b} as a consequence of the LB/LA stabilization in **7**, leading to weakened B-N multiple bonding in the HBNH unit.

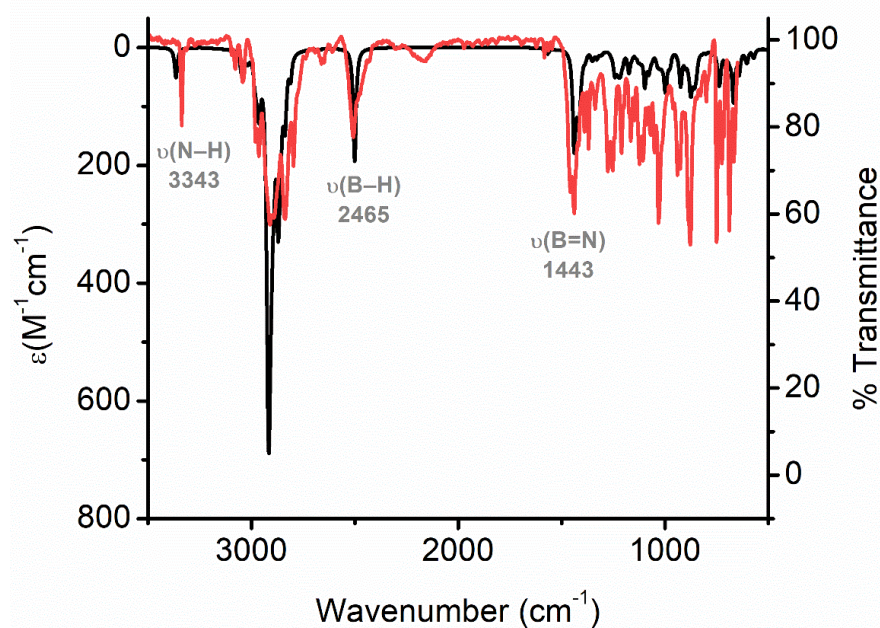


Figure 3.9. Computed (black trace; at a M06-2X¹³/cc-pVTZ¹⁴ level of theory) and measured (red trace) IR spectra (powder, KBr plate) of $[\text{PB}\{\text{HBNH}\}]$ (**7**). Computed IR frequencies were corrected by a scaling factor of 0.946.²² Selected measured IR bands (cm^{-1}) are labelled on the graph in grey: 1443 (s, $\nu\text{B}=\text{N}$), 2465 (s, $\nu\text{B}-\text{H}$), 3343 (s, $\nu\text{N}-\text{H}$).

The DFT-computed HOMO and LUMO of **7** show B–N π and B–N π^* orbital contributions, respectively (Figure 3.10). In particular, the expected B=N π and π^* MOs¹⁹ are shown in Figure 3.11a/b, alongside a computed Wiberg bond index (WBI) of 1.41 for the B=N unit in **7**, which is consistent with double bond character; a similar WBI of 1.32 for the B=N unit was reported earlier in IPr•HB=NH•BAr^F₃ (Figure 3.11).⁷

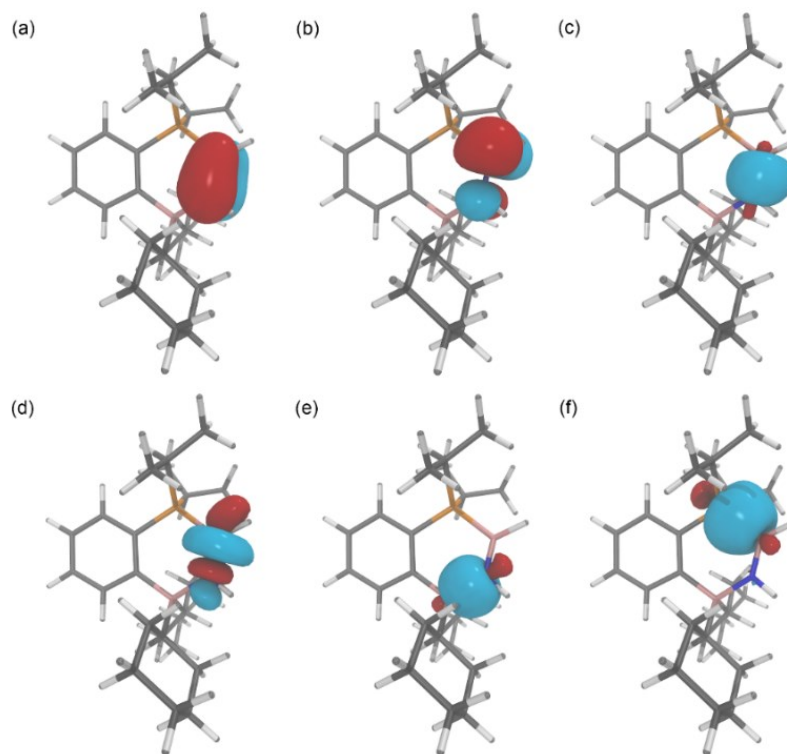


Figure 3.10. Computed natural bond orbitals (NBOs; at a M06-2X¹³/cc-pVTZ¹⁴ level of theory) of [PB{HBNH}] (**7**) depicting [with e[−] occupancy]:¹⁹ (a) the B–N π orbital [2.0 e[−]]; (b) the B–N π^* orbital [0.0 e[−]]; (c and d) B–N σ and σ^* orbitals [2.0 and 0.0 e[−]]; (e and f) B–N and P–B σ -orbital [each 2.0 e[−]] involving the **PB** ligand.

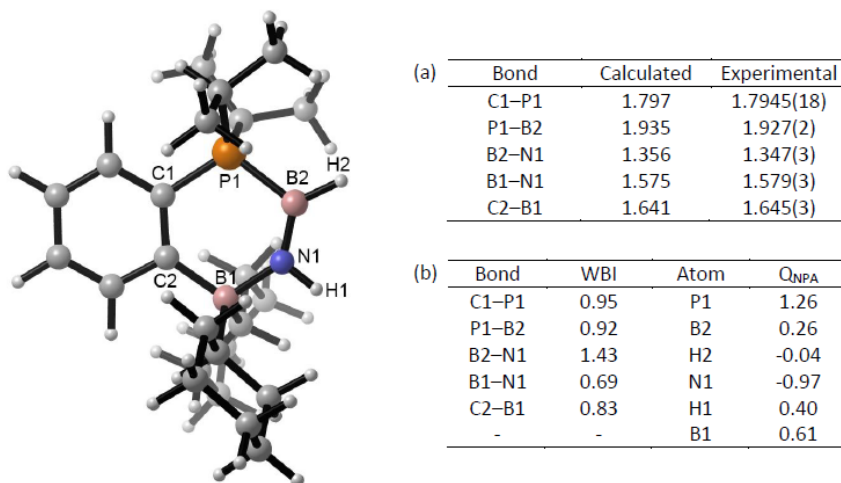


Figure 3.11. Optimized gas phase geometry of [PB{HBNH}] (**7**) computed at a M06-2X¹³/cc-pVTZ¹⁴ level of theory with (a) calculated and experimental bond lengths [Å], and (b) Wiberg bond indices (WBI)¹⁹ and natural charges (Q_{NPA}) for [PB{HBNH}] (**7**).

Similar to [PB{H₂BNH₂}] (**1**), all dehydrogenation attempts involving **7** using 5 mol % [Rh(COD)Cl]₂, 5 mol % [Rh(COD)Cl]₂/Li[HBET₃] or 6 mol % (dppp)Rh(η³-CH₂Ph) as catalysts led to no reaction (up to 110 °C in toluene). The stoichiometric dehydrogenation of **7** with [(^{Mes}Nacnac)Mg-Mg(^{Mes}Nacnac)] (^{Mes}Nacnac = [(HC(MeCNMe)₂]⁻)²³ was attempted, but led to no reaction. Attempted coordination of **7** by the Lewis bases DMAP, Me₃P and ImMe₄ (DMAP = 4-dimethylaminopyridine, ImMe₄ = (MeCNMe)₂C:) at room temperature in THF led to no reactions. While treating **7** with the iron carbonyls, Fe(CO)₅ and Fe₃CO₁₂, followed by photolysis with a 125 W Hg lamp in THF for 8 hrs led to a complicated mixture of products by NMR monitoring. It should be noted that an analogue of **7**, [PB{NBH₂}], was prepared by Brandon L. Frenette (Ph.D. student, Rivard lab), which undergoes rapid coordination by DMAP at the BH₂ unit to form the adduct [PB{NBH₂}•DMAP].¹¹

Given that the adducts [PB{H₂BNH₂}] (**1**) and [PB{HBNH}] (**7**) bear hydridic B–H and acidic N–H hydrogen atoms, it was hoped that dehydrogenation could be induced to yield **7** from **1**, and further H₂ loss from **7** would yield a FLP-complexed (BN)_x unit *en route* to the deposition to bulk boron nitride. When **7** was heated in toluene for 110 °C for 12 hrs, no observable change was noted by *in-situ* ¹¹B and ³¹P NMR analysis; however, heating **7** at 110 °C in toluene for 5 days, afforded *ca.* 20 % of free **PB** with the remaining soluble product being unreacted [PB{HBNH}] (**7**). This is in stark contrast to the previously reported [PB{EH₂}] (E = Si, Ge) complexes (**B** and **C**)⁹ that cleanly release bulk E(0), **PB** and H₂ gas at 110 °C, likely due to weaker intraring P–E/E–B bonds in comparison to the P–B and B–N linkages in **7** (Scheme 3.1c). Moreover, computations show that the B–H bond in [PB{HBNH}] (**7**) is essentially non-polar, with a computed charge at the hydride [Q_{NPA}] of only -0.04 (Figure 3.11); the lack of substantial hydridic character within the B–H unit in **7** would suppress its activation by metal centers, as B–H bond cleavage is often postulated as an important step towards metal-mediated amine-borane dehydrogenation.^{4,24}

To examine further the thermal properties of [PB{H₂BNH₂}] (**1**) and [PB{HBNH}] (**7**), thermal gravimetric analysis (TGA) data were collected (Figures 3.12 and 3.13). For [PB{H₂BNH₂}] (**1**), an onset of decomposition (temperature at which 95 % weight loss is observed) was observed at 201 °C, with 5.6 wt. % residual mass after heating to 500 °C (Figure 3.12). For [PB{HBNH}] (**7**), an onset of decomposition was observed at the same temperature of 201 °C, with 19.9 wt. % residual mass after heating to 500 °C (Figure 3.13). Notably, free **PB** begins to show a

weight loss of 5.0 % at 191 °C, thus one cannot rule out loss of **PB** during the decomposition of **1** and **7** above 200 °C.⁹ If compounds **1** and **7** each liberated volatile **PB** and all equiv. of H₂ to yield bulk BN, then a residual mass of *ca.* 6 wt. % is expected in each case. While **1** affords a remaining mass that fits the expected trend, the much larger residual mass of 20 wt. % when **7** is heated to 500 °C suggests that a different path of degradation is transpiring *vs.* **1**, possibly *via* activation of the **PB** ligand.

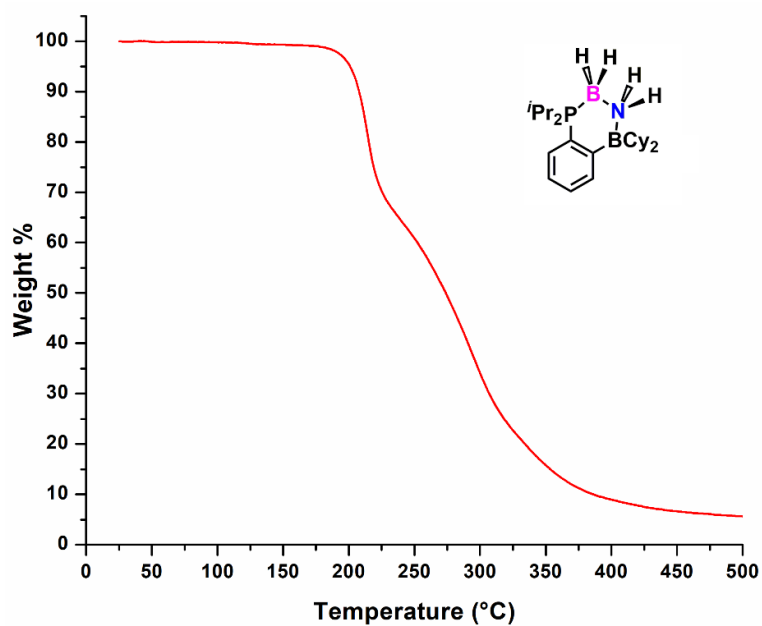


Figure 3.12. TGA profile of [PB{H₂BNH₂}] (**1**), ranging from 25 °C to 500 °C in a N₂ atmosphere at a heating rate of 10 °C/min.

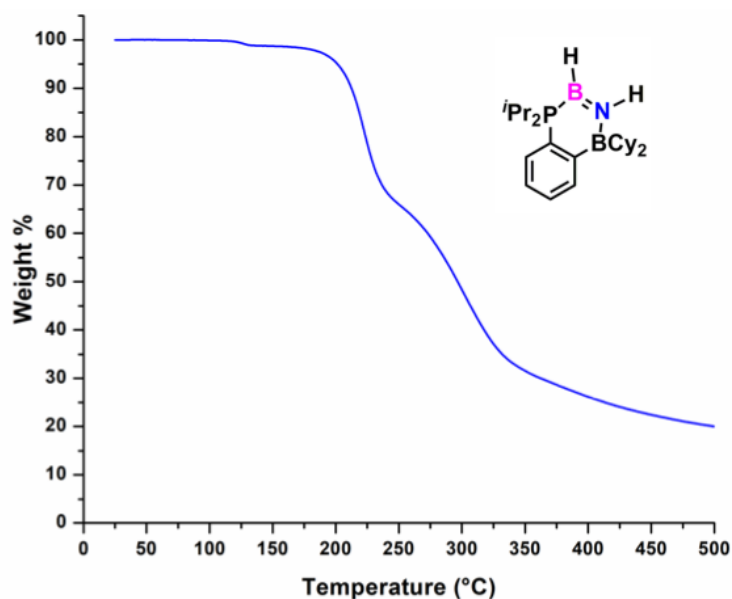
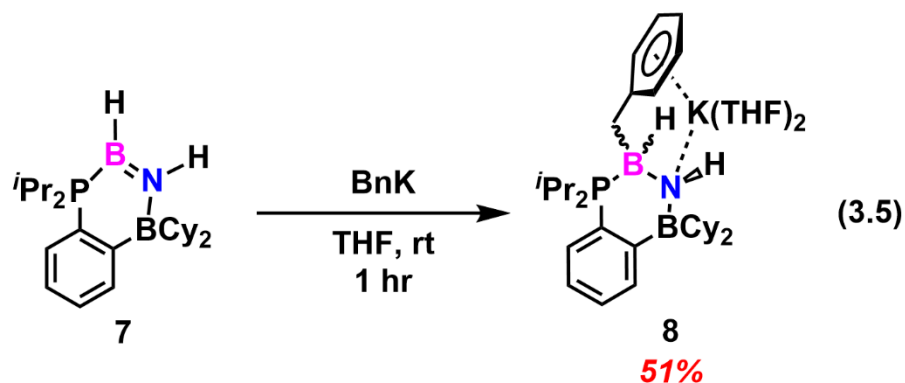


Figure 3.13. TGA profile of [PB{HBNH}] (**7**), ranging from 25 °C to 500 °C in a N₂ atmosphere at a heating rate of 10 °C/min.

The aforementioned reactivity of [PB{HBNH}] (**7**) centered on B–H bond activation, however, possible activation of the N–H linkage in this complex was also probed by combining **7** with BnK²⁵ (Bn = CH₂Ph) (Equation 3.5). In contrast to the targeted deprotonation at N, nucleophilic addition of BnK to **7** gave the nucleophilic addition product [PB{H(Bn)BNH}{K(THF)₂}] (**8**), which was isolated as analytically pure colorless X-ray quality crystals in a 51 % yield.



The solid-state structure of $[\text{PB}\{\text{H}(\text{Bn})\text{BNH}\}\{\text{K}(\text{THF})_2\}]$ (**8**) is shown in Figure 3.14, and reveals twisting of the HBNH array into a *gauche* arrangement, supported by $\text{N}\cdots\text{K}$ coordination [$\text{N1}\cdots\text{K1} = 2.7855(13) \text{ \AA}$]. Addition of the Bn group at boron led to the expected loss of B–N π -bonding, as evidenced by the elongation of the N1–B2 bond length to a value of $1.5019(17) \text{ \AA}$; for comparison, the internal B=N distance that belongs to the HBNH unit in **7** is $1.347(3) \text{ \AA}$.¹¹ Lastly, $\text{K}\cdots\text{arene}$ interactions [*avg.* $\text{K}-\text{C}(\text{Ar}) = 3.2206(16) \text{ \AA}$] can be observed which help anchor the $\text{K}(\text{THF})_2$ unit into close proximity to the complexed amido-borane $\{\text{Bn}(\text{H})\text{B}-\text{NH}\}$ unit.

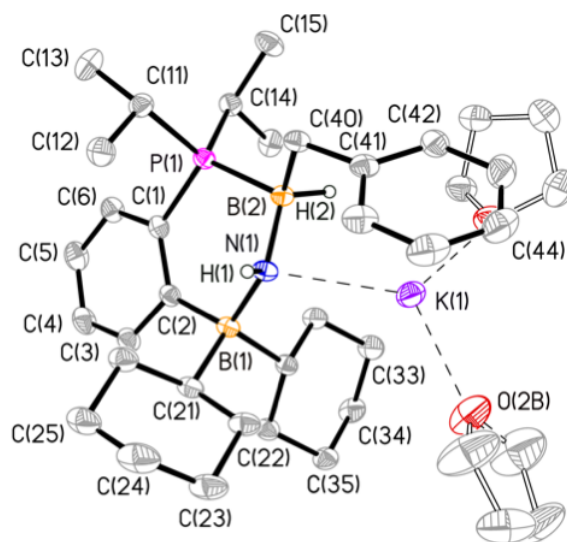
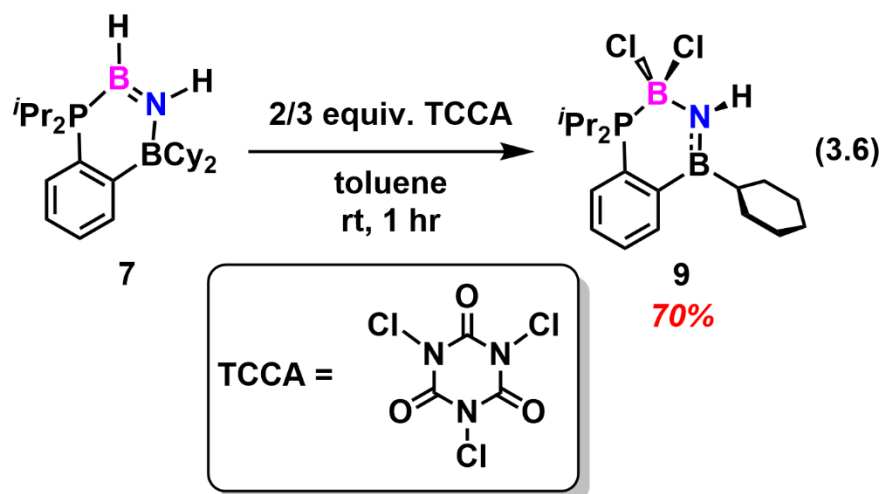


Figure 3.14. Molecular structure of $[\text{PB}\{\text{H}(\text{Bn})\text{BNH}\}\{\text{K}(\text{THF})_2\}]$ (**8**) with thermal ellipsoids at a 30 % probability level. All carbon-bound hydrogen atoms have been omitted for clarity. H atoms bound to boron and nitrogen were located in the difference Fourier maps and refined isotropically. Only one orientation of each disordered THF molecule is shown for clarity. Selected bond lengths [Å] and angles [°]: $\text{K1}\cdots\text{O2B}$ 2.681(8), $\text{K1}\cdots\text{N1}$ 2.7855(13), P1-B2 2.0070(15), N1-B1 1.5653(17), N1-B2 1.5019(17), N1-H1 0.826(19), B2-H2 1.175(17); O1B-K1-O2B 105.1(2), O2B-K1-N1 120.51(15), C1-P1-B2 110.40(6).

In a final attempt to isolate a viable precursor to molecular $(\text{BN})_x$ complex(es), the formation of the unknown *B*-chloroiminoborane adduct $[\text{PB}\{\text{ClBNH}\}]$ was targeted, which could be formed by treatment of $[\text{PB}\{\text{HBNH}\}]$ (**7**) with a suitable chlorinating agent. From $[\text{PB}\{\text{ClBNH}\}]$, it may be possible to instigate HCl loss with addition of base or even alkali metal to give $[\text{PB}\{\text{BN}\}]_x$. In pursuit of this goal, $[\text{PB}\{\text{HBNH}\}]$ (**7**) was treated with the strong chlorinating agent TCCA (TCCA = trichloroisocyanuric acid). While $^{11}\text{B}\{^1\text{H}\}$ NMR analysis of the new product formed (in

C_6D_6) showed distinct resonances at -1.4 and 42.1 ppm, assigned to the four- and three-coordinate boron environments, respectively; however, only the four-coordinate resonance at -1.4 ppm showed (unexpected) coupling to phosphorus ($^1J_{BP} = 153$ Hz). Growth of colorless crystals of suitable quality for single-crystal X-ray crystallography (70 % yield) revealed the formation of the ligand-activated product [$iPr_2P(C_6H_4)BCy\{Cl_2BNH\}$] (**9**) (Equation 3.6), wherein loss of a cyclohexyl group from the initial $-BCy_2$ unit transpired with generation of an intraring Cl_2BNH unit.



The solid-state structure of **9** is depicted in Figure 3.15, showing a B–N single bond that joins the four-coordinate $-BCl_2-$ center [$B2-N1 = 1.481(2)$ Å] and a shorter B1–N1 bond [$1.397(2)$ Å] that suggests partial B–N π -character (computed Wiberg bond index,¹⁹ $WBI = 1.11$ at a $M06-2X^{13}/cc-pVTZ^{14}$ level of theory). Furthermore, evidence for B–N multiple bonding between within the $-B(Cy)NH-$ unit in **9** emerged from the computed HOMO and LUMO of **9**, wherein B–N π and π^* contributions could be discerned (Figure 3.16).

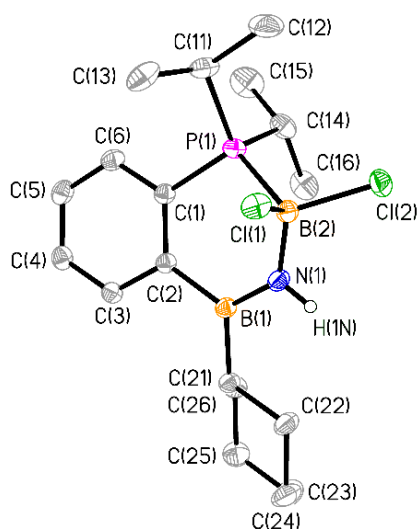


Figure 3.15. Molecular structure of $[i\text{Pr}_2\text{P}(\text{C}_6\text{H}_4)\text{BCy}\{\text{Cl}_2\text{BNH}\}]$ (**9**) with thermal ellipsoids at a 30 % probability level. All carbon-bound hydrogen atoms have been omitted for clarity. H atom bound to nitrogen was located in the difference Fourier maps and refined isotropically. Selected bond lengths [\AA] and angles [$^\circ$]: C11–B2 1.893(2), C12–B2 1.874(2), N1–H1N 0.81(2), P1–B2 1.9781(19), N1–B1 1.397(2), N1–B2 1.481(2); B1–N1–B2 131.31(15), P1–B2–N1 108.14(11), C11–B2–N1 111.81(13), P1–B1–Cl2 108.20(10).

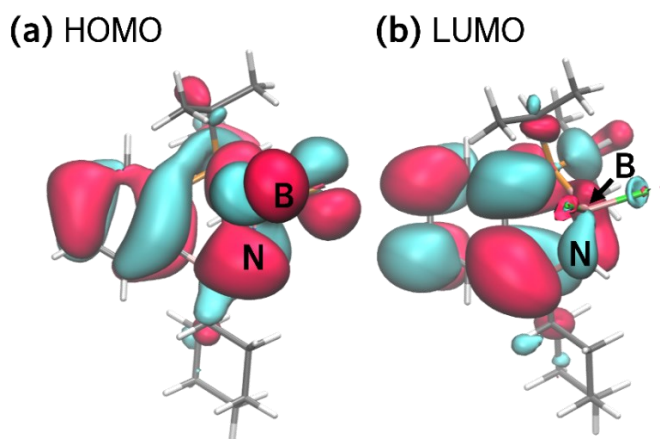
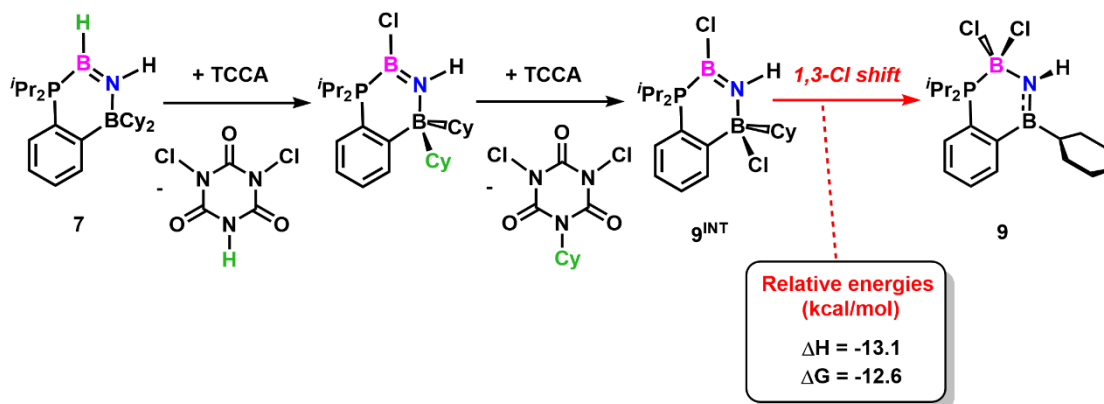


Figure 3.16. Computed molecular orbitals for $[i\text{Pr}_2\text{P}(\text{C}_6\text{H}_4)\text{BCy}\{\text{Cl}_2\text{BNH}\}]$ (**9**) at a M06-2X¹³/cc-pVTZ¹⁴ level of theory depicting: (a) HOMO with B-N π orbital character; (b) LUMO with B-N π^* orbital character.

The path by which [$i\text{Pr}_2\text{P}(\text{C}_6\text{H}_4)\text{BCy}\{\text{Cl}_2\text{BNH}\}$] (**9**) is formed could involve the intended, yet unselective, chlorination at boron in **7** with TCCA to yield [$\text{PB}\{\text{ClBNH}\}$], followed by Cy/Cl exchange at boron to give the reactive intermediate [$i\text{Pr}_2\text{P}(\text{C}_6\text{H}_4)\text{B}(\text{Cl})\text{Cy}\{\text{ClBNH}\}$] (**9^{INT}**, Scheme 3.5). Notably, the required 1,3-chloride migration to convert **9^{INT}** into the final product **9** has been computed to be exergonic (ΔG) by -12.6 kcal/mol in the gas phase (M06-2X¹³/cc-pVTZ¹⁴ level of theory), adding some support to the proposed mechanism shown in Scheme 3.5. The reactivity between [$\text{PB}\{\text{HBNH}\}$] (**7**) and TCCA highlights that these phosphine-borane FLP chelates are prone to ligand cleavage in the presence of chlorination agents, a process that is facilitated by the nucleophilic character of the Cy groups bound to boron.



Scheme 3.5. Proposed route involved in the chlorination of [$\text{PB}\{\text{HBNH}\}$] (**7**) by TCCA to yield [$i\text{Pr}_2\text{P}(\text{C}_6\text{H}_4)\text{BCy}\{\text{Cl}_2\text{BNH}\}$] (**9**), and the computed energies associated with the isomerization of intermediate **9^{INT}** into **9** via a 1,3-chloride shift.

3.3 Conclusions

The reactivity of the aminoborane and iminoborane adducts $[\text{PB}\{\text{H}_2\text{BNH}_2\}]$ (**1**) and $[\text{PB}\{\text{HBNH}\}]$ (**7**) was examined, with focus on potentially releasing bulk boron nitride *via* dehydrogenation and ligand (**PB**) loss. It appears that for these adducts, a low degree of hydridic character within the B–H bonds is suppressing metal-mediated dehydrogenation. Moreover, formation of an FLP- H_2BNH_2 complex (**4**) bearing a less hindered Lewis acidic BBN borane group failed to release H_2 for a similar reason. Rapid nucleophilic attack and ligand activation was observed upon combining $[\text{PB}\{\text{HBNH}\}]$ (**7**) with BnK and TCCA, respectively, yield $[\text{PB}\{\text{H}(\text{Bn})\text{BNH}\}\{\text{K}(\text{THF})_2\}]$ (**8**) and $[\text{Pr}_2\text{P}(\text{C}_6\text{H}_4)\text{BCy}\{\text{Cl}_2\text{BNH}\}]$ (**9**). Future work will involve the development of new intramolecular FLP constructs, including those with strongly donating *N*-heterocyclic olefin (NHO) units,²⁶ to promote the loss of H_2 and yield viable $(\text{BN})_x$ precursors for the low temperature deposition of boron nitride.

3.4 Experimental Details

3.4.1 General Considerations

All reactions were performed using Schlenk and glovebox (Innovative Technology, Inc.) techniques. All solvents were dried (except heptane, hexamethyldisiloxane, fluorobenzene and pentane) using a solvent purification system provided by Innovative Technology, Inc., degassed (freeze-pump-thaw method), and stored under nitrogen prior to use. Heptane was sparged with N₂ for 30 min prior to use. Pentane was degassed *via* three freeze-pump-thaw cycles and dried over 4 Å molecular sieves prior to use. Hexamethyldisiloxane (Me₃SiOSiMe₃) and fluorobenzene were refluxed over calcium hydride overnight under a N₂ atmosphere, distilled, and stored over 4 Å molecular sieves prior to use. Ammonia-borane (H₃B•NH₃), Me₂S•BH₃ (2.0 M solution in THF), H₃B•NH₂Me, H₃B•NH^{*i*}Pr₂, Li[HBEt₃] (1.0 M solution in THF), ^{*n*}BuLi (2.5 M solution in hexanes), [Ir(COE)Cl]₂, CpFe(CO)₂I, DMAP, Me₃P (1.0 M solution in THF) and trichloroisocyanuric acid (TCCA) were purchased from Sigma-Aldrich and used as received. [Rh(COD)Cl]₂ was purchased from Pressure Chemical Co. and used as received. Cp₂TiCl₂ was purchased from Arapahoe Chemicals Inc. and used as received. Fe(CO)₅ was purchased from Alfa Aesar and used as received. Fe₃CO₁₂ was purchased from Strem Chemicals and used as received. Potassium *bis*(trimethylsilyl)amide (K[N(SiMe₃)₂]) was purchased from Sigma-Aldrich and recrystallized from a saturated toluene solution at -35 °C prior to use. Dimethylsulfide (Me₂S) was purchased from Sigma-Aldrich and stored over 4 Å molecular sieves at -35 °C under N₂. **PB**,^{8b,9} BnK²⁵ (Bn = benzyl), [(dppp)Rh(CH₂Ph)],²⁴ ImMe₄²⁷ (ImMe₄ =

(MeCNMe)₂C:), H₂B=N^{*i*}Pr₂,²⁸ **P9B**²⁵ (P9B = ^{*i*}Pr₂P(C₆H₄)BBN) were synthesized according to literature procedures. BI₃²⁹ and Me₂S•BI₃³⁰ were synthesized according to modified synthetic procedures with specific additional details provided in Section 3.4.2.. ¹H, ¹¹B, ¹³C {¹H}, and ³¹P NMR spectra were recorded at room temperature using a Varian Inova-400, VNMRS-500, or VNMRS-700 spectrometer and referenced to Me₄Si (¹H, ¹³C {¹H}), 85 % H₃PO₄ (³¹P), and 15 % F₃B•OEt₂ (¹¹B). Chemical shifts are reported in parts per million (ppm) and coupling constants (*J*) are reported in Hertz (Hz). Elemental analyses and thermal gravimetric analyses were performed at the Analytical and Instrumentation Laboratory at the University of Alberta using the Thermo Flash 2000 Elemental Analyzer and the Perkin Elmer Pyris 1, respectively. Melting points were measured in sealed glass capillaries under nitrogen using MelTemp apparatus. Infrared (IR) spectra were recorded either as Nujol mulls on KBr plates with a Nicolet IR100 FTIR spectrometer or as powders in an air-free (N₂-filled) KBr plate chamber with a Thermo Nicolet 8700 FTIR Spectrometer and Continuum Microscope.

3.4.2 Synthetic Procedures

Synthesis of [PB{H₂BNH₂}] (1). A solution of H₃B•NH₃ (0.0117 g, 0.379 mmol) in 5 mL of THF was added to a solution of ^{*i*}Pr₂P(C₆H₄)BCy₂ (**PB**)^{8b,9} (0.138 g, 0.373 mmol) in 5 mL of THF. After stirring the mixture for 12 hrs at room temperature, the volatiles were removed under vacuum. 5 mL of hexanes were then added to the crude reaction product and the resulting mixture was filtered through Celite. Afterwards, volatiles were removed from the filtrate to give [PB{H₂BNH₂}] (**1**) as a white solid (0.1125 g, 75 %).

Colorless X-ray quality crystals of **1** were grown from a concentrated solution of cold (-35 °C) hexanes. $^1\text{H}\{^{11}\text{B}\}$ NMR (498.1 MHz, C_6D_6): $\delta = 7.77$ (dd, $^3J_{\text{HP}} = 3.6$ Hz, $^3J_{\text{HH}} = 8.4$ Hz, 1H, ArH), 7.26-7.28 (m, 1H, ArH), 6.95-6.97 (m, 1H, ArH), 6.88-6.91 (m, 1H, ArH), 2.42 (br d, $^1J_{\text{BH}} = \text{ca. } 138$ Hz, 2H, BH_2), 2.00 (pseudo-d, 2H, H_{Cy}), 1.87-1.95 (m, 6H, H_{Cy}), 1.76-1.82 (m, 2H, $\text{CH}(\text{CH}_3)_2$), 1.64-1.72 (m, 2H, H_{Cy}), 1.43-1.61 (m, 4H, H_{Cy}), 1.32-1.37 (m, 2H, H_{Cy}), 1.02-1.08 (m, 2H, H_{Cy}), 0.81-0.92 (m, 4H, H_{Cy}), 0.86 (dd, $^3J_{\text{HH}} = 8.4$ Hz, $^3J_{\text{HP}} = 15.4$ Hz, 6H, $\text{CH}(\text{CH}_3)_2$), 0.80 (dd, $^3J_{\text{HH}} = 6.9$ Hz, $^3J_{\text{HP}} = 13.9$ Hz, 6H, $\text{CH}(\text{CH}_3)_2$). *Note: the resonance for the NH_2 protons could not be located.* $^{13}\text{C}\{^1\text{H}\}$ NMR (176.0 MHz, C_6D_6): $\delta = 135.1$ (d, $J_{\text{CP}} = 14.1$ Hz, ArC), 130.5 (d, $J_{\text{CP}} = 3.7$ Hz, ArC), 130.0 (d, $J_{\text{CP}} = 2.6$ Hz, ArC), 123.6 (d, $J_{\text{CP}} = 7.9$ Hz, ArC), 120.9 (d, $J_{\text{CP}} = 50.5$ Hz, ArC), 34.6 (br, BCy_2), 31.7 (s, BCy_2), 30.9 (s, BCy_2), 30.2 (s, BCy_2), 29.9 (s, BCy_2), 28.5 (s, BCy_2), 23.1 (d, $^1J_{\text{CP}} = 36.8$ Hz, $\text{CH}(\text{CH}_3)_2$), 17.1 (s, $\text{CH}(\text{CH}_3)_2$), 16.9 (s, $\text{CH}(\text{CH}_3)_2$). *Note: the resonance for the ArC bound to boron could not be located.* $^{31}\text{P}\{^1\text{H}\}$ NMR (161.9 MHz, C_6D_6): $\delta = 3.5$ (br, $i\text{Pr}_2\text{P}$). $^{11}\text{B}\{^1\text{H}\}$ NMR (128.3 MHz, C_6D_6): $\delta = -6.0$ (br, BCy_2 , FWHM = 180 Hz), -24.6 (br, BH_2 , FWHM = 160 Hz). Selected IR bands (Nujol mull, cm^{-1}): 2727 (s, $\nu\text{B-H}$), 3280 (s, $\nu\text{N-H}$), 3322 (s, $\nu\text{N-H}$). Anal. Calcd. for $\text{C}_{24}\text{H}_{44}\text{B}_2\text{NP}$ (%): C 72.21, H 11.11, N 3.51; Found: C 72.16, H 11.06, N 3.55. M.p. 110-112 °C.

Independent synthesis of $[\text{PB}\{\text{BH}_3\}]$ (2**).** $\text{Me}_2\text{S}\cdot\text{BH}_3$ (2.0 M solution in THF, 213.7 μL , 0.43 mmol) was added quickly to a stirring solution of **PB** (158.3 mg, 0.4274 mmol) in 5 mL of C_6H_6 and the mixture was stirred at room temperature for 8 hrs. Afterwards,

the volatiles were removed under vacuum and the reaction mixture was extracted into 5 mL of hexanes. After filtering the reaction mixture, the filtrate was concentrated to a final volume of *ca.* 2 mL under vacuum and the solution was cooled to -35 °C for 8 hrs to yield [PB{BH₃}] (**2**) as clear colorless X-ray quality crystals (0.1282 g, 78 %). ¹H{¹¹B} NMR (498.1 MHz, C₆D₆): δ = 7.33 (dd, ³J_{HP} = 2.5 Hz, ³J_{HH} = 7.5 Hz, 1H, ArH), 7.24 (t, ³J_{HH} = 7.5 Hz, 1H, ArH), 7.03 (t, ³J_{HH} = 6.9 Hz, 1H, ArH), 6.95-6.97 (m, 1H, ArH), 2.16 (pseudo-d, 2H, H_{Cy}), 1.78-1.94 (m, 9H, H_{Cy} and CH(CH₃)₂), 1.30-1.44 (m, 9H, H_{Cy}), 1.19-1.27 (m, 4H, H_{Cy}), 0.92 (dd, ³J_{HH} = 6.9 Hz, ³J_{HP} = 7.9 Hz, 6H, CH(CH₃)₂), 0.85 (dd, ³J_{HH} = 6.9 Hz, ³J_{HP} = 7.9 Hz, 6H, CH(CH₃)₂), 0.33 (s, 3H, BH₃). ¹³C{¹H} NMR (175.9 MHz, C₆D₆): δ = 131.1 (d, J_{CP} = 14.6 Hz, ArC), 130.6 (d, J_{CP} = 4.7 Hz, ArC), 130.4 (d, J_{CP} = 2.6 Hz, ArC), 127.6 (s, ArC), 127.3 (s, ArC), 125.3 (d, J_{CP} = 8.1 Hz, ArC), 34.6 (s, BCy₂), 32.4 (s, BCy₂), 32.2 (s, BCy₂), 29.5 (s, BCy₂), 29.2 (s, BCy₂), 28.1 (s, BCy₂), 23.6 (d, ¹J_{CP} = 36.6 Hz, CH(CH₃)₂), 17.7 (s, CH(CH₃)₂), 17.2 (s, CH(CH₃)₂). ³¹P{¹H} NMR (201.6 MHz, C₆D₆): δ = 25.0 (br, ⁱPr₂P). ¹¹B{¹H} NMR (159.8 MHz, C₆D₆): δ = 34.4 (s, BCy₂), -31.1 (s, BH₃). Anal. Calcd. for C₂₄H₄₃B₂P (%): C 75.03, H 11.28; Found: C 74.61, H 11.11. M.p. 73-75 °C.

Synthesis of [PB{H₂BN(Me)H}] (3**).** A solution of H₂(Me)N•BH₃ (0.0054 g, 0.12 mmol) in 5 mL of THF was added to a solution of ⁱPr₂P(C₆H₄)BCy₂ (**PB**) (0.0443 g, 0.119 mmol) in 5 mL of THF. After stirring the mixture for 24 hrs at room temperature, the volatiles were removed under vacuum. 5 mL of hexanes were then added to the product, then the mixture was filtered through Celite, and the volatiles were removed

from the filtrate to give [PB{H₂BN(Me)H}] (**3**) as a white solid (0.0301 g, 61 %). Colorless X-ray quality crystals of **3** were grown from of a concentrated solution of cold (-35 °C) hexanes. ¹H{¹¹B} NMR (498.1 MHz, C₆D₆): δ = 7.96 (dd, ³J_{HP} = 4.4 Hz, ³J_{HH} = 7.9 Hz, 1H, ArH), 7.31 (pseudo-t, 1H, ArH), 6.98 (pseudo-t, 1H, ArH), 6.91 (pseudo-t, 1H, ArH), 2.49 (br s, 3H, NCH₃), 2.35 (br s, 1H, NH), 2.21 (pseudo-d, 1H, H_{Cy}), 2.03 (pseudo-d, 1H, H_{Cy}), 1.89-1.97 (m, 6H, H_{Cy} and CH(CH₃)₂), 1.81 (septet, ³J_{HH} = 8.9 Hz, 1H, CH(CH₃)₂), 1.49-1.56 (m, 4H, H_{Cy}), 1.34-1.46 (m, 4H, H_{Cy}), 1.27-1.34 (m, 2H, H_{Cy}), 1.19-1.24 (m, 2H, H_{Cy}), 1.10-1.17 (m, 2H, H_{Cy}), 1.04 (pseudo-d, 1H, H_{Cy}), 0.80-0.91 (m, 12H, CH(CH₃)₂). *Note: the BH₂ resonance could not be located by ¹H NMR, even upon ¹¹B decoupling.* ¹³C{¹H} NMR (175.9 MHz, C₆D₆): δ = 135.8 (d, J_{CP} = 14.8 Hz, ArC), 130.3 (d, J_{CP} = 3.8 Hz, ArC), 129.9 (d, J_{CP} = 2.6 Hz, ArC), 123.8 (d, J_{CP} = 7.9 Hz, ArC), 41.3 (d, J_{CP} = 15.3 Hz, NCH₃), 35.9 (s, BC_{y2}), 33.3 (s, BC_{y2}), 32.9 (s, BC_{y2}), 32.5 (s, BC_{y2}), 31.7 (s, BC_{y2}), 30.7 (s, BC_{y2}), 30.6 (s, BC_{y2}), 30.4 (s, BC_{y2}), 30.0 (s, BC_{y2}), 28.7 (s, BC_{y2}), 28.6 (s, BC_{y2}), 25.1 (d, ¹J_{CP} = 35.5 Hz, CH(CH₃)₂), 21.3 (d, ¹J_{CP} = 38.5 Hz, CH(CH₃)₂), 17.4 (s, CH(CH₃)₂), 17.3 (s, CH(CH₃)₂), 17.0 (s, CH(CH₃)₂), 16.3 (s, CH(CH₃)₂). *Note: the resonances for the ArC bound to boron and phosphorus could not be located by ¹³C{¹H} NMR spectroscopy.* ³¹P{¹H} NMR (201.6 MHz, C₆D₆): δ = 3.9 (s, ⁱPr₂P). ¹¹B{¹H} NMR (159.8 MHz, C₆D₆): δ = -2.5 (s, BC_{y2}), -20.5 (s, BH₂). Selected IR bands (powder, KBr plate, cm⁻¹): 2352 (s, νB-H), 2427 (s, νB-H), 3276 (s, νN-H). Anal. Calcd. for C₂₅H₄₆B₂NP (%): C 72.66, H 11.22, N 3.39; Found: C 73.58, H 11.36, N 3.95. M.p. 105-107 °C.

Synthesis of [P9B{H₂BNH₂}] (4). A solution of H₃B•NH₃ (34.6 mg, 1.12 mmol) in 2 mL of C₆H₆ was added to a stirring solution of **P9B** (351.0 mg, 1.117 mmol) in 10 mL of C₆H₆. The reaction mixture was then heated to 65 °C for 24 hrs. The reaction mixture was then cooled to room temperature and the volatiles were removed under vacuum. 15 mL of toluene were then added and the mixture was filtered through Celite. The filtrate was evaporated to dryness to yield [P9B{H₂BNH₂}] (**4**) as a white solid (0.3552 g, 93 %). Colorless X-ray quality crystals of **4** were grown from a concentrated solution in cold (-35 °C) hexanes after 16 hrs. ¹H{¹¹B} NMR (498.1 MHz, C₆D₆): δ = 8.30 (dd, ³J_{HH} = 7.9 Hz, ³J_{HP} = 11.8 Hz, 1H, ArH), 7.31 (pseudo-t, 1H, ArH), 7.05 (pseudo-t, 1H, ArH), 6.97 (pseudo-t, 1H, ArH), 2.55 (br s, 2H, BH₂), 2.28-2.37 (m, 3H, BCH and CH₂), 2.18-2.27 (m, 2H, CH₂), 2.04-2.09 (m, 4H, CH₂), 1.89-1.98 (m, 4H, CH(CH₃)₂ and CH₂), 1.75 (pentet, ³J_{HH} = 6.9 Hz, 1H, BCH), 1.12 (br, 2H, CH₂), 0.88 (dd, ³J_{HH} = 6.5 Hz, ³J_{HP} = 14.4 Hz, 6H, CH(CH₃)₂), 0.82 (dd, ³J_{HH} = 6.9 Hz, ³J_{HP} = 14.9 Hz, 6H, CH(CH₃)₂). *Note: the resonance for the NH₂ protons could not be located by ¹H NMR.* ¹³C{¹H} NMR (175.9 MHz, C₆D₆): δ = 136.5 (d, J_{CP} = 13.4 Hz, ArC), 130.9 (d, J_{CP} = 3.3 Hz, ArC), 129.8 (d, J_{CP} = 2.6 Hz, ArC), 124.7 (d, J_{CP} = 7.9 Hz, ArC), 124.4 (s, ArC), 124.2 (s, ArC), 32.9 (s, CH₂), 32.6 (s, CH₂), 25.5 (br, BCH), 25.2 (s, CH₂), 23.8 (d, ¹J_{CP} = 35.7 Hz, CH(CH₃)₂), 23.7 (s, CH₂), 17.5 (s, CH(CH₃)₂), 16.6 (s, CH(CH₃)₂). ³¹P{¹H} NMR (201.6 MHz, C₆D₆): δ = 4.0 (br, ⁱPr₂P). ¹¹B{¹H} NMR (159.8 MHz, C₆D₆): δ = -7.7 (s, BCH), -26.1 (br, BH₂). Selected IR bands (powder, KBr plate, cm⁻¹): 2328 (s, νB-H), 2390 (s, νB-H), 3274 (s, νN-H), 3315 (s, νN-H). Anal. Calcd. for C₂₀H₃₆B₂NP (%): C 70.01, H 10.58, N 4.08; Found: C 69.97, H 10.48, N 4.06. M.p. 163-164 °C.

Independent synthesis of [P9B{BH₃}] (5). Me₂S•BH₃ (2.0 M solution in THF, 14.0 μL, 0.028 mmol) was added quickly to **P9B** (0.0083 mg, 0.026 mmol) in 5 mL of THF and the mixture was stirred at room temperature for 8 hrs. Afterwards, the volatiles were removed under vacuum to yield [P9B{BH₃}] (**5**) as a spectroscopically pure white powder (0.0085 g, 98 %). ¹H{¹¹B} NMR (498.1 MHz, C₆D₆): δ = 8.03 (dd, ³J_{HP} = 2.9 Hz, ³J_{HH} = 7.9 Hz, 1H, ArH), 7.25 (pseudo-t, 1H, ArH), 7.02 (pseudo-t, 1H, ArH), 6.91 (pseudo-t, 1H, ArH), 2.59-2.62 (m, 4H, CH₂), 2.38-2.43 (m, 2H, CH₂), 2.20-2.26 (m, 4H, CH₂), 2.09 (br, 1H, BCH), 1.92 (br, 1H, BCH), 1.75 (septet, ³J_{HH} = 6.9 Hz, 2H, CH(CH₃)₂), 1.53-1.56 (m, 2H, CH₂). 0.81 (dd, ³J_{HP} = 16.4 Hz, ³J_{HH} = 5.4 Hz, 6H, CH(CH₃)₂), 0.71 (dd, ³J_{HP} = 14.4 Hz, ³J_{HH} = 6.4 Hz, 6H, CH(CH₃)₂), 0.56 (br, 3H, BH₃). ¹³C{¹H} NMR (125.6 MHz, C₆D₆): δ = 132.2 (d, J_{CP} = 13.8 Hz, ArC), 131.0 (d, J_{CP} = 5.0 Hz, ArC), 131.3 (d, J_{CP} = 2.5 Hz, ArC), 125.0 (d, J_{CP} = 8.8 Hz, ArC), 124.6 (s, ArC), 124.1 (s, ArC), 36.7 (s, CH₂), 32.6 (s, CH₂), 28.7 (s, BCH), 25.4 (s, CH₂), 24.5 (s, CH₂), 21.6 (d, ¹J_{CP} = 36.4 Hz, CH(CH₃)₂), 16.7 (s, CH(CH₃)₂), 16.4 (s, CH(CH₃)₂). ³¹P{¹H} NMR (201.6 MHz, C₆D₆): δ = 24.8 (br, ⁱPr₂P). ¹¹B{¹H} NMR (159.8 MHz, C₆D₆): δ = 32.6 (s, BCH), -27.8 (pseudo-d, ¹J_{BP} = ca. 92 Hz, BH₃).

Synthesis of BI₃. This compound was made according to a modified literature procedure.²⁹ Iodine (I₂, 25.0 g, 98.5 mmol) was added quickly to a stirring solution of Li[BH₄] (1.07 g, 49.3 mmol) in 40 mL of heptane, resulting in a purple-colored reaction mixture. The reaction mixture was then heated to reflux for 1 hr, leading to the

consumption of I₂, which was observed by a color change of the reaction mixture from purple to yellow. After cooling the mixture to room temperature and removing the volatiles under vacuum, the crude product was loaded into a sublimation apparatus, followed by heating at 40 °C for 24 hrs at 0.020 mbar to afford pure colorless crystals of BI₃ on the water-cooled sublimation finger. The recovered crystals (8.06 g, 42 %) were stored in the freezer at -35 °C prior to use. ¹¹B{¹H} NMR (159.8 MHz, C₆D₆): δ = -7.5 (s, BI₃).

Synthesis of Me₂S•BI₃. This compound was made according to a modified literature procedure.³⁰ Dimethylsulfide (Me₂S, 280 μL, 3.78 mmol) was added quickly to a stirring solution of BI₃ (1.44 g, 3.67 mmol) in 10 mL of hexanes, resulting in the formation of a white crystalline precipitate after 1 min. After stirring for 1 hr at room temperature, the precipitate was allowed to settle for 5 min and the mother liquor was subsequently decanted. Removal of the volatiles from the remaining solid afforded Me₂S•BI₃ (1.08 g, 65 %) as a colorless solid. In addition, the decanted hexanes solution (mother liquor) was stored in the freezer (-35 °C) for 16 hrs to afford colorless X-ray quality crystals of Me₂S•BI₃. ¹H NMR (699.7 MHz, C₆D₆): δ = 1.44-1.45 (m, 6H, (H₃C)₂S). ¹³C{¹H} NMR (175.9 MHz, C₆D₆): δ = 25.3 (s, (H₃C)₂S). ¹¹B{¹H} NMR (128.3 MHz, C₆D₆): δ = -68.5 (s, BI₃). Anal. Calcd. for C₂H₆BI₃S (%): C 5.30, H 1.33, S 7.07; Found: C 6.02, H 1.46, S 7.09.

Synthesis of [PB{H(I)BNH₂}] (6). A solution of Me₂S•BI₃ (0.4361 g, 0.9624 mmol) in 2 mL of toluene was added to a solution of [PB{H₂BNH₂}] (1) (0.3838 g, 0.9614 mmol) in 10 mL of toluene, resulting in the formation of a white precipitate. The reaction mixture was then stirred for 8 hrs and the volatiles were removed under vacuum. The product was then washed with 3 × 2 mL of pentane, followed by the addition of 5 mL of C₆H₆. The C₆H₆ solution was then frozen and placed under high vacuum to lyophilize the product. Once the C₆H₆ was removed, 5 mL of hexanes were added and the extracted mixture was filtered through a 2 cm plug of silica gel in a glass Pasteur pipette. The filtrate was concentrated to a volume of *ca.* 1 mL and cooled to -35 °C for 16 hrs to yield [PB{H(I)BNH₂}] (6) as colorless crystals of suitable quality for single-crystal X-ray crystallography (0.1135 g, 22 % yield, 92 % purity by ¹H NMR spectroscopy). *Note: 6 could not be isolated in high enough purity to obtain suitable elemental analyses due to a persistent Me₂S•BI₂H by-product that could not be removed.* ¹H{¹¹B} NMR (498.1 MHz, C₆D₆): δ = 7.64 (dd, ³J_{HP} = 3.9 Hz, ³J_{HH} = 7.9 Hz, 1H, ArH), 7.20-7.24 (m, 1H, ArH), 6.88-6.92 (m, 1H, ArH), 6.74-6.78 (m, 1H, ArH), 4.20 (br 1H, BH), 3.00-3.08 (m, 1H, NH), 2.78 (br s, 1H, NH), 2.66 (septet, ³J_{HH} = 6.9 Hz, 1H, CH(CH₃)₂), 1.98 (septet, ³J_{HH} = 6.9 Hz, 1H, CH(CH₃)₂), 1.76-1.89 (m, 8H, H_{Cy}), 1.62-1.69 (m, 1H, H_{Cy}), 1.44-1.53 (m, 1H, H_{Cy}), 1.32-1.39 (m, 6H, H_{Cy}), 1.18-1.28 (m, 2H, H_{Cy}), 1.15 (dd, ³J_{HH} = 6.9 Hz, ³J_{HP} = 8.5 Hz, 3H, CH(CH₃)₂), 0.90-0.97 (m, 1H, H_{Cy}), 0.78-0.88 (m, 6H, CH(CH₃)₂), 0.63-0.72 (m, 5H, CH(CH₃)₂ and H_{Cy}), 0.46-0.52 (m, 1H, H_{Cy}). ¹³C{¹H} NMR (175.9 MHz, C₆D₆): δ = 134.9 (d, J_{CP} = 14.6 Hz, ArC), 130.6 (d, J_{CP} = 2.6 Hz, ArC), 130.4 (d, J_{CP} = 4.9 Hz, ArC), 124.0 (d, J_{CP} = 8.6 Hz, ArC), 117.6 (d, J_{CP} = 55.5

Hz, ArC), 34.8 (br, BCy₂), 33.7 (br, BCy₂), 31.9 (s, BCy₂), 31.8 (s, BCy₂), 31.3 (s, BCy₂), 30.4 (s, BCy₂), 30.3 (s, BCy₂), 29.6 (s, BCy₂), 29.4 (s, BCy₂), 28.3 (s, BCy₂), 28.1 (s, BCy₂), 24.1 (d, ¹J_{CP} = 39.1 Hz, CH(CH₃)₂), 21.7 (d, ¹J_{CP} = 41.3 Hz, CH(CH₃)₂), 17.6 (s, CH(CH₃)₂), 17.1 (s, CH(CH₃)₂), 17.0 (s, CH(CH₃)₂), 15.4 (s, CH(CH₃)₂). *Note: the resonance for the ArC bound to boron could not be located.* ³¹P{¹H} NMR (161.9 MHz, C₆D₆): δ = -8.0 (s, ⁱPr₂P). ¹¹B{¹H} NMR (128.3 MHz, C₆D₆): δ = -3.2 (br, BCy₂, FWHM = 25 Hz), -21.9 (br, BH, FWHM = 55 Hz). Selected IR bands (Nujol mull, cm⁻¹): 2730 (s, νB-H), 3271 (s, νN-H), 3314 (s, νN-H). M.p. 170-172 °C.

Synthesis of [PB{HBNH}] (7). A solution of K[N(SiMe₃)₂] (0.0214 g, 0.107 mmol) in 1 mL of toluene was added to a solution of [PB{H(I)BNH₂}] (6) (0.0563 g, 0.107 mmol) in 5 mL of toluene, resulting in the formation of a white precipitate. The reaction mixture was then stirred for 1 hr and the volatiles were removed under vacuum. 5 mL of hexanes were then added and the mixture was filtered through Celite. The filtrate was concentrated to a volume of *ca.* 2 mL under vacuum and cooled to -35 °C for 16 hrs to yield [PB{HBNH}] (7) as colorless crystals of suitable quality for single-crystal X-ray crystallography (0.0205 g, 48 %). ¹H{¹¹B} NMR (498.1 MHz, C₆D₆): δ = 8.01 (dd, ³J_{HP} = 2.9 Hz, ³J_{HH} = 7.9 Hz, 1H, ArH), 7.29-7.33 (m, 1H, ArH), 6.94-6.97 (m, 1H, ArH), 6.80-6.84 (m, 1H, ArH), 6.60 (br d, ³J_{HP} = 29.9 Hz, 1H, NH), 4.97 (br d, ²J_{HP} = 59.8 Hz, 1H, BH), 1.93-2.00 (m, 10H, H_{Cy}), 1.78-1.81 (m, 2H, H_{Cy}), 1.68-1.75 (m, 1H, CH(CH₃)₂), 1.52-1.65 (m, 3H, CH(CH₃)₂ and H_{Cy}), 1.35-1.42 (m, 2H, H_{Cy}), 1.19-1.28 (m, 2H, H_{Cy}), 0.82-0.95 (m, 4H, H_{Cy}), 0.79 (dd, ³J_{HH} = 7.0 Hz, ³J_{HP} = 15.9 Hz, 6H,

CH(CH₃)₂), 0.73 (dd, ³J_{HH} = 7.0 Hz, ³J_{HP} = 15.4 Hz, 6H, CH(CH₃)₂). ¹³C{¹H} NMR (175.9 MHz, C₆D₆): δ = 135.2 (d, J_{CP} = 14.1 Hz, ArC), 130.2 (d, J_{CP} = 3.5 Hz, ArC), 129.8 (d, J_{CP} = 5.3 Hz, ArC), 123.5 (d, J_{CP} = 10.5 Hz, ArC), 118.0 (d, J_{CP} = 65.0 Hz, ArC), 35.0 (br, BCy₂), 31.8 (s, BCy₂), 31.0 (s, BCy₂), 30.3 (s, BCy₂), 30.2 (s, BCy₂), 28.8 (s, BCy₂), 22.8 (d, ¹J_{CP} = 40.4 Hz, CH(CH₃)₂), 17.8 (s, CH(CH₃)₂), 17.6 (s, CH(CH₃)₂). *Note: the resonance for the ArC bound to boron could not be located.* ³¹P{¹H} NMR (161.9 MHz, C₆D₆): δ = -11.8 (s, ⁱPr₂P). ¹¹B{¹H} NMR (128.3 MHz, C₆D₆): δ = 28.2 (br s, BH, FWHM = 32 Hz), -5.8 (s, Cy₂B). Selected IR bands (powder, KBr plate, cm⁻¹): 1443 (s, νN=B), 2465 (s, νB-H), 3343 (s, νN-H). Anal. Calcd. for C₂₄H₄₂B₂NP (%): C 72.57, H 10.66, N 3.53; Found: C 72.06, H 10.41, N 3.24. M.p. 118-120 °C.

Synthesis of [PB{H(Bn)BNH}{K(THF)₂}] (8). A solution of BnK (8.3 mg, 0.064 mmol) in 1 mL of THF was added to a stirring solution of [PB{HBNH}] (7) (22.6 mg, 0.0569 mmol) in 10 mL of THF, resulting in the formation of a turbid yellow mixture. The reaction mixture was stirred for 1 hr and then filtered through Celite. The filtrate was concentrated to a volume of *ca.* 2 mL, layered with 2 mL of Me₃SiOSiMe₃ and cooled to -35 °C for 16 hrs to yield [PB{H(Bn)BNH}{K(THF)₂}] (8) as colorless crystals (0.0196 g, 51 %). ¹H{¹¹B} NMR (399.9 MHz, C₆D₆): δ = 8.05-8.08 (m, 1H, ArH), 7.41 (t, ³J_{HH} = 7.8 Hz, 1H, ArH), 7.17-7.19 (m, 2H, ArH), 7.09 (pseudo-t, 2H, ArH), 6.89 (pseudo-t, 2H, ArH), 6.72 (pseudo-t, 1H, ArH), 3.50-3.53 (m, 8H, coordinated THF CH₂), 2.14-2.19 (m, 4H, benzyl-CH₂ and CH(CH₃)₂), 2.08 (pseudo-d,

2H, H_{Cy}), 1.94-1.97 (m, 6H, H_{Cy}), 1.74-1.86 (m, 4H, H_{Cy}), 1.48-1.57 (m, 4H, H_{Cy}), 1.39-1.43 (m, 8H, coordinated THF CH_2), 1.28-1.38 (m, 4H, H_{Cy}), 1.04-1.13 (m, 12H, $CH(CH_3)_2$), 0.72-0.82 (m, 2H, H_{Cy}), 0.34 (br s, 1H, BH). *Note: The resonance for the NH proton could not be located.* $^{13}C\{^1H\}$ NMR (175.9 MHz, C_6D_6): δ = 152.2 (d, J_{CP} = 19.3 Hz, ArC), 134.7 (d, J_{CP} = 10.6 Hz, ArCH), 130.7 (s, ArCH), 128.5 (s, ArCH), 127.8 (s, ArCH), 127.7 (s, ArCH), 125.5 (s, ArC), 125.3 (s, ArC), 122.9 (s, ArCH), 122.0 (d, $^1J_{CP}$ = 6.9 Hz, ArCH), 67.9 (s, CH_2 , coordinated THF), 36.2 (br s, BCy_2), 32.2 (s, BCy_2), 32.0 (s, BCy_2), 31.7 (s, BCy_2), 31.1 (s, BCy_2), 31.0 (s, BCy_2), 29.1 (s, CH_2 , $BCH_2(C_6H_5)$), 25.8 (s, CH_2 , coordinated THF), 21.6 (d, $^1J_{CP}$ = 19.7 Hz, $CH(CH_3)_2$), 18.5 (s, $CH(CH_3)_2$), 17.5 (s, $CH(CH_3)_2$). $^{31}P\{^1H\}$ NMR (161.9 MHz, C_6D_6): δ = -24.7 (s, iPr_2P). $^{11}B\{^1H\}$ NMR (128.3 MHz, C_6D_6): δ = -7.9 (s, Cy_2B), -10.1 (s, BH). Anal. Calcd. for $C_{39}H_{65}B_2KNO_2P$ (%): C 69.74, H 9.76, N 2.09; Found: C 69.58, H 9.36, N 2.18. M.p. 133-134 °C.

Synthesis of [$^iPr_2P(C_6H_4)BCy\{Cl_2BNH\}$] (9). A solution of TCCA (14.6 mg, 0.0628 mmol) in 1 mL of toluene was added to a stirring solution of $[PB\{HBNH\}]$ (7) (40.4 mg, 0.102 mmol) in 5 mL of toluene, leading to the formation of a white slurry. The reaction mixture was then stirred for 1 hr and the volatiles were removed under vacuum. 20 mL of hexanes were then added, and the mixture was filtered through Celite. The filtrate was concentrated to a volume of *ca.* 2 mL and cooled to -35 °C for 16 hrs to yield [$^iPr_2P(C_6H_4)BCy\{Cl_2BNH\}$] (9) as a white microcrystalline solid (0.0274 g, 70

%). Colorless X-ray quality crystals of **9** were grown out of a concentrated solution of a cold (-35 °C) 1:1 fluorobenzene:Me₃SiOSiMe₃ solvent mixture. ¹H NMR (499.7 MHz, C₆D₆): δ = 7.79 (dd, ³J_{HP} = 3.9 Hz, ³J_{HH} = 7.6 Hz, 1H, ArH), 7.18-7.21 (m, 1H, ArH), 7.03-7.06 (m, 1H, ArH), 6.82-6.85 (m, 1H, ArH), 5.18 (br d, ³J_{HP} = 19.9 Hz, 1H, NH), 2.31 (septet, ³J_{HH} = 6.9 Hz, 1H, CH(CH₃)₂), 2.29 (septet, ³J_{HH} = 6.9 Hz, 1H, CH(CH₃)₂), 1.71 (pseudo-d, 2H, H_{Cy}), 1.63 (pseudo-d, 2H, H_{Cy}), 1.36-1.42 (m, 2H, H_{Cy}), 1.28-1.33 (m, 2H, H_{Cy}), 1.14 (dd, ³J_{HH} = 6.8 Hz, ³J_{HP} = 15.9 Hz, 6H, CH(CH₃)₂), 0.98-1.04 (m, 3H, H_{Cy}), 0.91 (dd, ³J_{HH} = 7.2 Hz, ³J_{HP} = 13.9 Hz, 6H, CH(CH₃)₂). ¹³C{¹H} NMR (125.7 MHz, C₆D₆): δ = 136.3 (d, J_{CP} = 11.8 Hz, ArC), 132.6 (d, J_{CP} = 2.6 Hz, ArC), 131.7 (d, J_{CP} = 2.6 Hz, ArC), 129.2 (d, J_{CP} = 8.0 Hz, ArC), 122.2 (s, ArC), 121.8 (s, ArC), 29.8 (s, BCy), 29.0 (br, BCy), 28.4 (s, BCy), 27.3 (s, BCy), 20.9 (d, ¹J_{CP} = 34.8 Hz, CH(CH₃)₂), 16.9 (s, CH(CH₃)₂), 16.3 (s, CH(CH₃)₂). ³¹P{¹H} NMR (161.9 MHz, C₆D₆): δ = -5.7 (br quartet, ⁱPr₂P, ¹J_{BP} = ca. 161 Hz). ¹¹B{¹H} NMR (128.3 MHz, C₆D₆): δ = 42.1 (s, BCy), -1.4 (pseudo-d, Cl₂B, ¹J_{BP} = ca. 153 Hz). Anal. Calcd. for C₁₈H₃₀B₂Cl₂NP (%): C 56.31, H 7.88, N 3.65; Found: C 56.94, H 7.67, N 3.89. M.p. 96-97 °C.

3.4.3 X-ray Crystallography

Appropriate X-ray quality crystals were coated with a small amount of hydrocarbon oil (Paratone-N) and removed from the glovebox in a vial. Crystals were quickly mounted onto a glass fiber and placed in a low temperature stream of nitrogen

on the X-ray diffractometer. All data was collected using a Bruker APEX II CCD detector/D8 or PLATFORM diffractometer using Mo K α (0.71073 Å) or Cu K α (1.54178 Å) radiation, with the crystals cooled to -80 °C or -100 °C. The data was corrected for absorption through Gaussian integration from the indexing of crystal faces.³¹ Crystal structures were solved using intrinsic phasing (SHELXT)³² and refined using SHELXL-2014.³³ The assignment of hydrogen atom positions are based on the sp^2 - or sp^3 -hybridization geometries of their attached carbon atoms and were given thermal parameters 20 % greater than those of their parent atoms. Molecular structures are shown with thermal ellipsoids at a 30 % probability level and have been generated using SHELXP.

Table 3.1. X-ray crystallographic data for [PB{H₂BNH₂}] (**1**), [PB{BH₃}] (**2**), and [PB{H₂BN(Me)H}] (**3**).

Compound	1^b	2^b	3^b
Formula	C ₂₄ H ₄₄ B ₂ NP	C ₂₄ H ₄₃ B ₂ P	C ₂₅ H ₄₆ B ₂ NP
Formula weight	399.19	384.17	413.22
Crystal system	Monoclinic	Orthorhombic	Monoclinic
Space group	<i>P2₁/c</i> (No. 14)	<i>Pbca</i> (No. 61)	<i>P2₁/n</i>
Crystal dimensions (mm)	0.29×0.18×0.10	0.26×0.23×0.23	0.13×0.05×0.02
<i>a</i> (Å)	19.7455(6)	21.1816(4)	11.7168(5)
<i>b</i> (Å)	10.9680(3)	9.5950(2)	9.3707(4)
<i>c</i> (Å)	23.1511(7)	23.2387(5)	22.5993(9)
α (°)	90	90	90
β (°)	102.217(2)	90	91.399(3)
γ (°)	90	90	90
<i>V</i> (Å ³)	4900.3(3)	4722.97(17)	2480.54(18)
<i>Z</i>	8	8	4
ρ (g/cm ³)	1.082	1.081	1.106
Abs coeff (mm ⁻¹)	1.032	1.042	1.034
<i>T</i> (°C)	-100	-100	-100
$2\theta_{\max}$ (°)	148.42	145.09	148.38
Total data	112848	178745	42610
Unique data	9929 (0.1008)	4681 (0.0479)	4995 (0.0698)
Obs data [<i>I</i> >2 σ (<i>I</i>)] ^a	7806	4422	3944
Params	545	260	275
<i>R</i> ₁ [<i>I</i> >2 σ (<i>I</i>)] ^a	0.0432	0.0333	0.0372
<i>wR</i> ₂ [all data] ^a	0.1175	0.0931	0.0986
Max/min $\Delta\rho$ (e ⁻ Å ⁻³)	0.390/-0.330	0.310/-0.354	0.230/-0.225

$$^a R_1 = \frac{\sum ||F_o| - |F_c||}{\sum |F_o|}; wR_2 = [\frac{\sum w(F_o^2 - F_c^2)^2}{\sum w(F_o^4)}]^{1/2}.$$

^bHydrogen atoms bound to boron or nitrogen were located in the difference maps and refined isotropically; all other H atoms were placed in idealized positions and refined using a riding model.

Table 3.2. X-ray crystallographic data for [P9B{H₂BNH₂}] (**4**), Me₂S•BI₃, and [PB{H(I)BNH₂}] (**6**).

Compound	4^b	Me ₂ S•BI ₃	6^b
Formula	C ₂₀ H ₃₂ B ₂ NP	C ₂ H ₆ BSI ₃	C ₂₇ H ₅₀ B ₂ NPI
Formula weight	357.14	453.64	568.17
Crystal system	Triclinic	Monoclinic	Monoclinic
Space group	<i>P</i> -1	<i>P</i> 2 ₁ / <i>c</i> (<i>No. 14</i>)	<i>P</i> 2 ₁ / <i>c</i> (<i>No. 14</i>)
Crystal dimensions (mm)	0.15×0.13×0.07	0.07×0.06×0.11	0.12×0.05×0.04
<i>a</i> (Å)	9.5254(2)	7.0765(4)	18.2679(5)
<i>b</i> (Å)	10.5750(3)	7.2293(3)	11.4128(4)
<i>c</i> (Å)	11.1920(3)	18.9898(9)	14.6131(4)
α (°)	117.2440(10)	90	90
β (°)	95.4150(10)	92.749(2)	107.048(2)
γ (°)	92.8900(10)	90	90
V (Å ³)	992.25(4)	970.36(8)	2912.78(15)
Z	2	4	4
ρ (g/cm ³)	1.148	3.105	1.296
Abs coeff (mm ⁻¹)	1.201	77.20	9.241
T (°C)	-100	-100	-100
2θ _{max} (°)	159.39	149.46	147.90
Total data	41320	37103	38672
Unique data	3854 (0.0291)	1973 (0.0628)	5714 (0.1170)
Obs data [<i>I</i> >2σ(<i>I</i>)] ^a	3719	1912	4015
Params	237	67	276 ^{c,d}
R ₁ [<i>I</i> >2σ(<i>I</i>)] ^a	0.0309	0.0297	0.0539
wR ₂ [all data] ^a	0.0838	0.0787	0.1380
Max/min Δρ (e ⁻ Å ⁻³)	0.276/-0.248	1.551/-1.295	1.238/-0.995

$$^a R_1 = \frac{\sum ||F_o| - |F_c||}{\sum |F_o|}; wR_2 = \left[\frac{\sum w(F_o^2 - F_c^2)^2}{\sum w(F_o^4)} \right]^{1/2}.$$

^bHydrogen atoms bound to boron or nitrogen were located in the difference maps and refined isotropically; all other H atoms were placed in idealized positions and refined using a riding model.

^cAttempts to refine peaks of residual electron density as disordered or partial-occupancy solvent hexane atoms were unsuccessful. The data were corrected for disordered electron density through use of the SQUEEZE procedure as implemented in PLATON.³⁴ A total solvent-accessible void volume of 444 Å³ with a total electron count of 107 (0.5 hexane molecules per formula unit of **6**) was found in the unit cell.

^dThe bond lengths of N–H1N and N–H2N are restrained to be similar by SHELXL command SADI (total of 2 restraints).

Table 3.3. X-ray crystallographic data for [PB{HBNH}] (7), [PB{H(Bn)BNH}{K(THF)₂}] (8), and [ⁱPr₂P(C₆H₄)BCy{Cl₂BNH}] (9).

Compound	7 ^b	8 ^b	9 ^b
Formula	C ₂₄ H ₄₂ B ₂ NP	C ₃₉ H ₆₅ B ₂ KNO ₂ P	C ₂₄ H ₃₅ B ₂ Cl ₂ FNP
Formula weight	397.17	671.61	480.02
Crystal system	Monoclinic	Monoclinic	Triclinic
Space group	<i>P</i> 2 ₁ / <i>c</i> (No. 14)	<i>P</i> 2 ₁ / <i>c</i> (No. 14)	<i>P</i> $\bar{1}$ (No. 2)
Crystal dimensions (mm)	0.27×0.27×0.13	0.29×0.28×0.20	0.24×0.15×0.02
<i>a</i> (Å)	11.1624(4)	15.7833(8)	9.0010(2)
<i>b</i> (Å)	9.3546(3)	12.1282(6)	11.2467(3)
<i>c</i> (Å)	23.6269(8)	20.9485(10)	13.4916(3)
α (°)	90	90	83.2092(10)
β (°)	99.5776(19)	93.981(2)	89.9913(9)
γ (°)	90	90	71.6062(10)
<i>V</i> (Å ³)	2432.73(14)	4000.3(3)	1285.91(5)
<i>Z</i>	4	4	2
ρ (g/cm ³)	1.084	1.115	1.240
Abs coeff (mm ⁻¹)	1.039	1.769	3.001
<i>T</i> (°C)	-100	-100	-100
2 θ _{max} (°)	145.55	148.42	148.51
Total data	92836	157905	56310
Unique data	4766 (0.0584)	8123 (0.0416)	5015 (0.0427)
Obs data [<i>I</i> >2 σ (<i>I</i>)] ^a	4438	7633	4554
Params	261	514	324 ^e
<i>R</i> ₁ [<i>I</i> >2 σ (<i>I</i>)] ^a	0.0519	0.0401 ^{d,a}	0.0375
<i>wR</i> ₂ [all data] ^a	0.1376	0.1185 ^d	0.1140
Max/min $\Delta\rho$ (e ⁻ Å ⁻³)	0.605 ^c /-0.231	0.374/-0.563	0.696/-0.407

$$^a R_1 = \frac{\sum ||F_o| - |F_c||}{\sum |F_o|}; wR_2 = \left[\frac{\sum w(F_o^2 - F_c^2)^2}{\sum w(F_o^4)} \right]^{1/2}.$$

^bHydrogen atoms bound to boron or nitrogen were located in the difference maps and refined isotropically; all other H atoms were placed in idealized positions and refined using a riding model.

^cThe largest peak (0.605 e⁻ Å⁻³) in the difference map was located 1.5 Å from C21 (of a cyclohexyl group) and likely arises from a small amount of unresolved disorder of the Cy group (atoms C21 to C26). Given that the largest *U*_{eq} for any of the carbon atoms in that Cy group was only 0.072 and that there were no anomalies with the bond distances or angles, it was decided that it was not worth pursuing a highly restrained/constrained disorder model for that group.

^d $S = [\sum w(F_o^2 - F_c^2)^2 / (n - p)]^{1/2}$ (n = number of data; p = number of parameters varied; $w = [\sigma^2(F_o^2) + (0.0991P)^2 + 0.9680P]^{-1}$ where $P = [\text{Max}(F_o^2, 0) + 2F_c^2]/3$); $S = 1.031$ for **8**.

^eThe disordered fluorobenzene molecule was constrained to be an idealized hexagon and the C–F and C···F distances within both components were restrained to be approximately the same by use of the *SHELXL* **SADI** instruction. Additionally, the ADPs of the atoms of the fluorobenzene were restrained by use of the *SHELXL* **RIGU** (rigid-bond) restraint (total of 97 restraints).

3.5 References and Notes

1. Z. Zhao, B. Xu, Y. Tian, *Annu. Rev. Mater. Res.* **2016**, *46*, 383–406.
2. a) R. T. Paine, C. K. Narula, *Chem. Rev.* **1990**, *90*, 73–91; b) P. J. Fazen, J. S. Beck, A. T. Lynch, E. E. Remsen, L. G. Sneddon, *Chem. Mater.* **1990**, *2*, 96–97; c) D. J. Heldebrant, A. Karkamkar, N. J. Hess, M. Bowden, S. Rassat, F. Zheng, K. Rappe, T. Autrey, *Chem. Mater.* **2008**, *20*, 5332–5336; d) S. Frueh, R. Kellett, C. Mallery, T. Molter, W. S. Willis, C. King'onde, S. L. Suib, *Inorg. Chem.* **2011**, *50*, 783–792; e) D. Golberg, Y. Bando, C. C. Tang, C. Y. Zhi, *Adv. Mater.* **2007**, *19*, 2413–2432; f) X.-F. Jiang, Q. Weng, X.-B. Wang, X. Li, J. Zhang, D. Golberg, Y. Bando, *J. Mater. Sci. Tech.* **2015**, *31*, 589–598.
3. Y. Tian, B. Xu, D. Yu, Y. Ma, Y. Wang, Y. Jiang, W. Hu, C. Tang, Y. Gao, K. Luo, Z. Zhao, L.-M. Wang, B. Wen, J. He, Z. Liu, *Nature* **2013**, *493*, 385–388.
4. a) A. Staubitz, A. P. M. Robertson, I. Manners, *Chem. Rev.* **2010**, *110*, 4079–4124; b) Z. Mo, A. Rit, J. Campos, E. L. Kolychev, S. Aldridge, *J. Am. Chem. Soc.* **2016**, *138*, 3306–3309; c) D. A. Resendiz-Lara, G. R. Whittell, E. M. Leitao, I. Manners, *Macromolecules* **2019**, *52*, 7052–7064; d) G. Zhang, D. Morrison, G. Bao, H. Yu, C. W. Yoon, T. Song, J. Lee, A. T. Ung, Z. Huang, *Angew. Chem. Int. Ed.* **2021**, *60*, 11725–11729.
5. a) E. R. Lory, R. F. Porter, *J. Am. Chem. Soc.* **1973**, *95*, 1766–1770; b) T. Kawashima, K. Kawaguchi, E. Hirota, *J. Chem. Phys.* **1987**, *87*, 6331–6333; c) C. A. Thompson, L. Andrews, *J. Am. Chem. Soc.* **1995**, *117*, 10125–10126; d) C. A. Thompson, L. Andrews, J. M. L. Martin, J. El-Yazal, *J. Phys. Chem.* **1995**, *99*, 13839–13849; e) F. Zhang, P.

Maksyutenko, R. I. Kaiser, A. M. Mebel, A. Gregušová, S. A. Perera, R. J. Bartlett, *J. Phys. Chem. A* **2010**, *114*, 12148–12154.

6. For related work on unsaturated BN π -systems: a) P. Paetzold, *Pure Appl. Chem.* **1991**, *63*, 345–350; b) H. Nöth, *Angew. Chem. Int. Ed. Engl.* **1988**, *27*, 1603–1623; c) E. Rivard, W. A. Merrill, J. C. Fettinger, R. Wolf, G. H. Spikes, P. P. Power, *Inorg. Chem.* **2007**, *46*, 2971–2978; d) F. Dahcheh, D. Martin, D. W. Stephan, G. Bertrand, *Angew. Chem. Int. Ed.* **2014**, *53*, 13159–13163; e) T. Lorenz, M. Crumbach, T. Eckert, A. Lik, H. Helten, *Angew. Chem. Int. Ed.* **2017**, *56*, 2780–2784; f) M.-A. Légaré, G. Bélanger-Chabot, M. Rang, R. D. Dewhurst, I. Krummenacher, R. Bertermann, H. Braunschweig, *Nat. Chem.* **2020**, *12*, 1076–1080; g) R. Guo, T. Li, R. Wei, X. Zhang, Q. Li, L. L. Liu, C.-H. Tung, L. Kong, *J. Am. Chem. Soc.* **2021**, *143*, 13483–13488.

7. a) A. K. Swarnakar, C. Hering-Junghans, K. Nagata, M. J. Ferguson, R. McDonald, N. Tokitoh, E. Rivard, *Angew. Chem. Int. Ed.* **2015**, *54*, 10666–10669; b) A. K. Swarnakar, C. Hering-Junghans, M. J. Ferguson, R. McDonald, E. Rivard, *Chem. Sci.* **2017**, *8*, 2337–2343; c) M. R. Momeni, L. Shulman, E. Rivard, A. Brown, *Phys. Chem. Chem. Phys.* **2015**, *17*, 16525–16535.

8. a) D. W. Stephan, G. Erker, *Angew. Chem. Int. Ed.* **2010**, *49*, 46–76. For FLP chelation and their use in bond activation processes, see: b) S. Bontemps, G. Bouhadir, K. Miqueu, D. Bourissou, *J. Am. Chem. Soc.* **2006**, *128*, 12056–12057; c) C. Appelt, H. Westenberg, F. Bertini, A. W. Ehlers, J. C. Slootweg, K. Lammertsma, W. Uhl, *Angew. Chem. Int. Ed.* **2011**, *50*, 3925–3928; d) M.-A. Légaré, M. A. Courtemanche, É. Rochette, F.-G. Fontaine, *Science* **2015**, *349*, 513–516; e) D. H. A. Boom, E. J. J. de

- Boed, E. Nicolas, M. Nieger, A. W. Ehlers, A. R. Jupp, J. C. Sloatweg, *Z. Anorg. Allg. Chem.* **2020**, *646*, 586–592.
9. A. A. Omaña, R. K. Green, R. Kobayashi, Y. He, E. R. Antoniuk, M. J. Ferguson, Y. Zhou, J. G. C. Veinot, T. Iwamoto, A. Brown, E. Rivard, *Angew. Chem. Int. Ed.* **2021**, *60*, 228–231.
10. M. M. D. Roy, A. A. Omaña, A. S. S. Wilson, M. S. Hill, S. Aldridge, E. Rivard, *Chem. Rev.* **2021**, *121*, 12784–12965.
11. B. L. Frenette, A. A. Omaña, M. J. Ferguson, Y. Zhou, E. Rivard. *Chem. Commun.* **2021**, *57*, 10895–10898.
12. M. E. Bowden, G. J. Gainsford, W. T. Robinson, *Aust. J. Chem.* **2007**, *60*, 149–153.
13. Y. Shao, D. Truhlar, *Theor. Chem. Acc.* **2008**, *120*, 215–241.
14. T. H. Dunning Jr., *J. Chem. Phys.* **1989**, *90*, 1007–1023.
15. a) E. M. Leitao, N. E. Stubbs, A. P. M. Robertson, H. Helten, R. J. Cox, G. C. Lloyd-Jones, I. Manners, *J. Am. Chem. Soc.* **2012**, *134*, 16805–16816; b) N. E. Stubbs, A. Schäfer, A. P. M. Robertson, E. M. Leitao, T. Jurca, H. A. Sparkes, C. H. Woodall, M. F. Haddow, I. Manners, *Inorg. Chem.* **2015**, *54*, 10878–10889; c) M. W. Lui, N. R. Paisley, R. McDonald, M. J. Ferguson, E. Rivard, *Chem. Eur. J.* **2016**, *22*, 2134–2145.
16. F. Dankert, J.-E. Siewert, P. Gupta, F. Weigend, C. Hering-Junghans, *Angew. Chem. Int. Ed.* **2022**, *61*, e202207064.
17. a) C. A. Jaska, K. Temple, A. J. Lough, I. Manners, *J. Am. Chem. Soc.* **2003**, *125*, 9424–9434; b) A. Staubitz, A. Presa Soto, I. Manners, *Angew. Chem. Int. Ed.* **2008**, *47*, 6212–6215.

18. R. Ayyappan, Y. Coppel, L. Vendier, S. Ghosh, S. Sabo-Etienne, S. Bontemps, *Chem. Commun.* **2021**, *57*, 375–378.
19. E. D. Glendening, J. K. Badenhoop, A. E. Reed, J. E. Carpenter, J. A. Bohmann, C. M. Morales, C. R. Landis, F. Weinhold, *NBO 6.0*, Theoretical Chemistry Institute, University of Wisconsin, Madison WI, 2013.
20. For similar hydride-halide exchanges, see: a) P. Bag, A. Porzelt, P. J. Altmann, S. Inoue, *J. Am. Chem. Soc.* **2017**, *139*, 14384–14387; b) J. H. Muessig, M. Thaler, R. D. Dewhurst, V. Paprocki, J. Seufert, J. D. Mattock, A. Vargas, H. Braunschweig, *Angew. Chem. Int. Ed.* **2019**, *58*, 4405–4409.
21. R. Conrady, W. Müller-Warmuth, B. Krebs, G. Schwetlik, M. Wienkenhöver, *Ber. Bunsenges. Phys. Chem.* **1987**, *91*, 1322–1326.
22. I. M. Alecu, J. Zheng, Y. Zhao and D. G. Truhlar, *J. Chem. Theory Comput.* **2010**, *6*, 2872–2887.
23. C. Jones, *Nat. Rev. Chem.* **2017**, *1*, 0059.
24. D. E. Ryan, K. A. Andrea, J. J. Race, T. M. Boyd, G. C. Lloyd-Jones, A. S. Weller, *ACS Catal.* **2020**, *10*, 7443–7448.
25. M. Schlosser, J. Hartmann, *Angew. Chem. Int. Ed. Engl.* **1973**, *12*, 508–509.
26. M. M. D. Roy, E. Rivard, *Acc. Chem. Res.* **2017**, *50*, 2017–2025.
27. N. Kuhn, T. Kratz, *Synthesis* **1993**, 561–562.
28. L. Pasumansky, D. Haddenham, J. W. Clary, G. B. Fisher, C. T. Goralski, B. Singaram, *J. Org. Chem.* **2008**, *73*, 1898–1905.
29. S. Oda, K. Ueura, B. Kawakami, T. Hatakeyama, *Org. Lett.* **2020**, *22*, 700–704.

30. M. Schmidt, H. D. Block, *Chem. Ber.* **1970**, *103*, 3705–3710.
31. R. H. Blessing, *Acta. Cryst.* **1995**, *A51*, 33–38.
32. G. M. Sheldrick, *Acta. Cryst.* **2015**, *A71*, 3–8.
33. G. M. Sheldrick, *Acta. Cryst.* **2015**, *C71*, 3–8.
34. A. L. Spek, *Acta Cryst.* **2015**, *C71*, 9–18.

Chapter 4 – Frustrated Lewis Pair-ligated Tetrelenes

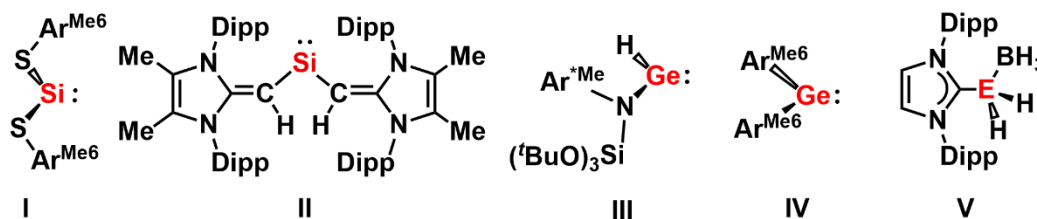
4.1 Introduction

Motivated by the reactivity of transition metal complexes, the study of main group elements has seen a recent “renaissance”, particularly in the synthesis of new kinetically-stabilized main group metal hydrides^{1,2} as well as low-valent main group element species in general.³ As a result of their often low HOMO-LUMO energy gaps,^{3a} tetrelenes (ER_2 ; E = Group 14 element, R = anionic ligand) can activate and functionalize industrially valuable molecules, such as H_2 , CO, or CO_2 .² Furthermore, related Group 14 element hydride complexes (REH) have also been targeted as catalysts for controlled hydride transfer to unsaturated substrates.²

Examples of highly reactive tetrelenes (Si or Ge) feature predominantly C- or N-ligands (Figure 4.1a, **I-V**).⁴ The most active Group 14 element (Si or Ge) hydride catalysts take advantage of kinetic stabilization (*i.e.*, use of bulky ligands) to prevent degradative pathways that eventually release $E(0)$; kinetic stabilization also provides access to the low-coordinate environments required for catalysis (Figure 4.1b, **VI-VII**).⁵

Selected examples of:

(a) C-/N-donor-stabilized tetrelenes (I-IV) and the EH₂ adducts V (E = Si, Ge)



(b) Miscellaneous/mixed low-oxidation state Si and Ge hydride complexes

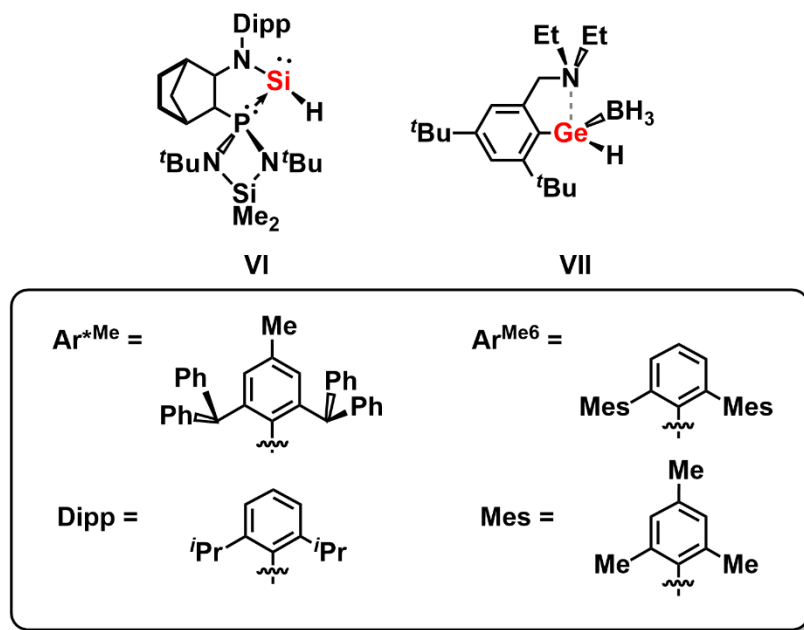
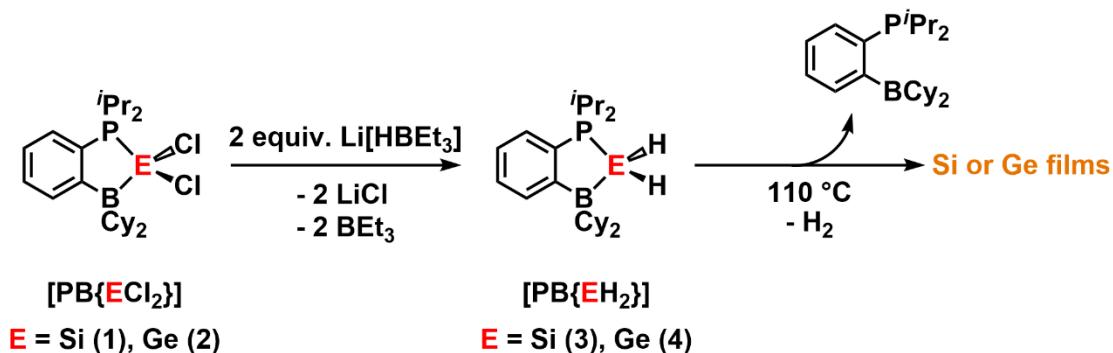


Figure 4.1. Selected examples of: (a) C-/N-donor-stabilized tetrelenes and EH₂ complexes (E = Si or Ge); (b) miscellaneous/mixed donor Si and Ge hydride complexes.

In Chapter 2, the use of frustrated Lewis pairs (FLPs)⁶ to isolate rare examples of “donor-acceptor” stabilized dihydridotetrelenes (EH₂) was documented.^{7,8} Specifically, the intramolecular FLP, ^tPr₂P(C₆H₄)BCy₂⁹ (Cy = cyclohexyl) or **PB** afforded the [PB{EH₂}] complexes [E = Si or Ge].⁷ These hydride complexes can be

used to deposit films of elemental silicon and germanium, respectively, upon mild heating (< 110 °C) in toluene (Scheme 4.1).⁷



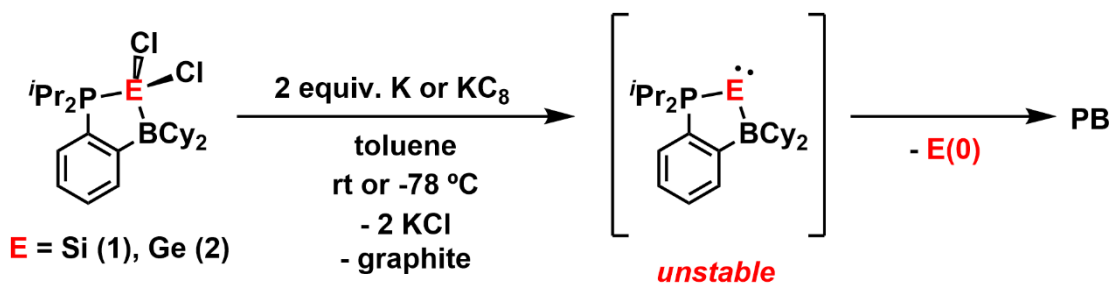
Scheme 4.1. Syntheses of [PB{EH₂}] [E = Si, Ge (**3** and **4**)] and their use as precursors to bulk Si and Ge, respectively.

This Chapter documents an alternative synthetic route to FLP-supported SiCl₂ and SiBr₂ complexes *via* Lewis base-assisted disproportionation of higher halosilanes (Si₂Cl₆ or Si₂Br₆) in the presence of **PB**. Salt metathesis between [PB{ECl₂}] [E = Si (**1**), Ge (**2**)] and Cp*Li (Cp* = [C₅Me₅][−]) was observed to form Cp*₂E complexes in high yields. In addition, lighter [PB{CR₂}] (R = H or Cl) analogues were isolated such that a partial FLP-dihydridotetrelene series (EH₂ = CH₂, SiH₂, and GeH₂) can be compared. Finally, new intramolecular phosphine-borane chelates featuring methylene linkers are reported, which exhibit differing reactivity with Cl₂Ge•dioxane in comparison to **PB**.

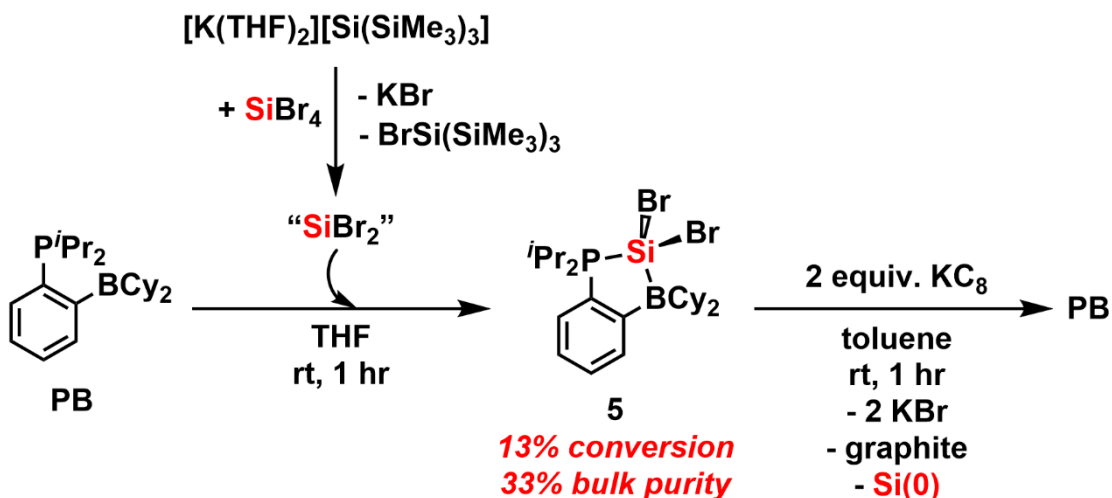
4.2 Results and Discussion

To begin, low-valent FLP-stabilized tetrelones or tetrylones of the general formulas $[\text{PB}\{\text{E}:\}]$ or $[\text{PB}\{\text{E}=\text{E}\}\text{PB}]$ ($\text{E} = \text{Si}, \text{Ge}$),⁷ were targeted by the alkali metal-mediated reduction of $[\text{PB}\{\text{SiCl}_2\}]$ (**1**) and $[\text{PB}\{\text{GeCl}_2\}]$ (**2**) with either K or KC_8 in toluene (from $-78\text{ }^\circ\text{C}$ to room temperature) (Scheme 4.2). Multinuclear (^1H , ^{31}P , ^{11}B) NMR spectroscopy of the crude reaction mixtures showed only free **PB** ligand, which suggests that elimination/release of element Si or Ge transpired. To facilitate more gentle reduction chemistry, $[\text{PB}\{\text{SiBr}_2\}]$ (**5**) was chosen as a target precursor since the LUMO (consisting of Si–Br σ^* character) has been computed to be lower in energy by 0.11 eV than the corresponding Si–Cl σ^* MO in **1**. Initially, the synthesis of **5** involved combining **PB**, Khyp^{10} ($\text{Khyp} = [\text{K}(\text{THF})_2][\text{Si}(\text{SiMe}_3)_3]$) and SiBr_4 in THF; however, this route did not afford **5** in sufficient purity to allow its reactivity to be explored (Scheme 4.3). A variety of solvents (Et_2O , toluene, or THF), temperatures ($-78\text{ }^\circ\text{C}$ to room temperature), reaction times (30 min, 1 hr, 1-3 days) and stoichiometric ratios (1-3 equiv. SiBr_4) were attempted, but the highest conversion (13 % according to ^1H NMR integration) from **PB** to **5** was achieved using one equiv. of SiBr_4 in THF at room temperature for 1 hr (Scheme 4.3). *In-situ* reduction of the **PB**/ SiBr_4 reaction mixture by addition of KC_8 was also attempted (Scheme 4.3), but multinuclear (^1H , ^{31}P , ^{11}B) NMR spectroscopy showed only free **PB** ligand alongside insoluble material, which is proposed to consist of KCl, elemental silicon, and graphite.

Proposed degradation pathway:



Scheme 4.2. Potassium-mediated reduction of $[\text{PB}\{\text{SiCl}_2\}]$ (1) and $[\text{PB}\{\text{GeCl}_2\}]$ (2).



Scheme 4.3. Synthesis of $[\text{PB}\{\text{SiBr}_2\}]$ (5) from Khyp ($\text{Khyp} = [\text{K}(\text{THF})_2][\text{Si}(\text{SiMe}_3)_3]$) and SiBr_4 and attempted reductions using two equiv. of KC_8 .

Despite the abovementioned synthetic barriers to $[\text{PB}\{\text{SiBr}_2\}]$ (5), a few X-ray quality single crystals of this SiBr_2 adduct were isolated by cooling the recovered reaction mixture (from $\text{PB}/\text{Khyp}/\text{SiBr}_4$) in cold ($-35\text{ }^\circ\text{C}$) hexanes. The solid-state structure of **5** is depicted in Figure 4.2, which features a Si1-P1 bond length of $2.3008(12)\text{ \AA}$ that is the same value within experimental error as the Si1-P1 distance of $2.3058(4)\text{ \AA}$ in $[\text{PB}\{\text{SiCl}_2\}]$ (1).⁷ In addition, the intraring P1-Si1-B1 bond angle

[96.81(11)°] in **5** is identical within experimental error to the P1–Si1–B1 bond angle [96.94(4)°] in **1**. Compared to the Si–Br bond lengths in Filippou’s landmark dibromosilylene complex, IPr•SiBr₂¹¹ (IPr = (HCNDipp)₂C:), [avg. Si–Br 2.3493(8) Å] the Si–Br bond lengths in **5** are significantly shortened [avg. Si–Br 2.2478(11) Å], likely as a result of increased *s*-orbital character within the Si–Br bonds that join the four-coordinate Si center in **5**.

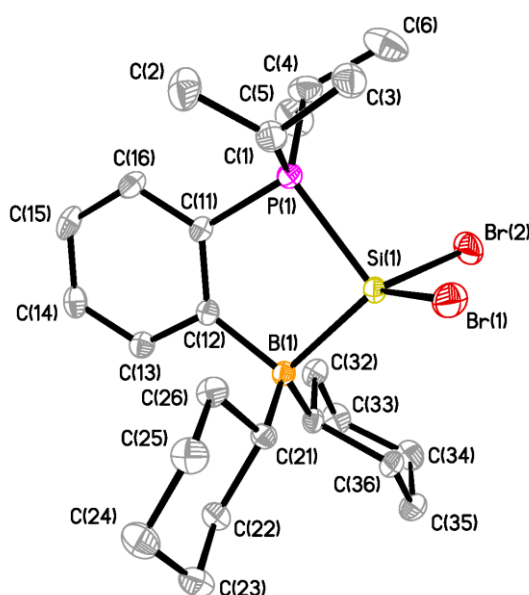
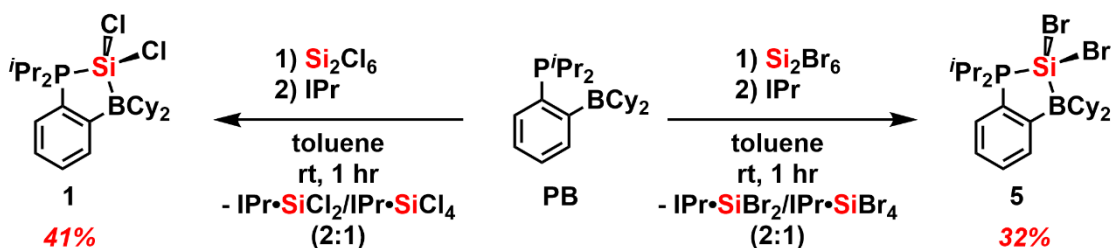


Figure 4.2. Molecular structure of [PB{SiBr₂}] (**5**) with thermal ellipsoids at a 30 % probability level. All hydrogen atoms have been omitted for clarity. Selected bond lengths [Å] and angles [°]: Si1–P1 2.3008(12), Si1–B1 2.082(4), Si1–Br1 2.2480(11), Si1–Br2 2.2477(11); P1–Si1–B1 96.81(11), Br1–Si1–Br2 102.53(4).

In order to isolate [PB{SiCl₂}] (**1**) and [PB{SiBr₂}] (**5**) in pure form and in higher yields, the Lewis base-assisted disproportionation of higher halosilanes¹² (Si₂X₆; X = Cl, Br) in the presence of **PB** was explored. Addition of the *N*-heterocyclic carbene

*i*Pr to Si₂X₆ in the presence of **PB** gave pure [PB{SiCl₂}] (**1**) and [PB{SiBr₂}] (**5**) in a 41 % and 32 % isolated yield, respectively (Scheme 4.4). It should be noted that **PB** itself does not induce the disproportionation of Si₂X₆ into SiX₄ and SiX₂; a strong σ -donor, such as *i*Pr, is needed to facilitate transfer of SiX₂ to **PB**. In both of these successful disproportionation reactions, the by-products *i*Pr•SiX₂ and *i*Pr•SiX₄ (X = Cl¹³ or Br¹¹) could be identified in a *ca.* 2:1 ratio by ¹H NMR analysis of the crude product mixture. Now that [PB{SiBr₂}] (**5**) could be isolated on a preparative scale, this allowed for the collection of ²⁹Si{¹H} NMR data, which shows a doublet resonance at 41.9 ppm with a ¹J_{PSi} value of 106 Hz; for comparison, the ²⁹Si{¹H} NMR resonance for [PB{SiCl₂}] (**1**) [¹J_{PSi} = 117 Hz] is located at 53.8 ppm in C₆D₆.⁷

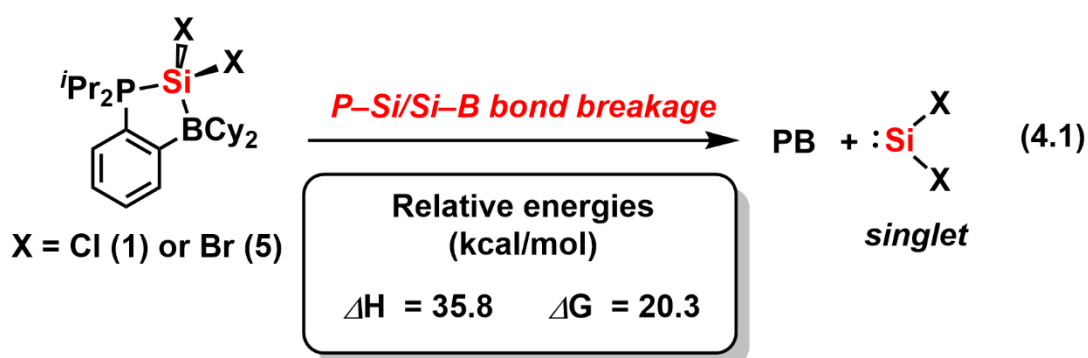


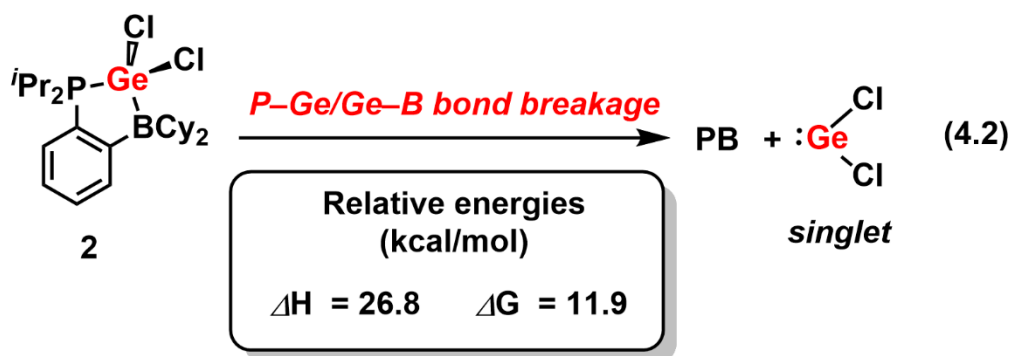
Scheme 4.4. Lewis base-induced disproportionation of higher halosilanes, Si₂Cl₆ or Si₂Br₆, with *i*Pr in the presence of **PB**, leading to the formation of [PB{SiCl₂}] (**1**) and [PB{SiBr₂}] (**5**).

With [PB{SiBr₂}] (**5**) in hand, its reduction was attempted using two equiv. of sodium naphthalenide [THF:toluene (1:2), -78 °C, 1 hr], two equiv. of KC₈ [toluene, rt, 1 hr], Zn/xs. PMe₃ [toluene, rt, 1 hr], or Zn/B(C₆F₅)₃ [toluene, rt, 1 hr]; however, in all cases, free **PB** was formed as the major FLP-containing product (*ca.* > 90 % by ¹H

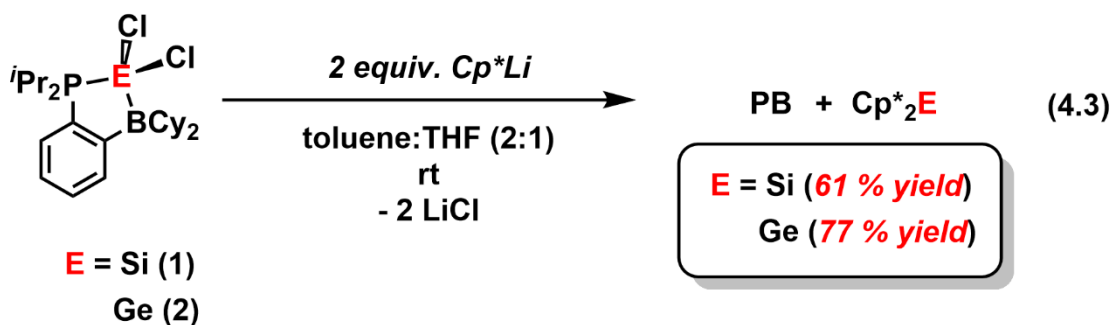
NMR integration). These abovementioned results suggest that the degradative loss of a tetrel center from the FLP adducts **1**, **2**, and **5** is highly favorable.

To obtain a sense of the P–E and B–E bond strengths within the FLP-stabilized SiCl₂, SiBr₂, and GeCl₂ adducts, computations were performed on the release of singlet¹⁴ EX₂ (E = Si, Ge; X = Cl, Br) from **1**, **2** and **5** in the gas phase. The energy barrier in these reactions (ΔG^\ddagger) cannot be directly discussed since transition states for P–E/E–B bond scission could not be located.⁷ For both **1** and **5**, the propensity to release singlet¹⁴ SiX₂ (X = Cl for **1**, Br for **5**) alongside free **PB** appears to be identical in magnitude and endergonic (ΔG) by 20.3 kcal/mol, respectively (gas phase computations at a M06-2X¹⁵/cc-pVTZ¹⁶ level of theory; Equation 4.1). It is expected that the P–Ge and Ge–B bonds in [PB{GeCl₂}] (**2**) should be easier to break compared to the P–Si and Si–B bonds in [PB{SiCl₂}] (**1**). Accordingly, the energy penalty (ΔG) associated with the release of singlet GeCl₂ from [PB{GeCl₂}] (**2**) was computed to be lower than the loss of SiX₂ from either **1** or **5** by 8.4 kcal/mol (Equation 4.2). Thus, the release of dihalotetrelenes by **PB** via P–E/E–B bond breakage has been examined computationally, confirming that release of the singlet GeCl₂ from **2** is more favorable than the release of singlet SiCl₂ or SiBr₂ from **1** or **5**, respectively.



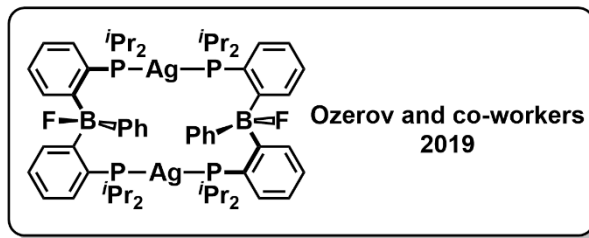
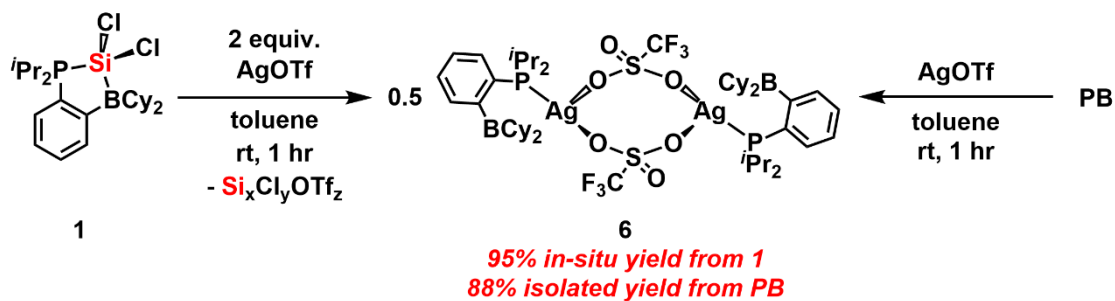


To probe the reactivity of these [PB{ECl₂}] [E = Si (1) or Ge (2)] adducts further, Cp*Li (Cp* = [C₅Me₅]⁻) was chosen to induce salt metathesis within [PB{SiCl₂}] (1), and combining these reactants in a 2:5 THF:toluene mixture afforded Jutzi's Cp*₂Si¹⁷ complex in a 61 % isolated yield (Equation 4.3). The first report of Cp*₂Si includes two synthetic routes: (1) reduction of Cp*₂SiCl₂ with sodium naphthalenide at -50 °C (41 % isolated yield) and, (2) reduction of Cp*₂SiBr₂ with potassium anthracenide at -20 °C (95 % isolated yield).¹⁷ While the synthesis of Cp*₂Si from **1** only offers a moderate isolated yield (61 %), it can be done at room temperature while avoiding the use of highly reactive alkali metals.¹⁷ Similarly, rapid salt metathesis was observed by combining [PB{GeCl₂}] (**2**) with two equiv. of Cp*Li at room temperature to afford Cp*₂Ge¹⁸ in a 77 % isolated yield (Equation 4.3). This isolated yield is comparable to that found in the first synthesis of Cp*₂Ge (74 %) *via* combining Cp*Li with Cl₂Ge•dioxane at -78 °C.^{18a} Notably, quantitative formation of Cp*₂Ge (CH₃ resonance at 1.67 ppm in C₆D₆; see section 4.4.2. for independent synthesis) was observed by ¹H NMR spectroscopic analysis of the crude mixture (*i.e.*, from **2** and two equiv. of Cp*Li) after 1 hr.



Since $[\text{PB}\{\text{Si}\}]$ does not appear to be isolable, cationic $[\text{PB}\{\text{SiR}\}]^+$ ($\text{R} = \text{Cl}$ or H) salts were targeted next in the hope that they would behave similarly to silylium $[\text{R}_3\text{Si}]^+$ species, which have been reported to be highly reactive catalysts.¹⁹ Moreover, the cationic $[\text{PB}\{\text{SiH}\}]^+$ target was expected to be very Lewis acidic (due to an empty p -orbital on Si), while the remaining polarized $\text{Si}^{\delta+}-\text{H}^{\delta-}$ bond could be used for effective hydride transfer to small substrates (*i.e.*, in hydrosilylation catalysis). Alternatively, the analogous $[\text{PB}\{\text{SiCl}\}]^+$ species could be of interest as pre-catalysts in the abovementioned hydrosilylation catalysis after initiation with R_3SiH or R_2SiH_2 feedstocks. To start, hydride abstraction to access possible $[\text{PB}\{\text{SiH}\}]^+$ species was attempted by combining $[\text{PB}\{\text{SiH}_2\}]$ (**3**) with five equiv. of MeOTf in C_6D_6 at 80 °C for 7 days. This led to the formation of one new product with a ^{31}P NMR resonance at 41.2 ppm (22 % conversion by ^1H NMR integration alongside 51 % of free **PB** and 27 % remaining **3**). Unfortunately, this new product could not be separated from unreacted **3** or **PB**. Si–Cl bond activation was also attempted to access a $[\text{PB}\{\text{SiCl}\}]^+$ salt, by combining $[\text{PB}\{\text{SiCl}_2\}]$ (**1**) with one equiv. of AgOTf in toluene at room temperature for 12 hrs; however, one new product was observed by ^1H and $^{31}\text{P}\{^1\text{H}\}$ NMR spectroscopy in a *ca.* 49 % *in-situ* yield with a ^{31}P resonance at 37.8 ppm (doublet of

doublets). Repeating this reaction using two equiv. of AgOTf (toluene, 1 hr, room temperature) converted **1** efficiently into the silver complex $[\text{PB}\{\text{AgOTf}\}]_2$ (**6**) in a 95 % *in-situ* yield according to ^1H NMR spectroscopy (Scheme 4.5). Compound **6** can also be prepared independently in an 88 % isolated yield from **PB** and AgOTf (Scheme 4.5) and its solid-state structure is depicted in Figure 4.3. Compared to the previously reported silver phosphine-borane complex (structure included in Scheme 4.5 for clarity) by Ozerov and co-workers, the Ag1–P1 bond length in **6** is significantly shorter [2.3571(5) Å vs. 2.4342(6) Å in Ozerov’s complex].^{20a} The Ag1···B1 distance in **6** is greater than > 3 Å [*ca.* Ag···B distance = 2.7 Å in related silver halide phosphine-borane complexes]^{20b} with a trigonal planar B center ($\sum_{\text{B1}} = 359.7(8)^\circ$), confirming a lack of significant bonding between these two centers. Although the intended cationic $[\text{PB}\{\text{SiR}\}]^+$ (R = H or Cl) products were not observed, the abovementioned studies show that controlled hydride abstraction is difficult from $[\text{PB}\{\text{SiH}_2\}]$ (**3**) and formation of strong Ag–P bonds (alongside release of undefined $\text{Si}_x\text{Cl}_y\text{OTf}_z$ species) in **6** is favored as opposed to the expected formation of $[\text{PB}\{\text{SiCl}\}]^+[\text{OTf}]$.



Scheme 4.5. Synthesis of $[\text{PB}\{\text{AgOTf}\}]_2$ (**6**) from **PB** or $[\text{PB}\{\text{SiCl}_2\}]$ (**1**).

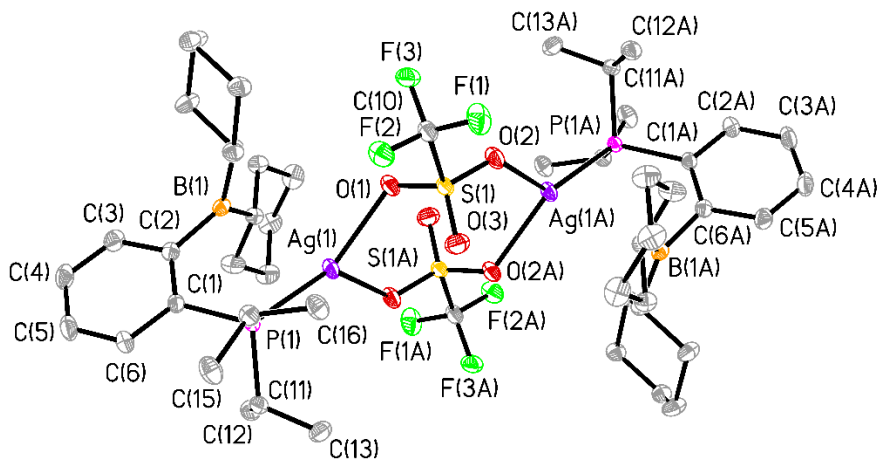
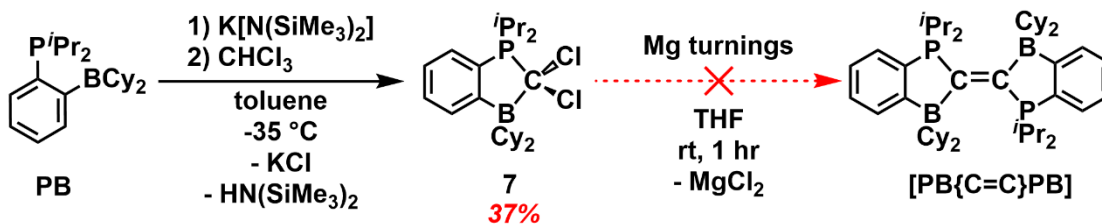
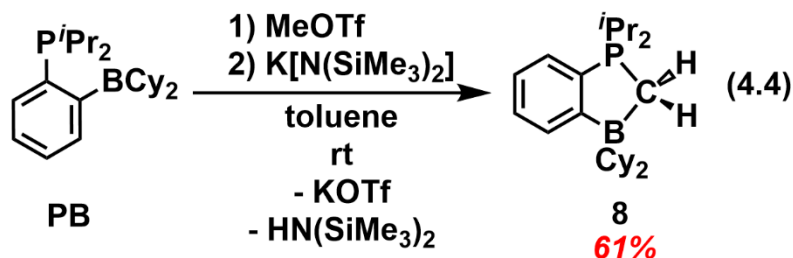


Figure 4.3. Molecular structure of $[\text{PB}\{\text{AgOTf}\}]_2$ (**6**) with thermal ellipsoids at a 30% probability level. All hydrogen atoms have been omitted for clarity. Only one orientation of the disordered cyclohexyl rings is shown. Selected bond lengths [\AA] and angles [$^\circ$]: Ag1-P1 2.3571(5), Ag1-O1 2.3005(14), S1-O1 1.4526(16), S1-O2 1.4496(16), S1-O3 1.4305(17), P1-C1 1.825(2); P1-Ag1-O1 141.13(4), O1-S1-O3 114.70(10), Ag1-P1-C1 115.31(7).

Expanding from the previously discussed FLP silylene and germylene chemistry in this Thesis, the isolation of the lighter analogues, $[\text{PB}\{\text{CCl}_2\}]$ (**7**) and $[\text{PB}\{\text{CH}_2\}]$ (**8**), was targeted. This was inspired partially from a previous reported phosphine-borane $[\text{Ph}_2\text{P}(\text{C}_6\text{H}_4)\text{Bpin}\{\text{CF}_2\}]$ (Bpin = pinacolborate) adduct by Dilman and co-workers.²¹ $[\text{PB}\{\text{CR}_2\}]$ (R = H, X, or organic group) adducts may be able to release CR_2 upon mild heating^{7,21} and hence could be useful synthetic reagents in organic chemistry. In addition, $[\text{PB}\{\text{CR}_2\}]$ adducts may be of use in the isolation of C_2 complexes (*via* $\text{PB}\{\text{C}=\text{C}\}\text{PB}$), which are of high interest for the development of “bottom-up” routes to carbon-based nanomaterials, in particular graphene.²² To start, the dihalomethylene adduct $[\text{PB}\{\text{CCl}_2\}]$ (**7**), was isolated as a white solid (37 % yield) from the deprotonation of CHCl_3 with $\text{K}[\text{N}(\text{SiMe}_3)_2]$ in the presence of **PB** (Scheme 4.6). While **7** has been characterized by multinuclear NMR spectroscopy and elemental analyses, a single-crystal X-ray structure of **7** has not been obtained thus far. The aforementioned $[\text{PB}\{\text{C}=\text{C}\}\text{PB}]$ dimer was targeted by combining **7** with one equiv. of Mg turnings in THF at room temperature for 1 hr; however, this only led to a mixture of inseparable products according to multinuclear NMR (^1H , ^{31}P , ^{11}B) spectroscopy (Scheme 4.6).



Scheme 4.6. Preparation of the methylene complex $[\text{PB}\{\text{CCL}_2\}]$ (**7**) and attempted reduction.



Following a related deprotonation strategy as used to form $[\text{PB}\{\text{CCL}_2\}]$ (**7**), **PB** was combined with MeOTf and $\text{K}[\text{N}(\text{SiMe}_3)_2]$ to afford $[\text{PB}\{\text{CH}_2\}]$ (**8**) in a 61 % yield (Equation 4.4). The solid-state structure of $[\text{PB}\{\text{CH}_2\}]$ (**8**) (Figure 4.4) features a central C_2PCB heterocyclic moiety with typical P–C and B–C single bond lengths of 1.778(5) Å and 1.641(8) Å, respectively. With a partial FLP-dihydridotetrelene (EH_2) series ($\text{E} = \text{C}–\text{Ge}$) in hand, some general comments with respect to their structures can be made (Table 4.1). Descending from C to Ge, there is an expected elongation in both the P–E and B–E bond lengths, which is accompanied by a narrowing of the P–E–B bond angle to approach 90° in the GeH_2 adduct.

Table 4.1. Notable crystallographic features in the partial FLP-dihydridotetrelene series isolated so far.

Compound	P–E [Å]	E–B [Å]	P–E–B [°]
[PB{CH ₂ }] (8)	1.778(5)*	1.641(8)*	107.7(4)*
[PB{SiH ₂ }] (3) ⁷	2.3058(4)	2.0597(4)	94.09(4)
[PB{GeH ₂ }] (4) ⁷	2.3942(5)	2.198(2)	92.32(4)

*For molecule A (occupancy of 89 %) in the unit cell.

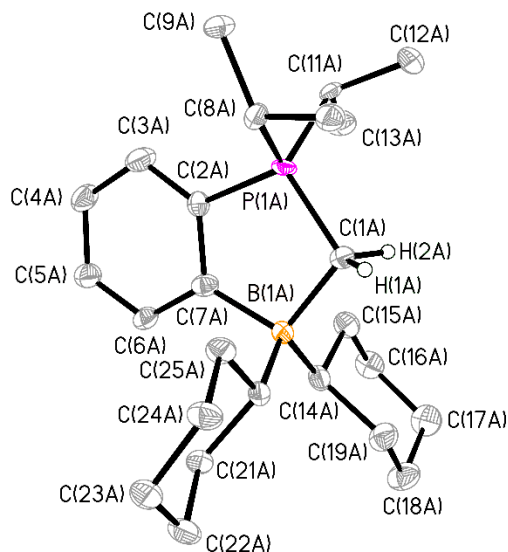
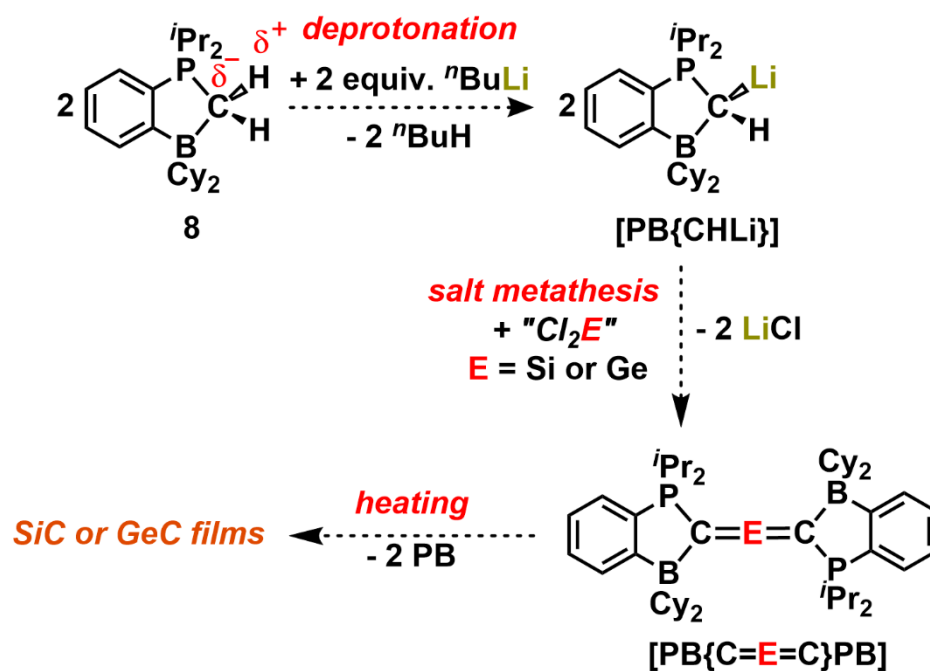


Figure 4.4. Molecular structure of [PB{CH₂}] (**8**) with thermal ellipsoids at a 30 % probability level. All hydrogen atoms were refined isotropically in idealized positions and only those bound to C(1A) are shown for clarity. **8** exhibited whole molecule disorder, such that two distinct molecules (89 % occupancy for molecule A, shown above, and 11 % occupancy for molecule B) were refined in the unit cell. Selected bond lengths [Å] and angles [°] for molecules A and [B]: P1–C1 1.778(5) [2.059(10)], C1–B1 1.694(8) [1.671(10)], P1–C2 1.790(6) [1.775(9)], B1–C7 1.641(8) [1.633(10)]; P1–C1–B1 107.7(4) [107.0(6)], C2–P1–C11 109.6(5) [115.4(7)].

Compared to its heavier congeners, [PB{SiH₂}] (**3**) and [PB{GeH₂}] (**4**), [PB{CH₂}] (**8**) is air-stable, silica-stable and does not react with water in toluene at 110 °C after 8 hrs. In contrast with previously reported dihydridotetrelene adducts,

[PB{SiH₂}] (**3**) and [PB{GeH₂}] (**4**),⁷ **8** does not appear to release **PB** and CH₂ units upon heating in toluene at 110 °C. Turning to computations, the energy penalty for the release of triplet CH₂¹⁴ and free **PB** from **8** appears to be highly endergonic (ΔG) by 88.1 kcal/mol (gas phase computations at a M06-2X¹⁵/cc-pVTZ¹⁶ level of theory). The enhanced stability of **8** is consistent with stronger P–C and C–B bonds in **8** compared to its heavier congeners, **3** and **4** (Table 4.1).⁷

A possible avenue to access FLP-stabilized element carbides would be to first deprotonate [PB{CH₂}] (**8**) to give [PB{CHLi}], which could be subsequently reacted with ECl₂ (E = Si or Ge) sources to yield precursors for the low temperature deposition of silicon carbide or germanium carbide, namely [PB{C=E=C}PB] complexes (Scheme 4.7).⁷ To probe whether deprotonation of **8** is a viable reaction pathway, natural bonding orbital (NBO)²³ analysis on **8** was conducted (Figure 4.5), showing a slightly positive charge ($Q_{\text{NPA}} = 0.25$) at each hydrogen atom of the CH₂ unit, whereas a highly protic site is expected to have Q_{NPA} values much closer to the ideal value of 1.0. In addition, the LUMO in **8** shows little orbital (σ^*) contribution from the C–H units (Figure 4.6); instead, significant P–C(^{*t*}Pr) σ^* character is observed, suggesting bond breakage at that site may be a viable pathway in the presence of nucleophiles.



Scheme 4.7. Proposed route to silicon or germanium carbide precursors [PB{C=E=C}PB] (E = Si or Ge).

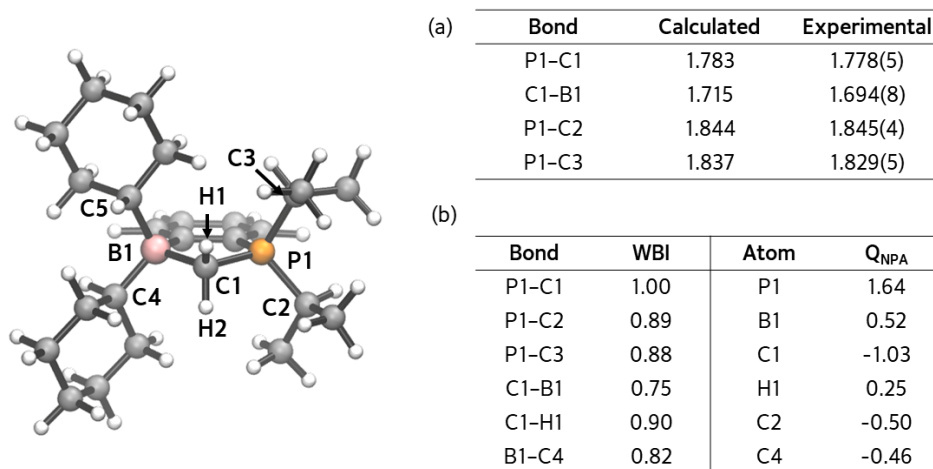


Figure 4.5. Optimized gas phase geometry of [PB{CH₂}] (**8**) computed at a M06-2X¹⁵/cc-pVTZ¹⁶ level of theory with (a) calculated and experimental bond lengths for molecule A in the crystallographic unit cell of **8** [Å], and (b) Wiberg bond indices (WBI)²³ and natural charges (Q_{NPA}) for [PB{CH₂}] (**8**).

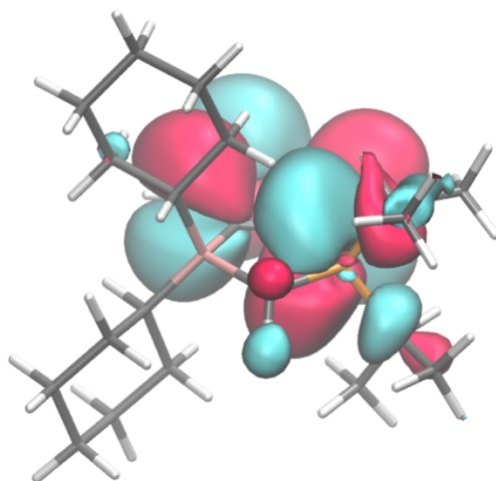
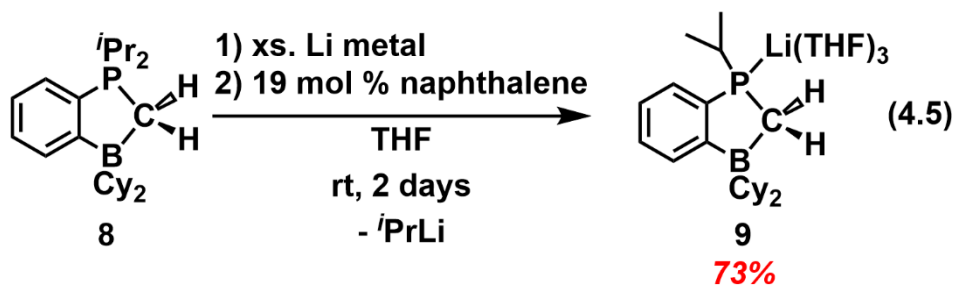


Figure 4.6. Lowest unoccupied molecular orbital (LUMO; at a M06-2X¹⁵/cc-pVTZ¹⁶ level of theory) of [PB{CH₂}] (**8**) depicting significant P–C(Pr) σ^* character.

As a first attempt to deprotonate [PB{CH₂}] (**8**), ⁿBuLi was combined with **8** and the mixture was stirred for 8 hrs at room temperature in THF. This only showed *ca.* 21 % conversion of **8** into a new product with a ³¹P{¹H} NMR resonance at 16.0 ppm, which was inseparable from **8**. As a second attempt, a mixture of ^tBuLi and TMEDA (TMEDA = *N,N,N',N'*-tetramethylethylenediamine) was added to **8** in THF and stirred for 8 hrs at room temperature, but this procedure resulted in a low conversion (*ca.* 30 %) of **8** into a mixture of unidentifiable products according to ¹H and ³¹P{¹H} NMR spectroscopy. Alternatively, the addition of three equiv. of ⁿBuLi or heating stoichiometric ⁿBuLi/**8** mixtures up to 60 °C in THF led to degradation of **8** into a mixture of inseparable products, as determined by (¹H, ³¹P, ¹¹B) NMR spectroscopy.

In a final attempt to deprotonate [PB{CH₂}] (**8**), excess Li metal and catalytic (19 mol %) naphthalene (a well-known electron transfer agent)²⁴ were added. In place of forming [PB{CHLi}], P–C bond breakage was observed, affording

[{(THF)₃Li}ⁱPrP(C₆H₄)BCy₂{CH₂}] (**9**) in a 73 % isolated yield (Equation 4.5). While P–C bond activation in the presence of lithium²⁵ has been reported previously for an alternative route to (2-pyridinyl)phosphine pincer ligands²⁶ commonly used for transition metal complexation, this type of ligand activation has not been observed in FLP adducts thus far. Previous electron paramagnetic resonance (EPR) studies on the reaction between Ph₂P(CH₂)_nPPh₂ (n = 1-5) and Li metal in THF confirm that P–C bond breakage proceeds predominantly through red-colored radical dianionic [R₂P]⁻ intermediates.²⁷ The combination of Li metal and naphthalene allows for more effective one-electron transfer,²⁴ which may explain why this route offers higher conversions and product purity from **8** to **9** compared to using ⁿBuLi or ⁿBuLi/TMEDA mixtures.



The single-crystal X-ray structure of **9** (Figure 4.7) shows a typical coordinative P1–Li1 bond length of 2.616(8) Å, as well as an elongated intraring P1–C1 bond length of 1.859(5) Å when compared to the P1–C1 bond in **8** [1.778(5) Å]. As expected, the B1–C1 bond length of 1.694(6) Å in **9** is identical within experimental error to the B1–C1 bond length of **8** [1.694(8) Å], in line with the retention of a four-coordinate *sp*³-hybridized B environment in both **8** and **9**.

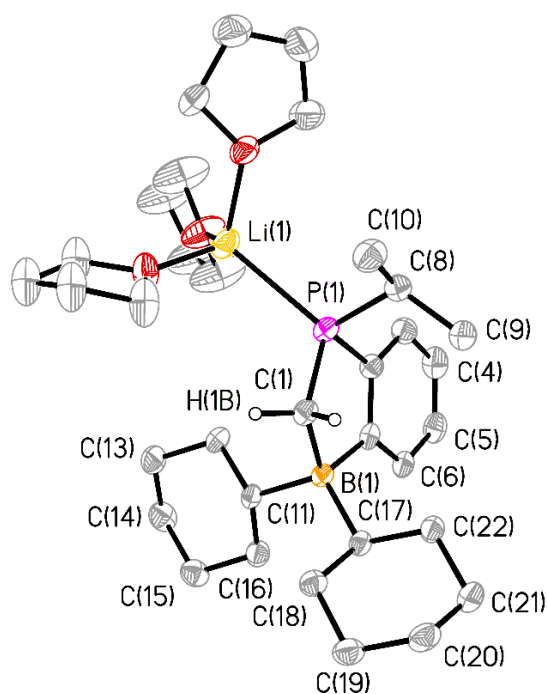
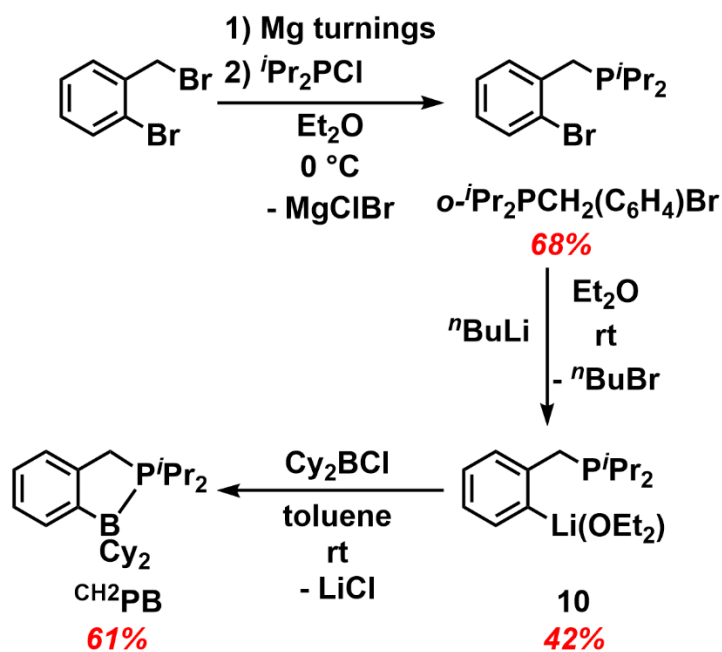


Figure 4.7. Molecular structure of $[(\text{THF})_3\text{Li}]^i\text{PrP}(\text{C}_6\text{H}_4)\text{BCy}_2\{\text{CH}_2\}$ (**9**) with thermal ellipsoids at a 30 % probability level. All hydrogen atoms were refined isotropically in idealized positions and only those bound to C1 are shown for clarity. Only one orientation of the disordered THF molecules is shown. Selected bond lengths [Å] and angles [°]: P1–C1 1.825(4), P1–Li1 2.616(8), P1–C2 1.826(4), B1–C1 1.694(6); C1–P1–Li1 115.9(2), B1–C1–P1 109.6(3).

While the isolated $[\text{PB}\{\text{CR}_2\}]$ [$\text{R} = \text{Cl}$ (**7**) or H (**8**)] species do not show promise as CR_2 transfer materials (thus far), the observed PB ligand activation in the attempted deprotonation of **8** points towards some electrophilic character at the P center within the PB adducts. Combined with the observed B–Cy bond cleavage studied in Chapter 3, the development of new phosphine-borane ligands would be of great interest for FLP chelation so as to avoid unwanted ligand activation.

To tease out the steric and thermodynamic factors behind effective FLP-adduct formation and to potentially suppress ligand activation *via* P–C bond cleavage, an alternative FLP was investigated featuring a methylene linker adjacent to the phosphorus center (Scheme 4.8). As a first step, *o*-ⁱPr₂PCH₂(C₆H₄)Br was prepared as a viscous colorless oil in 68 % yield from the sequential combination of 2-bromobenzyl bromide, Mg metal, and ClPⁱPr₂ in Et₂O (Scheme 4.8). Addition of ⁿBuLi to *o*-ⁱPr₂PCH₂(C₆H₄)Br then yielded pure [ⁱPr₂PCH₂(C₆H₄)Li(OEt₂)]₂ (**10**) in a 42 % yield; the single-crystal X-ray structure of **10** is shown in Figure 4.8 and features an identical dimeric C₂Li₂ motif as in [ⁱPr₂P(C₆H₄)Li(OEt₂)]₂⁷ with typical P–Li bond lengths [P2–Li1 = 2.650(5) Å; P1–Li2 = 2.747(5) Å]. Finally, [ⁱPr₂PCH₂(C₆H₄)Li(OEt₂)]₂ (**10**) was then combined with ClBCy₂ to yield ⁱPr₂PCH₂(C₆H₄)BCy₂ (**CH²PB**) as a white powder in a 61 % yield (Scheme 4.8). Of note, **PB** shows a ³¹P{¹H} NMR resonance at 7.8 ppm and a ¹¹B{¹H} NMR resonance at 75.8 ppm in C₆D₆ (consistent with a three-coordinate boron center).⁷ However, **CH²PB** affords a deshielded ³¹P{¹H} NMR resonance at 34.3 ppm and a ¹¹B{¹H} NMR resonance at -0.6 ppm, suggesting a strong P–B interaction is present in solution, since the latter resonance is consistent with a four-coordinate boron center. As expected, the single-crystal X-ray structure of **CH²PB** (Figure 4.9) confirms the presence of a shorter P–B distance [2.0754(15) Å] compared to **PB** [2.2771(14) Å and 2.1964(13) Å, two independent molecules in the unit cell].⁷



Scheme 4.8. Synthetic route to a new methylene-linked FLP, CH_2PB .

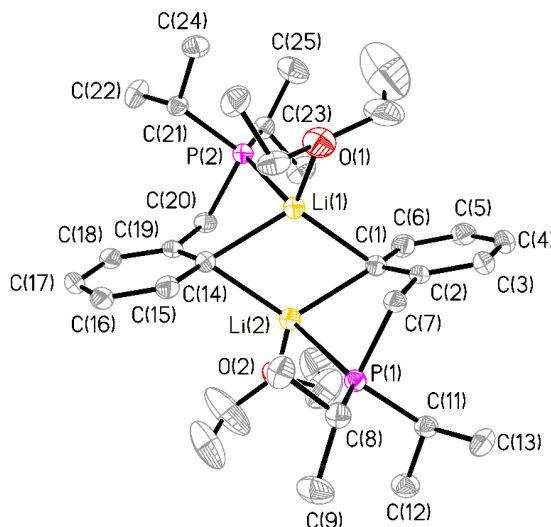


Figure 4.8. Molecular structure of $[\text{}^i\text{Pr}_2\text{PCH}_2(\text{C}_6\text{H}_4)\text{Li}(\text{OEt}_2)]_2$ (**10**) with thermal ellipsoids at a 30 % probability level. All hydrogen atoms have been omitted for clarity. Selected bond lengths [\AA] and angles [$^\circ$]: P1–Li2 2.747(5), P2–Li1 2.650(5), Li2–C1 2.232(5), Li2–C14 2.202(5), Li1–C1 2.241(5), Li1–C14 2.217(5); C1–Li1–C14 66.52(19), C1–Li1–O1 126.9(3).

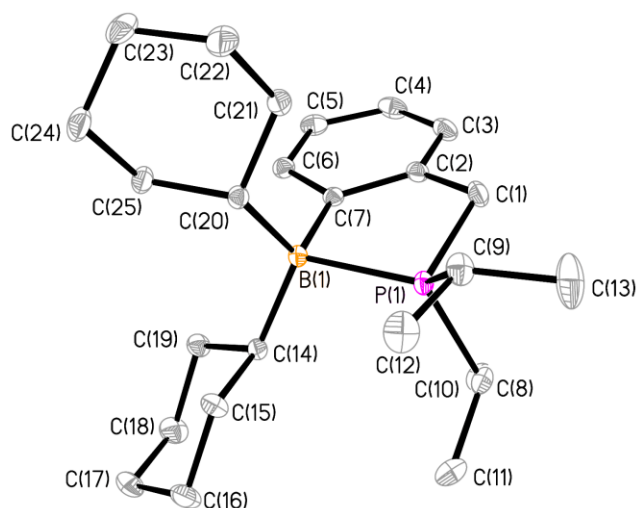
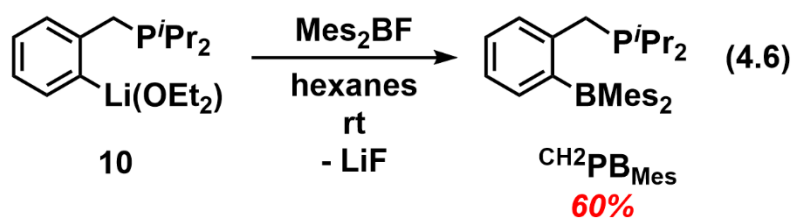
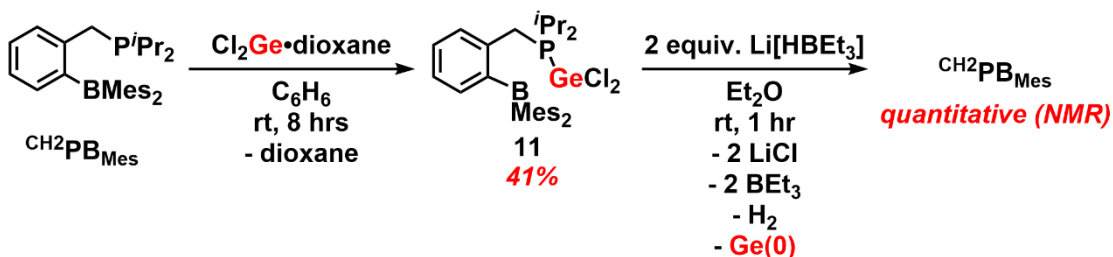


Figure 4.9. Molecular structure of CH_2PB with thermal ellipsoids at a 30 % probability level. All carbon-bound hydrogen atoms have been omitted for clarity. Selected bond lengths [Å] and angles [°]: P1–C1 1.8249(15), P1–B1 2.0754(15), B1–C7 1.6398(19); C1–P1–B1 97.18(6), P1–B1–C7 94.71(8), C7–C2–C1–P1 18.52(15).

CH_2PB was initially proposed as an FLP ligand for ER_2 complexation since the methylene unit should allow the phosphorus center to adopt narrower ligand bite angles that may be more suitable for the isolation of heavier element tetrelenes (based on Sn or Pb), while the P center in CH_2PB is expected to be a better σ -donor than the P center in **PB**. However, the strong P–B interaction present in CH_2PB , does not allow for reaction with SnCl_2 , PbCl_2 , PbBr_2 , or transient Si(II) sources (*via* $\text{IPr}/\text{HSiCl}_3$ mixtures). To sterically separate the phosphorus and boron centers from interacting, a new PB chelate, ${}^i\text{Pr}_2\text{PCH}_2(\text{C}_6\text{H}_4)\text{BMes}_2$ ($\text{CH}_2\text{PB}_{\text{Mes}}$) was synthesized in a 60 % yield from **10** with Mes_2BF (Equation 4.6). While $\text{CH}_2\text{PB}_{\text{Mes}}$ was characterized by multinuclear NMR spectroscopy, elemental analyses and HR-MS (see section 4.4.2), crystals of suitable quality for single-crystal X-ray crystallography have not been isolated thus far.



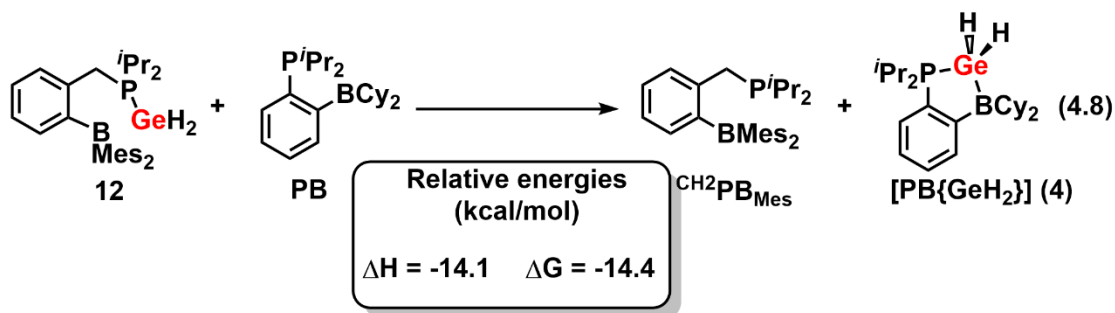
While CH_2PB shows a $^{31}\text{P}\{^1\text{H}\}$ NMR resonance at 34.3 ppm and a $^{11}\text{B}\{^1\text{H}\}$ NMR resonance at -0.6 ppm in C_6D_6 (*vide supra*), $\text{CH}_2\text{PB}_{\text{Mes}}$ affords a more shielded $^{31}\text{P}\{^1\text{H}\}$ NMR resonance at 13.0 ppm and a $^{11}\text{B}\{^1\text{H}\}$ NMR resonance at 73.1 ppm in CDCl_3 , suggesting that there is minimal P–B interaction in solution. Unfortunately, in a similar manner as $^i\text{Pr}_2\text{P}(\text{C}_6\text{H}_4)\text{BMe}_2$ (PB_{Mes}), $\text{CH}_2\text{PB}_{\text{Mes}}$ did not react with SnCl_2 , PbCl_2 , or transient Si(II) sources (*via* $\text{IPr}/\text{HSiCl}_3$ mixtures). The quantitative formation of a new product was observed upon mixing of $\text{CH}_2\text{PB}_{\text{Mes}}$ with $\text{Cl}_2\text{Ge}\cdot$ dioxane in C_6H_6 for 8 hrs (Scheme 4.9). The resulting analytically pure product is formulated as $[\text{}^i\text{Pr}_2\text{PCH}_2(\text{C}_6\text{H}_4)\text{BMe}_2\{\text{GeCl}_2\}]$ (**11**) (41 % isolated yield) on the basis of NMR data (see below).



Scheme 4.9. Synthesis of $[\text{}^i\text{Pr}_2\text{PCH}_2(\text{C}_6\text{H}_4)\text{BMe}_2\{\text{GeCl}_2\}]$ (**11**) and attempted synthesis of $[\text{}^i\text{Pr}_2\text{PCH}_2(\text{C}_6\text{H}_4)\text{BMe}_2\{\text{GeH}_2\}]$ (**12**).

In contrast with other PB-bound tetrelene complexes, $[\text{}^i\text{Pr}_2\text{PCH}_2(\text{C}_6\text{H}_4)\text{BMe}_2\{\text{GeCl}_2\}]$ (**11**) retains a three-coordinate boron environment

energy minima by frequency analysis. Next, the ΔG for the following ligand displacement reaction (**12** + **PB** \rightarrow [PB{GeH₂}] (**4**) + ^{CH₂}**PB**_{Mes}; Equation 4.8) was computed, and this process is exergonic by -14.4 kcal/mol; thus, [PB{GeH₂}] (**4**) is significantly more stable than the target complex [ⁱPr₂PCH₂(C₆H₄)BMe₂{GeH₂}] (**12**). This is in line with the observed reactivity of **11** upon combination with Li[HBET₃], and suggests that further ligand modification will be necessary to stabilize EH₂ adducts with a methylene-linked phosphine-borane chelate.



4.3 Conclusions

This Chapter explores the alkali metal-mediated reduction and Cp*Li-mediated salt metathesis of [PB{EX₂}] complexes [EX₂ = SiCl₂ (**1**), GeCl₂ (**2**), or SiBr₂ (**5**)]. In addition, the isolation of the lighter Group 14 element congeners [PB{CCL₂}] (**7**), [PB{CH₂}] (**8**) and subsequent ligand activation *via* reductive P–C bond breakage to form [{(THF)₃Li}ⁱPrP(C₆H₄)BCy₂{CH₂}] (**9**) was noted. Finally, new phosphine-borane FLPs, ^{CH₂}**PB** and ^{CH₂}**PB**_{Mes}, featuring methylene linkers were synthesized. As a result of a strong intramolecular P–B interaction, ^{CH₂}**PB** was unable to bind *in-situ* formed SiCl₂, Cl₂Ge•dioxane, SnCl₂, or PbCl₂. In contrast, the bulkier ^{CH₂}**PB**_{Mes} readily

reacted with $\text{Cl}_2\text{Ge}\cdot\text{dioxane}$ to form $[\text{}^i\text{Pr}_2\text{PCH}_2(\text{C}_6\text{H}_4)\text{BMes}_2\{\text{GeCl}_2\}]$ (**11**), as confirmed by NMR spectroscopy and elemental analyses. The presence of a three-coordinate boron center in **11**, according to $^{11}\text{B}\{^1\text{H}\}$ NMR spectroscopy, suggests that a coordinative Ge–B interaction is not present, which may explain why the desired $[\text{}^i\text{Pr}_2\text{PCH}_2(\text{C}_6\text{H}_4)\text{BMes}_2\{\text{GeH}_2\}]$ (**12**) adduct does not form upon reaction of **11** with $\text{Li}[\text{HBET}_3]$. Since it appears that any modification of the **PB** ligand can have drastic effects on the FLP reactivity, future work will involve more careful screening of different organic groups on the P center, as well as substitution of the B center with heavier Group 13 element-based Lewis acids (Al or Ga) to form stronger chelates with ER_2 units, including cases where $\text{E} = \text{Pb}$.

4.4 Experimental Details

4.4.1 General Considerations

All reactions were performed using standard Schlenk and glovebox (Innovative Technology, Inc.) techniques. All solvents were dried using a solvent purification system provided by Innovative Technology, Inc., degassed (freeze-pump-thaw method), and stored under nitrogen prior to use. $n\text{BuLi}$ (2.5 M solution in hexanes), chlorodicyclohexylborane (ClBCy_2), SiBr_4 , $\text{Cl}_2\text{Ge}\cdot\text{dioxane}$, AgOTf , and Mes_2BF ($\text{Mes} = 2,4,6\text{-Me}_3\text{C}_6\text{H}_2$) were purchased from Sigma-Aldrich and used as received. Hexachlorodisilane (Si_2Cl_6) was purchased from Gelest and used as received. Chloroform was obtained from Sigma-Aldrich, degassed *via* three freeze-pump-thaw cycles, and stored in a Teflon-capped Schlenk flask over 4 Å molecular sieves prior to

use. Chlorodiisopropylphosphine (ClP^iPr_2) was purchased from Acros Organics and used as received. Methyl triflate (MeOTf) and 2-bromobenzyl bromide ($o\text{-BrCH}_2(\text{C}_6\text{H}_4)\text{Br}$) were purchased from Oakwood Chemicals and used as received. $\text{K}[\text{N}(\text{SiMe}_3)_2]$ was purchased from Sigma-Aldrich and recrystallized from a saturated toluene solution at $-35\text{ }^\circ\text{C}$ prior to use. **PB**,^{7,9} $[\text{PB}\{\text{SiCl}_2\}]$ (**1**),⁷ $[\text{PB}\{\text{GeCl}_2\}]$ (**2**),⁷ Si_2Ph_6 ,²⁹ Si_2Br_6 ,³⁰ Khyp^{10} ($\text{Khyp} = [\text{K}(\text{THF})_2][\text{Si}(\text{SiMe}_3)_3]$), $\text{Cp}^*\text{Li}^{31}$ ($\text{Cp}^* = [\text{C}_5\text{Me}_5]^-$), and IPr^{32} ($\text{IPr} = (\text{HCNDipp})_2\text{C}; \text{Dipp} = 2,6\text{-}^i\text{Pr}_2\text{C}_6\text{H}_3$) were synthesized as reported previously. ^1H , ^7Li , ^{11}B , $^{13}\text{C}\{^1\text{H}\}$, $^{19}\text{F}\{^1\text{H}\}$, ^{29}Si , and $^{31}\text{P}\{^1\text{H}\}$ NMR spectra were recorded at room temperature using a Varian Inova-400, VNMRS-500, or VNMRS-700 spectrometer and referenced to Me_4Si (^1H , $^{13}\text{C}\{^1\text{H}\}$, and ^{29}Si), a 9.7 M solution of LiCl in D_2O (^7Li), 85 % H_3PO_4 ($^{31}\text{P}\{^1\text{H}\}$), 15 % $\text{F}_3\text{B}\cdot\text{OEt}_2$ (^{11}B), and CFCl_3 ($^{19}\text{F}\{^1\text{H}\}$). Chemical shifts are reported in parts per million (ppm) and coupling constants (J) are reported in Hertz (Hz). Elemental analyses and thermal gravimetric analyses were performed at the Analytical and Instrumentation Laboratory at the University of Alberta using the Thermo Flash 2000 Elemental Analyzer and the Perkin Elmer Pyris 1, respectively. High-resolution mass spectra were obtained on an Agilent 6220 spectrometer or Kratos Analytical MS-50G instrument by the Mass Spectrometry Facility at the University of Alberta. Melting points were measured in sealed glass capillaries under nitrogen using MelTemp apparatus.

4.4.2 Synthetic Procedures

Attempted synthesis of [PB{SiBr₂}] (5) from SiBr₄ and [K(THF)₂][Si(SiMe₃)₃]. A solution of [K(THF)₂][Si(SiMe₃)₃] (0.1190 g, 0.2761 mmol) in 1.5 mL of THF was added to **PB** (0.1000 g, 0.2700 mmol) in 2 mL of THF. Afterwards, SiBr₄ (33.5 μ L, 0.289 mmol) was added quickly to the reaction mixture, resulting in a brown suspension. After stirring for 30 min at room temperature, the reaction mixture was evaporated to dryness and re-dissolved in *ca.* 0.7 mL of C₆D₆ to verify the degree of conversion from **PB** to [PB{SiBr₂}] (**5**). By comparing one *ArH* resonance of **PB** (7.29 ppm) with one *ArH* resonance of [PB{SiBr₂}] (**5**) (7.73 ppm in C₆D₆) in ¹H NMR spectrum, the % conversion from **PB** to [PB{SiBr₂}] (**5**) in the crude reaction mixture was estimated to be 13 % as leftover free **PB** and the BrSi(SiMe₃)₃ by-product could not be removed. After the crude NMR spectrum was collected, the volatiles were then removed from the NMR sample and the product was extracted into 2 mL of hexanes. The mixture was filtered through a plug of Celite and the filtrate was concentrated to a final volume of \sim 1 mL before cooling to -35 $^{\circ}$ C to yield [PB{SiBr₂}] (**5**) as colorless X-ray quality crystals (0.0024 g, 33 % bulk purity according to ¹H NMR spectroscopy). The NMR data for pure [PB{SiBr₂}] (**5**) is provided below.

Synthesis of [PB{SiBr₂}] (5) from Si₂Br₆ and IPr. A solution of IPr (0.0338 g, 0.0869 mmol) in 1 mL of toluene was added rapidly over 5 seconds, to a stirring solution of **PB** (0.0290 g, 0.0783 mmol) and Si₂Br₆ (0.0462 g, 0.0862 mmol) in 15 mL of toluene,

resulting in a yellow solution. After stirring this mixture at room temperature for 1 hr, the slightly opaque yellow mixture was exposed to vacuum to remove the volatiles. Afterwards, 10 mL of hexanes was added and the mixture was filtered. The filtrate was then concentrated to a volume of ~2 mL and cooled to -35 °C for 8 hrs to yield colorless crystals of [PB{SiBr₂}] (**5**), which were washed with cold (-35 °C) acetonitrile (2 × 1 mL) and cold (-35 °C) pentane (2 × 1 mL) to further remove residual free **PB** (final yield of **5** = 0.0141 g, 32 %). ¹H NMR (399.9 MHz, C₆D₆): δ = 7.73 (dd, ³J_{HP} = 3.9 Hz, ³J_{HH} = 7.6 Hz, 1H, ArH), 7.26-7.21 (m, 1H, ArH), 6.90-6.93 (m, 1H, ArH), 6.79-6.82 (m, 1H, ArH), 2.20 (d of septets, ³J_{HH} = 6.8 Hz, ²J_{HP} = 9.9 Hz, 2H, CH(CH₃)₂), 2.02 (pseudo-d, 2H, H_{Cy}), 1.94 (pseudo-d, 4H, H_{Cy}), 1.87 (pseudo-d, 4H, H_{Cy}), 1.52-1.60 (m, 4H, H_{Cy}), 1.42-1.50 (m, 4H, H_{Cy}), 0.99-1.20 (m, 4H, H_{Cy}), 0.84-0.88 (m, 12H, CH(CH₃)₂). ¹³C{¹H} NMR (125.6 MHz, C₆D₆): δ = 135.3 (d, J_{CP} = 11.7 Hz, ArC), 131.2 (d, J_{CP} = 2.7 Hz, ArC), 130.4 (d, J_{CP} = 6.0 Hz, ArC), 125.0 (s, ArC), 124.6 (d, J_{CP} = 8.5 Hz, ArC), 124.5 (s, ArC), 34.5 (s, BCy₂), 33.1 (s, BCy₂), 31.8 (s, BCy₂), 30.1 (s, BCy₂), 29.6 (s, BCy₂), 28.3 (s, BCy₂), 24.8 (d, ¹J_{CP} = 24.9 Hz, CH(CH₃)₂), 17.8 (d, ²J_{CP} = 2.9 Hz, CH(CH₃)₂), 17.5 (s, CH(CH₃)₂). ³¹P{¹H} NMR (201.6 MHz, C₆D₆): δ = -8.3 (s, with ²⁹Si-³¹P satellites ¹J_{PSi} = 106 Hz, ⁱPr₂P). ¹¹B{¹H} NMR (128.3 MHz, C₆D₆): δ = -1.9 (s, Cy₂B). ²⁹Si{¹H} NMR (79.4 MHz, C₆D₆): δ = 41.9 (d, ¹J_{PSi} = 105.9 Hz, SiBr₂). Anal. Calcd. for C₂₄H₄₀BBBr₂PSi (%): C 51.64, H 7.22; Found: C 52.16, H 6.91. M.p. 179-180 °C (decomp.).

Synthesis of [PB{SiCl₂}] (1) from Si₂Cl₆ and IPr. A solution of IPr (0.0416 g, 0.107 mmol) in 1 mL of toluene was added rapidly over 5 seconds, to a stirring solution of **PB** (0.0395 g, 0.107 mmol) and Si₂Cl₆ (18.4 μL, 0.107 mmol) in 10 mL of toluene, leading to a yellow solution. After stirring at room temperature for 1 hr, the solution turned opaque. The volatiles were then removed under vacuum. Then 10 mL of hexanes was added to the reaction mixture and the extract was filtered. The filtrate was then concentrated to a volume of ~2 mL and cooled to -35 °C for 8 hrs to yield [PB{SiCl₂}] (**1**) as a white microcrystalline solid, which was washed with cold (-35 °C) pentane (2 × 1 mL) (final yield of **1** = 0.0206 g, 41 %). The NMR data for [PB{SiCl₂}] (**1**) synthesized using this procedure matched those reported previously (see section 2.4.2).⁷

Independent synthesis of Cp*₂Ge. Since the ¹H NMR spectrum of Cp*₂Ge has not been reported in C₆D₆, this compound was synthesized independently according to a modified literature procedure.^{18a} A solution of Cp*Li (0.0128 g, 0.178 mmol) in 2 mL of THF was added to a stirring solution of Cl₂Ge•dioxane (0.0201 g, 0.0867 mmol) in 5 mL of toluene. The reaction mixture was then stirred for 1 hr at room temperature. Subsequently, the reaction mixture was evaporated to dryness, 2 mL of hexanes was added and the mixture was filtered. Removal of the volatiles from the filtrate under vacuum afforded Cp*₂Ge as white microcrystalline needles (0.0115 g, 65 %). ¹H NMR (699.7 MHz, C₆D₆): δ = 1.67 (s, 30H, CH₃). ¹³C{¹H} NMR (175.9 MHz, C₆D₆): δ = 120.2 (s, Me₅C₅), 9.5 (s, Me₅C₅).

Synthesis of Cp*₂Si from [PB{SiCl₂}] (1) and Cp*Li. A solution of Cp*Li (0.0099 g, 0.14 mmol) in 2 mL of THF was added to a stirring solution of [PB{SiCl₂}] (1) (0.0319 g, 0.0679 mmol) in 5 mL of toluene. The reaction mixture was then stirred for 1 hr at room temperature. Subsequently, the reaction mixture was evaporated to dryness, 5 mL of hexanes was added, and the mixture was filtered. The filtrate was concentrated to a volume of ~2 mL and cooled to -35 °C to yield Cp*₂Si as a white microcrystalline powder (0.0124 g, 61 %).¹⁷

Synthesis of Cp*₂Ge from [PB{GeCl₂}] (2) and Cp*Li. A solution of Cp*Li (0.0088 g, 0.12 mmol) in 2 mL of THF was added to a stirring solution of [PB{GeCl₂}] (2) (0.0315 g, 0.0613 mmol) in 5 mL of toluene. The reaction mixture was then stirred for 1 hr at room temperature. Subsequently, the reaction mixture was evaporated to dryness, 5 mL of hexanes was added, and the mixture was filtered. The filtrate was concentrated to a volume of ~2 mL and cooled to -35 °C to yield Cp*₂Ge as a white microcrystalline powder (0.0161 g, 77 %).

Independent synthesis of [PB{AgOTf}]₂ (6). A solution of AgOTf (0.0155 g, 0.0603 mmol) was added to a stirring solution of PB (0.0175 g, 0.0472 mmol) in 5 mL of toluene. The reaction mixture was then stirred for 1 hr. Afterwards, the volatiles were removed under vacuum, 5 mL of fluorobenzene was added, and the mixture was filtered. The volatiles were removed from the filtrate under vacuum to afford [PB{AgOTf}]₂ (6) as a white powder (0.0262 g, 89 %). Colorless X-ray quality crystals

of **6** were grown from a concentrated mixture of cold (-35 °C) 1:1:1 THF:Et₂O:hexanes. ¹H NMR (699.8 MHz, C₆D₆): δ = 7.14-7.19 (m, 2H, ArH), 6.99-7.05 (m, 4H, ArH), 6.77 (pseudo-d, 2H, ArH), 2.22 (pseudo-d, 4H, H_{Cy}), 2.06-2.09 (m, 4H, H_{Cy}), 1.98-2.02 (m, 4H, CH(CH₃)₂), 1.93 (pseudo-d, 4H, H_{Cy}), 1.86 (pseudo-d, 4H, H_{Cy}), 1.73 (d, ³J_{HH} = 11.2 Hz, 6H, CH(CH₃)₂), 1.44-1.55 (m, 8H, H_{Cy}), 1.26-1.34 (m, 8H, H_{Cy}), 1.16-1.21 (m, 8H, H_{Cy}), 1.10 (dd, ³J_{HH} = 7.0 Hz, ³J_{HP} = 19.4 Hz, 12H, CH(CH₃)₂), 1.02-1.06 (m, 4H, H_{Cy}), 0.87 (dd, ³J_{HH} = 7.1 Hz, ³J_{HP} = 16.2 Hz, 6H, CH(CH₃)₂). ¹³C{¹H} NMR (175.9 MHz, C₆D₆): δ = 157.7 (s, J_{CP} = 30.4 Hz, ArC), 133.3 (d, J_{CP} = 10.2 Hz, ArC), 132.4 (s, ArC), 131.8 (d, J_{CP} = 7.4 Hz, ArC), 129.6 (s, ArC), 128.6 (s, ArC), 128.3 (s, ArC), 127.6 (d, J_{CP} = 9.5 Hz, ArC), 127.5 (d, J_{CP} = 9.8 Hz, ArC), 126.6 (s, ArC), 126.5 (s, ArC), 126.3 (s, ArC), 121.5 (q, ¹J_{CF} = 319.9 Hz, CF₃), 39.6 (s, BCy₂), 30.7 (s, BCy₂), 28.8 (s, BCy₂), 28.3 (s, BCy₂), 27.9 (s, BCy₂), 27.3 (s, BCy₂), 26.3 (d, ¹J_{CP} = 20.1 Hz, CH(CH₃)₂), 20.0 (d, ²J_{CP} = 8.5 Hz, CH(CH₃)₂), 19.5 (s, CH(CH₃)₂). ³¹P{¹H} NMR (161.9 MHz, C₆D₆): δ = 37.8 (dd, ¹J_{107AgP} = 700.7 Hz, ¹J_{109AgP} = 810.8 Hz, ⁱPr₂P). ¹¹B{¹H} NMR (128.3 MHz, C₆D₆): δ = 81.1 (br s, Cy₂B). ¹⁹F{¹H} NMR (376.1 MHz, C₆D₆): δ = -76.7 (s, OTf). Anal. Calcd. for C₅₁H₈₃Ag₂B₂F₅O₆P₂S₂ (%): C 48.98, H 6.69; S 5.13; Found: C 49.51, H 7.01, S 4.03. M.p. 49-50 °C (decomp.).

Synthesis of [PB{CCl₂}] (7). To a solution of **PB** (0.1696 g, 0.4579 mmol) and K[N(SiMe₃)₂] (0.0911 g, 0.457 mmol) stirring at -35 °C in 8 mL of toluene, was added CHCl₃ at -35 °C (38.5 μL, 0.480 mmol) drop-wise over 1 min, whereupon the initially colorless solution turned orange-red and a white precipitate formed. After warming the

mixture to room temperature and stirring for 4 hrs, the mixture was filtered and concentrated under vacuum to a volume of ~2 mL. Upon concentrating, an off-white precipitate slowly formed and it was allowed to settle. Subsequently, the mother liquor was decanted away, and the remaining solid was dried under vacuum. This solid was washed with 2×1.5 mL of toluene and subsequently washed with 2×1 mL of $\text{Me}_3\text{SiOSiMe}_3$, 2×1 mL of pentane to afford $[\text{PB}\{\text{CCl}_2\}]$ (**7**) as a white powder (0.0759 g, 37 %). $^1\text{H}\{^3\text{P}\}$ NMR (399.9 MHz, C_6D_6): $\delta = 7.89$ (d, $^3J_{\text{HH}} = 7.6$ Hz, 1H, ArH), 7.22 (t, $^3J_{\text{HH}} = 7.5$ Hz, 1H, ArH), 6.91 (t, $^3J_{\text{HH}} = 7.0$ Hz, 1H, ArH), 6.83-6.85 (m, 1H, ArH), 2.71 (pseudo-d, 2H, H_{Cy}), 2.54 (septet, $^3J_{\text{HH}} = 7.3$ Hz, 2H, $\text{CH}(\text{CH}_3)_2$), 2.11-2.14 (m, 2H, H_{Cy}), 2.04 (pseudo-d, 2H, H_{Cy}), 1.90-1.97 (m, 6H, H_{Cy}), 1.76-1.87 (m, 2H, H_{Cy}), 1.43-1.63 (m, 8H, H_{Cy}), 1.04 (d, $^3J_{\text{HH}} = 7.0$ Hz, 1H, $\text{CH}(\text{CH}_3)_2$), 0.92 (d, $^3J_{\text{HH}} = 7.3$ Hz, 1H, $\text{CH}(\text{CH}_3)_2$). $^{13}\text{C}\{^1\text{H}\}$ NMR (125.7 MHz, C_6D_6): $\delta = 135.7$ (d, $J_{\text{CP}} = 14.9$ Hz, ArC), 131.3 (d, $J_{\text{CP}} = 3.1$ Hz, ArC), 130.0 (d, $J_{\text{CP}} = 11.8$ Hz, ArC), 124.5 (d, $J_{\text{CP}} = 11.3$ Hz, ArC), 122.6 (s, ArC), 121.9 (s, ArC), 37.1 (br, BCy_2), 33.2 (s, BCy_2), 32.8 (s, BCy_2), 31.0 (s, BCy_2), 30.9 (s, BCy_2), 28.8 (s, BCy_2), 27.1 (d, $^1J_{\text{CP}} = 36.1$ Hz, $\text{CH}(\text{CH}_3)_2$), 18.4 (d, $^2J_{\text{CP}} = 3.9$ Hz, $\text{CH}(\text{CH}_3)_2$), 17.9 (d, $^2J_{\text{CP}} = 3.3$ Hz, $\text{CH}(\text{CH}_3)_2$). *Note: The CCl_2 resonance could not be located in $^{13}\text{C}\{^1\text{H}\}$ NMR spectrum.* $^{31}\text{P}\{^1\text{H}\}$ NMR (201.6 MHz, C_6D_6): $\delta = 56.6$ (s, $^i\text{Pr}_2\text{P}$). $^{11}\text{B}\{^1\text{H}\}$ NMR (159.8 MHz, C_6D_6): $\delta = -3.6$ (s, BCy_2). Anal. Calcd. for $\text{C}_{25}\text{H}_{40}\text{BCl}_2\text{P}$ (%): C 66.24, H 8.89; Found: C 65.88, H 8.86. M.p. 97-99 °C.

Synthesis of $[\text{PB}\{\text{CH}_2\}]$ (8**).** A solution of MeOTf (50.2 μL , 0.458 mmol) was added to a stirring solution of **PB** (0.1130 g, 0.3050 mmol) in 10 mL of toluene. The reaction

mixture was then stirred for 2 hrs. Then a solution of K[N(SiMe₃)₂] (0.0913 g, 0.458 mmol) in 5 mL of toluene was added drop-wise over 5 min to the reaction mixture, resulting in a white slurry. After stirring for 2 hrs, the precipitate was allowed to settle, the supernatant decanted away, and 5 mL of toluene were added; this procedure was repeated a total of 4 times (giving 20 mL total of decanted solution). Afterwards, the decanted solutions were combined and concentrated under vacuum to a volume of *ca.* 5 mL and cooled to -35 °C for 8 hrs to yield [PB{CH₂}] (**8**) as a white microcrystalline solid (0.0715 g, 61 %). Colorless X-ray quality crystals of **8** were grown from a concentrated solution of cold (-35 °C) 2:1 hexanes:THF. ¹H NMR (499.7 MHz, C₆D₆): δ = 7.89 (d, ³J_{HH} = 7.6 Hz, 1H, ArH), 7.32 (t, ³J_{HH} = 7.6 Hz, 1H, ArH), 6.98-7.03 (m, 1H, ArH), 7.86 (pseudo-t, ³J_{HH} = 7.2 Hz, 1H, ArH), 1.97-2.11 (m, 8H, H_{Cy}), 1.82-1.91 (m, 4H, H_{Cy} overlapping with CH(CH₃)₂), 1.47-1.69 (m, 6H, H_{Cy}), 1.24-1.34 (m, 2H, H_{Cy}), 1.13-1.22 (m, 2H, H_{Cy}), 1.00-1.07 (m, 2H, H_{Cy}), 0.72 (dd, ³J_{HH} = 6.4 Hz, ³J_{HP} = 7.2 Hz, 6H, CH(CH₃)₂), 0.68 (dd, ³J_{HH} = 6.4 Hz, ³J_{HP} = 7.2 Hz, 6H, CH(CH₃)₂), 0.65 (d, ²J_{HP} = 6.3 Hz, 2H, CH₂). ¹³C{¹H} NMR (175.9 MHz, C₆D₆): δ = 133.7 (s, ArC), 133.6 (s, ArC), 131.2 (d, J_{CP} = 2.9 Hz, ArC), 128.7 (s, ArC), 128.6 (s, ArC), 124.6 (d, J_{CP} = 10.9 Hz, ArC), 32.7 (s, BCy₂), 32.5 (s, BCy₂), 30.5 (s, BCy₂), 30.3 (s, BCy₂), 28.9 (s, BCy₂), 24.0 (d, ¹J_{CP} = 40.8 Hz, CH(CH₃)₂), 17.4 (d, ²J_{CP} = 1.4 Hz, CH(CH₃)₂), 16.4 (d, ²J_{CP} = 2.3 Hz, CH(CH₃)₂), 0.60 (br s, PCH₂). *Note: The resonance for the cyclohexyl CH bound to boron could not be located. While the P-CH₂ resonance could not be located directly by ¹³C{¹H} NMR spectroscopy (likely due to quadrupolar broadening from neighbouring B atom), ¹H-¹³C gHSQC NMR confirms the CH₂ moiety is located*

at 0.60 ppm. $^{31}\text{P}\{^1\text{H}\}$ NMR (161.9 MHz, C_6D_6): $\delta = 63.1$ (s, $^i\text{Pr}_2\text{P}$). $^{11}\text{B}\{^1\text{H}\}$ NMR (128.3 MHz, C_6D_6): $\delta = -4.6$ (s, Cy_2B). Anal. Calcd. for $\text{C}_{25}\text{H}_{42}\text{BP}$ (%): C 78.12, H 11.01; Found: C 77.82, H 10.99. M.p. 141-143 °C.

Synthesis of $[\{(\text{THF})_3\text{Li}\}^i\text{PrP}(\text{C}_6\text{H}_4)\text{BCy}_2\{\text{CH}_2\}]$ (9**).** Excess lithium metal (0.0531 g, 7.38 mmol) was added to a stirring solution of naphthalene (0.0046 g, 0.036 mmol) in 5 mL of THF. After stirring at room temperature for 30 min, a permanent dark green color was observed and a solution of $[\text{PB}\{\text{CH}_2\}]$ (**8**) (0.0731 g, 0.190 mmol) in 2 mL of THF was added quickly over 10 seconds. The reaction mixture rapidly turned dark red and then light red-orange, and this mixture was left stirring at room temperature for 2 days. Afterwards, the reaction mixture was filtered and the volatiles were removed from the filtrate under vacuum. Once dry, 10 mL of a 2:1 mixture of hexanes:THF was added and the resulting solution was cooled to -35 °C for 8 hrs to yield $[\{(\text{THF})_3\text{Li}\}^i\text{PrP}(\text{C}_6\text{H}_4)\text{BCy}_2\{\text{CH}_2\}]$ (**9**) as a yellow microcrystalline solid (0.0789 g, 73 %). ^1H NMR spectroscopy was used to determine the amount of coordinated THF, which showed three THF equiv. by integration. X-ray quality colorless crystals of **9** were grown from a cold (-35 °C) solution of 1:1 hexanes:THF. ^1H NMR (498.1 MHz, C_6D_6): $\delta = 7.96$ (d, $^3J_{\text{HH}} = 6.9$ Hz, 1H, ArH), 7.37 (t, $^3J_{\text{HH}} = 6.9$ Hz, 1H, ArH), 7.28 (t, $^3J_{\text{HH}} = 5.9$ Hz, 1H, ArH), 7.19-7.22 (m, 1H, ArH), 3.33-3.35 (m, 12H, coordinated THF, CH_2), 2.53 (pseudo-d, 1H, H_{Cy}), 2.36 (pseudo-d, 1H, H_{Cy}), 2.24 (pseudo-d, 1H, H_{Cy}), 2.15 (pseudo-d, 1H, H_{Cy}), 2.04-2.11 (m, 3H, H_{Cy}), 1.93-2.00 (m, 2H, H_{Cy} and $\text{CH}(\text{CH}_3)_2$), 1.87 (pseudo-d, 1H, H_{Cy}), 1.79 (pseudo-d, 2H, H_{Cy}), 1.51-1.71 (m, 6H,

H_{Cy}), 1.41 (pseudo-d, 2H, H_{Cy}), 1.29-1.32 (m, 12H, coordinated THF, CH_2), 1.22 (dd, $^3J_{HH} = 7.5$ Hz, $^3J_{HP} = 14.4$ Hz, 3H, $CH(CH_3)_2$), 1.16 (dd, $^3J_{HH} = 4.9$ Hz, $^3J_{HP} = 11.9$ Hz, 3H, $CH(CH_3)_2$), 1.00-1.03 (m, 1H, H_{Cy}), 0.84-0.91 (m, 2H, H_{Cy}), 0.63 (dd, $^3J_{HH} = 6.5$ Hz, $^3J_{HP} = 20.4$ Hz, 2H, CH_2). $^{13}C\{^1H\}$ NMR (175.9 MHz, C_6D_6): $\delta = 132.8$ (d, $J_{CP} = 8.3$ Hz, ArC), 127.1 (d, $J_{CP} = 20.4$ Hz, ArC), 126.2 (s, ArC), 122.7 (d, $J_{CP} = 7.7$ Hz, ArC), 68.5 (s, coordinated THF, CH_2), 33.5 (s, BCy_2), 33.4 (s, BCy_2), 33.3 (s, BCy_2), 32.3 (s, BCy_2), 31.5 (s, BCy_2), 31.2 (s, BCy_2), 31.1 (s, BCy_2), 31.0 (s, BCy_2), 30.8 (s, BCy_2), 29.7 (s, BCy_2), 29.4 (s, BCy_2), 29.0 (s, $CH(CH_3)_2$), 25.4 (s, coordinated THF, CH_2), 20.5 (d, $^2J_{CP} = 11.3$ Hz, $CH(CH_3)_2$), 19.4 (d, $^2J_{CP} = 5.3$ Hz, $CH(CH_3)_2$), 11.9* (br, CH_2). *Note: Resonances for the ArC bound to P, the ArC bound to B and the cyclohexyl CH bound to boron could not be located. *While the P-CH₂ resonance could not be located directly by $^{13}C\{^1H\}$ NMR spectroscopy (likely due to quadrupolar broadening from neighbouring B atom), 1H - ^{13}C gHSQC NMR confirms the CH_2 moiety is located at 11.9 ppm.* $^{31}P\{^1H\}$ NMR (201.6 MHz, C_6D_6): $\delta = 15.6$ (s, $iPrP$). $^{11}B\{^1H\}$ NMR (159.8 MHz, C_6D_6): $\delta = -4.2$ (s, BCy_2). $^7Li\{^1H\}$ NMR (193.6 MHz, C_6D_6): $\delta = -0.2$ (s, $Li(THF)$). Anal. Calcd. for $C_{34}H_{59}BLiO_3P$ (%): C 72.33, H 10.53; Found: C 71.13, H 10.45. M.p. 192-193 °C (decomp.).

Synthesis of $iPr_2PCH_2(C_6H_4)Br$. Under N_2 , solid 2-bromobenzyl bromide (4.47 g, 17.9 mmol) was heated gently to melt (M.p = 29-32 °C) and added drop-wise over 10 min to an ice-bath cooled (0 °C) mixture of dried magnesium shavings (0.4400 mg, 18.10 mmol) dispersed in 250 mL of Et_2O . The reaction mixture was left stirring at room

temperature for 8 hrs. Afterwards, the reaction mixture was once again cooled to 0 °C and ClP^iPr_2 (2.88 mL, 18.1 mmol) was added drop-wise over 5 min. The reaction mixture was warmed up to room temperature and left stirring for 4 hrs, resulting in a yellow slurry. The volatiles were then removed under vacuum and the crude product was combined with 20 mL of hexanes and filtered through a 5 cm plug of silica gel in a glass fiber-packed pipette. The volatiles were removed from the filtrate under vacuum to yield $^i\text{Pr}_2\text{PCH}_2(\text{C}_6\text{H}_4)\text{Br}$ as a viscous yellow oil (3.50 g, 68 %). ^1H NMR (699.7 MHz, C_6D_6): δ = 7.38-7.40 (m, 2H, ArH), 6.91 (t, $^3J_{\text{HH}}$ = 8.4 Hz, 1H, ArH), 6.65 (t, $^3J_{\text{HH}}$ = 7.7 Hz, 1H, ArH), 2.86 (s, 2H, CH_2), 1.65 (septet, $^3J_{\text{HH}}$ = 6.9 Hz, 2H, $\text{CH}(\text{CH}_3)_2$), 1.00 (d, $^3J_{\text{HH}}$ = 6.9 Hz, 6H, $\text{CH}(\text{CH}_3)_2$), 0.98 (dd, $^3J_{\text{HH}}$ = 6.9 Hz, $^3J_{\text{HP}}$ = 12.1 Hz, 6H, $\text{CH}(\text{CH}_3)_2$). $^{13}\text{C}\{^1\text{H}\}$ NMR (175.9 MHz, C_6D_6): δ = 140.3 (s, ArC), 133.2 (s, ArC), 131.9 (d, J_{CP} = 11.1 Hz, ArC), 127.4 (d, J_{CP} = 1.9 Hz, ArC), 127.3 (s, ArC), 125.3 (d, J_{CP} = 3.7 Hz, ArC), 29.9 (d, $^1J_{\text{CP}}$ = 22.7 Hz, CH_2), 23.9 (d, $^1J_{\text{CP}}$ = 16.4 Hz, $\text{CH}(\text{CH}_3)_2$), 19.8 (d, $^2J_{\text{CP}}$ = 13.9 Hz, $\text{CH}(\text{CH}_3)_2$), 19.5 (d, $^2J_{\text{CP}}$ = 12.1 Hz, $\text{CH}(\text{CH}_3)_2$). $^{31}\text{P}\{^1\text{H}\}$ NMR (201.6 MHz, C_6D_6): δ = 10.2 (s, $^i\text{Pr}_2\text{P}$). Anal. Calcd. for $\text{C}_{13}\text{H}_{20}\text{BrP}$ (%): C 54.37, H 7.02; Found: C 54.34, H 6.88. HR-MS (EI): m/z calcd. for $[\text{C}_{13}\text{H}_{21}\text{BrP}]^+$: 287.0486; found: 287.0559 (Δppm = 0.06).

Synthesis of $[^i\text{Pr}_2\text{PCH}_2(\text{C}_6\text{H}_4)\text{Li}(\text{OEt}_2)]_2$ (10). $n\text{BuLi}$ (2.5 M solution in hexanes, 1.09 mL, 2.7 mmol) was added drop-wise over 2 min to a solution of $^i\text{Pr}_2\text{PCH}_2(\text{C}_6\text{H}_4)\text{Br}$ (0.7840 g, 2.732 mmol) in 10 mL of Et_2O at room temperature, resulting in a light yellow solution. After stirring for 10 min at room temperature, the mixture was cooled

to -35 °C for 16 hrs to afford [ⁱPr₂PCH₂(C₆H₄)Li(OEt₂)]₂ (**10**) as colorless X-ray quality crystals. After vacuum drying the crystals to constant weight, **10** was determined to be a monoetherate lithium salt according to ¹H NMR spectroscopy (0.5389 g, 42 %). ¹H NMR (399.9 MHz, C₆D₆): δ = 8.22-8.25 (m, 1H, ArH), 7.23-7.26 (m, 2H, ArH), 7.18-7.20 (m, 1H, ArH), 3.12 (d, ²J_{HP} = 4.4 Hz, 2H, CH₂), 3.07 (q, ³J_{HH} = 6.8 Hz, 4H, coordinated Et₂O, CH₂), 1.69 (d of septets, ³J_{HH} = 7.2 Hz, ³J_{HP} = 9.6 Hz, 2H, CH(CH₃)₂), 1.04 (dd, ³J_{HH} = 7.2 Hz, ³J_{HP} = 9.6 Hz, 6H, CH(CH₃)₂), 0.98 (dd, ³J_{HH} = 7.2 Hz, ³J_{HP} = 12.8 Hz, 6H, CH(CH₃)₂), 0.93 (t, ³J_{HH} = 7.2 Hz, 6H, coordinated Et₂O, CH₃). ¹³C{¹H} NMR (175.9 MHz, C₆D₆): δ = 182.6 (d, J_{CP} = 17.6 Hz, ArC), 152.4 (d, J_{CP} = 6.1 Hz, ArC), 142.9 (s, ArC), 126.3 (d, J_{CP} = 4.2 Hz, ArC), 125.7 (s, ArC), 123.1 (d, J_{CP} = 2.6 Hz, ArC), 65.8 (s, O(CH₂CH₃)₂), 37.3 (d, ¹J_{CP} = 1.6 Hz, CH₂), 22.8 (d, ²J_{CP} = 6.1 Hz, CH(CH₃)₂), 20.0 (d, ¹J_{CP} = 11.1 Hz, CH(CH₃)₂), 19.7 (d, ²J_{CP} = 8.1 Hz, CH(CH₃)₂), 15.0 (s, O(CH₂CH₃)₂). ³¹P{¹H} NMR (201.6 MHz, C₆D₆): δ = 9.9 (s, ⁱPr₂P). ⁷Li NMR (193.6 MHz, C₆D₆): δ = 2.9 (s, Li(OEt₂)). Anal. Calcd. for C₁₇H₃₀LiOP (%): C 70.81, H 10.49; Found: C 70.25, H 10.22. M.p. 58-59 °C.

Synthesis of ⁱPr₂PCH₂(C₆H₄)BCy₂ (^{CH₂}PB). ClBCy₂ (370 μL, 1.69 mmol) was added drop-wise over 5 min at 0 °C to a solution of [ⁱPr₂PCH₂(C₆H₄)Li(Et₂O)] (**10**) (0.4830 g, 1.671 mmol) in 10 mL of toluene. The reaction mixture was stirred for 2 hrs at 0 °C before removing the volatiles under vacuum. The product was extracted into 20 mL of Et₂O and the mixture was filtered through Celite. The filtrate was concentrated under vacuum to a volume of *ca.* 5 mL and cooled to -35 °C to afford ^{CH₂}PB as colorless X-

ray quality crystals (0.3955 g, 61 %). *Note:* ^{CH_2}PB is stable in air as a C_6D_6 solution for at least 2 days. 1H NMR (399.9 MHz, C_6D_6): δ = 7.54 (d, $^3J_{HH}$ = 7.6 Hz, 1H, ArH), 7.25 (t, $^3J_{HH}$ = 7.2 Hz, 1H, ArH), 7.14-7.18 (m, 1H, ArH overlapping with C_6D_5H), 7.07-7.09 (m, 1H, ArH), 2.65 (d, $^2J_{HP}$ = 8.4 Hz, 2H, CH_2), 1.95-2.02 (m, 6H, H_{Cy} and $CH(CH_3)_2$), 1.85-1.93 (m, 6H, H_{Cy}), 1.42-1.55 (m, 4H, H_{Cy}), 1.29-1.39 (m, 4H, H_{Cy}), 1.09-1.20 (m, 4H, H_{Cy}), 0.91 (dd, $^3J_{HH}$ = 7.2 Hz, $^3J_{HP}$ = 13.2 Hz, 6H, $CH(CH_3)_2$), 0.79 (dd, $^3J_{HH}$ = 7.2 Hz, $^3J_{HP}$ = 11.9 Hz, 6H, $CH(CH_3)_2$). $^{13}C\{^1H\}$ NMR (175.9 MHz, C_6D_6): δ = 140.3 (s, ArC), 140.2 (s, ArC), 132.4 (d, J_{CP} = 16.5 Hz, ArC), 126.2 (d, J_{CP} = 2.1 Hz, ArC), 125.4 (d, J_{CP} = 10.5 Hz, ArC), 125.3 (d, J_{CP} = 1.9 Hz, ArC), 33.3 (d, J_{CP} = 5.8 Hz, BCy_2), 32.3 (d, J_{CP} = 7.4 Hz, BCy_2), 31.6 (br s, BCy_2), 30.2 (s, BCy_2), 29.9 (s, BCy_2), 29.4 (d, $^1J_{CP}$ = 33.4 Hz, CH_2), 28.2 (s, BCy_2), 22.4 (d, $^1J_{CP}$ = 15.5 Hz, $CH(CH_3)_2$), 19.3 (d, $^2J_{CP}$ = 2.5 Hz, $CH(CH_3)_2$), 18.9 (s, $CH(CH_3)_2$). $^{31}P\{^1H\}$ NMR (201.6 MHz, C_6D_6): δ = 34.3 (s, iPr_2P). $^{11}B\{^1H\}$ NMR (128.3 MHz, C_6D_6): δ = -0.6 (s, Cy_2B). Anal. Calcd. for $C_{25}H_{42}BP$ (%): C 78.12, H 11.01; Found: C 77.82, H 10.73. M.p. 160-161 °C.

Synthesis of $^iPr_2PCH_2(C_6H_4)BMes_2$ ($^{CH_2}PB_{Mes}$). Mes_2BF (0.1465 g, 0.5463 mmol) was added as a solid to a stirring solution of [$^iPr_2PCH_2(C_6H_4)Li(Et_2O)$] (**10**) (0.1575 g, 0.5462 mmol) in 20 mL of hexanes. The reaction mixture was stirred for 2 hrs at room temperature before being heated to 70 °C for 5 min. Once hot, the reaction mixture was filtered through Celite and the volatiles were removed from the filtrate to afford $^iPr_2PCH_2(C_6H_4)BMes_2$ ($^{CH_2}PB_{Mes}$) as a white powder (0.1494 g, 60 %). *Note:*

Multinuclear NMR spectra (^1H , $^1\text{H}\{^31\text{P}\}$, $^{13}\text{C}\{^1\text{H}\}$, $^31\text{P}\{^1\text{H}\}$) were collected at $-40\text{ }^\circ\text{C}$ to minimize rotational broadening from Mes groups. At $-40\text{ }^\circ\text{C}$, VT-NMR showed no $^{11}\text{B}\{^1\text{H}\}$ resonance; therefore, the $^{11}\text{B}\{^1\text{H}\}$ resonance at $25\text{ }^\circ\text{C}$ is reported below.

$^1\text{H}\{^31\text{P}\}$ NMR (399.9 MHz, $-40\text{ }^\circ\text{C}$, CDCl_3): $\delta = 7.27\text{-}7.32$ (m, 2H, ArH), 7.12 (t, $^3J_{\text{HH}} = 7.2$ Hz, 1H, ArH), 7.17-7.19 (m, 1H, ArH), 6.83 (s, 1H, Mes-CH), 6.77 (s, 1H, Mes-CH), 6.74 (s, 1H, Mes-CH), 6.71 (s, 1H, Mes-CH), 3.05 (d, $^2J_{\text{HH}} = 13.2$ Hz, 1H, CH_2), 2.47 (d, $^2J_{\text{HH}} = 13.2$ Hz, 1H, CH_2), 2.30 (s, 3H, Mes- CH_3), 2.23 (s, 3H, Mes- CH_3), 2.17 (s, 3H, Mes- CH_3), 2.16 (s, 3H, Mes- CH_3), 1.92 (s, 3H, Mes- CH_3), 1.82 (s, 3H, Mes- CH_3), 1.45 (septet, $^3J_{\text{HH}} = 7.2$ Hz, 2H, $\text{CH}(\text{CH}_3)_2$), 0.92 (d, $^3J_{\text{HH}} = 6.8$ Hz, 3H, $\text{CH}(\text{CH}_3)_2$), 0.85-0.88 (m, 6H, $\text{CH}(\text{CH}_3)_2$), 0.54 (d, $^3J_{\text{HH}} = 6.8$ Hz, 3H, $\text{CH}(\text{CH}_3)_2$).

$^{13}\text{C}\{^1\text{H}\}$ NMR (100.6 MHz, $-40\text{ }^\circ\text{C}$, CDCl_3): $\delta = 146.7$ (s, ArC), 145.8 (s, ArC), 145.7 (d, $J_{\text{CP}} = 6.4$ Hz, ArC), 143.8 (s, ArC), 141.6 (s, ArC), 141.5 (s, ArC), 140.2 (d, $J_{\text{CP}} = 39.5$ Hz, ArC), 138.6 (d, $J_{\text{CP}} = 40.7$ Hz, ArC), 136.3 (s, ArC), 130.8 (s, ArC), 129.9 (d, $J_{\text{CP}} = 6.0$ Hz, ArC), 129.4 (s, ArC), 128.1 (s, ArC), 127.9 (s, ArC), 127.8 (s, ArC), 125.8 (s, ArC), 31.2 (d, $^1J_{\text{CP}} = 18.1$ Hz, PCH_2), 25.1-25.2 (m, Mes CH_3), 23.8-24.0 (m, Mes CH_3), 23.6-23.7 (m, Mes CH_3), 22.7 (s, Mes CH_3), 21.7-21.9 (m, Mes CH_3), 21.3-21.4 (m, Mes CH_3), 20.1-20.4 (m, $\text{CH}(\text{CH}_3)_2$), 18.7-18.9 (m, $\text{CH}(\text{CH}_3)_2$), 17.6-17.7 (m, $\text{CH}(\text{CH}_3)_2$).

$^31\text{P}\{^1\text{H}\}$ NMR (161.9 MHz, $-40\text{ }^\circ\text{C}$, CDCl_3): $\delta = 13.0$ (s, $i\text{Pr}_2\text{P}$).

$^{11}\text{B}\{^1\text{H}\}$ NMR (128.3 MHz, $25\text{ }^\circ\text{C}$, CDCl_3): $\delta = 73.1$ (br, Mes $_2\text{B}$). Anal. Calcd. for $\text{C}_{31}\text{H}_{42}\text{BP}$ (%): C 81.57, H 9.27; Found: C 79.92, H 9.19. HR-MS (EI): m/z calcd. for $[\text{C}_{30}\text{H}_{39}^{11}\text{BP}]^+$: 441.28824; found: 441.28874 ($\Delta\text{ppm} = 0.05$). M.p. $124\text{-}125\text{ }^\circ\text{C}$.

Synthesis of [¹Pr₂PCH₂(C₆H₄)BMes₂{GeCl₂}] (11). Cl₂Ge•dioxane (0.1098 g, 0.4739 mmol) was added as a solid to a stirring solution of ^{CH₂}PB_{Mes} (0.2004 g, 0.4390 mmol) in 10 mL of C₆H₆. The reaction mixture was stirred for 8 hrs at room temperature. After removal of the volatiles under vacuum, the reaction mixture was extracted using 2 × 20 mL of hexanes and filtered. The combined filtrates were concentrated under vacuum and 5 mL of C₆H₆ was added. The C₆H₆ solution was then frozen and placed under high vacuum to lyophilize the product, affording [¹Pr₂PCH₂(C₆H₄)BMes₂{GeCl₂}] (11) as an off-white powder (0.1092 g, 41 %). *Note: Multinuclear NMR spectra (¹H, ¹³C{¹H}, ³¹P{¹H}) were collected at -40 °C to minimize rotational broadening from Mes groups. At -40 °C, VT-NMR showed no ¹¹B{¹H} resonance; therefore, the ¹¹B{¹H} resonance at 25 °C is reported below.* ¹H{³¹P} NMR (399.9 MHz, -40 °C, CDCl₃): δ = 7.41-7.47 (m, 2H, ArH), 7.36 (d, ³J_{HH} = 7.3 Hz, 1H, ArH), 7.23 (t, ³J_{HH} = 5.5 Hz, 1H, ArH), 6.83 (s, 1H, ArH), 6.79-6.81 (m, 3H, ArH), 3.29 (s, 2H, CH₂), 2.35-2.47 (m, 2H, CH(CH₃)₂), 2.30 (s, 3H, Mes-CH₃), 2.25 (s, 3H, Mes-CH₃), 2.08 (s, 3H, Mes-CH₃), 2.02 (s, 3H, Mes-CH₃), 2.01 (s, 3H, Mes-CH₃), 1.79 (s, 3H, Mes-CH₃), 1.18 (d, ³J_{HH} = 7.3 Hz, 3H, CH(CH₃)₂), 1.04 (d, ³J_{HH} = 7.1 Hz, 3H, CH(CH₃)₂), 0.95 (d, ³J_{HH} = 7.1 Hz, 3H, CH(CH₃)₂), 0.76 (d, ³J_{HH} = 7.1 Hz, 3H, CH(CH₃)₂). ¹³C{¹H} NMR (100.6 MHz, -40 °C, CDCl₃): δ = 147.3 (d, J_{CP} = 2.0 Hz, ArC), 142.5 (s, ArC), 142.3 (s, ArC), 141.1 (s, ArC), 140.8 (s, ArC), 140.0 (s, ArC), 139.6 (s, ArC), 139.5 (s, ArC), 138.6 (s, ArC), 138.1 (s, ArC), 136.9 (s, ArCH), 132.1 (s, ArCH), 129.9 (d, J_{CP} = 4.1 Hz, ArCH), 129.0 (s, ArCH), 128.9 (s, ArCH), 128.5 (s, ArCH), 128.3 (s, ArCH), 127.3 (s, ArCH), 24.6 (s, MesCH₃), 23.6 (s, MesCH₃), 23.0 (s, MesCH₃), 22.8 (d, ¹J_{CP} = 13.9 Hz, CH(CH₃)₂),

22.6 (s, MesCH₃), 22.5 (s, PCH₂), 22.0 (d, ¹J_{CP} = 12.3 Hz, CH(CH₃)₂), 21.4 (s, MesCH₃), 21.3 (s, MesCH₃), 18.4 (s, CH(CH₃)₂), 18.2 (s, CH(CH₃)₂), 17.5 (s, CH(CH₃)₂), 17.3 (s, CH(CH₃)₂). ³¹P{¹H} NMR (161.9 MHz, -40 °C, CDCl₃): δ = 10.4 (s, ⁱPr₂P). ¹¹B{¹H} NMR (128.3 MHz, 25 °C, CDCl₃): δ = 74.2 (br, Mes₂B). Anal. Calcd. for C₃₁H₄₂BCl₂GeP (%): C 62.06, H 7.06; Found: C 61.82, H 7.15. M.p. 122-124 °C.

Synthesis of Cp*₂Ge from [ⁱPr₂PCH₂(C₆H₄)BMes₂{GeCl₂}] (11) and Cp*Li. A solution of Cp*Li (0.0052 g, 0.072 mmol) in 2 mL of THF was added to a stirring solution of [ⁱPr₂PCH₂(C₆H₄)BMes₂{GeCl₂}] (**11**) (0.0215 g, 0.0358 mmol) in 5 mL of toluene. The reaction mixture was then stirred for 1 hr at room temperature. Subsequently, the reaction mixture was concentrated under vacuum, 5 mL of hexanes was added, and the mixture was filtered. The filtrate was concentrated to a volume of ~2 mL and cooled to -35 °C for 8 hrs to yield Cp*₂Ge as a white microcrystalline powder (0.0109 g, 89 %).

4.4.3 X-ray Crystallography

Appropriate X-ray quality crystals were coated with a small amount of hydrocarbon oil (Paratone-N) and removed from the glovebox in a vial. Crystals were quickly mounted onto a glass fiber and placed in a low temperature stream of nitrogen on the X-ray diffractometer. All data was collected using a Bruker APEX II CCD detector/D8 or PLATFORM diffractometer using Mo Kα (0.71073 Å) or Cu Kα

(1.54178 Å) radiation, with the crystals cooled to -80 °C or -100 °C. The data was corrected for absorption through Gaussian integration from the indexing of crystal faces.³³ Crystal structures were solved using intrinsic phasing (SHELXT)³⁴ and refined using SHELXL-2014.³⁵ For [PB{CH₂}] (**8**), [{(THF)₃Li}ⁱPrP(C₆H₄)BCy₂{CH₂}] (**9**), [ⁱPr₂PCH₂(C₆H₄)Li(OEt₂)]₂ (**10**) and ^{CH₂}PB, Olex2 was used as a Graphical User Interface (GUI).³⁶ The assignment of hydrogen atom positions are based on the *sp*²- or *sp*³-hybridization geometries of their attached carbon atoms and were given thermal parameters 20 % greater than those of their parent atoms. Molecular structures are shown with thermal ellipsoids at a 30 % probability level and have been generated using SHELXP.

Table 4.2. X-ray crystallographic data for [PB{SiBr₂}] (**5**), [PB{AgOTf}]₂ (**6**), and [PB{CH₂}] (**8**).

Compound	5	6	8
Formula	C ₂₄ H ₄₀ BBr ₂ PSi	C ₆₄ H ₉₆ Ag ₂ B ₂ F ₆ O ₆ P ₂ S ₂	C ₂₅ H ₄₂ BP
Formula weight	558.25	1438.82	384.36
Crystal system	Monoclinic	Triclinic	Monoclinic
Space group	<i>P2₁/c</i> (No. 14)	<i>P</i> $\bar{1}$ (No. 2)	<i>P2₁/c</i> (No. 14)
Crystal dimensions (mm)	0.15×0.12×0.06	0.17×0.15×0.04	0.154×0.113×0.045
<i>a</i> (Å)	9.9653(2)	11.0509(3)	10.5854(3)
<i>b</i> (Å)	15.4219(4)	11.8386(3)	9.8043(2)
<i>c</i> (Å)	17.1801(4)	14.3836(4)	22.5734(5)
α (°)	90	99.1129(11)	90
β (°)	105.5652(13)	105.9672(11)	91.2950(10)
γ (°)	90	108.6188(9)	90
<i>V</i> (Å ³)	2586.70(10)	1650.69(8)	2342.12(10)
<i>Z</i>	4	1	4
ρ (g/cm ³)	1.433	1.447	1.090
Abs coeff (mm ⁻¹)	5.053	6.350	1.058
<i>T</i> (°C)	-100	-100	-80
2 θ _{max} (°)	140.41	148.16	147.81
Total data	13910	72300	88291
Unique data	4905 (0.0260)	6441 (0.0333)	4607 (0.0637)
Obs data [<i>I</i> >2 σ (<i>I</i>)] ^a	4172	6261	4070
Params	262	445 ^b	496 ^{c,d}
<i>R</i> ₁ [<i>I</i> >2 σ (<i>I</i>)] ^a	0.0444 ^a	0.0263 ^b	0.0479 ^{c,d}
<i>wR</i> ₂ [all data] ^a	0.1394	0.0725	0.1356
Max/min $\Delta\rho$ (e ⁻ Å ⁻³)	1.441/-1.029	0.770/-0.521	0.87/-0.34

$$^a R_1 = \frac{\sum ||F_o| - |F_c||}{\sum |F_o|}; wR_2 = \left[\frac{\sum w(F_o^2 - F_c^2)^2}{\sum w(F_o^4)} \right]^{1/2}.$$

^bThe disordered cyclohexyl group (atoms C21A to C26A and C21B to C26B) were restrained to have approximately the same bond lengths by using the SHELXL **SADI** instruction on the following: B1–C21A and B1–C21B; all C–C distances. Additionally, the anisotropic displacement parameters were restrained by use of the SHELXL **SIMU** instruction. Finally, the disordered solvent toluene molecule was constrained to have an idealized phenyl group, the methyl carbon to ipso-carbon distance was restrained to be approximately 1.50 Å by use of a SHELXL **DFIX** instruction, and the angles about the ipso carbon atoms were restrained to be approximately 120°. Further, the anisotropic displacement parameters of carbon atoms of the major orientation of the toluene were restrained by use of the SHELXL **RIGU** instruction.

^cData were collected with the detector set at three different positions. Low-angle (detector $2\theta = -33^\circ$) data frames were collected using a scan time of 5 s, medium-angle (detector $2\theta = 75^\circ$) frames using a scan time of 5 s, and high-angle (detector $2\theta = 117^\circ$) frames using a scan time of 10 s.

^dDue to whole molecule disorder, molecule was split into two parts (using **PART** keywords); both refined anisotropically. **SIMU**, **RIGU** and **DELU** restraints were added, alongside **SAME P1 > C25**.

Table 4.3. X-ray crystallographic data for [$\{(THF)_3Li\}^iPrP(C_6H_4)BCy_2\{CH_2\}$] (**9**), [$^iPr_2PCH_2(C_6H_4)Li(Et_2O)$]₂ (**10**), and **CH²PB**.

Compound	9	10	CH²PB
Formula	C ₃₄ H ₅₉ BLiO ₃ P	C ₁₇ H _{28.17} LiOP	C ₂₅ H ₄₂ BP
Formula weight	564.53	288.49	384.36
Crystal system	Orthorhombic	Monoclinic	Monoclinic
Space group	<i>P2₁2₁2₁</i> (No. 19)	<i>P2₁/n</i>	<i>P2₁/c</i> (No. 14)
Crystal dimensions (mm)	0.235×0.173×0.132	0.174×0.147×0.061	0.065×0.164×0.253
<i>a</i> (Å)	9.9428(10)	12.7778(6)	10.7112(4)
<i>b</i> (Å)	16.8849(17)	18.1916(8)	11.6101(4)
<i>c</i> (Å)	20.512(2)	15.8870(7)	18.4751(6)
α (°)	90	90	90
β (°)	90	95.1640(10)	90.8680(10)
γ (°)	90	90	90
<i>V</i> (Å ³)	3443.6(6)	3676.1(3)	2297.28(14)
<i>Z</i>	4	8	4
ρ (g/cm ³)	1.089	1.043	1.111
Abs coeff (mm ⁻¹)	0.110	0.144	0.127
<i>T</i> (°C)	-80	-100	-100
2 θ_{max} (°)	102.76	102.9	107.6
Total data	28282	56424	26118
Unique data	6531 (0.0730)	7023 (0.0715)	4835 (0.0397)
Obs data [<i>I</i> >2 σ (<i>I</i>)] ^a	4451	7023	3947
Params	410 ^c	393 ^b	248
<i>R</i> ₁ [<i>I</i> >2 σ (<i>I</i>)] ^a	0.0579 ^d	0.0607 ^b	0.0377
<i>wR</i> ₂ [all data] ^a	0.1595	0.1769 ^b	0.0997
Max/min $\Delta\rho$ (e ⁻ Å ⁻³)	0.42/-0.26	0.74/-0.48	0.31/-0.22

$$^a R_1 = \frac{\sum ||F_o| - |F_c||}{\sum |F_o|}; wR_2 = \left[\frac{\sum w(F_o^2 - F_c^2)^2}{\sum w(F_o^4)} \right]^{1/2}.$$

^bThe disorder in the coordinated Et₂O solvent molecules for **10** could not be fully resolved by splitting into parts, as they are disordered over more than three locations. Thus, only **SIMU**, **RIGU**, **DELU** restraints were applied to the Et₂O molecules.

^cDue to disordered THF molecules, **RIGU**, **SADI** and **EADP** restraints were used for C23 to C26, C31 to C34.

^dRefined as an inversion twin: $I_c = (1-x)I_s^+ + xI_s^-$. The Flack parameter (*x*) was determined to be 0.29(19); therefore, the absolute configuration of **9** cannot be conclusively determined and it must be considered a racemic mixture.

4.5 References and Notes

1. M. M. D. Roy, A. A. Omaña, A. S. S. Wilson, M. S. Hill, S. Aldridge, E. Rivard, *Chem. Rev.* **2021**, *121*, 12784–12965.
2. a) M. S. Hill, D. J. Liptrot, C. Weetman, *Chem. Soc. Rev.* **2018**, *118*, 3608–3680; b) T. J. Hadlington, M. Driess, C. Jones, *Chem. Soc. Rev.* **2018**, *47*, 4176–4197; c) R. J. Less, H. R. Simmonds, S. B. J. Dane, D. S. Wright, *Dalton Trans.* **2013**, *42*, 6337–6343.
3. a) P. P. Power, *Nature* **2010**, *463*, 171–177; b) R. Rodriguez, D. Gau, Y. Contie, T. Kato, N. Saffon-Merceron, A. Bacciredo, *Angew. Chem. Int. Ed.* **2011**, *50*, 11492–11495; c) S. Yao, Y. Xiong, M. Driess, *Acc. Chem. Res.* **2017**, *50*, 2026–2037; d) V. Nesterov, D. Reiter, P. Bag, P. Frisch, R. Holzner, A. Porzelt, S. Inoue, *Chem. Rev.* **2018**, *118*, 9678–9842; e) J. Hicks, P. Vasko, J. M. Goicoechea, S. Aldridge, *Nature* **2018**, *557*, 92–95; f) R. Kobayashi, S. Ishida, T. Iwamoto, *Angew. Chem. Int. Ed.* **2019**, *58*, 9425–9428; g) M.-A. Légaré, M. Rang, G. Bélanger-Chabot, J. I. Schweizer, I. Krummenacher, R. Bertermann, M. Arrowsmith, M. C. Holthausen, H. Braunschweig, *Science* **2019**, *363*, 1329–1332; h) W. Lu, Y. Li, R. Kinjo, *J. Am. Chem. Soc.* **2019**, *141*, 5164–5168; i) K. M. Marczenko, J. A. Zurakowski, K. L. Bamford, J. W. M. MacMillan, S. S. Chitnis, *Angew. Chem. Int. Ed.* **2019**, *58*, 18096–18101; j) T. Sugahara, J.-D. Guo, D. Hashizume, T. Sasamori, N. Tokitoh, *J. Am. Chem. Soc.* **2019**, *141*, 2263–2267; k) S. Kurumada, S. Takamori, M. Yamashita, *Nat. Chem.* **2020**, *12*, 36–39; l) S. Fujimori, S. Inoue, *Eur. J. Inorg. Chem.* **2020**, 3131–3142; m) C. Shan, S. Yao, M. Driess, *Chem. Soc. Rev.* **2020**, *49*, 6733–6754; n) P. P. Power, *Organometallics*

2007, 26, 4362–4372; o) C. Weetman, S. Inoue, *Chem. Cat. Chem.* **2018**, 19, 4213–4228.

4. a) B. D. Rekken, T. M. Brown, J. C. Fettinger, H. M. Tuononen, P. P. Power, *J. Am. Chem. Soc.* **2012**, 134, 6504–6507; b) T. J. Hadlington, B. Schwarze, E. I. Izgorodina, C. Jones, *Chem. Commun.* **2015**, 51, 6854–6857; c) Y. Peng, J.-D. Guo, B. D. Ellis, Z. Zhu, J. C. Fettinger, S. Nagase, P. P. Power, *J. Am. Chem. Soc.* **2009**, 131, 16272–16282; d) S. M. I. Al-Rafia, A. C. Malcolm, R. McDonald, M. J. Ferguson, E. Rivard, *Chem. Commun.* **2012**, 48, 1308–1310; e) S. M. I. Al-Rafia, P. A. Lummis, A. K. Swarnakar, K. C. Deutsch, M. J. Ferguson, R. McDonald, E. Rivard, *Aust. J. Chem.* **2013**, 66, 1235–1245; f) M. M. D. Roy, S. R. Baird, E. Dornsiepen, L. A. Paul, L. Miao, M. J. Ferguson, Y. Zhou, I. Siewert, E. Rivard, *Chem. Eur. J.* **2021**, 27, 8572–8579.

5. a) R. Rodriguez, Y. Contie, R. Nougúé, A. Baceiredo, N. Saffon-Merceron, J. M. Sotiropoulos, T. Kato, *Angew. Chem. Int. Ed.* **2016**, 55, 14355–14358; b) J. Tremmel, J. Tydlitát, L. Dostál, A. Ružička, X. Deraet, J. Turek, R. Jambor, *Chem. Eur. J.* **2020**, 26, 6070–6075.

6. a) R. Dobrovetsky, D. W. Stephan, *J. Am. Chem. Soc.* **2013**, 135, 4974–4977; b) D. W. Stephan, *Science* **2016**, 354, aaf7229; c) J. Li, C. G. Daniliuc, G. Kehr, G. Erker, *Angew. Chem. Int. Ed.* **2019**, 58, 6737–6741.

7. A. A. Omaña, R. K. Green, R. Kobayashi, Y. He, E. R. Antoniuk, M. J. Ferguson, Y. Zhou, J. G. C. Veinot, T. Iwamoto, A. Brown, E. Rivard, *Angew. Chem. Int. Ed.* **2021**, 60, 228–231.

8. B. L. Frenette, A. A. Omaña, M. J. Ferguson, Y. Zhou, E. Rivard, *Chem. Commun.* **2021**, 57, 10895–10898.
9. S. Bontemps, G. Bouhadir, K. Miqueu, D. Bourissou, *J. Am. Chem. Soc.* **2006**, 128, 12056–12057.
10. Selected examples for the use of Khyp in the syntheses of related Si species: a) C. Marschner, *Eur. J. Inorg. Chem.* **1998**, 221–226; b) M. M. D. Roy, M. J. Ferguson, R. McDonald, Y. Zhou, E. Rivard, *Chem. Sci.* **2019**, 10, 6476–6481; c) A. V. Protchenko, A. D. Schwarz, M. P. Blake, C. Jones, N. Kaltsoyannis, P. Mountford, S. Aldridge, *Angew. Chem. Int. Ed.* **2013**, 52, 568–571; d) D. Wendel, A. Porzelt, F. A. D. Herz, D. Sakar, C. Jandl, S. Inoue, B. Rieger, *J. Am. Chem. Soc.* **2017**, 139, 8134–8137.
11. A. C. Filippou, O. Chernov, G. Schnakenburg, *Angew. Chem. Int. Ed.* **2009**, 48, 5687–5690.
12. a) F. Meyer-Wegner, A. Nadj, M. Bolte, N. Auner, M. Wagner, M. C. Holthausen, H.-W. Lerner, *Chem. Eur. J.* **2011**, 17, 4715–4719; b) J. I. Schweizer, A. G. Sturm, T. Porsch, M. Berger, M. Bolte, N. Auner, M. C. Holthausen, *Z. Anorg. Allg. Chem.* **2018**, 644, 982–988; c) R. S. Ghadwal, K. Pröpper, B. Dittrich, P. G. Jones, H. W. Roesky, *Inorg. Chem.* **2011**, 50, 358–364.
13. a) Y. Wang, Y. Xie, P. Wei, R. B. King, H. F. Schaefer III, P. v. R. Schleyer, G. H. Robinson, *Science* **2008**, 321, 1069–1071; b) R. S. Ghadwal, H. W. Roesky, S. Merkel, J. Henn, D. Stalke, *Angew. Chem. Int. Ed.* **2009**, 48, 5683–5686.
14. a) J. L. Berkowitz, J. P. Green, H. Cho, R. Ruscic, *J. Chem. Phys.* **1987**, 86, 1235–1248; b) Y. Apeloig, R. Pauncz, M. Karni, R. West, W. Steiner, D. Chapman,

- Organometallics* **2003**, *22*, 3250–3256; c) S. K. Shin, W. A. Goddard III, J. L. Beauchamp, *J. Phys. Chem.* **1990**, *94*, 6963–6969; d) M. Benavides-Garcia, K. Balasubramanian, *J. Phys. Chem.* **1992**, *97*, 7537–7544; e) J.-C. Barthelat, B. S. Roch, G. Trinquier, J. Satgé, *J. Am. Chem. Soc.* **1980**, *102*, 4080–4085.
15. Y. Shao, D. Truhlar, *Theor. Chem. Acc.* **2008**, *120*, 215–241.
16. T. H. Dunning Jr., *J. Chem. Phys.* **1989**, *90*, 1007–1023.
17. P. Jutzi, U. Holtmann, D. Kanne, C. Krüger, R. Blom, R. Gleiter, I. Hyla-Kryspin, *Chem. Ber.* **1989**, *122*, 1629–1639.
18. a) P. Jutzi, F. Kohl, P. Hofmann, C. Krüger, Y.-H. Tsay, *Chem. Ber.* **1980**, *113*, 757–769; b) P. Jutzi, B. Hielscher, *Organometallics* **1986**, *5*, 1201–1204.
19. a) H. F. T. Klare, M. Oestreich, *Dalton Trans.* **2010**, *39*, 9176–9184; b) J. C. L. Walker, H. F. T. Klare, M. Oestreich, *Nat. Rev. Chem.* **2020**, *4*, 54–62; c) E. Fritz-Langhals, *Org. Process Res. Dev.* **2019**, *23*, 2369–2377; d) E. Fritz-Langhals, S. Werge, S. Kneissl, P. Piroutek, *Org. Process Res. Dev.* **2020**, *24*, 1484–1495.
20. a) Y. Cao, W.-C. Shih, N. Bhuvanesh, O. V. Ozerov, *Dalton Trans.* **2019**, *48*, 9959–9961; b) M. Sircoglou, S. Bontemps, M. Mercy, N. Saffon, M. Takahashi, G. Bouhadir, L. Maron, D. Bourissou, *Angew. Chem. Int. Ed.* **2007**, *46*, 8583–8586.
21. V. O. Smirnov, A. D. Volodin, A. A. Korlyukov, A. D. Dilman, *Angew. Chem. Int. Ed.* **2020**, *59*, 12428–12431.
22. K. Miyamoto, S. Narita, Y. Masumoto, T. Hashishin, T. Osawa, M. Kimura, M. Ochiai, M. Uchiyama, *Nat. Commun.* **2020**, *11*, 2134.

23. E. D. Glendening, J. K. Badenhop, A. E. Reed, J. E. Carpenter, J. A. Bohmann, C. M. Morales, C. R. Landis, F. Weinhold, *NBO 6.0*, Theoretical Chemistry Institute, University of Wisconsin, Madison WI, 2013.
24. a) P. E. M. Berthelot, *Arch. Pharm. Pharm. Med. Chem.* **1868**, *185*, 268–269; b) N. G. Connelly, W. E. Geiger, *Chem. Rev.* **1996**, *96*, 877–910.
25. R. J. Bowen, A. C. Garner, S. J. Berners-Price, I. D. Jenkins, R. E. Sue, *J. Organomet. Chem.* **1998**, *29*, 181–184.
26. a) T. F. Vaughan, J. L. Spencer, *Inorg. Chim. Acta.* **2016**, *442*, 24–29; b) S. J. Berners-Price, R. J. Bowen, P. Galettis, P. C. Healy, M. J. McKeage, *Coord. Chem. Rev.* **1999**, *185-186*, 823–836; c) P. Espinet, K. Soulantica, *Coord. Chem. Rev.* **1999**, *193-195*, 499–556; d) B. A. Trofimov, N. K. Gusarova, A. V. Artem'ev, S. F. Malysheva, N. A. Belogorlova, A. O. Korocheva, O. N. Kazheva, G. G. Alexandrov, O. A. Dyachenko, *Mendeleev Commun.* **2012**, *22*, 187–188.
27. J. Dogan, J. B. Schulte, G. F. Swiegers, S. B. Wild, *J. Org. Chem.* **2000**, *65*, 951–957.
28. J. Sinclair, W. Medroa del Pino, K. Aku-Dominguez, Y. Minami, A. Kiran, M. J. Ferguson, M. Yasuda, E. Rivard, *Dalton Trans.* **2021**, *50*, 17688–17696.
29. H. Gilman, G. E. Dunn, *J. Am. Chem. Soc.* **1951**, *73*, 5077–5079.
30. M. Berger, N. Auner, M. Bolte, *Acta Cryst.* **2014**, *C70*, 1088–1091.
31. F. X. Kohl, P. Jutzi, *Chem. Ber.* **1987**, *120*, 1539–1543.
32. L. Jafarpour, E. D. Stevens, S. P. Nolan, *Organomet. Chem.* **2000**, *606*, 49–54.
33. R. H. Blessing, *Acta Cryst.* **1995**, *A51*, 33–38.

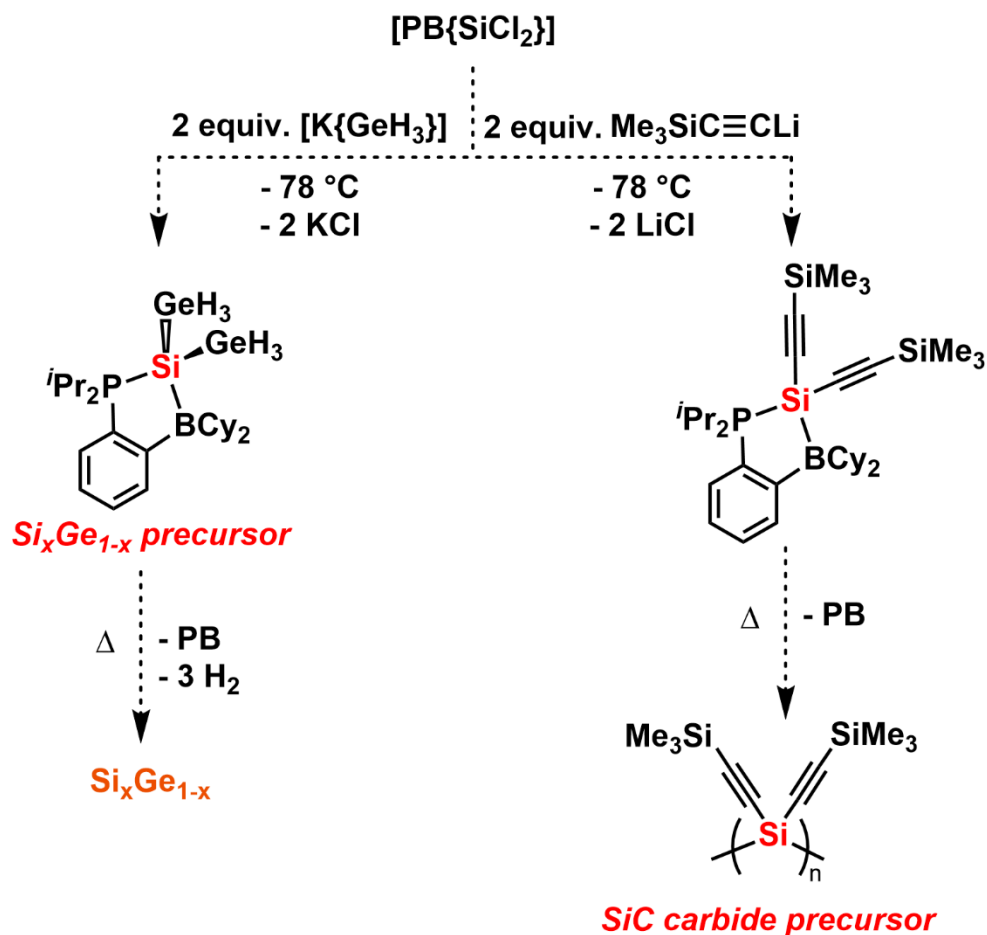
34. G. M. Sheldrick, *Acta Cryst.* **2015**, *A71*, 3–8.
35. G. M. Sheldrick, *Acta Cryst.* **2015**, *C71*, 3–8.
36. O. V. Dolomanov, L. J. Bourhis, R. J. Gildea, J. A. K. Howard, H. Puschmann, *J. Appl. Cryst.* **2009**, *42*, 339–341.

Chapter 5 – Summary and Future Directions

Starting with Chapter 2, an intramolecular frustrated Lewis pair (FLP), ${}^i\text{Pr}_2\text{P}(\text{C}_6\text{H}_4)\text{BCy}_2$ or **PB**, was used to isolate $[\text{PB}\{\text{SiH}_2\}]$ and $[\text{PB}\{\text{GeH}_2\}]$ adducts, which proved to be useful precursors for the low temperature deposition of amorphous Si and Ge films, respectively. By heating at moderate temperatures ($> 110\text{ }^\circ\text{C}$) in toluene for 8 hrs, $[\text{PB}\{\text{SiH}_2\}]$ and $[\text{PB}\{\text{GeH}_2\}]$ showed the release of H_2 gas and free **PB** ligand by NMR spectroscopy, allowing for a “closed-loop” approach where **PB** could be recovered (73-74 %) and re-used. Furthermore, SEM/EDX, XPS and Raman spectroscopy of the deposited material confirmed the identity of amorphous bulk Si(0) and Ge(0), respectively. Repeating this process in the presence of a substrate (germanium wafer for $[\text{PB}\{\text{SiH}_2\}]$ or a silicon wafer for $[\text{PB}\{\text{GeH}_2\}]$) showed the growth of uncontaminated (from P or B) Si and Ge films with thicknesses of 110(15) nm and 14(4) μm , respectively.

The solution-based, recyclable deposition method described above is useful as a “proof-of-concept” towards the development of bottleable precursors for Si and Ge film growth, as opposed to the hazardous SiH_4/H_2 or GeH_4/H_2 gas mixtures commonly used in industry.¹ Subsequently, a new monomer, $[\text{PB}\{\text{SiMe}_2\}]$ was reported, the thermolysis of which deposited polydimethylsilane [number average molecular weight (M_n) = 2.7 kDa, polydispersity index (PDI) = 2.2]. Thus, the deposition of both amorphous Si films and a polysilane at low temperatures ($< 110\text{ }^\circ\text{C}$) have been demonstrated using FLP-chelated single-source Si precursors.

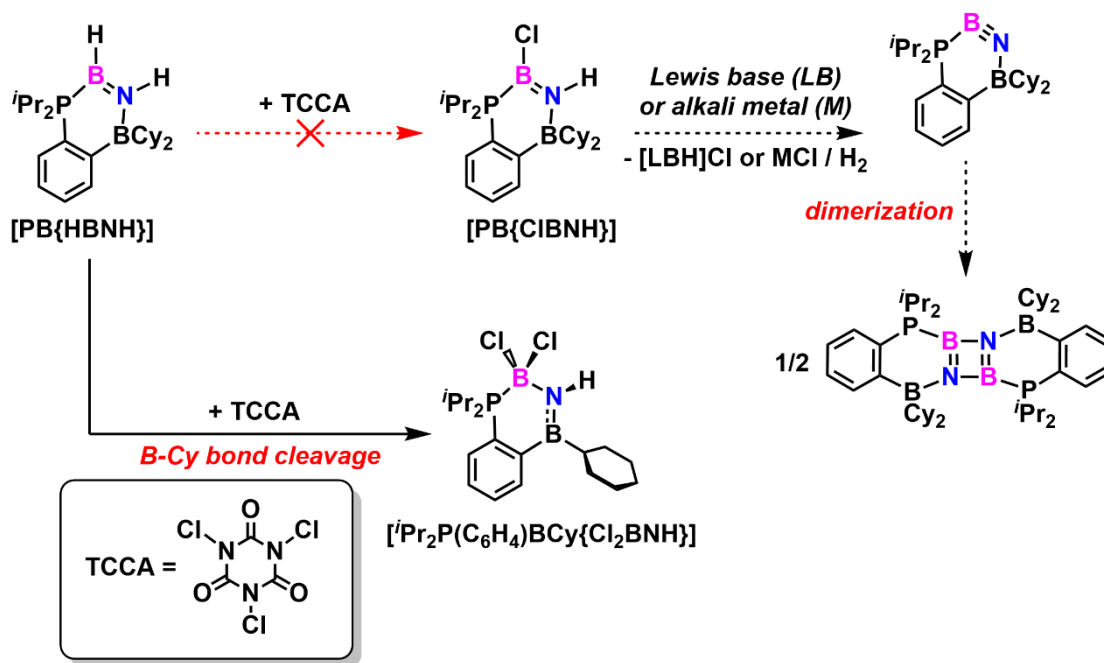
Future work to expand the scope of FLP-mediated recyclable deposition methods should focus on the synthesis of mixed silicon-element precursors. A proposed route to a $\text{Si}_x\text{Ge}_{1-x}$ ² precursor is outlined in Scheme 5.1. As opposed to previously reported $\{\text{H}_2\text{Si-GeH}_2\}$ complexes³ from the Rivard group, $[\text{PB}\{\text{Si}(\text{GeH}_3)_2\}]$ would allow for retention of high atom economy by recycling of the free **PB** ligand by-product after heating (Scheme 5.1). In addition, salt metathesis of $[\text{PB}\{\text{SiCl}_2\}]$ could be used to isolate $[\text{PB}\{\text{Si}(\text{C}\equiv\text{CSiMe}_3)_2\}]$, a possible precursor to silicon carbide⁴ films *via the in-situ* formation of poly(dialkynylsilane) (Scheme 5.1).



Scheme 5.1. Proposed routes to Si_xGe_{1-x} and SiC precursors.

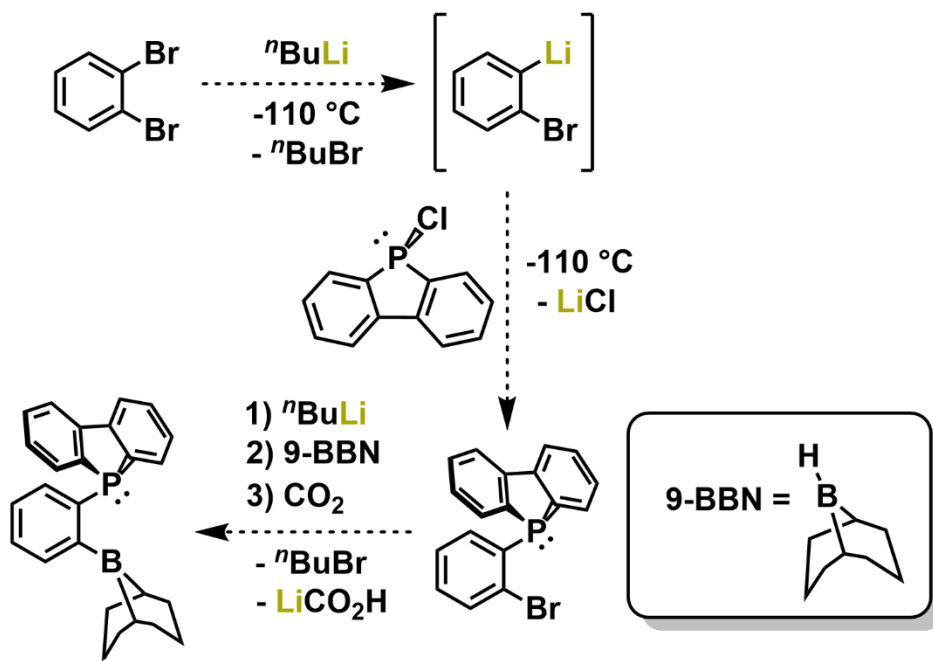
Continuing to Chapter 3, **PB** was used to dehydrogenate H₃B•NH₃ and bind a monomeric {H₂BNH₂} fragment, which was followed by a halogenation/dehydrohalogenation route to access [PB{HBNH}], a rare adduct of the parent iminoborane HBNH. With these adducts in hand, the hope was that they would behave as suitable precursors for the low temperature deposition of valuable (BN)_x materials; however, thus far, the thermolysis and attempted catalytic dehydrogenations of [PB{H₂BNH₂}] and [PB{HBNH}] have failed to yield well-defined (BN)_x materials.

Computations on the H_2BNH_2 and HBNH adducts showed low hydridic and protic character within the B–H and N–H linkages, in line with the aforementioned failed catalytic dehydrogenation attempts. A partial factor in their divergent thermolytic behavior (as compared to $[\text{PB}\{\text{SiH}_2\}]$ and $[\text{PB}\{\text{GeH}_2\}]$) may be the stronger P–B/B–N bonds involving the PB-chelates in $[\text{PB}\{\text{H}_2\text{BNH}_2\}]$ and $[\text{PB}\{\text{HBNH}\}]$. The target complex $[\text{PB}\{\text{BN}\}]_x$ might be an ideal $(\text{BN})_x$ precursor as the central BN unit should exhibit stronger B–N bonding (*i.e.*, weaker P–B/B(Cy)–N bonding) with less chance of degradative pathways as a result of the absence of B–H and N–H bonds (Scheme 5.2). As described in Chapter 3, attempts to access a potentially useful BN precursor, $[\text{PB}\{\text{ClBNH}\}]$, from $[\text{PB}\{\text{HBNH}\}]$ resulted in B–Cy bond breakage, hindering further progress to the target $[\text{PB}\{\text{BN}\}]_2\text{PB}$ dimer (Scheme 5.2).

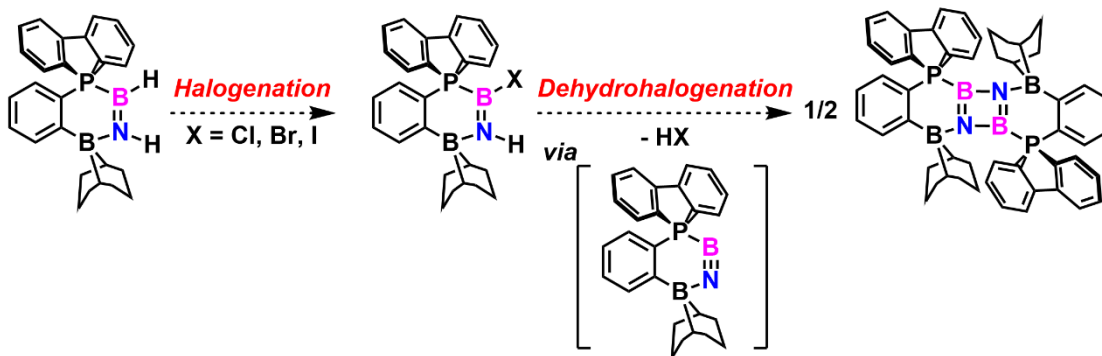


Scheme 5.2. Attempted route to the dimeric species $[\text{PB}\{\text{BN}\}_2\text{PB}]$ (dashed arrows) and B–Cy ligand activation of $[\text{PB}\{\text{HBNH}\}]$ from Chapter 3.

Through the exploration of PB-chelated tetrelenes $[\text{PB}\{\text{ER}_2\}]$ ($\text{E} = \text{Si}, \text{Ge}$; $\text{R} =$ organic group) in Chapter 4 (*vide infra*), P–C($i\text{Pr}$) bond cleavage has also been observed, which suggests that both Lewis basic P and Lewis acidic B sites within the PB chelates must be protected to prevent ligand activation. A possible strategy to enhance PB-chelate stability could be to isolate a FLP ligand that features both bidentate-bound $-\text{PR}_2$ and $-\text{BR}_2$ centers (Scheme 5.3).^{5,6} Subsequently, isolation of the resulting $\{\text{HBNH}\}$ complex and application of a halogenation/dehydrohalogenation strategy may afford the target $[\text{FLP}\{\text{BN}\}]_x$ complex, as shown in Scheme 5.4.



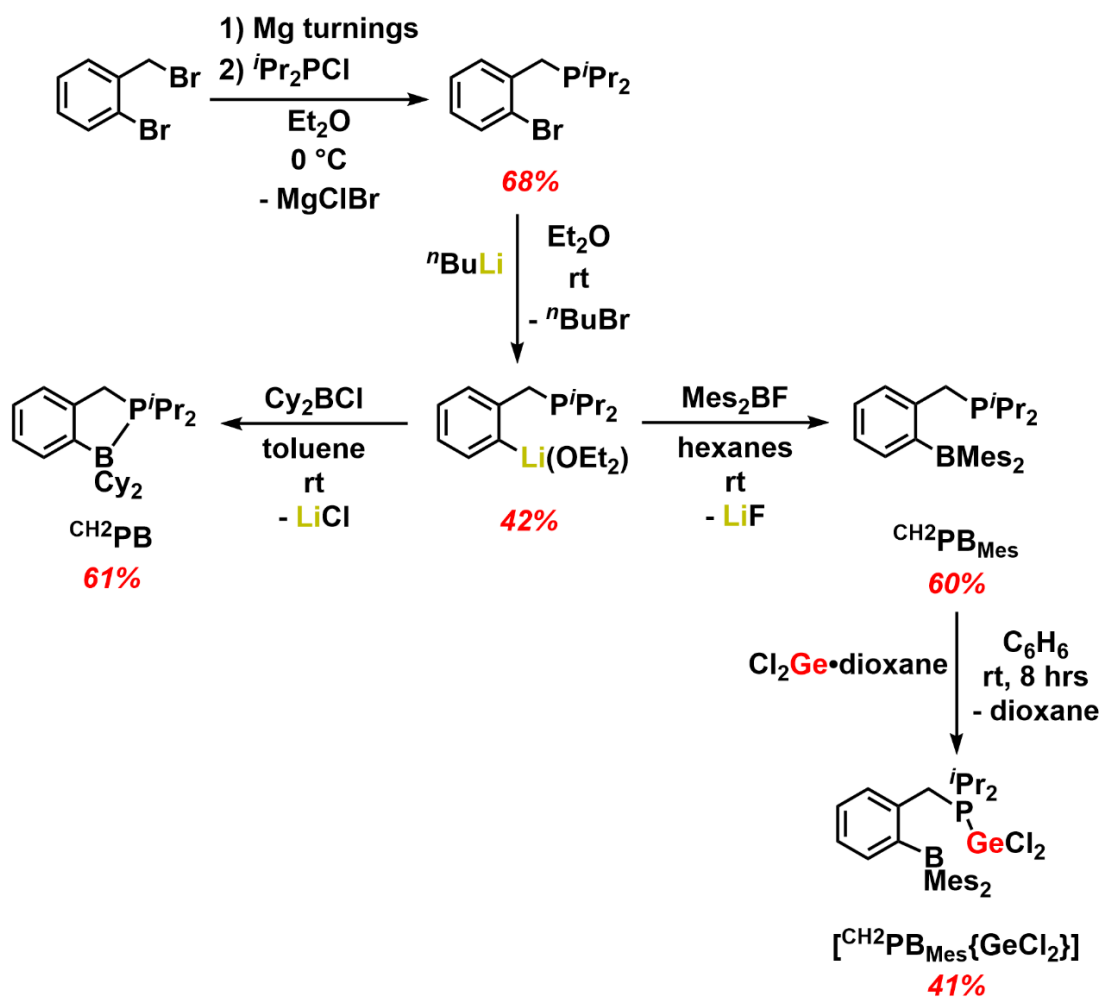
Scheme 5.3. Proposed route to new sterically protected FLPs.



Scheme 5.4. Proposed synthesis of a dimeric FLP-stabilized BN precursor.

Finally, Chapter 4 focused on the largely unexplored reactivity of the $[\text{PB}\{\text{ECl}_2\}]$ and $[\text{PB}\{\text{EH}_2\}]$ species ($\text{E} = \text{Si}$ or Ge) from Chapter 2. A major target of this Chapter was FLP-stabilized $[\text{PB}\{\text{E}\}]_x$ ($\text{E} = \text{C}, \text{Si}, \text{Ge}$) adducts by the attempted reductions of $[\text{PB}\{\text{CCl}_2\}]$, $[\text{PB}\{\text{SiX}_2\}]$ ($\text{X} = \text{Cl}$ or Br) and $[\text{PB}\{\text{GeCl}_2\}]$. Rapid degradation of the products into free **PB** and insoluble materials might be the result of

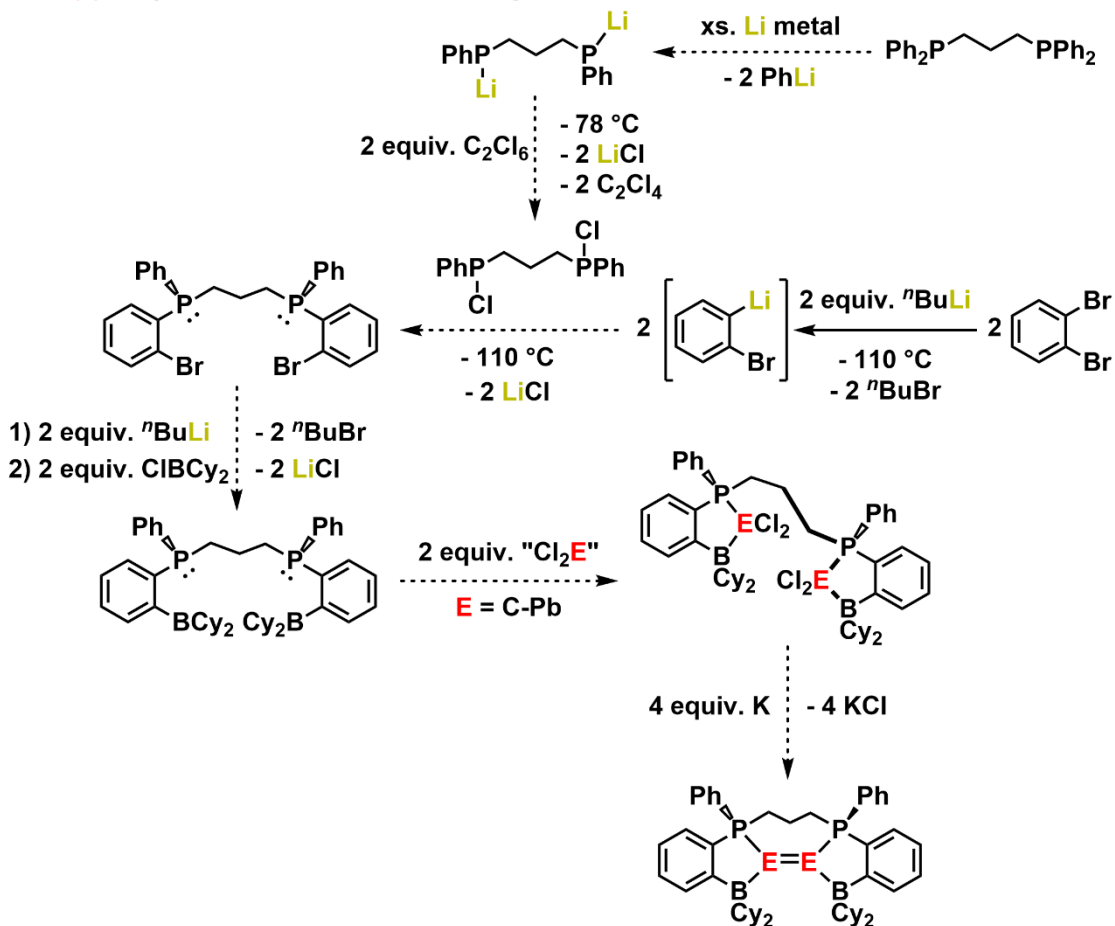
insufficient kinetic stabilization by the **PB** chelate in each case. As mentioned above, Chapter 4 also includes the lithium-mediated P–C(*i*Pr) bond cleavage of the new methylene complex, [PB{CH₂}] into [{(THF)₃Li} ^{*i*}PrP(C₆H₄){CH₂}BCy₂]. As shown in Scheme 5.5, further attempts to isolate ER₂ species using the methylene-bridged FLP chelates ^{CH₂}**PB** and ^{CH₂}**PB**_{Mes} ligands were not successful, aside from the observed formation of the phosphine-coordinated Ge(II) dichloride adduct [^{CH₂}**PB**_{Mes}{GeCl₂}].}



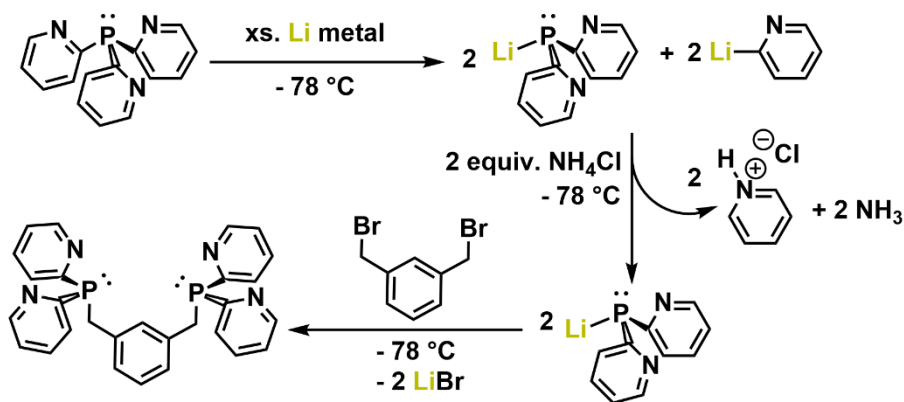
Scheme 5.5. Syntheses of ^{CH₂}**PB**, ^{CH₂}**PB**_{Mes} and [^{CH₂}**PB**_{Mes}{GeCl₂}].}

Regarding the (thus far) unsuccessful isolation of FLP-stabilized $[\text{PB}\{\text{E}\}]_x$ complexes, increased kinetic stabilization may be provided by using a dimeric FLP ligand to give $[\text{FLP}\{\text{E}=\text{E}\}\text{FLP}]$ adducts (Scheme 5.6a). P–C bond cleavage of $\text{C}_{\text{aryl}}\text{–P}$ bonds in $\text{Ph}_2\text{P}(\text{CH}_2)_3\text{PPh}_2$ using lithium is well-documented, and can be used to form the dilithio species $\text{Ph}(\text{Li})\text{P}(\text{CH}_2)_3\text{P}(\text{Li})\text{Ph}$.^{7a} In separate steps, $\text{Ph}(\text{Li})\text{P}(\text{CH}_2)_3\text{P}(\text{Li})\text{Ph}$ could be combined with C_2Cl_6 , *o*- $\text{Li}(\text{C}_6\text{H}_4)\text{Br}$, *n*-BuLi and ClBCy₂ to yield the dimeric FLP (Scheme 5.6a). In support of this synthetic route, the reported preparation of a benzyl-linked *bis*(2-pyridinyl)phosphine pincer ligand is shown in Scheme 5.6b. As a first step in this reported route, *tris*(2-pyridinyl)phosphine was combined with excess lithium metal, forming both *bis*(2-pyridinyl)phosphidolithium and 2-lithiopyridine *in-situ*.^{7b} Subsequently, the 2-lithiopyridine was reacted with $[\text{NH}_4]\text{Cl}$ to precipitate the $[\text{C}_5\text{H}_5\text{NH}]\text{Cl}$ salt and the left-over *bis*(2-pyridinyl)phosphidolithium in solution was carefully combined with dibromo-*m*-xylene to yield the final *bis*(2-pyridinyl)phosphine pincer ligand (Scheme 5.6b).^{7b} By using an extended methylene linker instead, the σ -donating P centers should be flexible enough to adopt different ligand bite angles with the absence of a formal P–B single bond (as in CH_2PB) since the linker should restrict formation of an intramolecular P–B interaction (Scheme 5.6a). Finally, *via* addition of “ Cl_2E ” ($\text{E} = \text{C–Pb}$; formed *in-situ* for both C and Si) and subsequent potassium-mediated reduction, the complete tetrelene series of $[\text{FLP}\{\text{E}=\text{E}\}\text{FLP}]$ adducts may be accessed and their reactivity with substrates (such as H_2 activation or catalytic hydroboration of CO_2) may be studied. As an added note, these $[\text{FLP}\{\text{E}=\text{E}\}\text{FLP}]$ adducts are expected to be chiral, which might give way to chiral products in catalytic processes.

(a) Proposed route to dimeric FLP ligands:



(b) Previously reported route to 2-pyridinyl phosphine pincer ligands:



Scheme 5.6. (a) Proposed route to dimeric FLP ligands and their target [FLP{E=E}FLP] complexes; (b) reported route to 2-pyridinyl-phosphine ligands.

This Thesis focused on the use of FLPs as suitable ligands for the isolation of highly reactive Group 14 and mixed Group 13/15 element species, the likes of which are largely observed as fleeting intermediates in highly controlled plasma or extremely cold matrices (*e.g.*, SiH₂). Historically, a large portion of main group element chemistry has focused on the use of anionic carbon- and nitrogen-based σ -donors as ligands; however, the work presented here illustrates that stabilization using neutral heteronuclear donor and acceptor pairs can unlock unique properties and reactivity pathways not accessible using traditional ligands. While the development of new synthetic routes or precursors in materials chemistry presents many challenges, the combination of FLPs and main group element chemistry may provide a crucial toolset for the future.

5.1 References

1. For an overview of SiH₄ and GeH₄ use in the production of Si and Ge films, see: a) R. A. Street, *Technology and Applications of Amorphous Silicon*; Springer-Verlag; Berlin **2000**, 37, 94–146; b) H. Ishii, Y. Takahashi, J. Murota, *Appl. Phys. Lett.* **1985**, 47, 863–864 and references therein.
2. R. Basu, *Mater. Adv.* **2022**, 3, 4489–4513.
3. S. M. I. Al-Rafia, A. C. Malcolm, R. McDonald, M. J. Ferguson, E. Rivard, *Angew. Chem. Int. Ed.* **2011**, 50, 8354–8357.
4. M. Fraga, R. Pessoa, *Micromachines* **2020**, 11, 799–799.

5. H. T. Teunissen, C. B. Hansen, F. Bickelhaupt, *Phosphorus Sulfur Silicon Relat. Elem.* **1996**, *118*, 309–312.
6. R. Ayyappan, Y. Coppel, L. Vendier, S. Ghosh, S. Sabo-Etienne, S. Bontemps, *Chem. Commun.* **2021**, *57*, 375–378.
7. a) J. Dogan, J. B. Schulte, G. F. Swiegers, S. B. Wild, *J. Org. Chem.* **2000**, *65*, 951–957; b) T. F. Vaughan, J. L. Spencer, *Inorg. Chim. Acta.* **2016**, *442*, 24–29.

Complete Bibliography

Chapter 1

1. R. West, *Polyhedron* **2002**, *21*, 467–472.
2. T. J. Hadlington, M. Driess, C. Jones, *Chem. Soc. Rev.* **2018**, *47*, 4176–4197.
3. P. W. N. M. van Leeuwen, ed., *Homogeneous Catalysis*, 1st ed. (Internet Version, Springer Science and Business, Dordrecht, The Netherlands, **2004**).
4. P. Kalck, C. Le Berre, P. Serp, *Coord. Chem. Rev.* **2020**, *402*, 213078 and references therein.
5. P. P. Power, *Nature* **2010**, *463*, 171–177.
6. P. Jutzi, *Angew. Chem. Int. Ed. Engl.* **1975**, *14*, 232–245.
7. P. J. Davidson, M. F. Lappert, *J. Chem. Soc., Chem. Commun.* **1973**, 317a.
8. A. G. Brook, F. Abdesaken, B. Gutekunst, G. Gutekunst, R. K. Kallury, *J. Chem. Soc., Chem. Commun.* **1981**, 191–192.
9. a) R. West, M. J. Fink, J. Michl, *Science* **1981**, *214*, 1343–1344; b) M. J. Fink, M. J. Michalczyk, K. J. Haller, R. West, J. Michl, *J. Chem. Soc., Chem. Commun.* **1983**, 1010–1011.
10. M. Yoshifuji, I. Shima, N. Inamoto, K. Hirotsu, T. Higuchi, *J. Am. Chem. Soc.* **1981**, *103*, 4587–4589.
11. J.-E. Siewert, A. Schumann, C. Hering-Junghans, *Dalton Trans.* **2021**, *50*, 15111–15117.
12. P. Jutzi, D. Kanne, C. Krüger, *Angew. Chem. Int. Ed. Engl.* **1986**, *25*, 164.
13. D. J. Liptrot, P. P. Power, *Nat. Rev. Chem.* **2017**, *1*, 0004.

14. F. S. Kipping, J. E. Sands, *J. Chem. Soc., Trans.* **1921**, 119, 830–847.
15. a) A. G. Moiseev, W. J. Leigh, *Organometallics* **2007**, 26, 6268–6276; b) A. G. Moiseev, W. J. Leigh, *Organometallics* **2007**, 26, 6277–6289.
16. R. C. Fischer, P. P. Power, *Chem. Rev.* **2010**, 110, 3877–3923.
17. H. B. Wedler, P. Wendelboe, P. P. Power, *Organometallics* **2018**, 37, 2929–2936.
18. a) M. Driess, H. Grützmacher, *Angew. Chem. Int. Ed. Engl.* **1996**, 35, 828–856 and references therein; b) Y. Apeloig, R. Pauncz, M. Karni, R. West, W. Steiner, D. Chapman, *Organometallics* **2003**, 22, 3250–3256.
19. S. Fujimori, S. Inoue, *Eur. J. Inorg. Chem.* **2020**, 3131–3142.
20. a) R. Fornari, *Handbook of Crystal Growth: Thin Films and Epitaxy*; T. Kauch, Ed.; Elsevier B. V.; Amsterdam, The Netherlands, **2015**, 3, 1–49; b) H. Ibach, H. Lüth, eds., *Solid-State Physics: An Introduction to Principles for Materials Science*, 4th ed. (Internet Version, Springer-Verlag Berlin, Heidelberg, **2009**).
21. a) L. Andrews, X. Wang, *J. Phys. Chem. A* **2002**, 106, 7696–7702; b) X. Wang, L. Andrews, G. P. Kushto, *J. Phys. Chem. A* **2002**, 106, 5809–5816.
22. E. Rivard, *Dalton Trans.* **2014**, 43, 8577–8586.
23. M. J. S. Gynane, D. H. Harris, M. F. Lappert, P. P. Power, P. Rivière, M. Rivière-Baudet, *J. Chem. Soc., Dalton Trans.* **1977**, 2004–2009.
24. a) V. Nesterov, D. Reiter, P. Bag, P. Frisch, R. Holtzner, A. Porzelt, S. Inoue, *Chem. Rev.* **2018**, 118, 9678–9842; b) M. Melaimi, R. Jazzar, M. Soleilhavoup, G. Bertrand, *Angew. Chem. Int. Ed.* **2017**, 56, 10046–10068.

25. a) Y. Wang, Y. Xie, P. Wei, R. B. King, H. F. Schaefer III, P. v. R. Schleyer, G. H. Robinson, *Science* **2008**, *321*, 1069–1071; b) A. Sidiropoulos, C. Jones, A. Stasch, S. Klein, G. Frenking, *Angew. Chem. Int. Ed.* **2009**, *48*, 9701–9704.
26. C. Jones, *Nat. Rev. Chem.* **2017**, *1*, 0059.
27. a) S. Yao, Y. Xiong, A. Saddington, M. Driess, *Chem. Commun.* **2021**, *57*, 10139–10153 and references therein; b) J. Xu, S. Pan, S. Yao, G. Frenking, M. Driess, *Angew. Chem. Int. Ed.* **2022**, e202209442.
28. M. Denk, R. Lennon, R. Hayashi, R. West, A. V. Belyakov, H. P. Verne, A. Haaland, M. Wagner, N. Metzler, *J. Am. Chem. Soc.* **1994**, *116*, 2691–2692.
29. a) R. S. Ghadwal, H. W. Roesky, S. Merkel, J. Henn, D. Stalke, *Angew. Chem. Int. Ed.* **2009**, *48*, 5683–5686; b) A. C. Filippou, O. Chernov, G. Schnakenburg, *Angew. Chem. Int. Ed.* **2009**, *48*, 5687–5690; c) M. M. D. Roy, S. R. Baird, E. Dornsiepen, L. A. Paul, L. Miao, M. J. Ferguson, Y. Zhou, I. Siewert, E. Rivard, *Chem. Eur. J.* **2021**, *27*, 8572–8579.
30. a) F. Meyer-Wegner, A. Nadj, M. Bolte, N. Auner, M. Wagner, M. C. Holthausen, H.-W. Lerner, *Chem. Eur. J.* **2011**, *17*, 4715–4719; b) J. I. Schweizer, A. G. Sturm, T. Porsch, M. Berger, M. Bolte, N. Auner, M. C. Holthausen, *Z. Anorg. Allg. Chem.* **2018**, *644*, 982–988; c) R. S. Ghadwal, K. Pröpper, B. Dittrich, P. G. Jones, H. W. Roesky, *Inorg. Chem.* **2011**, *50*, 358–364.
31. M. M. D. Roy, A. A. Omaña, A. S. S. Wilson, M. S. Hill, S. Aldridge, E. Rivard, *Chem. Rev.* **2021**, *121*, 12784–12965.

32. S. M. I. Al-Rafia, A. C. Malcolm, R. McDonald, M. J. Ferguson, E. Rivard, *Chem. Commun.* **2012**, 48, 1308–1310.
33. S. M. I. Al-Rafia, A. C. Malcolm, R. McDonald, M. J. Ferguson, E. Rivard, *Angew. Chem. Int. Ed.* **2011**, 50, 8354–8357.
34. a) A. V. Protchenko, K. H. Birj Kumar, D. Dange, A. D. Schwarz, D. Vidovic, C. Jones, N. Kaltsoyannis, P. Mountford, S. Aldridge, *J. Am. Chem. Soc.* **2012**, 134, 6500–6503; b) B. D. Reken, T. M. Brown, J. C. Fettinger, H. M. Tuononen, P. P. Power, *J. Am. Chem. Soc.* **2012**, 134, 6504–6507; c) D. Wendel, A. Porzelt, F. A. D. Herz, D. Sarkar, C. Jandl, S. Inoue, B. Rieger, *J. Am. Chem. Soc.* **2017**, 139, 8134–8137; d) R. Holzner, D. Reiter, P. Frisch, S. Inoue, *RSC Adv.* **2020**, 10, 3402–3406; e) A. V. Protchenko, A. D. Schwarz, M. P. Blake, C. Jones, N. Kaltsoyannis, P. Mountford, S. Aldridge, *Angew. Chem. Int. Ed.* **2013**, 52, 568–571.
35. a) A. Meltzer, S. Inoue, C. Präsang, M. Driess, *J. Am. Chem. Soc.* **2010**, 132, 3038–3046; b) M. Y. Abraham, Y. Wang, Y. Xie, P. Wei, H. F. Schaefer III, P. v. R. Schleyer, G. H. Robinson, *J. Am. Chem. Soc.* **2011**, 133, 8874–8876; c) M. Stoelzel, C. Präsang, S. Inoue, S. Enthaler, M. Driess, *Angew. Chem. Int. Ed.* **2012**, 51, 399–403.
36. a) Y. Ding, H. Hao, H. W. Roesky, M. Noltemeyer, H.-G. Schmidt, *Organometallics* **2001**, 20, 4806–4811; b) L. W. Pineda, V. Jancik, K. Starke, R. B. Oswald, H. W. Roesky, H. W. *Angew. Chem. Int. Ed.* **2006**, 45, 2602–2605; c) Y. Peng, J.-D. Guo, B. D. Ellis, Z. Zhu, J. C. Fettinger, S. Nagase, P. P. Power, *J. Am. Chem. Soc.* **2009**, 131, 16272–16282; d) S. M. I. Al-Rafia, P. A. Lummis, M. J. Ferguson, R. McDonald, E. Rivard, *Inorg. Chem.* **2010**, 49, 9709–9717; e) S. K. Liew, S. M. I. Al-Rafia, J. T.

Goettel, P. A. Lummis, S. M. McDonald, L. J. Miedema, M. J. Ferguson, R. McDonald, E. Rivard, *Inorg. Chem.* **2012**, *51*, 5471–5480; f) M. W. Lui, C. Merten, M. J. Ferguson, R. McDonald, Y. Xu, E. Rivard, *Inorg. Chem.* **2015**, *54*, 2040–2049; g) T. J. Hadlington, B. Schwarze, E. I. Izgorodina, C. Jones, *Chem. Commun.* **2015**, *51*, 6854–6857; h) C. Hering-Junghans, P. Andreiuk, M. J. Ferguson, R. McDonald, E. Rivard, *Angew. Chem. Int. Ed.* **2017**, *56*, 6272–6275; i) J. Tremmel, J. Tydlitát, L. Dostál, A. Ružička, X. Deraet, J. Turek, R. Jambor, *Chem. Eur. J.* **2020**, *26*, 6070–6075.

37. J. Sinclair, W. Medroa del Pino, K. Aku-Dominguez, Y. Minami, A. Kiran, M. J. Ferguson, M. Yasuda, E. Rivard, *Dalton Trans.* **2021**, *51*, 17688–17696.

38. J. Schneider, C. P. Sindlinger, K. Eichele, H. Schubert, L. Wesemann, *J. Am. Chem. Soc.* **2017**, *139*, 6542–6545.

39. a) R. Rodriguez, Y. Contie, R. Nougúé, A. Baceiredo, N. Saffon-Merceron, J. M. Sotiropoulos, T. Kato, T. *Angew. Chem. Int. Ed.* **2016**, *55*, 14355–14358; b) R. Rodriguez, D. Gau, Y. Contie, T. Kato, N. Saffon-Merceron, A. Baceiredo, *Angew. Chem. Int. Ed.* **2011**, *50*, 11492–11495.

40. a) L. Zhao, M. Hermann, C. Jones, G. Frenking, *Chem. Eur. J.* **2016**, *22*, 11728–11735; b) T. J. Hadlington, M. Hermann, G. Frenking, C. Jones, *Chem. Sci.* **2015**, *6*, 7249–7257.

41. T. J. Hadlington, M. Hermann, G. Frenking, C. Jones, *J. Am. Chem. Soc.* **2014**, *136*, 3028–3031.

42. J. Li, C. Schenk, C. Goedecke, G. Frenking, C. Jones, *J. Am. Chem. Soc.* **2011**, *133*, 18622–18625.

43. T. J. Hadlington, M. Hermann, J. Li, G. Frenking, C. Jones, *Angew. Chem. Int. Ed.* **2013**, *52*, 10199–10203.
44. J. Schneider, C. P. Sindlinger, S. M. Freitag, H. Schubert, L. Wesemann, *Angew. Chem. Int. Ed.* **2017**, *56*, 333–337.
45. a) B.-X. Leong, J. Lee, Y. Li, M.-C. Yang, C.-K. Siu, M.-D. Su, C.-W. So, *J. Am. Chem. Soc.* **2019**, *141*, 17629–17636; b) V. S. V. S. N. Swamy, M. K. Bisai, T. Das, S. S. Sen, *Chem. Commun.* **2017**, *53*, 6910–6913.
46. For selected articles on molecular frustrated Lewis pairs (FLPs), see: a) D. W. Stephan, G. Erker, *Angew. Chem. Int. Ed.* **2010**, *49*, 46–76; b) D. W. Stephan, G. Erker, *Angew. Chem. Int. Ed.* **2015**, *54*, 6400–6441; c) D. W. Stephan, *Science* **2016**, *354*, aaf7229; d) F.-G. Fontaine, D. W. Stephan, *Phil. Trans. R. Soc. A.* **2017**, *375*, 20170004; e) D. W. Stephan, *J. Am. Chem. Soc.* **2021**, *143*, 20002–20014 and references therein.
47. G. C. Welch, R. R. San Juan, J. D. Masuda, D. W. Stephan, *Science* **2006**, *314*, 1124–1126.
48. a) W. E. Piers, T. Chivers, *Chem. Soc. Rev.* **1997**, *26*, 345–354; b) G. Erker, *Dalton Trans.* **2005**, 1883–1890; c) J. R. Lawson, R. L. Melen, *Inorg. Chem.* **2017**, *56*, 8627–8643.
49. For selected articles on one-electron transfer involving FLPs: a) L. L. Liu, L. L. Cao, Y. Shao, G. Ménard, D. W. Stephan, *Chem.* **2017**, *3*, 259–267; b) F. Holtrop, A. R. Jupp, B. J. Kooij, N. P. van Leest, B. de Bruin, J. C. Slootweg, *Angew. Chem. Int. Ed.* **2020**, *59*, 22210–22216; c) F. Holtrop, A. R. Jupp, N. P. Van Leest, M. Paradiz

Dominguez, R. M. Williams, A. M. Brouwer, B. De Bruin, A. W. Ehlers, J. C. Slootweg, *Chem. Eur. J.* **2020**, *26*, 9005–9011; d) Y. Soltani, A. Dasgupta, T. A. Gazis, D. M. C. Ould, E. Richards, B. Slater, K. Stefkova, V. Y. Vladimirov, L. C. Wilkins, D. Wilcox, R. L. Melen, *Cell Rep. Phys. Chem.* **2020**, *1*, 10016; e) A. Dasgupta, E. Richards, R. L. Melen, *Angew. Chem. Int. Ed.* **2021**, *60*, 53–65; f) A. Merk, H. Großekappenberg, M. Schmidtman, M.-P. Luecke, C. Lorent, M. Driess, M. Oestreich, H. F. T. Klare, T. Müller, *Angew. Chem. Int. Ed.* **2018**, *57*, 15267–15271.

50. a) M. Wang, F. Nudelman, R. R. Matthes, M. P. Shaver, *J. Am. Chem. Soc.* **2017**, *139*, 14232–14236; b) L. Chen, R. Liu, Q. Yan, *Angew. Chem. Int. Ed.* **2018**, *57*, 9336–9340; c) L. Chen, R. Liu, X. Hao, Q. Yan, *Angew. Chem. Int. Ed.* **2019**, *58*, 264–268; d) U. Yolsal, M. Wang, J. R. Royer, M. P. Shaver, *Macromolecules* **2019**, *52*, 3417–3425; e) B. Adelizzi, P. Chidchob, N. Tanaka, B. A. G. Lamers, S. C. J. Meskers, S. Ogi, A. R. A. Palmans, S. Yamaguchi, E. W. Meijer, *J. Am. Chem. Soc.* **2020**, *142*, 16681–16689; f) U. Yolsal, T. A. R. Horton, M. Wang, M. P. Shaver, *J. Am. Chem. Soc.* **2021**, *143*, 12980–12984; g) T. A. R. Horton, M. Wang, M. P. Shaver, *Chem. Sci.* **2022**, *13*, 3845–3850.

51. For selected articles on FLP-containing nanomaterials: a) J. L. Fiorio, R. V. Gonçalves, E. Teixeira-Neto, M. A. Ortuño, N. López, L. M. Rossi, *ACS Catal.* **2018**, *8*, 3516–3524; b) K. Mentoer, L. Twigge, J. W. H. Niemantsverdriet, J. C. Swarts, E. Erasmus, *Inorg. Chem.* **2021**, *60*, 55–69; c) A. Palazzolo, S. Carencio, *Chem. Mater.* **2021**, *33*, 7914–7922. For selected articles on surface-bound FLPs: d) H. Lee, Y. M. Choi, D.-W. Lim, M. M. Rahman, Y.-I. Kim, I. H. Cho, H. W. Kang, J.-H. Seo, C. Jeon,

K. B. Yoon, *Angew. Chem. Int. Ed.* **2015**, *54*, 13080–13084; e) K. C. Szeto, W. Sahyoun, N. Merle, J. L. Castelbou, N. Popoff, F. Lefebvre, J. Raynaud, C. Godard, C. Claver, L. Delevoye, R. M. Gauvin, M. Taoufik, *Catal. Sci. Technol.* **2016**, *6*, 882–889; f) J.-Y. Xing, J.-C. Buffet, N. H. Rees, P. Nørby, D. O’Hare, *Chem. Commun.* **2016**, *52*, 10478–10481; g) J. L. Fiorio, N. López, L. M. Rossi, *ACS Catal.* **2017**, *7*, 2973–2980.

52. a) J. Bauer, H. Braunschweig, R. D. Dewhurst, K. Radacki, *Chem. Eur. J.* **2013**, *19*, 8797–8805; b) Y. Jiang, O. Blacque, T. Fox, H. Berke, *J. Am. Chem. Soc.* **2013**, *135*, 7751–7760; c) S. J. K. Forrest, J. Clifton, N. Fey, P. G. Pringle, H. A. Sparkes, D. F. Wass, *Angew. Chem. Int. Ed.* **2015**, *54*, 2223–2227; d) J. Campos, *J. Am. Chem. Soc.* **2017**, *139*, 2944–2947; e) N. Hidalgo, J. J. Moreno, M. Pérez-Jiménez, C. Maya, J. López-Serrano, J. Campos, *Organometallics* **2020**, *39*, 2534–3544; f) N. Hidalgo, J. J. Moreno, M. Pérez-Jiménez, C. Maya, J. López-Serrano, J. Campos, *Chem. Eur. J.* **2020**, *26*, 5982–5993; g) H. Tinnermann, C. Fraser, R. D. Young, *Dalton Trans.* **2020**, *49*, 15184–15189; h) E. S. Osipova, E. S. Gulyaeva, E. I. Gutsul, V. A. Kirkina, A. A. Pavlov, Y. V. Nelyubina, A. Rossin, M. Peruzzini, L. M. Epstein, N. V. Belkova, O. A. Filippov, E. S. Shubina, *Chem. Sci.* **2021**, *12*, 3682–3692.

53. X. Sun, W. Su, K. Shi, Z. Xie, C. Zhu, *Chem. Eur. J.* **2020**, *26*, 5354–5359.

54. a) J. T. O’Brien, E. R. Williams, *J. Phys. Chem. A.* **2011**, *115*, 14612–14619; b) H. Ohtaki, T. Radnai, *Chem. Rev.* **1993**, *93*, 1157–1204.

55. a) T. V. O’Halloran, *Science* **1993**, *261*, 715–725; b) A. M. Pyle, *J. Biol. Inorg. Chem.* **2002**, *7*, 679–690.

56. a) R. W. Schaeffer, B. C. Chan, S. R. Marshall, B. Blasiolo, N. Khan, K. L. Yoder, M. E. Trainer, C. H. Yoder, *J. Chem. Educ.* **2000**, *77*, 509–510; b) R. Barlag, F. Nyasulu, *J. Chem. Educ.* **2011**, *88*, 643–645.
57. A. Staubitz, A. P. M. Robertson, M. E. Sloan, I. Manners, *Chem. Rev.* **2010**, *110*, 4023–4078 and references therein.
58. E. Vedejs, *Science* **1980**, *207*, 42–44.
59. H. C. Brown, H. I. Schlesinger, S. Z. Cardon, *J. Am. Chem. Soc.* **1942**, *64*, 325–329.
60. G. Wittig, E. Benz, *Chem. Ber.* **1959**, *92*, 1999–2013.
61. a) D. J. Parks, W. E. Piers, *J. Am. Chem. Soc.* **1996**, *118*, 9440–9441; b) S. Rendler, M. Oestreich, *Angew. Chem. Int. Ed.* **2008**, *47*, 5997–6000.
62. J. R. Rumble, ed., *CRC Handbook of Chemistry and Physics*, 100th ed. (Internet Version, CRC Press/Taylor & Francis, Boca Raton, Florida, **2019**).
63. a) A. Moroz, R. L. Sweany, *Inorg. Chem.* **1992**, *31*, 5236–5242; b) H.-J. Himmel, J. Vollet, *Organometallics* **2002**, *21*, 5972–9577; c) Z. L. Xiao, R. H. Hauge, J. L. Margrave, *Inorg. Chem.* **1993**, *32*, 642–646.
64. A. J. M. Miller, J. E. Bercaw, *Chem. Commun.* **2010**, *46*, 1709–1711.
65. G. R. Whittell, E. I. Balmond, A. P. M. Robertson, S. K. Patra, M. F. Haddow, I. Manners, *Eur. J. Inorg. Chem.* **2010**, 3967–3975.
66. D. W. Stephan, G. Erker, *Angew. Chem. Int. Ed.* **2009**, *49*, 46–76.
67. C. Appelt, J. C. Slootweg, K. Lammertsma, W. Uhl, *Angew. Chem. Int. Ed.* **2013**, *52*, 4256–4259.

68. Z. Mo, A. Rit, J. Campos, E. L. Kolychev, S. Aldridge, *J. Am. Chem. Soc.* **2016**, *138*, 3306–3309.
69. M. Boudjelel, E. D. Sosa-Carrizo, S. Mallet-Ladeira, S. Massou, K. Miqueu, G. Bouhadir, D. Bourissou, *ACS Catal.* **2018**, *8*, 4459–4464.
70. C. P. Sindlinger, F. S. W. Aicher, H. Schubert, L. Wesemann, *Angew. Chem. Int. Ed.* **2017**, *56*, 2198–2202.
71. S. Li, G. Li, W. Meng, H. Du, *J. Am. Chem. Soc.* **2016**, *138*, 12956–12962.
72. N. Kumar, J. Rani, R. Kurchania, *Mater. Today: Proc.* **2021**, *46*, 5570–5574.
73. a) H. Min, D. Y. Lee, J. Kim, G. Kim, K. S. Lee, J. Kim, M. J. Paik, Y. K. Kim, K. S. Kim, M. G. Kim, T. J. Shin, S. Il Seok, *Nature* **2021**, *598*, 444–450; b) National Renewable Energy Laboratory Energy Efficiencies Chart (as of August 2022): <https://www.nrel.gov/pv/assets/pdfs/best-research-cell-efficiencies-rev220630.pdf>
74. a) J. Czochralski, *Z. Phys. Chem.* **1918**, *92*, 219–221; b) J. Evers, P. Klüfers, R. Staudigl, P. Stallhofer, *Angew. Chem. Int. Ed.* **2003**, *42*, 5684–5698.
75. U. J. Gibson, L. Wei, J. Ballato, *Nat. Commun.* **2021**, *12*, 3990.
76. L. Sun, G. Yuan, L. Gao, J. Yang, M. Chhowalla, M. H. Gharahcheshmeh, K. K. Gleason, Y. S. Choi, B. H. Hong, Z. Liu, *Nat. Rev. Methods Primers* **2021**, *1*, 5.
77. R. Gordon, *J. Non-Cryst. Solids* **1997**, *218*, 81–91.
78. a) J. Bloem, W. A. P. Claassen, W. G. J. N. Valkenburg, *J. Cryst. Growth* **1982**, *57*, 177–184; b) R. C. Taylor, B. A. Scott, S.-T. Lin, F. LeGoues, J. C. Tsang, *MRS Online Proceedings Library* **1986**, *77*, 709–714; c) W. A. P. Claassen, J. Bloem, *J. Cryst.*

Growth **1980**, *50*, 807–815; d) Y. Ron, A. Raveh, U. Carmi, A. Inspektor, A. Avni, *Thin Solid Films* **1983**, *107*, 181–189.

79. a) K. Toshikawa, A. Yokotani, K. Kurosawa, *Jpn. J. Appl. Phys.* **2005**, *44*, 7785–7788; b) D. E. Carlson, C. R. Wronski, *Appl. Phys. Lett.* **1976**, *28*, 671–673; c) N. Herlin, M. Lefebvre, M. Péalat, J. Perrin, *J. Phys. Chem.* **1992**, *96*, 7063–7072; d) S. M. Han, E. S. Aydil, *J. Vac. Sci. Technol.* **1996**, *14*, 2062–2070; e) R. Kakkad, J. Smith, W. S. Lau, S. J. Fonash, R. Kerns, *J. Appl. Phys.* **1989**, *65*, 2069–2072.

80. Y. Mishima, M. Hirose, Y. Osaka, K. Nagamine, Y. Ashida, N. Kitagawa, K. Isogaya, *Jpn. J. Appl. Phys.* **1983**, *22*, L46–L48.

81. a) H. Kanoh, O. Sugaira, M. Matsumura, *Jpn. J. Appl. Phys.* **1993**, *32*, 2613–2619; b) T. Shimoda, Y. Matsuki, M. Furusawa, T. Aoki, I. Yudasaka, H. Tanaka, H. Iwasawa, D. Wang, M. Miyasaka, Y. Takeuchi, *Nature* **2006**, *440*, 783–786; c) M. Gerwig, A. S. Ali, D. Neubert, S. Polster, U. Böhme, G. Franze, M. Rosenkranz, A. Popov, I. Ponomarev, M. P. M. Jank, C. Viehweger, E. Brendler, L. Frey, P. Kroll, E. Kroke, *Adv. Electron. Mater.* **2021**, *7*, 2000422; d) M. Gerwig, U. Böhme, M. Friebe, F. Gründler, G. Franze, M. Rosenkranz, H. Schmidt, E. Kroke, *ChemistryOpen* **2020**, *9*, 762–773 and references therein; e) G. R. S. Iyer, E. K. Hobbie, S. Guruvenket, J. M. Hoey, K. J. Anderson, J. Lovaasen, C. Gette, D. L. Schulz, O. F. Swenson, A. Elangovan, P. Boudjouk, *ACS Appl. Mater. Interfaces* **2012**, *4*, 2680–2685.

82. a) A. Grill, V. Patel, *J. Appl. Phys.* **1999**, *85*, 3314–3318; b) S. Guruvenket, S. Andrie, M. Simon, K. W. Johnson, R. A. Sailer, *Plasma Process. Polym.* **2011**, *8*, 1126–1136; c) J. Dahlhaus, P. Jutzi, H.-J. Frenck, W. Kulisch, *Adv. Mater.* **1993**, *5*, 377–380;

- d) A. Klipp, F. Hamelmann, G. Haindl, J. Hartwich, U. Kleineberg, P. Jutzi, U. Heinzmann, *Chem. Vap. Deposition* **2000**, *6*, 63–66; e) A. Klipp, S. H. A. Petri, B. Neumann, H.-G. Stammler, P. Jutzi, *J. Organomet. Chem.* **2001**, *620*, 20–31.
83. K. Fujino, Y. Nishimoto, N. Tokumasu, K. Maeda, *J. Electrochem. Soc.* **1990**, *137*, 2883–2887.
84. a) H. G. Pryce Lewis, T. B. Casserly, K. K. Gleason, *J. Electrochem. Soc.* **2001**, *148*, F212–F220; b) V. Raballand, J. Benedikt, S. Hoffmann, M. Zimmermann, A. von Keudell, *J. Appl. Phys.* **2009**, *105*, 083304.
85. a) C. Winkler, *J. Prakt. Chem.* **1887**, *36*, 177–209; b) E. Voegelen, *Z. Anorg. Chem.* **1902**, *30*, 325–330.
86. a) H. Ishii, Y. Takahashi, *J. Electrochem. Sci.* **1988**, *135*, 1539–1543; b) D. T. Restrepo, K. E. Lynch, K. Giesler, S. M. Kuebler, R. G. Blair, *Mater. Res. Bull.* **2012**, *47*, 3484–3488; c) J.-S. Park, M. Curtin, C. Major, S. Bengtson, M. Carroll, A. Lochtefeld, *Electrochem. Solid-State Lett.* **2007**, *10*, H313–H316; d) J. Satgé, M. Massol, P. Rivière, *J. Organomet. Chem.* **1973**, *56*, 1–39; e) G. Jonkers, S. M. Van der Kerk, C. A. De Lange, *Chem. Phys.* **1982**, *70*, 69–75.
87. a) E. Muthuswamy, A. S. Iskandar, M. M. Amador, S. M. Kauzlarich, *Chem. Mater.* **2013**, *25*, 1416–1422; b) K. Tabatabaei, A. L. Holmes, K. A. Newton, E. Muthuswamy, R. Sfadia, S. A. Carter, S. M. Kauzlarich, *Chem. Mater.* **2019**, *31*, 7510–7521.
88. a) Z. Meng, Z. Jin, B. A. Gururaj, P. Chu, H. S. Kwok, M. Wong, *J. Electrochem. Soc.* **1997**, *144*, 1423–1429; b) V. Sorianello, L. Colace, N. Armani, F. Rossi, C. Ferrari, C. Lazzarini, L. Lazzarini, G. Assanto, *Opt. Mater. Express* **2011**, *1*, 856–865; c) G.

- Dushaq, M. Rasras, A. Nayfeh, *Thin Solid Films* **2017**, *636*, 585–592; d) F. Gencarelli, B. Vincent, L. Souriau, O. Richard, W. Vandervorst, R. Loo, M. Caymax, M. Heyns, *Thin Solid Films* **2012**, *520*, 3211–3215; e) J. Pola, J. P. Parsons, R. Taylor, *J. Chem. Soc., Faraday Trans.* **1992**, *88*, 1637–1641.
89. a) M. Jakoubová, Z. Bastl, P. Fiedler, J. Pola, *Infrared. Phys. Technol.* **1994**, *35*, 633–635; b) J. E. Boucham, F. Maury, R. Morancho, *J. Anal. Appl. Pyrol.* **1997**, *44*, 153–165; c) P. G. Harrison, C. de Cointet, D. Ograb, D. M. Podesta, *Chem. Mater.* **1994**, *6*, 1620–1626; d) K. Suda, T. Kijima, S. Ishihara, N. Sawamoto, H. Machida, M. Ishikawa, H. Sudoh, Y. Ohsita, A. Ogura, *ECS J. Solid State Sci. Technol.* **2015**, *4*, P152–P154; e) R. Fritzsche, D. R. Zahn, M. Mehring, *J. Mater. Sci.* **2021**, *56*, 9274–9286; f) K. Ditmar, P. Jutzi, J. Schmalhorst, G. Reiss, *Chem. Vap. Deposition* **2001**, *7*, 193–195; g) J. E. Taylor, T. S. Milazzo, *J. Phys. Chem.* **1978**, *82*, 847–852.
90. J. Sinclair, G. Dai, R. McDonald, M. J. Ferguson, A. Brown, E. Rivard, *Inorg. Chem.* **2020**, *59*, 10996–11008.
91. a) E. M. Leitao, T. Jurca, I. Manners, *Nat. Chem.* **2013**, *5*, 817–829 and references therein; b) T. M. Douglas, A. B. Chaplin, A. S. Weller, *J. Am. Chem. Soc.* **2018**, *130*, 14432–14433.
92. Y. Zhang, M. A. Hopkins, D. J. Liptrot, H. Khanbareh, P. Groen, X. Zhou, D. Zhang, Y. Bao, K. Zhou, C. R. Bowen, D. R. Carbery, *Angew. Chem. Int. Ed.* **2020**, *59*, 7808–7812.
93. a) W. Luo, P. G. Campbell, L. N. Zakharov, S.-Y. Liu, *J. Am. Chem. Soc.* **2011**, *133*, 19326–19329; b) C. W. Yoon, L. G. Sneddon, *J. Am. Chem. Soc.* **2006**, *128*,

13992–13993; c) W. Luo, L. N. Zakharov, S.-Y. Liu, *J. Am. Chem. Soc.* **2011**, *133*, 13006–13009; d) G. Chen, L. N. Zakharov, M. E. Bowden, A. J. Karkamkar, S. M. Whittemore, E. B. III, Garner, T. C. Mikulas, D. A. Dixon, T. Autrey, S.-Y. Liu, *J. Am. Chem. Soc.* **2015**, *137*, 134–137; e) Y. Dai, X. Zhang, Y. Liu, H. Yu, W. Su, J. Zhou, Q. Ye, Z. Huang, *J. Am. Chem. Soc.* **2022**, *144*, 8434–8438.

94. a) C. A. Jaska, K. Temple, I. Manners, *Chem. Commun.* **2001**, 962–963; b) C. A. Jaska, K. Temple, I. Manners, *J. Am. Chem. Soc.* **2003**, *125*, 9424–9434; c) C. A. Jaska, I. Manners, *J. Am. Chem. Soc.* **2004**, *126*, 9776–9785; d) M. C. Denney, V. Pons, T. J. Hebden, D. M. Heinekey, K. I. Goldberg, *J. Am. Chem. Soc.* **2006**, *128*, 12048–12049; e) A. Staubitz, A. P. Soto, I. Manners, *Angew. Chem. Int. Ed.* **2008**, *47*, 6212–6215; f) A. Staubitz, M. E. Sloan, A. P. M. Robertson, A. Friedrich, S. Schneider, P. J. Gates, J. R. Schmedt auf der Günne, I. Manners, *J. Am. Chem. Soc.* **2010**, *132*, 13332–13345.

95. A. P. M. Robertson, E. M. Leitao, I. Manners, *J. Am. Chem. Soc.* **2011**, *133*, 19322–19325.

96. a) C. A. De Albuquerque Pinheiro, C. Roiland, P. Jehan, G. Alcaraz, *Angew. Chem. Int. Ed.* **2018**, *57*, 1519–1522; b) A. Staubitz, *Angew. Chem. Int. Ed.* **2018**, *57*, 5990–5992.

97. a) A. Paul, C. B. Musgrave, *Angew. Chem. Int. Ed.* **2007**, *46*, 8153–8156; b) M. E. Sloan, A. Staubitz, T. J. Clark, C. A. Russell, G. C. Lloyd-Jones, I. Manners, *J. Am. Chem. Soc.* **2010**, *132*, 3831–3841; c) I. Göttker-Schnetmann, P. S. White, M. Brookhart, *Organometallics* **2004**, *23*, 1766–1776; d) Y. Luo, K. Ohno, *Organometallics* **2007**, *26*, 3597–3600.

98. C. N. Brodie, T. M. Boyd, L. Sotorríos, D. E. Ryan, E. Magee, S. Huband, J. S. Town, G. C. Lloyd-Jones, D. M. Haddleton, S. A. Macgregor, A. S. Weller, *J. Am. Chem. Soc.* **2021**, *143*, 21010–21023.
99. I. Amer, A. Van Reenen, T. Mokrani, *Mater. Sci.* **2016**, *22*, 381–389 and references therein.
100. V. A. Du, T. Jurca, G. R. Whittell, I. Manners, *Dalton Trans.* **2016**, *45*, 1055–1062.
101. S. Bernard, P. Miele, *Materials* **2014**, *7*, 7436–7459 and references therein.
102. a) P. B. Mirkarimi, K. F. McCarty, D. L. Medlin, *Mater. Sci. Eng.* **1997**, *R21*, 47–100 and references therein; b) A. V. Kurdyumov, V. L. Solozhenko, W. B. Zelyavski, *J. Appl. Cryst.* **1995**, *28*, 540–545.
103. Z. Zheng, M. Cox, B. Li, *J. Mater. Sci.* **2018**, *53*, 66–99 and references therein.
104. H. Pedersen, B. Alling, H. Högberg, A. Ektarawong, *J. Vac. Sci. Tech. A* **2019**, *37*, 040603.
105. A. Pakdel, Y. Bando, D. Golberg, *Chem. Soc. Rev.* **2014**, *43*, 934–959.
106. R. Riedel, *Adv. Mater.* **1994**, *6*, 549–560.
107. F. P. Bundy, W. A. Bassett, M. S. Weathers, R. J. Hemley, H. U. Mao, A. F. Concharov, *Carbon* **1996**, *34*, 141–153.
108. a) P. S. DeCarli, J. C. Jamieson, *Science* **1961**, *133*, 1821–1822; b) S. J. Turneaure, S. M. Sharma, T. J. Volz, J. M. Winey, Y. M. Gupta, *Sci. Adv.* **2017**, *3*, eaao3561.
109. N. Izyumskaya, D. O. Demchenko, S. Das, Ü. Özgür, V. Avrutin, H. Morkoç, *Adv. Electron. Mater.* **2017**, *3*, 1600485.

110. W. H. Balmain, *J. Prakt. Chem.* **1842**, 27, 422–430.
111. a) Z. Zhao, B. Xu, Y. Tian, *Annu. Rev. Mater. Res.* **2016**, 46, 383–406; b) Y. Tian, B. Xu, D. Yu, Y. Ma, Y. Wang, Y. Jiang, W. Hu, C. Tang, Y. Gao, K. Luo, Z. Zhao, L.-M. Wang, B. Wen, J. He, Z. Liu, *Nature* **2013**, 493, 385–388; c) R. T. Paine, C. K. Narula, *Chem. Rev.* **1990**, 90, 73–91; d) A.-K. Wolfrum, B. Matthey, A. Michaelis, M. Herrmann, *Materials* **2018**, 11, 255.
112. R. H. Wentorf, *J. Chem. Phys.* **1957**, 26, 956.
113. L. Vel, G. Demazeau, J. Etourneau, *Mater. Sci. Eng. B* **1991**, 10, 149–164.
114. a) M. Zastrow, *Nature* **2019**, 572, 429–432; b) T. Taniguchi, T. Teraji, S. Koizumi, K. Watanabe, S. Yameoka, *Jpn. J. Appl. Phys.* **2002**, 41, L109–L111; c) K. Watanabe, T. Taniguchi, H. Kanda, *Nat. Mater.* **2004**, 3, 404–409.
115. W. Zhang, I. Bello, Y. Lifshitz, K. M. Chan, X. Meng, Y. Wu, C. Y. Chan, S.-T. Lee, *Adv. Mater.* **2004**, 16, 1405–1408.
116. R. Dahal, J. Li, S. Majety, B. N. Pantha, X. K. Cao, J. Y. Lin, H. X. Jiang, *Appl. Phys. Lett.* **2011**, 98, 211110.
117. V. K. Gupta, C. C. Wamsley, M. W. Koch, G. W. Wicks, *J. Vac. Sci. Technol. B* **1999**, 17, 1246–1248.

Chapter 2

1. For recent advances and reviews, see: a) P. P. Power, *Nature* **2010**, 463, 171–177; b) R. Rodriguez, D. Gau, Y. Contie, T. Kato, N. Saffon-Merceron, A. Baceiredo, *Angew. Chem. Int. Ed.* **2011**, 50, 11492–11495; c) S. Yao, Y. Xiong, M. Driess, *Acc. Chem. Res.* **2017**, 50, 2026–2037; d) V. Nesterov, D. Reiter, P. Bag, P. Frisch, R. Holzner, A.

Porzelt, S. Inoue, *Chem. Rev.* **2018**, *118*, 9678–9842; e) J. Hicks, P. Vasko, J. M. Goicoechea, S. Aldridge, *Nature* **2018**, *557*, 92–95; f) R. Kobayashi, S. Ishida, T. Iwamoto, *Angew. Chem. Int. Ed.* **2019**, *58*, 9425–9428; g) M.-A. Légaré, M. Rang, G. Bélanger-Chabot, J. I. Schweizer, I. Krummenacher, R. Bertermann, M. Arrowsmith, M. C. Holthausen, H. Braunschweig, *Science* **2019**, *363*, 1329–1332; h) W. Lu, Y. Li, R. Kinjo, *J. Am. Chem. Soc.* **2019**, *141*, 5164–5168; i) K. M. Marczenko, J. A. Zurakowski, K. L. Bamford, J. W. M. MacMillan, S. S. Chitnis, *Angew. Chem. Int. Ed.* **2019**, *58*, 18096–18101; j) T. Sugahara, J.-D. Guo, D. Hashizume, T. Sasamori, N. Tokitoh, *J. Am. Chem. Soc.* **2019**, *141*, 2263–2267; k) S. Kurumada, S. Takamori, M. Yamashita, *Nat. Chem.* **2020**, *12*, 36–39; l) M. M. D. Roy, A. A. Omaña, A. S. S. Wilson, M. S. Hill, S. Aldridge, E. Rivard, *Chem. Rev.* **2021**, *121*, 12784–12965.

2. a) R. Dobrovetsky, D. W. Stephan, *J. Am. Chem. Soc.* **2013**, *135*, 4974–4977; b) D. W. Stephan, *Science* **2016**, *354*, aaf7229; c) J. Li, C. G. Daniliuc, G. Kehr, G. Erker, *Angew. Chem. Int. Ed.* **2019**, *58*, 6737–6741.

3. a) C. B. Caputo, L. J. Hounjet, R. Dobrovetsky, D.W. Stephan, *Science* **2013**, *341*, 1374–1377; b) M.-A. Légaré, M.-A. Courtemanche, É. Rochette, F.-G. Fontaine, *Science* **2015**, *349*, 513–516.

4. S. Bontemps, G. Bouhadir, K. Miqueu, D. Bourissou, *J. Am. Chem. Soc.* **2006**, *128*, 12056–12057.

5. For early studies on donor-acceptor (LB/LA) stabilization, see: a) T. J. Marks, *J. Am. Chem. Soc.* **1971**, *93*, 7090–7091; b) W. Petz, *Chem. Rev.* **1986**, *86*, 1019–1047; c) U. Vogel, A. Y. Timoshkin, M. Scheer, *Angew. Chem. Int. Ed.* **2001**, *40*, 4409–4412; d) P.

A. Rugar, M. C. Jennings, P. J. Ragona, K. M. Baines, *Organometallics* **2007**, *26*, 4109–4111; e) S. M. I. Al-Rafia, A. C. Malcolm, S. K. Liew, M. J. Ferguson, E. Rivard, *J. Am. Chem. Soc.* **2011**, *133*, 777–779; f) S. M. I. Al-Rafia, A. C. Malcolm, R. McDonald, M. J. Ferguson, E. Rivard, *Angew. Chem. Int. Ed.* **2011**, *50*, 8354–8357; g) A. K. Swarnakar, C. Hering-Junghans, K. Nagata, M. J. Ferguson, R. McDonald, N. Tokitoh, E. Rivard, *Angew. Chem. Int. Ed.* **2015**, *54*, 10666–10669; h) H. P. Hickox, Y. Wang, Y. Xie, P. Wei, H. F. Schaefer III, G. H. Robinson, *J. Am. Chem. Soc.* **2016**, *138*, 9799–9802.

6. a) T. K. Purkait, A. K. Swarnakar, G. B. De Los Reyes, F. A. Hegmann, E. Rivard, J. G. C. Veinot, *Nanoscale* **2015**, *7*, 2241–2244; b) A. K. Swarnakar, S. M. McDonald, K. C. Deutsch, P. Choi, M. J. Ferguson, R. McDonald, E. Rivard, *Inorg. Chem.*, **2014**, *53*, 8662–5671.

7. For selected studies on SiR₂ generation and complexation, see: a) H. Gilman, S. Gust Cottis, W. H. Atwell, *J. Am. Chem. Soc.* **1964**, *86*, 1596–1599; b) T. J. Drahnak, J. Michl, R. West, *J. Am. Chem. Soc.* **1979**, *101*, 5427–5428; c) D. H. Pae, M. Xiao, M. Y. Chiang, P. P. Gaspar, *J. Am. Chem. Soc.* **1991**, *113*, 1281–1288; d) H. Tobita, H. Kurita, H. Ogino, *Organometallics* **1998**, *17*, 2850–2856; e) R. Waterman, P. G. Hayes, T. D. Tilley, *Acc. Chem. Res.* **2007**, *40*, 712–719; f) A. Tahara, S. Nagino, Y. Sunada, R. Haige, H. Nagashima, *Organometallics* **2018**, *37*, 2531–2543.

8. a) S. Yajima, J. Hayashi, M. Omori, *Chem. Lett.* **1975**, *4*, 931–934; b) T. S. Radhakrishnan, *J. Appl. Polym. Sci.* **2006**, *99*, 2679–2686 and references therein.

9. M. W. P. Bebbington, S. Bontemps, G. Bouhadir, D. Bourissou, *Angew. Chem. Int. Ed.* **2017**, *46*, 3333–3336.
10. K. C. Thimer, S. M. I. Al-Rafia, M. J. Ferguson, R. McDonald, E. Rivard, *Chem. Commun.* **2009**, 7119–7121.
11. M. Walewska, J. Baumgartner, C. Marschner, *Chem. Commun.* **2015**, *51*, 276–278.
12. B. Rao, R. Kinjo, *Angew. Chem. Int. Ed.* **2019**, *58*, 18150–18153.
13. a) R. S. Ghadwal, R. Azhakar, H. W. Roesky, *Acc. Chem. Res.* **2013**, *46*, 444–456;
b) J. Teichmann, M. Wagner, *Chem. Commun.* **2018**, *54*, 1397–1412 and references therein.
14. S. M. I. Al-Rafia, A. C. Malcolm, R. McDonald, M. J. Ferguson, E. Rivard, *Chem. Commun.* **2012**, *48*, 1308–1310.
15. L. Zhu, J. Zhang, C. Cui, *Inorg. Chem.* **2019**, *58*, 12007–12010.
16. Y. Shao, D. Truhlar, *Theor. Chem. Acc.* **2008**, *120*, 215–241.
17. T. H. Dunning Jr., *J. Chem. Phys.* **1989**, *90*, 1007–1023.
18. NIST Chemistry Webbook. <http://webbook.nist.gov/chemistry/>
19. Oligosilanes also extrude H₂ upon strong UV-irradiation at room temperature to yield amorphous hydride-terminated Si: M. Haas, V. Christopoulos, J. Radebner, M. Holthausen, T. Lainer, L. Schuh, H. Fitzek, G. Kothleitner, A. Torvisco, R. Fischer, O. Wunnicke, H. Stueger, *Angew. Chem. Int. Ed.* **2017**, *56*, 14071–14074.
20. Similar surface oxidation of Ge nanofilms deposited from the precursor ImMe₂•GeH₂•BH₃ (ImMe₂ = (HCNMe₂)₂C:] was found. While the temperature of deposition (100 °C) was similar to that used in this Chapter, this approach could not be

- applied for the deposition of Si, nor could the donor- and acceptor-ligands involved be recycled: J. M. Sinclair, G. Dai, R. McDonald, M. J. Ferguson, A. Brown, E. Rivard, *Inorg. Chem.* **2020**, *59*, 10996–11008.
21. L. Armelao, D. Barreca, G. Bottaro, S. Gross, A. Gasparotto, C. Maragno, E. Tondello, A. Zattin, *Surf. Sci. Spect.* **2015**, *10*, 137–142.
22. D. Bermejo, M. Cardona, *J. Non-Cryst. Solids* **1979**, *32*, 405–419.
23. M. Wihl, M. Cardona, J. Tauc, *J. Non-Cryst. Solids* **1972**, *8*, 172–178.
24. R. L. C. Vink, G. T. Barkema, W. F. van der Weg, *Phys. Rev. B: Condens. Matter Phys.* **2001**, *63*, 115210.
25. J. P. Wesson, T. C. Williams, *J. Polym. Sci., Polym. Chem. Ed.* **1979**, *17*, 2833–2843.
26. A. L. Smith, *Spectrochim. Acta* **1960**, *16*, 87–105.
27. W. R. Schmidt, L. V. Interrante, R. H. Doremus, T. K. Trout, P. S. Marchetti, G. E. Maciel, *Chem. Mater.* **1991**, *3*, 257–267.
28. a) H. Kaji, F. Horii, *Macromolecules* **2007**, *40*, 5420–5423; b) K. Deller, B. Rieger, *RSC Adv.* **2015**, *5*, 87445–87455.
29. C. Zybill, D. L. Wilkinson, C. Leis, G. Müller, *Angew. Chem. Int. Ed. Engl.* **1989**, *28*, 203–205.
30. A. F. Burchat, M. J. Chong, N. Nielsen, *J. Org. Chem.* **1997**, *542*, 281–283.
31. J. C. DeMott, W. Gu, B. J., McCulloch, D. E. Herbert, M. D. Goshert, J. R. Walensky, J. Zhou, O. V. Ozerov, *Organometallics* **2015**, *34*, 3930–3933.

32. M. Sircoglou, Étude des modes de coordination des ligands ambiphiles PE (E = B, Al, Ga). Université Paul Sabatier: Toulouse, Doctoral Thesis **2009**.
33. E. Hupf, F. Kaiser, P. A. Lummis, M. M. D. Roy, R. McDonald, M. J. Ferguson, F. E. Kühn, E. Rivard, *Inorg. Chem.* **2020**, *59*, 1592–1601.
34. R. H. Blessing, *Acta. Cryst.* **1995**, *A51*, 33–38.
35. G. M. Sheldrick, *Acta. Cryst.* **2015**, *A71*, 3–8.
36. G. M. Sheldrick, *Acta. Cryst.* **2015**, *C71*, 3–8.

Chapter 3

1. Z. Zhao, B. Xu, Y. Tian, *Annu. Rev. Mater. Res.* **2016**, *46*, 383–406.
2. a) R. T. Paine, C. K. Narula, *Chem. Rev.* **1990**, *90*, 73–91; b) P. J. Fazen, J. S. Beck, A. T. Lynch, E. E. Remsen, L. G. Sneddon, *Chem. Mater.* **1990**, *2*, 96–97; c) D. J. Heldebrant, A. Karkamkar, N. J. Hess, M. Bowden, S. Rassat, F. Zheng, K. Rappe, T. Autrey, *Chem. Mater.* **2008**, *20*, 5332–5336; d) S. Frueh, R. Kellett, C. Mallery, T. Molter, W. S. Willis, C. King'onde, S. L. Suib, *Inorg. Chem.* **2011**, *50*, 783–792; e) D. Golberg, Y. Bando, C. C. Tang, C. Y. Zhi, *Adv. Mater.* **2007**, *19*, 2413–2432; f) X.-F. Jiang, Q. Weng, X.-B. Wang, X. Li, J. Zhang, D. Golberg, Y. Bando, *J. Mater. Sci. Tech.* **2015**, *31*, 589–598.
3. Y. Tian, B. Xu, D. Yu, Y. Ma, Y. Wang, Y. Jiang, W. Hu, C. Tang, Y. Gao, K. Luo, Z. Zhao, L.-M. Wang, B. Wen, J. He, Z. Liu, *Nature* **2013**, *493*, 385–388.
4. a) A. Staubitz, A. P. M. Robertson, I. Manners, *Chem. Rev.* **2010**, *110*, 4079–4124; b) Z. Mo, A. Rit, J. Campos, E. L. Kolychev, S. Aldridge, *J. Am. Chem. Soc.* **2016**, *138*, 3306–3309; c) D. A. Resendiz-Lara, G. R. Whittell, E. M. Leitao, I. Manners,

Macromolecules **2019**, *52*, 7052–7064; d) G. Zhang, D. Morrison, G. Bao, H. Yu, C. W. Yoon, T. Song, J. Lee, A. T. Ung, Z. Huang, *Angew. Chem. Int. Ed.* **2021**, *60*, 11725–11729.

5. a) E. R. Lory, R. F. Porter, *J. Am. Chem. Soc.* **1973**, *95*, 1766–1770; b) T. Kawashima, K. Kawaguchi, E. Hirota, *J. Chem. Phys.* **1987**, *87*, 6331–6333; c) C. A. Thompson, L. Andrews, *J. Am. Chem. Soc.* **1995**, *117*, 10125–10126; d) C. A. Thompson, L. Andrews, J. M. L. Martin, J. El-Yazal, *J. Phys. Chem.* **1995**, *99*, 13839–13849; e) F. Zhang, P. Maksyutenko, R. I. Kaiser, A. M. Mebel, A. Gregušová, S. A. Perera, R. J. Bartlett, *J. Phys. Chem. A* **2010**, *114*, 12148–12154.

6. For related work on unsaturated BN π -systems: a) P. Paetzold, *Pure Appl. Chem.* **1991**, *63*, 345–350; b) H. Nöth, *Angew. Chem. Int. Ed. Engl.* **1988**, *27*, 1603–1623; c) E. Rivard, W. A. Merrill, J. C. Fettinger, R. Wolf, G. H. Spikes, P. P. Power, *Inorg. Chem.* **2007**, *46*, 2971–2978; d) F. Dahcheh, D. Martin, D. W. Stephan, G. Bertrand, *Angew. Chem. Int. Ed.* **2014**, *53*, 13159–13163; e) T. Lorenz, M. Crumbach, T. Eckert, A. Lik, H. Helten, *Angew. Chem. Int. Ed.* **2017**, *56*, 2780–2784; f) M.-A. Légaré, G. Bélanger-Chabot, M. Rang, R. D. Dewhurst, I. Krummenacher, R. Bertermann, H. Braunschweig, *Nat. Chem.* **2020**, *12*, 1076–1080; g) R. Guo, T. Li, R. Wei, X. Zhang, Q. Li, L. L. Liu, C.-H. Tung, L. Kong, *J. Am. Chem. Soc.* **2021**, *143*, 13483–13488.

7. a) A. K. Swarnakar, C. Hering-Junghans, K. Nagata, M. J. Ferguson, R. McDonald, N. Tokitoh, E. Rivard, *Angew. Chem. Int. Ed.* **2015**, *54*, 10666–10669; b) A. K. Swarnakar, C. Hering-Junghans, M. J. Ferguson, R. McDonald, E. Rivard, *Chem. Sci.*

- 2017**, *8*, 2337–2343; c) M. R. Momeni, L. Shulman, E. Rivard, A. Brown, *Phys. Chem. Chem. Phys.* **2015**, *17*, 16525–16535.
8. a) D. W. Stephan, G. Erker, *Angew. Chem. Int. Ed.* **2010**, *49*, 46–76. For FLP chelation and their use in bond activation processes, see: b) S. Bontemps, G. Bouhadir, K. Miqueu, D. Bourissou, *J. Am. Chem. Soc.* **2006**, *128*, 12056–12057; c) C. Appelt, H. Westenberg, F. Bertini, A. W. Ehlers, J. C. Slootweg, K. Lammertsma, W. Uhl, *Angew. Chem. Int. Ed.* **2011**, *50*, 3925–3928; d) M.-A. Légaré, M. A. Courtemanche, É. Rochette, F.-G. Fontaine, *Science* **2015**, *349*, 513–516; e) D. H. A. Boom, E. J. J. de Boed, E. Nicolas, M. Nieger, A. W. Ehlers, A. R. Jupp, J. C. Slootweg, *Z. Anorg. Allg. Chem.* **2020**, *646*, 586–592.
9. A. A. Omaña, R. K. Green, R. Kobayashi, Y. He, E. R. Antoniuk, M. J. Ferguson, Y. Zhou, J. G. C. Veinot, T. Iwamoto, A. Brown, E. Rivard, *Angew. Chem. Int. Ed.* **2021**, *60*, 228–231.
10. M. M. D. Roy, A. A. Omaña, A. S. S. Wilson, M. S. Hill, S. Aldridge, E. Rivard, *Chem. Rev.* **2021**, *121*, 12784–12965.
11. B. L. Frenette, A. A. Omaña, M. J. Ferguson, Y. Zhou, E. Rivard. *Chem. Commun.* **2021**, *57*, 10895–10898.
12. M. E. Bowden, G. J. Gainsford, W. T. Robinson, *Aust. J. Chem.* **2007**, *60*, 149–153.
13. Y. Shao, D. Truhlar, *Theor. Chem. Acc.* **2008**, *120*, 215–241.
14. T. H. Dunning Jr., *J. Chem. Phys.* **1989**, *90*, 1007–1023.
15. a) E. M. Leitao, N. E. Stubbs, A. P. M. Robertson, H. Helten, R. J. Cox, G. C. Lloyd-Jones, I. Manners, *J. Am. Chem. Soc.* **2012**, *134*, 16805–16816; b) N. E. Stubbs, A.

- Schäfer, A. P. M. Robertson, E. M. Leitao, T. Jurca, H. A. Sparkes, C. H. Woodall, M. F. Haddow, I. Manners, *Inorg. Chem.* **2015**, *54*, 10878–10889; c) M. W. Lui, N. R. Paisley, R. McDonald, M. J. Ferguson, E. Rivard, *Chem. Eur. J.* **2016**, *22*, 2134–2145.
16. F. Dankert, J.-E. Siewert, P. Gupta, F. Weigend, C. Hering-Junghans, *Angew. Chem. Int. Ed.* **2022**, *61*, e202207064.
17. a) C. A. Jaska, K. Temple, A. J. Lough, I. Manners, *J. Am. Chem. Soc.* **2003**, *125*, 9424–9434; b) A. Staubitz, A. Presa Soto, I. Manners, *Angew. Chem. Int. Ed.* **2008**, *47*, 6212–6215.
18. R. Ayyappan, Y. Coppel, L. Vendier, S. Ghosh, S. Sabo-Etienne, S. Bontemps, *Chem. Commun.* **2021**, *57*, 375–378.
19. E. D. Glendening, J. K. Badenhoop, A. E. Reed, J. E. Carpenter, J. A. Bohmann, C. M. Morales, C. R. Landis, F. Weinhold, *NBO 6.0*, Theoretical Chemistry Institute, University of Wisconsin, Madison WI, 2013.
20. For similar hydride-halide exchanges, see: a) P. Bag, A. Porzelt, P. J. Altmann, S. Inoue, *J. Am. Chem. Soc.* **2017**, *139*, 14384–14387; b) J. H. Muessig, M. Thaler, R. D. Dewhurst, V. Paprocki, J. Seufert, J. D. Mattock, A. Vargas, H. Braunschweig, *Angew. Chem. Int. Ed.* **2019**, *58*, 4405–4409.
21. R. Conrady, W. Müller-Warmuth, B. Krebs, G. Schwetlik, M. Wienkenhöver, *Ber. Bunsenges. Phys. Chem.* **1987**, *91*, 1322–1326.
22. I. M. Alecu, J. Zheng, Y. Zhao and D. G. Truhlar, *J. Chem. Theory Comput.* **2010**, *6*, 2872–2887.
23. C. Jones, *Nat. Rev. Chem.* **2017**, *1*, 0059.

24. D. E. Ryan, K. A. Andrea, J. J. Race, T. M. Boyd, G. C. Lloyd-Jones, A. S. Weller, *ACS Catal.* **2020**, *10*, 7443–7448.
25. M. Schlosser, J. Hartmann, *Angew. Chem. Int. Ed. Engl.* **1973**, *12*, 508–509.
26. M. M. D. Roy, E. Rivard, *Acc. Chem. Res.* **2017**, *50*, 2017–2025.
27. N. Kuhn, T. Kratz, *Synthesis* **1993**, 561–562.
28. L. Pasumansky, D. Haddenham, J. W. Clary, G. B. Fisher, C. T. Goralski, B. Singaram, *J. Org. Chem.* **2008**, *73*, 1898–1905.
29. S. Oda, K. Ueura, B. Kawakami, T. Hatakeyama, *Org. Lett.* **2020**, *22*, 700–704.
30. M. Schmidt, H. D. Block, *Chem. Ber.* **1970**, *103*, 3705–3710.
31. R. H. Blessing, *Acta. Cryst.* **1995**, *A51*, 33–38.
32. G. M. Sheldrick, *Acta. Cryst.* **2015**, *A71*, 3–8.
33. G. M. Sheldrick, *Acta. Cryst.* **2015**, *C71*, 3–8.
34. A. L. Spek, *Acta Cryst.* **2015**, *C71*, 9–18.

Chapter 4

1. M. M. D. Roy, A. A. Omaña, A. S. S. Wilson, M. S. Hill, S. Aldridge, E. Rivard, *Chem. Rev.* **2021**, *121*, 12784–12965.
2. a) M. S. Hill, D. J. Liptrot, C. Weetman, *Chem. Soc. Rev.* **2018**, *118*, 3608–3680; b) T. J. Hadlington, M. Driess, C. Jones, *Chem. Soc. Rev.* **2018**, *47*, 4176–4197; c) R. J. Less, H. R. Simmonds, S. B. J. Dane, D. S. Wright, *Dalton Trans.* **2013**, *42*, 6337–6343.
3. a) P. P. Power, *Nature* **2010**, *463*, 171–177; b) R. Rodriguez, D. Gau, Y. Contie, T. Kato, N. Saffon-Merceron, A. Bacciredo, *Angew. Chem. Int. Ed.* **2011**, *50*, 11492–11495; c) S. Yao, Y. Xiong, M. Driess, *Acc. Chem. Res.* **2017**, *50*, 2026–2037; d) V.

Nesterov, D. Reiter, P. Bag, P. Frisch, R. Holzner, A. Porzelt, S. Inoue, *Chem. Rev.* **2018**, *118*, 9678–9842; e) J. Hicks, P. Vasko, J. M. Goicoechea, S. Aldridge, *Nature* **2018**, *557*, 92–95; f) R. Kobayashi, S. Ishida, T. Iwamoto, *Angew. Chem. Int. Ed.* **2019**, *58*, 9425–9428; g) M.-A. Légaré, M. Rang, G. Bélanger-Chabot, J. I. Schweizer, I. Krummenacher, R. Bertermann, M. Arrowsmith, M. C. Holthausen, H. Braunschweig, *Science* **2019**, *363*, 1329–1332; h) W. Lu, Y. Li, R. Kinjo, *J. Am. Chem. Soc.* **2019**, *141*, 5164–5168; i) K. M. Marczenko, J. A. Zurakowski, K. L. Bamford, J. W. M. MacMillan, S. S. Chitnis, *Angew. Chem. Int. Ed.* **2019**, *58*, 18096–18101; j) T. Sugahara, J.-D. Guo, D. Hashizume, T. Sasamori, N. Tokitoh, *J. Am. Chem. Soc.* **2019**, *141*, 2263–2267; k) S. Kurumada, S. Takamori, M. Yamashita, *Nat. Chem.* **2020**, *12*, 36–39; l) S. Fujimori, S. Inoue, *Eur. J. Inorg. Chem.* **2020**, 3131–3142; m) C. Shan, S. Yao, M. Driess, *Chem. Soc. Rev.* **2020**, *49*, 6733–6754; n) P. P. Power, *Organometallics* **2007**, *26*, 4362–4372; o) C. Weetman, S. Inoue, *Chem. Cat. Chem.* **2018**, *19*, 4213–4228.

4. a) B. D. Reken, T. M. Brown, J. C. Fettinger, H. M. Tuononen, P. P. Power, *J. Am. Chem. Soc.* **2012**, *134*, 6504–6507; b) T. J. Hadlington, B. Schwarze, E. I. Izgorodina, C. Jones, *Chem. Commun.* **2015**, *51*, 6854–6857; c) Y. Peng, J.-D. Guo, B. D. Ellis, Z. Zhu, J. C. Fettinger, S. Nagase, P. P. Power, *J. Am. Chem. Soc.* **2009**, *131*, 16272–16282; d) S. M. I. Al-Rafia, A. C. Malcolm, R. McDonald, M. J. Ferguson, E. Rivard, *Chem. Commun.* **2012**, *48*, 1308–1310; e) S. M. I. Al-Rafia, P. A. Lummis, A. K. Swarnakar, K. C. Deutsch, M. J. Ferguson, R. McDonald, E. Rivard, *Aust. J. Chem.*

2013, *66*, 1235–1245; f) M. M. D. Roy, S. R. Baird, E. Dornsiepen, L. A. Paul, L. Miao, M. J. Ferguson, Y. Zhou, I. Siewert, E. Rivard, *Chem. Eur. J.* **2021**, *27*, 8572–8579.

5. a) R. Rodriguez, Y. Contie, R. Noug  , A. Baceiredo, N. Saffon-Merceron, J. M. Sotiropoulos, T. Kato, *Angew. Chem. Int. Ed.* **2016**, *55*, 14355–14358; b) J. Tremmel, J. Tydlit  t, L. Dost  l, A. Ru  i  ka, X. Deraet, J. Turek, R. Jambor, *Chem. Eur. J.* **2020**, *26*, 6070–6075.

6. a) R. Dobrovetsky, D. W. Stephan, *J. Am. Chem. Soc.* **2013**, *135*, 4974–4977; b) D. W. Stephan, *Science* **2016**, *354*, aaf7229; c) J. Li, C. G. Daniliuc, G. Kehr, G. Erker, *Angew. Chem. Int. Ed.* **2019**, *58*, 6737–6741.

7. A. A. Oma  a, R. K. Green, R. Kobayashi, Y. He, E. R. Antoniuk, M. J. Ferguson, Y. Zhou, J. G. C. Veinot, T. Iwamoto, A. Brown, E. Rivard, *Angew. Chem. Int. Ed.* **2021**, *60*, 228–231.

8. B. L. Frenette, A. A. Oma  a, M. J. Ferguson, Y. Zhou, E. Rivard, *Chem. Commun.* **2021**, *57*, 10895–10898.

9. S. Bontemps, G. Bouhadir, K. Miqueu, D. Bourissou, *J. Am. Chem. Soc.* **2006**, *128*, 12056–12057.

10. Selected examples for the use of Khyp in the syntheses of related Si species: a) C. Marschner, *Eur. J. Inorg. Chem.* **1998**, 221–226; b) M. M. D. Roy, M. J. Ferguson, R. McDonald, Y. Zhou, E. Rivard, *Chem. Sci.* **2019**, *10*, 6476–6481; c) A. V. Protchenko, A. D. Schwarz, M. P. Blake, C. Jones, N. Kaltsoyannis, P. Mountford, S. Aldridge, *Angew. Chem. Int. Ed.* **2013**, *52*, 568–571; d) D. Wendel, A. Porzelt, F. A. D. Herz, D. Sakar, C. Jandl, S. Inoue, B. Rieger, *J. Am. Chem. Soc.* **2017**, *139*, 8134–8137.

11. A. C. Filippou, O. Chernov, G. Schnakenburg, *Angew. Chem. Int. Ed.* **2009**, *48*, 5687–5690.
12. a) F. Meyer-Wegner, A. Nadj, M. Bolte, N. Auner, M. Wagner, M. C. Holthausen, H.-W. Lerner, *Chem. Eur. J.* **2011**, *17*, 4715–4719; b) J. I. Schweizer, A. G. Sturm, T. Porsch, M. Berger, M. Bolte, N. Auner, M. C. Holthausen, *Z. Anorg. Allg. Chem.* **2018**, *644*, 982–988; c) R. S. Ghadwal, K. Pröpper, B. Dittrich, P. G. Jones, H. W. Roesky, *Inorg. Chem.* **2011**, *50*, 358–364.
13. a) Y. Wang, Y. Xie, P. Wei, R. B. King, H. F. Schaefer III, P. v. R. Schleyer, G. H. Robinson, *Science* **2008**, *321*, 1069–1071; b) R. S. Ghadwal, H. W. Roesky, S. Merkel, J. Henn, D. Stalke, *Angew. Chem. Int. Ed.* **2009**, *48*, 5683–5686.
14. a) J. L. Berkowitz, J. P. Green, H. Cho, R. Ruscic, *J. Chem. Phys.* **1987**, *86*, 1235–1248; b) Y. Apeloig, R. Pauncz, M. Karni, R. West, W. Steiner, D. Chapman, *Organometallics* **2003**, *22*, 3250–3256; c) S. K. Shin, W. A. Goddard III, J. L. Beauchamp, *J. Phys. Chem.* **1990**, *94*, 6963–6969; d) M. Benavides-Garcia, K. Balasubramanian, *J. Phys. Chem.* **1992**, *97*, 7537–7544; e) J.-C. Barthelat, B. S. Roch, G. Trinquier, J. Satgé, *J. Am. Chem. Soc.* **1980**, *102*, 4080–4085.
15. Y. Shao, D. Truhlar, *Theor. Chem. Acc.* **2008**, *120*, 215–241.
16. T. H. Dunning Jr., *J. Chem. Phys.* **1989**, *90*, 1007–1023.
17. P. Jutzi, U. Holtmann, D. Kanne, C. Krüger, R. Blom, R. Gleiter, I. Hyla-Kryspin, *Chem. Ber.* **1989**, *122*, 1629–1639.
18. a) P. Jutzi, F. Kohl, P. Hofmann, C. Krüger, Y.-H. Tsay, *Chem. Ber.* **1980**, *113*, 757–769; b) P. Jutzi, B. Hielscher, *Organometallics* **1986**, *5*, 1201–1204.

19. a) H. F. T. Klare, M. Oestreich, *Dalton Trans.* **2010**, 39, 9176–9184; b) J. C. L. Walker, H. F. T. Klare, M. Oestreich, *Nat. Rev. Chem.* **2020**, 4, 54–62; c) E. Fritz-Langhals, *Org. Process Res. Dev.* **2019**, 23, 2369–2377; d) E. Fritz-Langhals, S. Werge, S. Kneissl, P. Piroutek, *Org. Process Res. Dev.* **2020**, 24, 1484–1495.
20. a) Y. Cao, W.-C. Shih, N. Bhuvanesh, O. V. Ozerov, *Dalton Trans.* **2019**, 48, 9959–9961; b) M. Sircoglou, S. Bontemps, M. Mercy, N. Saffon, M. Takahashi, G. Bouhadir, L. Maron, D. Bourissou, *Angew. Chem. Int. Ed.* **2007**, 46, 8583–8586.
21. V. O. Smirnov, A. D. Volodin, A. A. Korlyukov, A. D. Dilman, *Angew. Chem. Int. Ed.* **2020**, 59, 12428–12431.
22. K. Miyamoto, S. Narita, Y. Masumoto, T. Hashishin, T. Osawa, M. Kimura, M. Ochiai, M. Uchiyama, *Nat. Commun.* **2020**, 11, 2134.
23. E. D. Glendening, J. K. Badenhoop, A. E. Reed, J. E. Carpenter, J. A. Bohmann, C. M. Morales, C. R. Landis, F. Weinhold, *NBO 6.0*, Theoretical Chemistry Institute, University of Wisconsin, Madison WI, 2013.
24. a) P. E. M. Berthelot, *Arch. Pharm. Pharm. Med. Chem.* **1868**, 185, 268–269; b) N. G. Connelly, W. E. Geiger, *Chem. Rev.* **1996**, 96, 877–910.
25. R. J. Bowen, A. C. Garner, S. J. Berners-Price, I. D. Jenkins, R. E. Sue, *J. Organomet. Chem.* **1998**, 29, 181–184.
26. a) T. F. Vaughan, J. L. Spencer, *Inorg. Chim. Acta.* **2016**, 442, 24–29; b) S. J. Berners-Price, R. J. Bowen, P. Galettis, P. C. Healy, M. J. McKeage, *Coord. Chem. Rev.* **1999**, 185–186, 823–836; c) P. Espinet, K. Soulantica, *Coord. Chem. Rev.* **1999**, 193–195, 499–556; d) B. A. Trofimov, N. K. Gusarova, A. V. Artem'ev, S. F.

- Malysheva, N. A. Belogorlova, A. O. Korocheva, O. N. Kazheva, G. G. Alexandrov, O. A. Dyachenko, *Mendeleev Commun.* **2012**, *22*, 187–188.
27. J. Dogan, J. B. Schulte, G. F. Swiegers, S. B. Wild, *J. Org. Chem.* **2000**, *65*, 951–957.
28. J. Sinclair, W. Medroa del Pino, K. Aku-Dominguez, Y. Minami, A. Kiran, M. J. Ferguson, M. Yasuda, E. Rivard, *Dalton Trans.* **2021**, *50*, 17688–17696.
29. H. Gilman, G. E. Dunn, *J. Am. Chem. Soc.* **1951**, *73*, 5077–5079.
30. M. Berger, N. Auner, M. Bolte, *Acta Cryst.* **2014**, *C70*, 1088–1091.
31. F. X. Kohl, P. Jutzi, *Chem. Ber.* **1987**, *120*, 1539–1543.
32. L. Jafarpour, E. D. Stevens, S. P. Nolan, *Organomet. Chem.* **2000**, *606*, 49–54.
33. R. H. Blessing, *Acta Cryst.* **1995**, *A51*, 33–38.
34. G. M. Sheldrick, *Acta Cryst.* **2015**, *A71*, 3–8.
35. G. M. Sheldrick, *Acta Cryst.* **2015**, *C71*, 3–8.
36. O. V. Dolomanov, L. J. Bourhis, R. J. Gildea, J. A. K. Howard, H. Puschmann, *J. Appl. Cryst.* **2009**, *42*, 339–341.

Chapter 5

1. For an overview of SiH₄ and GeH₄ use in the production of Si and Ge films, see: a) R. A. Street, *Technology and Applications of Amorphous Silicon*; Springer-Verlag; Berlin **2000**, *37*, 94–146; b) H. Ishii, Y. Takahashi, J. Murota, *Appl. Phys. Lett.* **1985**, *47*, 863–864 and references therein.
2. R. Basu, *Mater. Adv.* **2022**, *3*, 4489–4513.

3. S. M. I. Al-Rafia, A. C. Malcolm, R. McDonald, M. J. Ferguson, E. Rivard, *Angew. Chem. Int. Ed.* **2011**, *50*, 8354–8357.
4. M. Fraga, R. Pessoa, *Micromachines* **2020**, *11*, 799–799.
5. H. T. Teunissen, C. B. Hansen, F. Bickelhaupt, *Phosphorus Sulfur Silicon Relat. Elem.* **1996**, *118*, 309–312.
6. R. Ayyappan, Y. Coppel, L. Vendier, S. Ghosh, S. Sabo-Etienne, S. Bontemps, *Chem. Commun.* **2021**, *57*, 375–378.
7. a) J. Dogan, J. B. Schulte, G. F. Swiegers, S. B. Wild, *J. Org. Chem.* **2000**, *65*, 951–957; b) T. F. Vaughan, J. L. Spencer, *Inorg. Chim. Acta.* **2016**, *442*, 24–29.